

Computer Modeling of the Mesoscale Structure and Mechanical Behavior of Carbon
Nanotube Materials

A Dissertation

Presented to
the faculty of the School of Engineering and Applied Science
University of Virginia

in partial fulfillment
of the requirements for the degree

Doctor of Philosophy

by

Bernard Wittmaack

May

2018

APPROVAL SHEET

The dissertation
is submitted in partial fulfillment of the requirements
for the degree of
Doctor of Philosophy



AUTHOR

The dissertation has been read and approved by the examining committee:

Leonid Zhigilei

Advisor

Petra Reinke

Haydn Wadley

Pamela Norris

Alexey Volkov

Accepted for the School of Engineering and Applied Science:



Craig H. Benson, Dean, School of Engineering and Applied Science

May
2018

Abstract

Carbon nanotube (CNT) materials constitute a broad class of multifunctional hierarchical materials deriving their properties from the intimate connections between the atomistic structure of individual CNTs, the arrangements of CNTs into mesoscopic structural elements, such as CNT bundles and branching structures, and the structural organization of the mesoscopic elements into a macroscopic network. Due to their unique combination of structural (low density, high surface area, and nanoscale porosity), mechanical (high conformity, ability to support large reversible deformation, and absorb mechanical energy) and transport (thermal and electrical conductivity tunable over a broad range by structural modification) properties, CNT materials are attractive for a variety of applications. The strong structural sensitivity of the mechanical and thermal properties of CNT network materials makes it possible to tune the properties to the needs of practical applications, but also highlights the need for clear fundamental understanding of the structure-property relationships.

Under conditions when a systematic experimental exploration of the structure-properties relationships is hampered by the difficulty of growing CNT materials with well-controlled structures, computer modeling presents an attractive alternative. Therefore, in this study, the structure and mechanical properties of CNT network materials are investigated with a state-of-the-art mesoscale computational model. As the first step, an effective and flexible method for the generation of computational samples for mesoscopic modeling of anisotropic networks of CNT bundles with various degrees of CNT alignment is developed and applied for investigation of structural self-organization of nanotubes into vertically aligned CNT forests. Structural characteristics of the computational samples, such as bundle size distribution, average and maximum bundle sizes, magnitude of the Hermann orientation factor, and average tilt of CNT segments with respect to direction of alignment, are calculated and related to parameters of the sample preparation procedure. Good agreement between the computer-generated and experimentally grown network structures is demonstrated.

Once generated, the response of *in silico* vertically-aligned carbon nanotube (VACNT) forests with different densities and microstructures (bundle size distribution and degree of nanotube alignment) to uniaxial compression is measured, and a clear microscopic picture of the

structural changes in the networks of interconnected CNT bundles undergoing mechanical deformation is obtained. The simulation results reveal the important role of the collective buckling of CNTs across bundle cross-sections as well as a complex deformation behavior of VACNT arrays defined by an interplay of different modes of bundle deformation. The loading rate and the CNT attachment to the indenter are found to have a strong effect on the deformation mechanisms and the overall mechanical behavior of VACNT forests. A good agreement with experimental data from *in situ* mechanical tests is observed for the general trends and magnitudes of loss coefficients predicted in the simulations.

Mechanistically, the compressive deformation of sufficiently tall VACNT forests proceeds as a phase transformation. Mesoscale simulations of a 2-micron-high forest sample reveals the formation of a localized densified phase consisting of entangled CNT bundles oriented parallel to the indenter. At a given strain, the densified layer coexists with a rarified, vertically oriented phase characteristic of the unstrained forest, and the densification front advances with increasing compressive strain until it reaches the base of the forest. In addition, the simulations reveal the origin of the collective buckling of CNT bundles localized within a forest cross-section.

In the last part of this study, the resistance of CNT films to a high velocity impact by a metal nanoparticle is investigated. Modifications of a general coarse-grained model for the mesoscale representation of a metal projectile are introduced to make it suitable for use in simulations of high energy collisions, where local thermal equilibrium cannot be assumed. Specifically, a heat bath approach accounting for the heat capacity of the projectile material and a force scaling correction for accurate description of thermophysical properties are incorporated into the model. The first mesoscopic simulations of metal nanoparticle impact reveal an important role the network structure of the CNT films plays in defining the ballistic impact resistance. A simple analytical model is suggested for the estimation of the penetration depth of a nano-projectile into a bulk CNT network material for different impact velocities. The model is parametrized based on the results of the mesoscopic simulations, and represents an important advance in the understanding of the ballistic resistance of CNT materials.

Acknowledgements

I would like to first express my gratitude to my advisor, Prof. Leo Zhigilei. Throughout my time in his group, he has continued to make me a better and more independent researcher. His deep insight, rigorous approach to problem solving, and scholarly excellence make him a source of great inspiration to me. I am also grateful that he always made himself available for discussions even when he was very busy.

Another person crucial to not only my dissertation project but also my development as a researcher is Prof. Alexey Volkov at the University of Alabama. Prof. Volkov has written much of the code for the mesoscale modeling of carbon nanotubes that I used extensively throughout my graduate studies, and has provided me invaluable assistance in working with the code and identifying bugs. His guidance and insight have been instrumental in improving the scientific value of my work.

Furthermore, I would like to thank the rest of the members of my dissertation committee, Profs. Petra Reinke, Pamela Norris, and Haydn Wadley. In addition, I also want to acknowledge Drs. Kris Wise and Benjamin Jensen at NASA Langley Research Center for their support over the past few years.

All of the past and present members of the computational materials group at UVa have made a great impact on me as both friends and colleagues. I would especially like to thank Maxim Shugaev and Dr. Cheng-Yu Shih who have been among my closest friends. A special thanks to Miao He for his friendship and his invitation to work together on the MACC consulting project where I learned so much. In addition, I would like to thank group alumni, Drs. Eaman Karim, Marshall Tabetah, Richard Salaway, Chengping Wu, and visiting graduate students Wu Han and Hao Huang for many valuable and friendly discussions. Finally, I am glad to have met the newest members to the group, Dr. Kaushik Joshi, Chaobo Chen, and Mikhail Arefev.

Outside of my research group, graduate school would not have been the same if it were not for some of the incredible friendships that I have built here. In particular, I will remember the fun times I shared with Drs. Ehsan Monazami, Gopal Ramalingam, Balaji Kannan, Jishnu Bhattacharyya, Jatin Amatyia, Robert Golden, and Cameron Volders.

The staff of the MSE department have helped me on numerous occasions and have my deepest gratitude. I would like to thank Kim Fitzhugh-Higgins for her constant support and for our many interesting discussions. She always puts the graduate students of the MSE department first and deserves my special thanks. In addition, I would like to thank Eric Newsome, Jeannie Reese, Sherri Sullivan, and Rusty Wright for all of their help and support.

I have had two wonderful opportunities teach undergraduates during my time at UVa. The first was as a MSE teaching fellow under the mentorship of Prof. William Johnson for introductory calculus (APMA 1090). Prof. Johnson taught me every aspect of teaching an undergraduate class, from writing lesson plans and delivery of the material to writing and grading tests and quizzes. His caring and patient approach as a teacher and a mentor have impacted me greatly. The second opportunity was as a TA with Prof. Jerrold Floro for introduction to the science and engineering of materials (MSE 2090). Prof. Floro is a pioneer in the process oriented guided inquiry learning (POGIL) approach, a teaching philosophy that focuses on student, group-based exploration of the material through guided activities. With him, I helped design a class projected inspired by the POGIL method and learned so much about the pedagogical state of the art. His determination to make his students into better scientists by inspiring curiosity and exploration based learning is truly commendable, and I am grateful to have been a small part of it.

In addition to all of those who have guided and helped me during my time at UVa, I also would like to deeply thank the person who first introduced me to scientific research, Prof. Kelling Donald at the University of Richmond. I treasure the time that I worked in his research group on exploring the nature of the chemical bond throughout all of my undergraduate years and beyond. Under his mentorship I developed my foundations as a researcher and my passion for computational modeling.

The last several years of my graduate studies and life have been made immensely better by my partner, Amaya. With her, I have grown tremendously as a person and she has provided me with so much happiness and support. She has my enduring love and gratitude.

Finally, I owe so much to my family who has encouraged and supported me throughout my entire life. I especially would like to recognize my parents who have made this all possible and who believed in my dreams.

Contents

Abstract	i
Acknowledgements	iii
List of figures	ix
List of tables	xix
1. Introduction	1
1.1 Carbon nanotubes	1
1.2 Carbon nanotubes materials and their applications	3
1.3 Guide to dissertation	5
2 Coarse-grained model for the representation of CNT materials on the mesoscale	7
2.1 Atomistic molecular dynamics and its limitations	7
2.2 Overview of mesoscopic modeling of CNT materials	9
2.3 Tubular mesoscopic model for CNTs	11
2.3.1 Axial deformation	13
2.3.2 Bending deformation	14
2.3.3 Torsional deformation	16
2.3.4 Intertubular potential	16
2.4 Heat bath	21
2.4.1 Temperature control through thermostats	21
2.4.2 Inclusion of heat bath in mesoscopic code for CNTs	22
2.4.3 Heat capacity of the heat bath	23
2.4.4 Dissipation of stretching and bending vibrations into heat bath	25
2.4.5 Dissipation of acoustic vibrations in the mesoscopic model	26
2.4.6 Localized energy dissipation	28
3 Structural self-organization of carbon nanotubes into vertically aligned arrays	30

3.1	Introduction	30
3.2	Making VACNT forests <i>in silico</i>	31
3.3	Structural characteristics of VACNT forests	36
3.4	The effect of CNT length in short VACNT forests.....	42
3.5	Application of mesoscopic modeling to investigation of mechanical and thermal properties.....	45
3.6	Summary	51
4	Uniaxial compression and recovery of VACNT forests.....	53
4.1	Introduction	53
4.2	Computational samples of VACNT forests	57
4.3	Uniaxial compression of VACNT forests	59
4.3.1	Role of microstructure	59
4.3.2	Role of compression rate	66
4.3.3	Role of density	69
4.3.4	Role of CNT interaction with indenter	72
4.4	Recovery of VACNT forests.....	80
4.4.1	Repulsive CNT-indenter interaction.....	80
4.4.2	CNTs attached to indenter	85
4.5	Summary	88
5	Mechanism of deformation and phase transformation during uniaxial compression of VACNT forests.....	91
5.1	Introduction	91
5.2	Computational Method and Setup.....	94
5.2.1	Mesoscopic force field for carbon nanotube materials.....	94
5.2.2	VACNT forest samples.....	95
5.2.3	Simulation of the uniaxial compression.....	96

5.3	Deformation mechanisms and phase separation for 2 μm VACNT forest.....	99
5.3.1	Formation of densified phase.....	99
5.3.2	Stability of densified phase.....	104
5.3.3	Origins of coordinated buckling in VACNT forests.....	105
5.4	Effect of forest structure and length on deformation mechanisms.....	110
5.5	Role of fracture during uniaxial compression.....	115
5.6	Summary	117
6	Development of a coarse-grained potential for metals	118
6.1	Introduction	118
6.2	Quasi-coarse-grained dynamics	120
6.2.1	Choosing representative atoms	120
6.2.2	Interaction between the R-atoms	121
6.2.3	Energy scaling of R-atoms.....	122
6.3	Modification of the QCGD model	123
6.3.1	Formulation of heat bath for QCGD model.....	123
6.3.2	Determination of coupling constant τ	127
6.3.3	Force scaling.....	129
6.3.4	Testing of modified QCGD model	129
6.4	Metal-CNT interaction	131
7	Ballistic impact resistance of CNT films.....	133
7.1	Introduction	133
7.2	CNT films and metal projectile.....	135
7.2.1	CNT films	135
7.2.2	Pt nanoparticle	135
7.3	Analytical determination of projectile penetration.....	137

7.4	Impact simulations	138
7.5	Summary	142
8	Summary and future work	143
8.1	Summary of dissertation.....	143
8.2	Impact of work	146
8.3	Future work	147
8.3.1	Ballistic impact resistance of CNT films	147
8.3.2	Thermal properties of CNT materials	148
	References.....	149

List of figures

Figure 1.1: Schematic representation of (a) single-walled carbon nanotube (SWCNT), (b) multi-walled carbon nanotubes (MWCNTs). The color distinguishes separate walls [4].....	2
Figure 1.2: (a) Schematic of the roll-up of graphene to form a SWCNT structure. (b) \mathbf{OO}' defines the chiral vector, \mathbf{Ch} . Translation vector, \mathbf{T} , is along the nanotube axis and perpendicular to \mathbf{Ch} . The shaded area represents the unrolled unit cell formed by \mathbf{T} and \mathbf{Ch} . The chiral angle, θ , is defined as the angle between \mathbf{Ch} and the $(n, 0)$ zigzag direction. The $n, 0$ and (n, n) armchair SWCNTs are indicated in blue and red markings, respectively [4, 5].....	3
Figure 1.3: Ashby chart of loss coefficient vs the product of plateau stress and thermal conductivity of a variety of foam materials. Taken from ref. [32].	5
Figure 2.1: The MD algorithm. Reproduced from L. V. Zhigilei's course notes for Atomistic Simulations (MSE 4270/6270) at the University of Virginia	8
Figure 2.2: Typical length and time scales of various levels of computational modeling. Adapted from L. V. Zhigilei's course notes for Atomistic Simulations (MSE 4270/6270) at the University of Virginia.....	9
Figure 2.3: Overview of the coarse-grained model for mesoscale representation of CNTs. Schematic representation of a section of nanotube represented by four segments and five nodes (a). The position of the i^{th} node in the nanotube (\mathbf{rit}), the radius of the nanotube at node i (Rit), and the torsion angle at node i (θit) are the independent variables that describe the behavior of the nanotube. The equations that control the motion and thermal transport in CNT materials (b), and the components of the mesoscopic force field (c).	11
Figure 2.4: Schematic representation of the description of bending buckling in the mesoscopic model (a) and the dependence of the bending energy U^{bnd} on the bending angle θ in a uniformly bent CNT with a single buckling point appearing in the middle (point B in the insert) when the critical radius of curvature, R_{cr} , is reached (b). Bending energy in (b) is obtained by minimizing the strain energy associated with the bending and buckling. Values of the bending energy in (b) are scaled by $U^* = kbnd/LT$ where LT is the length of the CNT. Taken from ref. [76].	15
Figure 2.5: Schematic sketch illustrating the introduction of local coordinates $Oxyz$ and geometrical parameters used for characterization of the relative positions of two nonparallel (a) and parallel (b) straight cylindrical CNT segments. The side and top views are shown in panel a; only the side view is shown in panel b. In panel a, the axis x is directed along the vector \mathbf{OO}'	

defining the shortest distance between the axes of the segments. In panel b, for the origin of the Cartesian coordinates is chosen so that the axis Ox goes through the left end of the second segment $\eta_1 = 0$. Cross sections of the segments are shown in panel b, with angles ϕ_1 and ϕ_2 specifying positions of points in the cross sections used for integration over the surfaces of the two segments. Taken from ref [57]..... 17

Figure 2.6: Schematic representation of the tubular mesoscopic model (a), and the bead and spring model (b). The CNT configurations in the right panels are fragments of CNT networks obtained in the simulations performed with the two models. In (a) the CNTs are colored by their local radii of curvature where the red color corresponds to buckled segments. The configuration in (b) is from ref. [58] The CNTs do not bundle together due to the artificial friction present in the bead and spring model, but the mesoscopic model with the tubular potential does accurately reproduce this behavior..... 21

Figure 2.7: Snapshots from mesoscopic simulation of the high-velocity impact of a spherical projectile with a diameter of 100 nm, a density of 2.8 g/cm³ and an initial velocity of 1000 m/s on a free standing 20-nm-thick CNT film. The snapshots are shown for 55, 125, and 255 ps after the onset of the impact. The film has a density of 0.2 g/cm³, and the CNTs in the film are arranged in a continuous network of bundles. The nanotubes are colored by their local kinetic energy, and the projectile is not shown in the snapshots..... 23

Figure 2.8: Schematic illustration of the mapping of (a) the atomic model of a (10,10) CNT to a chain of coarse-grained particles and (b) a unit cell ring of the (10,10) CNT to a closed chain of 10 point masses. The coarse-grained representations are used in the analysis of the partitioning of the vibrational energy between the longitudinal, bending, and radial modes. Taken from ref [77]... 24

Figure 2.9: An illustration of the hysteresis approach to the localized energy dissipation upon buckling in the mesoscopic model. The compressive part of the axial strain energy is shown schematically in (a), and an enlarged view of the hysteresis region is shown in (b). The blue arrows in (b) represent the path followed when a buckling kink is created. The red segments of the plot are the irreversible parts of the strain energy hysteresis. ΔE_{strbcl} is the amount of energy transferred to the heat bath of the CNT in each buckling cycle. Taken from ref [77]..... 29

Figure 3.1: Chart showing the areal densities and CNT diameters of five representative SWCNT forests grown by CVD (marked as Zhong 2012 [78], Kang 2007 [76], Zhong 2006 [74], Einarsson

2007 [77], and Futaba 2006 [75]) along with the four SWCNT forests generated in silico in this work (marked as FA, FB, FC, and FD).....	32
Figure 3.2: Schematic representation of the procedure used for the generation of VACNT samples. Straight CNTs are first randomly placed on a substrate with a random inclination with respect to the substrate normal θ , ranging uniformly from zero to a maximum angle θ_{max} (a). The high temperature annealing followed by a relaxation at 300 K is used to induce self-organization of CNTs into a continuous metastable network of interconnected bundles (b). A single representative nanotube is highlighted, colored by its local bundle thickness, and shown in front of the other nanotubes. All other nanotubes are colored gray.....	36
Figure 3.3: Side views of computational samples of forests FA (a), FB (b), and FC (c) generated in mesoscopic simulations. The CNT segments are colored by the local bundle thickness (number of segments in a bundle cross section). Data files defining the structures of the computational samples shown in this figure are accessible from Ref. [110].	37
Figure 3.4: Enlarged views of computational VACNT forests FA (a), FB (b), and FC (c) illustrating the degree of interconnection among the bundles. The coloring scheme is the same as in Figure 3.3.....	37
Figure 3.5: The bundle thickness distributions calculated for computational samples FA (a), FB (b), and FC (c), as well as for a laboratory-grown forest analyzed in Ref. [77] (d). In the computational and experimental CNT forests, the bundle thickness is expressed in the number of nanotubes present in bundle cross sections, and each bin covers a thickness increment by 1 CNT segment. In (d), the filled bars are for SWCNT bundles where the number of nanotubes can be reliably counted in TEM images, while the unfilled bars are estimates based on the visual thickness of the bundle. The star marks the number of isolated SWCNTs, and could be higher than the estimate shown in the figure.	38
Figure 3.6: Scanning Electron Microscopy (SEM) images of CVD grown SWCNT forests with smaller [77] (a) and larger [75] (b) nanotube bundles.	40
Figure 3.7: The overall view (a), an enlarged fragment (b), and the bundle thickness distribution (c) of the computational sample FD. In (a) and (b), the CNT segments are colored by the local bundle thickness (number of segments in a bundle cross section), and in (c) each bin covers a thickness increment by 1 CNT segment. Data file defining the structure of the computational sample shown in this figure is accessible from Ref. [110].	42

- Figure 3.8: Side views of computational VACNT samples composed of nanotubes with lengths of 200 nm (a–c) and 600 nm (d–f) generated in mesoscopic simulations according to the procedure described in section 3.2. The CNT segments are colored by the local bundle thickness (number of segments in a bundle cross section). 43
- Figure 3.9: A series of snapshots (a–c) and a stress-strain dependence (d) obtained in a mesoscopic simulation of uniaxial compression of the VACNT forest composed of 200-nm-long (10,10) CNTs prepared with $\Theta_{max} = 27^\circ$ (see Figure 3.8c). The snapshots are shown for compressive engineering strain of 0.2 (a), 0.4 (b) and 0.6 (c). The indenter velocity is 10 m/s, which corresponds to a deformation rate of $5 \times 10^7 \text{ s}^{-1}$. The CNT segments adjacent to the buckling kinks are colored red. 47
- Figure 3.10: The steady-state heat flux along the nanotubes obtained in the calculations of thermal conductivity of the VACNT samples FA (a), FB (b), and FC (c), see Table 1. The calculations are done assuming an intrinsic conductivity of $2000 \text{ W m}^{-1}\text{K}^{-1}$ for individual CNTs, and the inter-tube conductance is parametrized based on the results of atomistic simulations as explained in Refs. [53, 60, 70, 76, 78]. 49
- Figure 3.11: Snapshots from a mesoscopic simulation of a high-velocity impact of a spherical Pt projectile with a diameter of 100 nm, a density of 21.45 g/cm^3 and an initial velocity of 100 m/s on the VACNT sample FB (see Table 3.1). The snapshots in (a), (b), and (c) are shown for 2.5 ns, 6.0 ns, and 10.0 ns after the impact, respectively. The nanotubes are colored by their local kinetic energy, and the location of the projectile is shown by a semitransparent circle drawn in front of the VACNT configuration. Note that although it appears that the projectile is exchanging energy with the CNTs only in its localized vicinity, the entire forest is deformed during the collision, as evidenced by the shrinking height of the sample. 51
- Figure 4.1: Snapshots from simulations of uniaxial compression of computational samples FA (a) and FB (b) up to a maximum strain of 0.8 with an indenter velocity of 10 m/s. From top to bottom, the strain is 0.2, 0.4, 0.6, and 0.8. The CNT segments adjacent to buckling kinks are colored red. Two bundles exemplifying the bowing and folding modes of deformation are outlined by blue dashed lines in the snapshots for 0.6 strain in (a) and (b), respectively. 61
- Figure 4.2: Stress-strain dependences obtained in the simulations of uniaxial compression of computational samples FA (a) and FB (b) with an indenter velocity of 10 m/s, and a typical experimental stress-strain curve measured for a VACNT forest compressed at 1000 nm/s (adapted

from Ref. [124]) (c). The white, blue, and red shaded regions in (a) and (b) correspond to the elastic, plateau, and densification regimes of the compressive deformation, respectively..... 62

Figure 4.3: Plots of the changes in (a) bending, (b) axial stretching, and (c) inter-tube interaction energies per nanotube in sample FA undergoing compression at an indenter velocity of 10 m/s.64

Figure 4.4: Snapshots of sample FB compressed at indenter velocities of (a) 10 m/s, (b) 20 m/s, and (c) 50 m/s to an engineering strain of 0.6..... 67

Figure 4.5: Stress-strain response of samples FA (a-c) and FB (d-f) compressed at indenter velocities of 10 m/s, 20 m/s, and 50 m/s. The corresponding strain rates are 5×10^7 , 10^8 , and 2.5×10^8 s^{-1} 67

Figure 4.6: The evolution of the average bundle thickness in samples FA and FB compressed with indenter velocities of 10, 20, and 50 m/s up to 0.8 engineering strain. 69

Figure 4.7: Snapshots from simulations of a computational sample FC compressed at indenter velocities of (a) 10 m/s and (b) 50 m/s up to a maximum strain of 0.8. From top to bottom, the strain is 0.2, 0.4, 0.6, and 0.8. The CNT segments adjacent to buckling kinks are colored red. . 70

Figure 4.8: Stress-strain response of sample FC compressed at indenter velocities of (a) 10 m/s and (b) 50 m/s. The corresponding deformation rates are 5×10^7 and 2.5×10^8 s^{-1} . Note the twice larger scale of the stress axis used in (b)..... 71

Figure 4.9: Snapshots from “glue” simulations of sample FA compressed at indenter velocities of (a) 10 m/s and (b) 50 m/s up to a maximum strain of 0.8. From top to bottom, the strain is 0.2, 0.4, 0.6, and 0.8. The tops of the nanotubes are attached to the indenter, and the CNT segments adjacent to buckling kinks are colored red. A bundle exemplifying the higher-order serpentine bending of CNT bundles is outlined by blue dashed lines in the snapshots for 0.2 strain in (b).. 73

Figure 4.10: Stress-strain response for sample FA compressed at indenter velocities of (a) 10 m/s and (b) 50 m/s, with the tops of the nanotubes attached to the indenter..... 75

Figure 4.11: Bending energy as a function of engineering strain for sample FA compressed at indenter velocities of (a) 10 m/s, (b) 20 m/s, and (c) 50 m/s, with the tops of the nanotubes attached to the indenter. The red dashed lines cross at a point where 50% of the total increase in the bending energy has occurred, with the corresponding engineering strain labeled in the figure..... 76

Figure 4.12: The evolution of the number of buckling kinks (a) and the average bundle thickness (b) in free (solid lines) and glue (dashed lines) simulations of sample FA compressed at indenter velocities of 10, 20, and 50 m/s up to 0.8 engineering strain. 78

- Figure 4.13: Snapshots from “glue” simulations of sample FC compressed at indenter velocities of (a) 10 m/s and (b) 50 m/s up to a maximum strain of 0.8. From top to bottom, the strain is 0.2, 0.4, 0.6, and 0.8. The tops of the nanotubes are attached to the indenter, and the CNT segments adjacent to buckling kinks are colored red. 79
- Figure 4.14: Stress-strain response for sample FC compressed at indenter velocities of (a) 10 m/s and (b) 50 m/s, with the tops of the nanotubes attached to the indenter. 80
- Figure 4.15: Snapshots from two simulations of cyclic loading of sample FA shown at the end of cycles 1, 3, and 5. Each cycle consists of loading and unloading parts performed at indenter velocity of 50 m/s and followed by 7.6 ns of relaxation of the forest in the unloaded state. The loading is done up to a maximum strain of 0.8 (a-c) and 0.6 (d-f). The nanotubes are free to slide with respect to the indenter, and the CNT segments adjacent to buckling kinks are colored red. 82
- Figure 4.16: The evolution of the average bundle size (a) and number of buckling kinks (b) in two simulations of cyclic loading of sample FA. Each of the five consecutive cycles consists of loading and unloading parts performed at indenter velocity of 50 m/s and followed by 7.6 ns of relaxation in the unloaded state. The loading is done up to a maximum strain of 0.8 (black line and dots) and 0.6 (red lines and triangles). The simulations are performed for nanotubes that are free to slide with respect to the indenter. 83
- Figure 4.17: Loss coefficient evaluated in simulations of cyclic loading of sample FA done up to a maximum strain of 0.8 and 0.6 (a) and the corresponding stress-strain curves shown for cycles 1, 3, and 5 (b,c). The simulations are performed for nanotubes that are free to slide with respect to the indenter. 85
- Figure 4.18: Snapshots from two simulations of a cyclic loading of sample FA performed with indenter velocities of 10 m/s (a-c) and 50 m/s (d-f). The unloading is done down to a strain of 0.2 with respect to the original height of the forest. The nanotubes are attached to the indenter, and the snapshots are shown at the ends of cycles 1, 3, and 5. The CNT segments adjacent to buckling kinks are colored red. 86
- Figure 4.19: The evolution of the average bundle size (a) and number of buckling kinks (b) in two simulations of cyclic loading of sample FA performed with indenter velocities of 10 m/s (black lines and dots) and 50 m/s (red lines and triangles). The nanotubes are attached to the indenter, and the unloading is done down to a strain of 0.2 with respect to the original height of the forest. 87

Figure 4.20: Loss coefficient evaluated in simulations of cyclic loading of sample FA performed with indenter velocities of 10 m/s and 50 m/s (a) and corresponding stress-strain curves shown for cycles 1, 3, and 5 (b,c). The nanotubes are attached to the indenter, and the unloading is done down to a strain of 0.2 with respect to the original height of the forest.	88
Figure 5.1: SEM showing deformation of a VACNT forest during the elastic, plateau, and densification regimes [164]. Note the formation of a localized densified layer of CNTs near the indenter in the plateau regime which broadens into the densification regime.....	92
Figure 5.2: Side views of computational VACNT samples composed of nanotubes with CNT lengths of 2 μm , FA (a) and 600 nm, FB, FC, and FD (b-d) generated by mesoscopic simulations. The CNT segments are colored by the local bundle thickness (number of segments in a bundle cross section).....	98
Figure 5.3: Snapshots of the side view from the compression of FA from 0 to 0.8 engineering strain. The two-tone coloring of CNT segments is by CNT-CNT interaction energy where red indicates less favorable interaction (isolated segments) and blue indicates more favorable interaction (highly bundled segments).....	100
Figure 5.4: Snapshots of the top-down view from the compression of FA from 0 to 0.6 engineering strain in 0.2 increments. The two-tone coloring of CNT segments is by CNT-CNT interaction energy where red indicates less favorable interaction (isolated segments) and blue indicates more favorable interaction (highly bundled segments).....	101
Figure 5.5: Image plots of mass density (a) and HOF (b) calculated from sets of segments partitioned by their original position in the uncompressed forest sample. The plots contain columns corresponding to a set of strains from 0 to 0.8 incremented by 0.05, all with 50 vertical divisions each representing the same CNT node IDs.....	103
Figure 5.6: Change in CNT-CNT interaction energy (a) and bending energy (b) with engineering strain of sample FA. Image plots of average CNT-CNT interaction energy (c) and average bending energy (d) calculated from sets of segments partitioned by their original position in the uncompressed forest sample. The plots in panels c and d contain columns corresponding to a set of strains from 0 to 0.8 incremented by 0.05, all with 50 vertical divisions each representing the same CNT node IDs.....	105
Figure 5.7: Snapshots of the side view from the compression of FA from 0 to 0.8 engineering strain with an overlay showing the geometries of five typical CNTs (a) and the magnitude of the	

average deviation in the lateral position of the forest relative to its unstrained state (Δr) and change in the number of buckling kinks relative to the uncompressed sample plotted as a function of height for strains from 0.2 to 0.8 (b).....	106
Figure 5.8: Buckling model of a VACNT forest under uniform compression. (a) Initial configuration. (b) Under compression the CNT segments closer to the bottom of the forest reorient laterally. Once the buckling load is reached, the bottom portion of the forest buckles in the direction of the initial lateral reorientation. Figure adapted from ref. [126].....	107
Figure 5.9: Stress-strain response of sample FA compressed at 50 m/s.....	110
Figure 5.10: Side view snapshots from simulations of uniaxial compression of computational samples FB (a), FC (b), and FD (c) up to 0.8 engineering strain with an indenter velocity of 50 m/s. The CNT segments are colored by their CNT-CNT interaction energy on a two-colored red-blue scale. Red corresponds to high interaction energy (less favorable nanotube interaction) and blue corresponds to low interaction energy (more favorable nanotube interaction).	112
Figure 5.11: Plots of the density, HOF, magnitude of the average deviation in the lateral position of the forest relative to its unstrained state, and the change in the number of buckling kinks its unstrained state along the normalized height of the forest for samples FB, FC, and FD compressed to 0.6 strain.....	114
Figure 5.12: Stress-strain response for sample FB, FC, and FD compressed at an indenter velocity of 50 m/s to 0.9 strain.	115
Figure 5.13: Fraction of CNTs fractured with strain (a) and comparison of stresses (a), bending energy (b), and CNT-CNT interaction energy (c) for forest FD where CNT fracture is included and neglected.	116
Figure 6.1: (a) A $2 \times 2 \times 2$ unit cell atomistic system (atoms shown by blue circles) and (b) the corresponding representation of the QCGD system (CG particles shown by orange circles at their locations). Taken from ref [202].....	121
Figure 6.2: Schematic of the approach used to determine the time constant, τ . Localized groups of atoms are initially assigned the same velocity vector and then are allowed to equilibrate. The amount of time this process takes allows for the determination of τ	128
Figure 6.3: Thermalization in atomistic systems where localized groups of atoms consisting of either 8, 64, 216, or 512 members are initially given the same velocity vector.	128

- Figure 6.4: Snapshots of Pt sphere ($d=6$ nm) before and after collision at 100 m/s with rigid surface for atomistic representation (a), $Ncg = 8$ (b), $Ncg = 64$ (c), and $Ncg = 216$ (d) with the original QCGD model. 130
- Figure 6.5: Snapshots of Pt sphere ($d=20$ nm) before and after collision with a rigid surface for the case where $Ncg = 128$ with the modified QCGD model (a) and the atomistic representation (b). Collisions are shown for initial velocities of 100 and 1,000 m/s. For (a) an additional snapshot shows the deformation to the CG metal after collision at 100 m/s using the original QCGD model. 131
- Figure 7.1: Image intensified charge coupled device (ICCD) images of blackbody emission from plumes generated in short pulse laser ablation of a 20 nm thick Pt film and impinging on a fused silica (a) and vertically-aligned CNT forest (b). SEM images of cleaved CNT forest with trapped nanoparticles implanted from the ablation plume are shown in (c). Unpublished results by Christopher Rouleau, Alex Puretzky, and David Geohegan, ORNL (shown with permission from the authors) [212]. 134
- Figure 7.2: Snapshots of CNT films with lateral dimensions of 500×500 nm² and thicknesses of (a) 100 nm and (b) 300 nm. Each film has a density of 0.2 g/cm³ and consists of 200 nm long CNTs. CNT coloring is by interaction energy where blue coloring indicates low (negative) energy and red indicates high energy. 136
- Figure 7.3: Snapshot of spherical Pt nanoparticle represented by the modified QCGD model. The particle consists of 20,004 CG units each representing 216 atoms. 136
- Figure 7.4: What role does the thickness of the CNT film play in arresting the projectile? Schematic visualization of the projectile penetration into a thick CNT film (a) and sequential penetration into multiple thinner films (b). A SEM micrograph of Pt nanoparticles trapped in a VACNT forest (c) [212]. 138
- Figure 7.5: Deceleration force for the five impact simulations on 100 nm thick CNT film for initial projectile velocities of 100, 300, 500, 1000, and 2000 m/s (a). The red line represents the fitted curve through the series of points. Estimated projectile penetration depth as a function of initial velocity (b). 140
- Figure 7.6: Snapshots of the impact of the 300 nm thick CNT film by a Pt projectile with initial velocity of 1000 m/s at times of $t=100$ ps (a), $t=250$ ps (b), and $t=350$ ps (c). The CNTs are colored by their local kinetic energies, and the projectile is blanked. 141

Figure 7.7: Comparison of the energy evolution, excluding the kinetic energy of the projectile, between projectile impact with the 100 nm thick film and the 300 nm thick film. The initial velocity of the projectile is 1000 m/s..... 141

List of tables

Table 3.1: Parameters of the CNT forests generated in the mesoscopic simulations. The CNT spacing is defined as center-to-center distance assuming hexagonal packing of the nanotubes. Data files defining the structures of computational samples listed in this table are accessible from Ref. [110].	34
Table 3.2: Statistical information on the structural parameters of three computational forests of the same density of 0.02 g/cm^3 . The average tilt of CNT segments θ , average bundle size NB , maximum bundle size $NBmax$, standard deviation (SD) of the bundle size, and magnitude of the Herman orientation factor (HOF) are listed for computational samples FA, FB, and FC. The coefficients of determination R^2 are listed for linear dependencies of the structural parameters on θ_{max} .	40
Table 3.3: Statistical information on structural parameters of six computational forests of the same density of 0.02 g/cm^3 composed of CNTs with lengths L_{CNT} of 200 nm and 600 nm. The average tilt of CNT segments θ , average bundle size NB , maximum bundle size $NBmax$, standard deviation (SD) of the bundle size, and magnitude of the Herman orientation factor (HOF) are listed for computational samples generated at maximum inclination angles θ_{max} of 0.6° , 12° , and 27° .	44
Table 4.1: Typical range of mechanical properties of multi-walled VACNT forests with mass densities ranging from 0.008 to 0.2 g/cm^3 [11].	54
Table 4.2: Statistical information on structural parameters of three computational forests used in the simulations of compressive deformation reported in this paper. The density ρ , average tilt of CNT segments θ , average bundle size NB , maximum bundle size $NBmax$, and Herman orientation factor HOF are listed for computational samples FA, FB, and FC.	59
Table 5.1: Statistical information on structural parameters of four computational forests of the same density of 0.02 g/cm^3 and composed of CNTs with lengths L_{CNT} of 2 and $0.6 \mu\text{m}$. The average tilt of CNT segments θ , average bundle size NB , maximum bundle size $NBmax$, standard deviation (SD) of the bundle size, and magnitude of the Herman orientation factor (HOF) are listed for computational samples generated at maximum inclination angles θ_{max} of 0.6° , 12° , and 27° .	98

1. Introduction

1.1 Carbon nanotubes

Carbon nanotubes (CNTs) are hollow, cylindrical carbon structures that are essentially seamless rolled up graphitic sheets (Figure 1.1). Like graphene, CNTs are arranged in a hexagonal pattern of sp^2 bonded atoms. These strong covalent bonds give CNTs their excellent stiffness and strength. Another partially occupied p orbital extends radially from the nanotube for each atom, contributing to the weak non-bonded interaction between CNTs. CNTs have garnered significant interest for their extraordinary mechanical and transport properties. In particular, CNTs are among the strongest and stiffest materials known, with the upper ranges of measured Young's modulus and tensile strength approaching 1 TPa and 63 GPa, respectively [1]. In addition, the axial thermal conductivity of CNTs can exceed that of Cu [2].

Two major types of CNTs exist. One type is made up of a single sheet it is termed a single-walled carbon nanotube (SWCNT), and if a CNT has multiple concentric cylinders around a single hollow core it is called a multi-walled carbon nanotube (MWCNT). The "nano" in nanotube comes from their small diameters, ranging from 0.4-4 nm for SWCNTs, and between 5-100 nm for MWCNTs. However, their aspect ratios are typically quite high, reaching 10^6 or greater [3]. Aside from the number of walls, CNTs are distinguished by their chirality, categorized by a chiral vector and angle. The length of the chiral vector, alternatively termed rollup vector, is equal to the circumference of the tube, and is perpendicular to the tube axis (Figure 1.2). The structure of SWCNTs is defined by the rollup vector (equation (1.1)).

$$\mathbf{C}_h = n\mathbf{a}_1 + m\mathbf{a}_2 \equiv (\mathbf{n}, \mathbf{m}) \quad (1.1)$$

The primitive vectors of graphene are denoted by \mathbf{a}_1 and \mathbf{a}_2 , with m and n as integers. The translation vector, \mathbf{T} is directed along the SWCNT axis and perpendicular to \mathbf{C}_h . Its magnitude relates to the length of the (n, m) SWCNT unit cell. The integers m and n can be used to determine other properties of the SWCNT, such as its diameter, d_{CNT} .

$$d_{CNT} = \left(\frac{\sqrt{3}}{\pi}\right) a_{cc} \sqrt{m^2 + mn + n^2} \quad (1.2)$$

where a_{cc} is the carbon atom nearest neighbor distance of 0.142 nm. The graphene sheet can be rolled up in different ways to form three types of CNTs: (i) armchair, (ii) zigzag, and (iii) chiral. Armchair CNTs result when two C–C bonds on opposite sides of each hexagon are perpendicular to the tube axis, so that $n = m$ and the chiral angle defined by equation (1.3), is equal to 30° .

$$\theta = \arctan \left[\frac{\sqrt{3} m}{2n + m} \right] \quad (1.3)$$

Zigzag tubes are formed when two C–C bonds are parallel to the tube axis, making either $n = 0$ or $m = 0$, and $\theta = 0$. Chiral CNTs makeup every other conformation, where $0^\circ < \theta < 30^\circ$. The type of CNT configuration can lead to different properties. For example, a (n, m) CNT is metallic if $n - m = 3q$, where q is an integer, and semiconducting if $n - m \neq 3q$. Armchair CNTs ($n = m$) are always metallic, zigzag ($n = 0$ or $m = 0$) tubes are semi-metallic with a zero band gap between the valence and conduction bands, and two-thirds of chiral tubes are semiconducting (with a non-zero band gap).

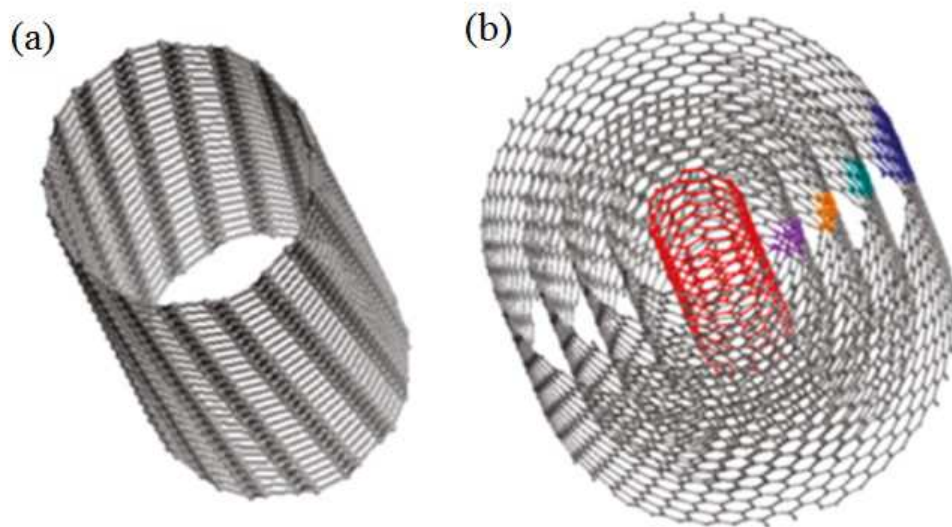


Figure 1.1: Schematic representation of (a) single-walled carbon nanotube (SWCNT), (b) multi-walled carbon nanotubes (MWCNTs). The color distinguishes separate walls [4].

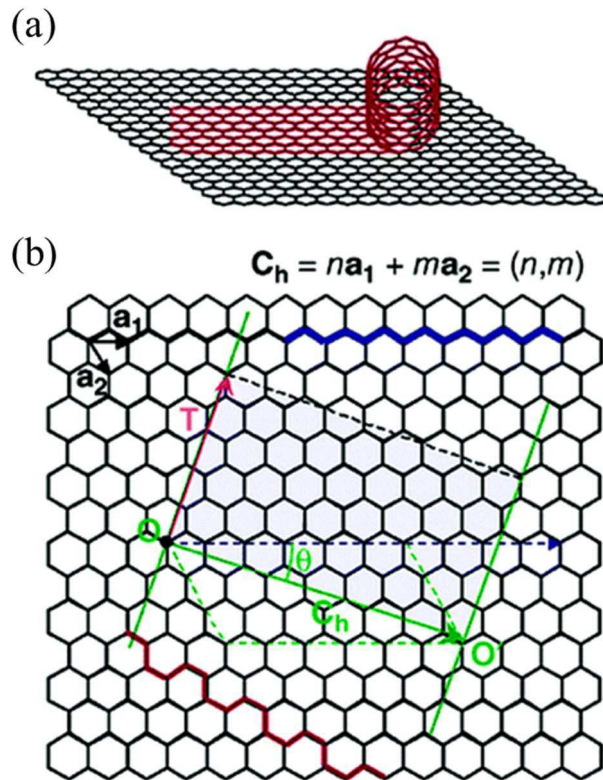


Figure 1.2: (a) Schematic of the roll-up of graphene to form a SWCNT structure. (b) OO' defines the chiral vector, C_h . Translation vector, T , is along the nanotube axis and perpendicular to C_h . The shaded area represents the unrolled unit cell formed by T and C_h . The chiral angle, θ , is defined as the angle between C_h and the $(n, 0)$ zigzag direction. The $(n, 0)$ and (n, n) armchair SWCNTs are indicated in blue and red markings, respectively [4, 5].

1.2 Carbon nanotubes materials and their applications

CNT materials constitute a broad class of hierarchical materials deriving their properties from the intimate connections between atomic structure of individual CNTs, the arrangements of CNTs into mesoscopic structural elements, such as CNT bundles and branching structures, and the structural organization of the mesoscopic elements into macroscopic networks materials. Depending on the material density and production method, the CNT materials exist in many forms, from low-density aerogels and sponges with densities of ~ 0.01 g/cm³ [6, 7], to medium-density CNT films [8-11], “forests” [12, 13], mats, and “buckypaper” [14-16] with densities of ~ 0.1 g/cm³, and to high-density super-aligned CNT fibers [17-19], forests [13] and films [20] with CNT arrangements approaching the ideal packing limit. While, in general, the van der Waals attraction between nanotubes [21] results in their self-assembly into networks of interconnected bundles [22,

23], the degree of CNT alignment, bundle and pore size distribution, and other structural characteristics of CNT networks are not uniquely defined by the length and flexural rigidity of CNTs and material density, but can be modulated by changing the parameters of the production process [23], mechanical [16] and chemical [24, 25] post-processing or radiative treatment.

The complex hierarchical organization of CNT materials and wide diversity of material structures give rise to a large variability of physical properties. For instance, the experimentally measured values of thermal conductivity of CNT materials fall into an amazingly broad range of values from 0.02 to 1000 W/m/K [19, 20, 26, 27], and suggest that the variation in structure and density of the CNT networks as well as the modulation of the intrinsic thermal conductivity of individual CNTs can turn CNT materials from perfect thermal conductors to insulators.

The mechanical properties of CNT materials also exhibit a wide range of values. Under uniaxial compression elastic properties such as the yield strength, elastic modulus, and the modulus of resilience can each vary over several orders of magnitude depending on the structural properties of the forest such as mass and tube densities, CNT radius, number of CNT walls [28]. The extent to which a CNT forest, also referred to as a vertically aligned carbon nanotube (VACNT) array or foam, recovers after it has undergone uniaxial compression is also highly variable, where some samples can withstand thousands of loading cycles [29] while deforming primarily elastically, while other forests show significant plastic deformation even after a single loading cycle [30, 31].

Although their mechanical and thermal properties can span over orders of magnitude, CNT materials and VACNT foams in particular, show promise as mechanically strong and resilient foams with exceptional thermal properties relative to conventional foam materials. Figure 1.3 shows an Ashby chart comparing the mechanical and thermal properties of VACNT foams to a variety of conventional foam materials taken from ref. [32]. From the chart, VACNT foams can be seen to have an attractive combination of mechanical and thermal properties unrivaled by conventional foams with a variety of structures.

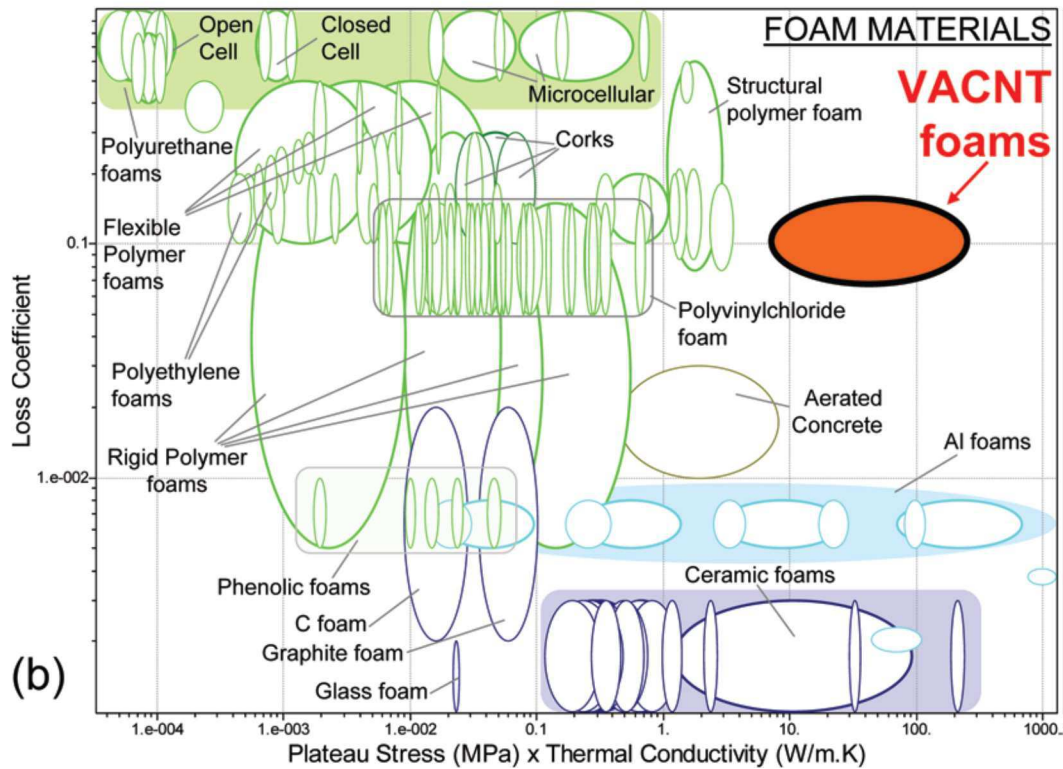


Figure 1.3: Ashby chart of loss coefficient vs the product of plateau stress and thermal conductivity of a variety of foam materials. Taken from ref. [32].

1.3 Guide to dissertation

The primary goal of this dissertation is to elucidate the structural dependence of the mechanical properties of CNT materials via computer simulation. Background on the coarse-grained model used to represent the CNTs is given in chapter 2. Next, chapter 3 details the generation of realistic, structurally distinct VACNT forest samples. The next two chapters report on the uniaxial compression of the *in silico* forest samples. Chapter 4 details the influence of the structural characteristics of the forest, *e.g.* density, microstructure, and CNT length on their deformation behavior and mechanical properties. In chapter 5 the results of a detailed investigation into the deformation mechanisms of uniaxial compression are reported. In particular, the formation of a localized dense phase during compression is described.

After chapter 5, the focus shifts away from VACNT forests and uniaxial compression, and to the high speed impact of CNT films with metallic nanoparticles. Chapter 6 outlines a model for

the coarse-grained representation of metals, and in chapter 7 the results of impact simulations on CNT films are described. This dissertation then concludes with a summary and suggestions for future work in chapter 8.

2 Coarse-grained model for the representation of CNT materials on the mesoscale

2.1 Atomistic molecular dynamics and its limitations

The computational modeling of materials is not a new development. Early atomistic modeling took off with the molecular dynamics (MD) method in the 1950s [33, 34]. This method is based on classical Newtonian mechanics and has become a popular tool for understanding atomic scale processes that cannot be reliably observed in experiments. In MD, the positions and velocities of every particle at some initial time are used to calculate the forces acting on them. Then, the equations of motion are solved for every particle, and other physical quantities such as the potential energy of the system are determined for the specified time interval. Figure 2.1 provides a schematic representation of this process, and more detailed information about MD modeling can be found in Allen and Tildesley's text, *Computer Simulations of Liquids* [35]. With a proper choice of interatomic potentials, atomistic MD modeling can accurately describe the properties of CNTs. But, this accuracy comes at a computational price, in particular from the many calculations that must be performed for each particle, or atom, in the system. Generally, computational cost of MD simulations scale with the number of particles to some power greater than one, depending on the potentials used, and the number of atoms scales as the length scale of the system cubed. Even with high performance supercomputers, simulations are confined to 10^4 – 10^8 atoms, corresponding to a maximum length scale on the order of 100 nm. Furthermore, the larger the length scale, the smaller the time scale needs to be in order to keep simulations at a reasonable cost (see Figure 2.2). There are some pioneering projects, however, that extended the atomistic MD range. For example, one simulation kept track of 10^{12} atoms and micron length scales [36], and another one pushed the millisecond timescale [37], but simulations such as these make use of extensive computational resources not commonly available to the majority of researchers.

For CNTs, atomistic MD has proven valuable for calculating mechanical and thermal transport properties of individual tubes [38-49], and small groups of CNTs, e.g., [50-53]. However, VACNTs are typically comprised of millions or more CNTs that are microns, if not millimeters, long. Furthermore, the tendency of CNTs to form networks of bundles can result in structural features that may span microns, and these features can strongly influence deformation behavior,

impact resistance, and transport properties of CNT materials. Therefore, atomistic MD is not a feasible option for modeling systems that are sensitive to mesoscale structure.

Schematic diagram of a basic MD code

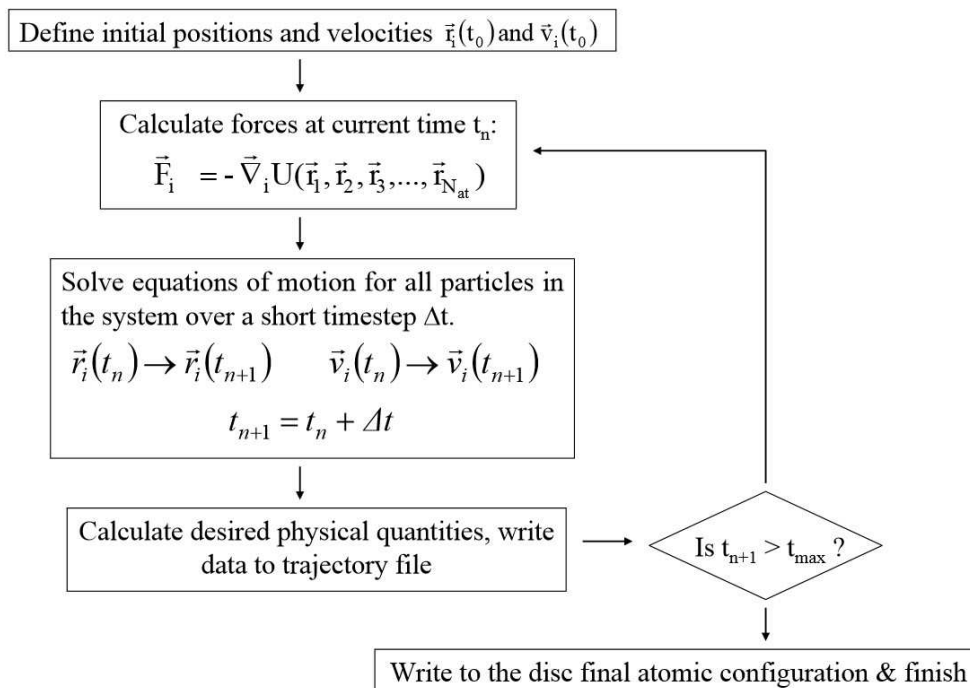


Figure 2.1: The MD algorithm. Reproduced from L. V. Zhigilei's course notes for Atomistic Simulations (MSE 4270/6270) at the University of Virginia

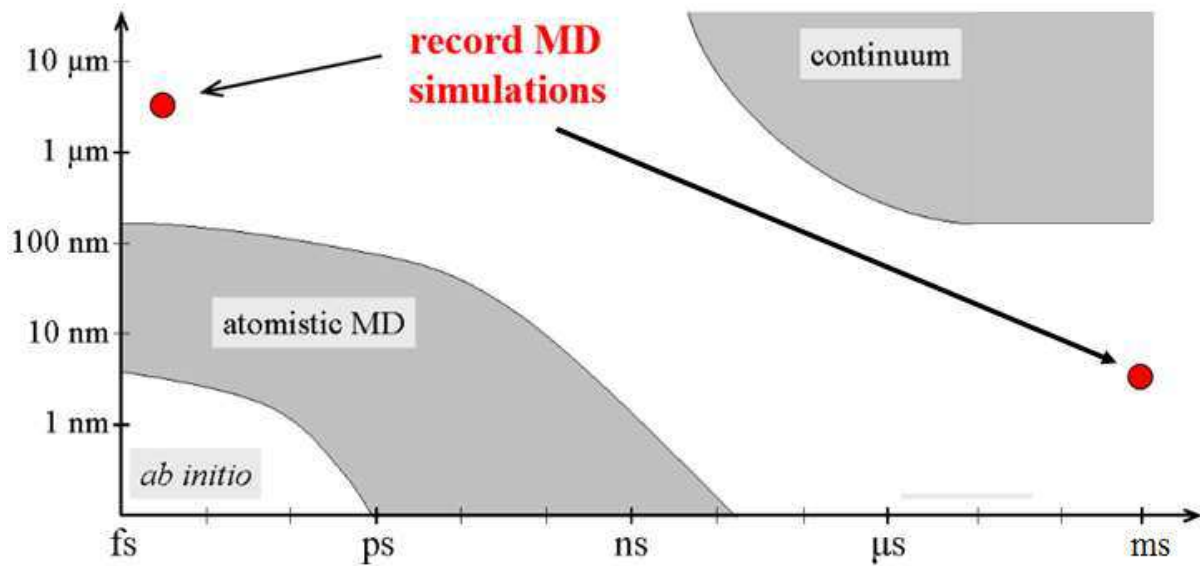


Figure 2.2: Typical length and time scales of various levels of computational modeling. Adapted from L. V. Zhigilei's course notes for Atomistic Simulations (MSE 4270/6270) at the University of Virginia.

2.2 Overview of mesoscopic modeling of CNT materials

The complexity and inherently multiscale nature of the structural organization of the CNT network materials suggest that complete understanding of the connections between the structural parameters and the effective (macroscopic) properties of these materials can only be achieved through a combination of various computational techniques. In particular, the atomistic molecular dynamics (MD) technique [35] is well suited for simulation of the mechanical and thermal transport properties of individual nanotubes, e.g., [38-49], and small groups of CNTs, e.g., [50-53]. The information gained from the atomistic simulations can be used for parameterization of mesoscopic models that adopt simplified representations of nanotubes [54-57] and are capable of simulating the collective behavior and properties of large CNT ensembles, e.g., [55, 57-60]. The results of the mesoscopic simulations can be, in turn, used for revealing general trends and formulating continuum-level constitutive relations that describe the macroscopic behavior and properties of the CNT network materials.

In the atomistic – mesoscopic – continuum chain of the multiscale computational treatment of CNT materials, the “weak member” is the mesoscopic modeling. While the atomistic and continuum models are well established and implemented in user-friendly computational software packages, the general framework of the mesoscopic computational treatment of nanotube materials is still being developed, validated, and redesigned. Several alternative approaches for mesoscopic modeling of CNT materials have been suggested in literature. One of the early models developed by Buehler [54] is based on the bead-and-spring model commonly used in simulations of polymers [61]. In this model, the van der Waals inter-tube interactions are represented through spherically symmetric pair-wise interactions between mesoscopic nodes arranged along the axes of nanotubes. Due to its simplicity and straightforward implementation, the bead-and-spring model has been adopted by several groups and used in a number of investigations of the structural and mechanical properties of CNT films [58, 62-68] and VACNT arrays [69]. The model, however, suffers from large artificial barriers for relative displacements of neighboring CNTs introduced by the pair-wise interactions between the “beads” in the bead-and-spring model. As discussed in Refs. [55, 57, 59, 70], the presence of these barriers prevents long-range rearrangements of CNTs into continuous networks of bundles and strongly affects the structure and mechanical behavior of the CNT materials. More recently, a finite element model [71] describing van der Waals inter-tube interactions by linear elastic bar elements added at localized “contacts” has been proposed and applied for simulation of mechanical behavior of two-dimensional CNT forests. The description of CNT-CNT interaction by strong localized bonds that cannot be broken in the course of the forest “growth” or compressive deformation casts doubt on the ability of the model to provide an adequate description of the structural self-organization or mechanical properties of the CNT materials.

More advanced descriptions of non-bonding inter-tube interactions that do not result in the artificial corrugated inter-tube interactions have been developed and include a mesoscopic model [55, 72, 73] based on the distinct element method [74, 75] and a model representing nanotubes as a sequence of cylindrical segments [56] interacting with each other through the tubular potential method [57]. The latter approach has been parametrized to provide a realistic description of nonlinear deformation, buckling [59, 76] and mechanical energy dissipation in individual CNTs [77], as well as collective heat transfer in CNT materials [51, 60, 76, 78]. This mesoscopic model

(Figure 2.3) is detailed in the remainder of this chapter, and is referred to all throughout this dissertation.

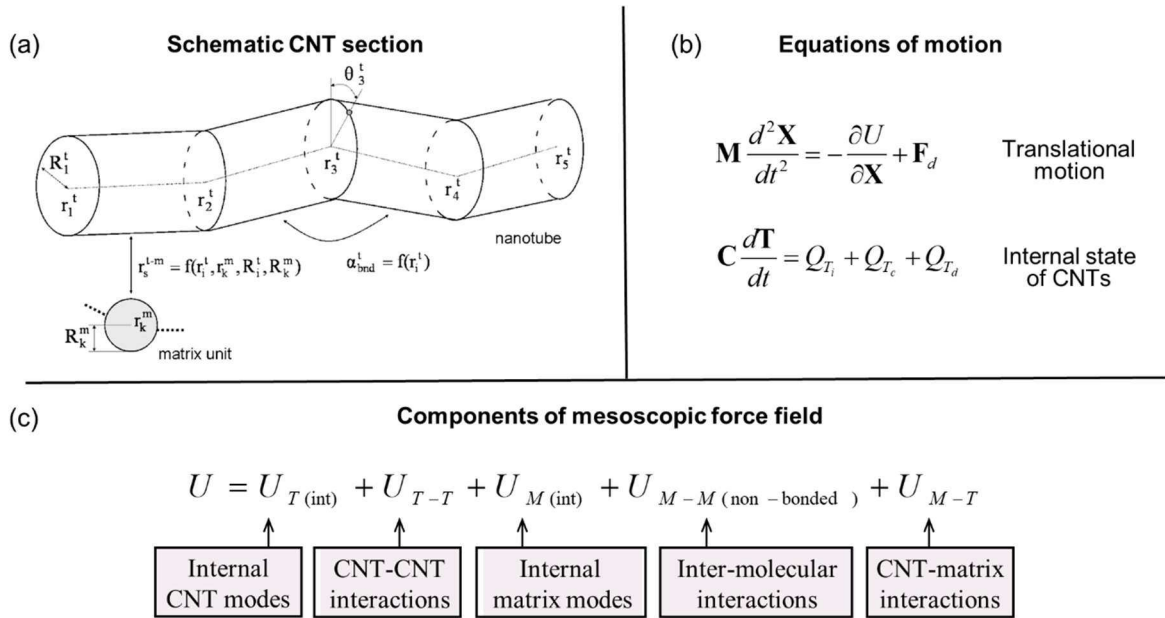


Figure 2.3: Overview of the coarse-grained model for mesoscale representation of CNTs. Schematic representation of a section of nanotube represented by four segments and five nodes (a). The position of the i^{th} node in the nanotube (r_i^t), the radius of the nanotube at node i (R_i^t), and the torsion angle at node i (θ_i^t) are the independent variables that describe the behavior of the nanotube. The equations that control the motion and thermal transport in CNT materials (b), and the components of the mesoscopic force field (c).

2.3 Tubular mesoscopic model for CNTs

The mesoscopic model includes terms accounting for stretching, bending, torsional deformation, radial breathing, and coupled stretching-bending, stretching-torsion, and stretching-breathing interactions, as well as bonded and non-bonded interactions between CNTs, CNT-matrix units, and matrix units. The Lagrangian (potential energy of system subtracted from its total kinetic energy) for CNT-polymer nanocomposites can be written as

$$\begin{aligned}
L = & \frac{1}{2} \sum_i m_i^t \left(\frac{dr_i^t}{dt} \right)^2 + \frac{1}{2} \sum_k m_k^m \left(\frac{dr_k^m}{dt} \right)^2 + \frac{1}{2} \sum_i M_i^t \left(\frac{dR_i^t}{dt} \right)^2 \\
& + \frac{1}{2} \sum_k M_k^m \left(\frac{dR_k^m}{dt} \right)^2 + \frac{1}{2} \sum_i M_{ki}^\theta \left(\frac{d\theta_i^t}{dt} \right)^2 - \sum_i U_i^{str} \\
& - \sum_i U_i^{bnd} - \sum_i U_i^{hb} - \sum_i U_i^{Rt} - \sum_i U_i^\theta - \sum_i U_i^{str-Rt} \\
& - \sum_i U_i^{str-bnd} - \sum_i U_i^{str-\theta} - \sum_{i,k} U_i^{t-m} - \sum_{i,k} U_i^{t-m(bond)} \\
& - \sum_{ij} U_{ij}^{t-t} - \sum_{kl} U_{kl}^{m-m} - \sum_{kl} U_{kl}^{m-m(bond)} - \sum_k U_k^{Rm}
\end{aligned} \tag{2.1}$$

Here, r_i^t is the position of the i th node in a nanotube, r_k^m is the position of the k th unit of the matrix, R_i^t is the radius of matrix unit k , θ_i is the torsion angle at node i , $m_i^t = \frac{1}{2}(m_{i-1,i} + m_{i,i+1})$ is the mass of a part of the nanotube, represented by the node i , $m_{i,i+1}$ is the mass of the segment $\{i, i+1\}$ of the nanotube located between nodes i and $i+1$, m_k^m is the mass of the k th unit of the matrix, M_i^t and M_k^m are the inertia parameters of the internal breathing motion of the nanotube at node i and matrix unit k , respectively, M_{ki}^θ is the inertia parameter for the twisting motion of the nanotube. The potential energy of the system consists of the internal energy ($U^{str}, U^{bnd}, U^{Rt}, U^\theta, U^{str-R}, U^{str-bnd}, U^{str-\theta}, U^{hb}$), as well as bonded ($U^{m-m(bond)}$), and nonbonded (U^{m-m}) interactions among the matrix units, bonded and nonbonded interaction terms among the nanotube (U^{t-t}) and matrix units ($U^{t-m}, U^{t-m(bond)}$), and the internal breathing motion of the matrix units (U^{Rm}). In particular, U^{str} is the internal stretching potential defined as a function of axial deformation of the nanotube segments; U^{bnd} is the bending potential defined as a function of local curvature of the nanotube segments; U^{Rt} is the internal breathing potential defined as a function of the local radii R_i^t at each node i along the nanotube; U^θ is the torsion term defined as a function of the torsional deformation of the nanotube; U^{str-R} and $U^{str-bnd}$ are the potential energy terms describing coupling between stretching of two segments adjacent to a node, radial contraction at the node and local curvature at the node; U^{t-m} is the potential for nonbonded van der Waals interaction between matrix molecules and nanotubes; $U^{t-m(bond)}$ describes the bonded interaction between matrix molecules and nanotubes due to the formation of chemical

bonds; U^{m-m} and $U^{m-m(bond)}$ describe the nonbonded and bonded interactions among the matrix units; and U^{Rm} is the internal breathing potential [79] for the matrix units.

The terms appearing in equation (2.1) can be parameterized by simulation or experimental data. In fact, this mesoscopic model can be fitted to a variety of CNT diameters, or even completely different types of tubular structures. After the potential energy of the system is defined, the equations of motion for the sets of independent variables in system, $\{q\} = \{\mathbf{r}_i^t, \mathbf{r}_k^m, R_i^t, R_k^m, \theta_i\}$ can be directly obtained from the equation (2.2) by substituting in equation (2.1).

$$\frac{d}{dt} \frac{\partial L}{\partial \dot{q}_i} - \frac{\partial L}{\partial q_i} = 0 \quad (2.2)$$

Just as in classical MD, the equations of motion for the independent dynamic degrees of freedom can be integrated to obtain their trajectories. These trajectories are sufficient to describe the dynamics of the nanotubes and the matrix molecules. Note that the mesoscopic model does not explicitly represent surfaces of nanotubes, and distances between “virtual surfaces” are calculated for particular interactions during the runtime of the code.

2.3.1 Axial deformation

At low tensile strains below the fracture limit and at compressive strains the tube deforms elastically, and a harmonic approximation is used to describe axial deformation.

$$U^{str} = \sum_{i=1}^{N-1} L_{i,i+1}^0 \frac{1}{2} k_{str} \epsilon_{i,i+1}^2 = \sum_{i=1}^{N-1} L_{i,i+1}^0 \frac{1}{2} k_{str} \left(\frac{L_{i,i+1} - L_{i,i+1}^0}{L_{i,i+1}^0} \right)^2 \quad (2.3)$$

Here, $L_{i,i+1}^0$ is the equilibrium length of the segment between i and $i+1$ nodes, $L_{i,i+1} = |\mathbf{r}_{i+1}^t - \mathbf{r}_i^t|$ is the length of the segment, $\epsilon_{i,i+1}$ is the local axial strain of the segment, and k_{str} is the stretching force constant. Atomistic simulations performed on infinitely long (by using periodic boundary conditions) CNTs, and the linear stretching force constant was determined to be well modeled by $k_{str} = 86.64 + 100.56R_{eq}^r$ for CNTs with a radii of greater than 4 Å. Beyond 4 Å, the force constant value becomes independent of radius and chirality of the nanotube at approximately 46.8 eV/atom. Nanotubes with smaller radii have somewhat higher force constants (~51-52 eV/atom).

2.3.2 Bending deformation

The bending energy of a CNT depends on its local curvature between segments, and takes on different functional forms based on the radius of curvature. At small curvatures, the bending potential can be approximated as a harmonic function

$$\begin{aligned}
 U^{bnd} &= \frac{1}{2} k_{bnd} \sum_{i=1}^{N-1} L_{i,i+1}^0 \left(\frac{1}{R_{i,i+1}^{curv}} \right)^2 \\
 &\approx \frac{1}{2} k_{bnd} \sum_{i=2}^{N-1} \left\{ \frac{1}{2} L_{i,i-1}^0 \left(\frac{1}{R_i^{curv}} \right)^2 + \frac{1}{2} L_{i,i+1}^0 \left(\frac{1}{R_i^{curv}} \right)^2 \right\}
 \end{aligned} \tag{2.4}$$

where $L_{i,i+1}^0$ is the equilibrium length of the segment between i and $i+1$ nodes, R_i^{curv} is the radius of curvature at node i , and k_{bnd} is the bending force constant. Atomistic simulations were run for CNTs of different radii and of different configuration (i.e. armchair, zigzag) without periodic boundary conditions. Each CNT is given a constant radius of curvature between 22,528 and 4,528 Å (corresponding to bending angles ranging from 0.0025 to 0.0127 degrees/Å). Taking the second derivative of the strain energy with respect to curvature, the bending force constant was determined to follow the function $k_{bnd} = 63.80 R_{eq}^{2.93}$. When the curvature of a CNT gets large enough, it buckles and the bending potential changes. This transition is included in the mesoscopic model [76] (see Figure 2.4) by using an almost linear dependence of the strain energy with curvature after buckling, compared to the harmonic dependence at lower curvatures. In the pre-buckling regime the bending energy takes on the form

$$U^{bnd} = \int_A^C \frac{1}{2} \frac{k^{bnd}}{(R^{curv})^2} dl \tag{2.5}$$

where the bending energy is integrated along the length of the unbuckled CNT, $\int_A^C dl$ using the local radius of curvature at each point (see Figure 2.4). Realizing that the bending angle relates to the radius of curvature as

$$\theta = \frac{L_T}{R} \tag{2.6}$$

then, in the case of a uniformly bent CNT of length L_T , the equation for bending energy simplifies to

$$U^{bnd} = \frac{k^{bnd}\theta^2}{2L_T} \quad (2.7)$$

When the CNT becomes buckled, the bending energy is modified to include an additional term for the energy of the buckling kink, $K^{blc}\psi^n$,

$$U^{bnd} = K^{blc}\psi^n + \int_A^B \frac{1}{2} \frac{k^{bnd}}{(R^{curv})^2} dl + \int_B^C \frac{1}{2} \frac{k^{bnd}}{(R^{curv})^2} dl \quad (2.8)$$

where ψ is the angle between the two tangents to the elastic line at the point of the kink (point B in Figure 2.4). The power, n , is set to one since the bending energy is approximately proportional to the bending angle. The remaining constants can be obtained from atomistic simulations, similar to those discussed previously in this section.

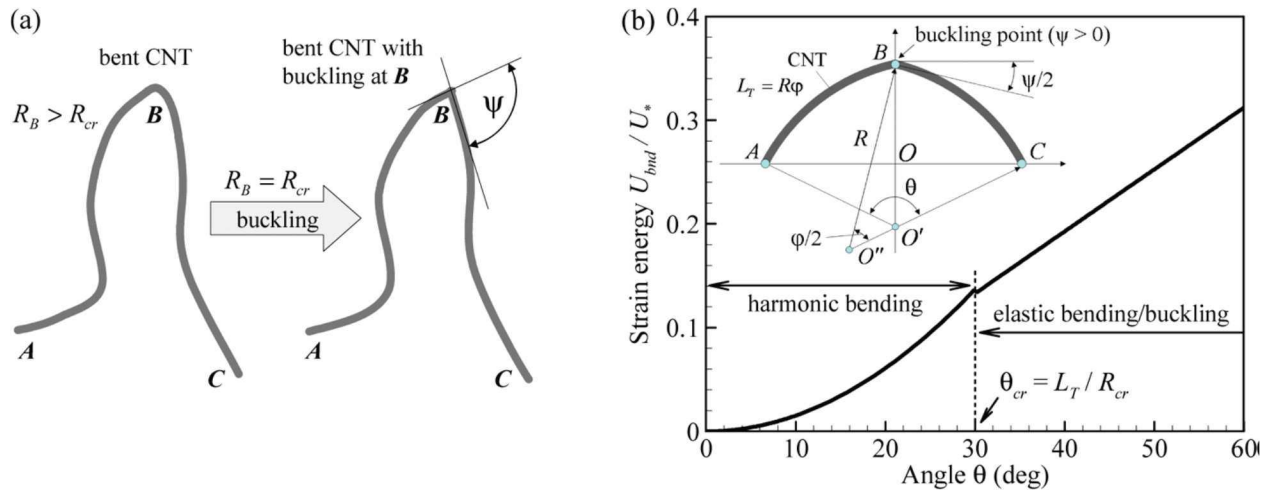


Figure 2.4: Schematic representation of the description of bending buckling in the mesoscopic model (a) and the dependence of the bending energy U^{bnd} on the bending angle θ in a uniformly bent CNT with a single buckling point appearing in the middle (point B in the insert) when the critical radius of curvature, R_{cr} , is reached (b). Bending energy in (b) is obtained by minimizing the strain energy associated with the bending and buckling. Values of the bending energy in (b) are scaled by $U_* = k_{bnd}/L_T$ where L_T is the length of the CNT. Taken from ref. [76].

It is worth noting that the buckling of CNTs is not necessarily a straightforward process of simply kinking the nanotube. The mesoscopic model currently only considers buckling for SWCNTs, but buckling in MWCNTs proceeds in a more complicated fashion due to the interaction of the multiple CNT walls, leading to a rippling effect [80] during bending rather than the single kink observed for SWCNTs. Parameterization of the mesoscopic model for MWCNTs will be the subject of future work.

2.3.3 Torsional deformation

In addition to bending and stretching terms, it is possible to account for the twisting of CNTs, although it is not included in the current computational implementation of the mesoscopic model. The torsion term is represented by

$$U^\theta = \sum_{i=1}^{N-1} L_{i,i+1}^0 \frac{1}{2} k_t \left(\frac{\theta_i - \theta_{i+1}}{L_{i,i+1}^0} \right)^2 \quad (2.9)$$

Here θ_i is the torsion angle at node i and k_t is the torsion force constant. The force constant is determined with a series of atomistic simulations for CNTs of different radii where they are initially twisted between 0.0025 to 0.0127 degree/Å and allowed to relax with the end segments fixed. The force constant is calculated from the second derivative of the strain energy with respect to the torsional deformation. At tube radii larger than 4 Å, the torsion force constant is given by $k_{trs} = 38.44R_{eq}^r{}^{3.01}$ and conforms to the expected cubic dependence on radius expected for a hollow cylinder.

2.3.4 Intertubular potential

The main advantage of the tubular mesoscopic model compared to the simpler bead and spring representation of CNTs is the introduction of a smooth non-bonded interaction between nanotubes which allows for the natural and realistic self-organization of nanotubes into networks. In the bead and spring potential, the CNTs interact artificially via a strongly corrugated potential centered at the “beads”, leading to poor CNT networking.

For classical MD atomistic simulations, the weak vdW potential is often approximated with the Lennard-Jones model [81],

$$\varphi(r) = 4\epsilon \left[\left(\frac{\sigma}{r} \right)^{12} - \left(\frac{\sigma}{r} \right)^6 \right] C(r) \quad (2.10)$$

where r is the distance between the interacting atoms, ϵ and σ are parameters of the potential that define the energy and length scales of the interatomic potential, respectively, and $C(r)$ is a cutoff function. For carbon-carbon interactions, the parameters and the form of the cutoff potential are taken from the AIREBO potential [82] for the MFF.

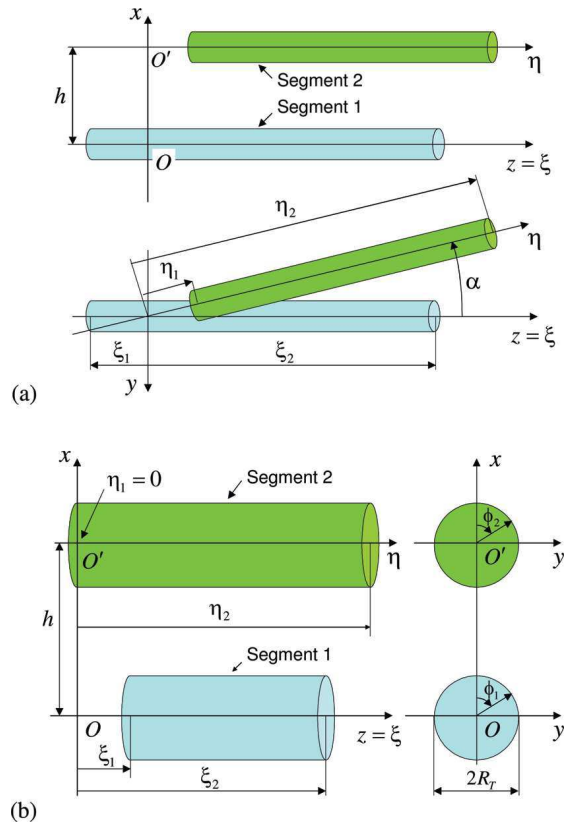


Figure 2.5: Schematic sketch illustrating the introduction of local coordinates $Oxyz$ and geometrical parameters used for characterization of the relative positions of two nonparallel (a) and parallel (b) straight cylindrical CNT segments. The side and top views are shown in panel a; only the side view is shown in panel b. In panel a, the axis x is directed along the vector \mathbf{OO}' defining the shortest distance between the axes of the segments. In panel b, for the origin of the Cartesian coordinates is chosen so that the axis Ox goes through the left end of the second segment ($\eta_1 = 0$). Cross sections of the segments are shown in panel b, with angles ϕ_1 and ϕ_2 specifying positions of points in the cross sections used for integration over the surfaces of the two segments. Taken from ref [57].

In the mesoscopic model, the relative position of two CNTs or CNT segments can be described by six independent geometric parameters as illustrated in Figure 2.5 where h denotes the shortest distance between the two CNT axes, α is the angle between them, η_1 and η_2 represent the ends of one CNT segment, and ξ_1 and ξ_2 are the ends for the second CNT segment. The CNTs are aligned along the O and O' axes. In this model, the atomic potential, described by equation (2.10), is integrated over the surfaces of the interacting nanotubes, but the atomic configuration is represented by an averaged continuous distribution of atoms with a surface density n_σ .

For two CNT segments with equal radii R_T , the interaction potential between them can therefore be expressed as

$$U_{SS}(h, \alpha, \xi_1, \xi_2, \eta_1, \eta_2) = n_\sigma^2 R_T^2 \int_{\xi_1}^{\xi_2} \int_0^{2\pi} \int_{\eta_1}^{\eta_2} \int_0^{2\pi} \varphi(r(h, \alpha, \xi, \phi_1, \eta, \phi_2)) d\phi_2 d\eta d\phi_1 d\xi \quad (2.11)$$

where the integral is taken over the lengths of the two axes, ξ and η , and the angles ϕ_1 and ϕ_2 that define the points in the cross sections of the segments (see Figure 2.5). The distance between two points on the surfaces, r , is written as

$$\begin{aligned} r(h, \alpha, \xi, \phi_1, \eta, \phi_2) &= \left[(h + R_T(\cos \phi_2 - \cos \phi_1))^2 \right. \\ &\quad + (R_T(\sin \phi_2 \cos \alpha - \sin \phi_1) - \eta \sin \alpha)^2 \\ &\quad \left. + (R_T \sin \phi_2 \sin \alpha + \eta \cos \alpha - \xi)^2 \right]^{\frac{1}{2}} \end{aligned} \quad (2.12)$$

Although, equation (2.11) is sufficient to describe the interaction of two segments of arbitrarily orientation and length, the accuracy is acceptable only with a large number of quadrature points, making the calculation too costly to do during the simulation. Furthermore, the six independent parameters in this equation make the tabulation of the potential impractical. Therefore, it is simplified using a series of approximations. First, if one of the tubes is assumed to be infinitely or semi-infinitely long, the one or both of the axes variables for that tube can be dropped. For a segment interacting with an infinitely long segment, the potential becomes

$$U_{S\infty}(h, \alpha, \xi_1, \xi_2) = n_\sigma^2 R_T^2 \int_{\xi_1}^{\xi_2} u_\infty(h, \alpha, \xi) d\xi \quad (2.13)$$

where $u_\infty(h, \alpha, \xi)$ is the interaction potential density along the axis of the segment. The simplest case is that of parallel tubes, and then the potential density does not depend on ξ , and the angle is fixed, so that equation (2.13) becomes

$$U_{S\infty||}(h, \xi_1, \xi_2) = (\xi_2 - \xi_1)u_{\infty||}(h) \quad (2.14)$$

where $u_{\infty||}(h)$ is the potential density for parallel and infinitely long tubes,

$$u_{\infty||}(h) = n_\sigma^2 R_T^2 \int_0^{2\pi} \int_{-\infty}^{\infty} \int_0^{2\pi} \varphi(r(h, \phi_1, \eta, \phi_2)) d\phi_2 d\eta d\phi_1 \quad (2.15)$$

And

$$r(h, \phi_1, \eta, \phi_2) = [(h + R_T(\cos \phi_2 - \cos \phi_1))^2 + R_T^2(\sin \phi_2 - \sin \phi_1 + \eta^2)^2]^{\frac{1}{2}} \quad (2.16)$$

Now, it is possible to record the potential in a one-dimensional table, cutting the computational cost of the vdW force calculations. Although this potential is only appropriate for infinitely long and parallel tubes, $u_{\infty||}(h)$ can be used to also determine the potential density for arbitrary tube orientations. The main idea is to approximate the potential density at arbitrary orientations with simple geometric relations, and then to resolve the discrepancy between the approximation and the true potential with a set of scaling functions, and thereby good accuracy for the vdW interaction force can be cheaply obtained. Further information on the details of this method and the analogous treatment of the semi-infinite case is provided in ref [57]. This method of modeling the vdW interactions between CNTs eliminates the artificial friction between tubes resulting from the bead and spring model, and is a computational efficient way to simulate the interaction of multiple CNTs with each other. Figure 2.6 shows the self-organization of CNTs with the MFF model and

the bead and spring model. Note that the poor alignment between the CNTs for the bead and spring model is attributed to its roughly corrugated vdW potential.

The mesoscopic force field does not include an explicit description of friction forces related to the relative displacement of tubes with respect to each other, as these forces are too weak to prevent room-temperature rearrangements of defect-free CNTs [83, 84]. The contribution to the static friction forces originating from the changes in the inter-tube interaction area, however, is fully accounted for in the mesoscopic model. Experimental measurements and simulations of the sliding force required to pull an inner tube from an outer one in a MWCNT [85] and the static friction between two highly crystalline double-walled CNTs and MWCNTs [57, 84] reveal that the friction force is independent of the overlap area and its magnitude is comparable to that expected from the changes in the inter-tube interaction area. Atomistic simulations predict that the oscillating force originating from the atomic-scale corrugation of the inter-tube potential is more than two orders of magnitude lower than the force related to the decrease in the surface area of van der Waals interaction [85] and cannot be expected to make any significant contribution to the static friction [85, 86]. As a result, the force required to pull out a nanotube from a bundle of pristine defect-free nanotubes is similar in the mesoscopic and atomistic simulations and is defined by the energy needed to create new surface [86, 87]. For (10,10) CNTs considered in the present study, the CNT-CNT interaction energy is ~ 1 eV/nm [21, 57], and the corresponding pullout force from a bundle is ~ 1 nN. The presence of defects, functional groups, and chemical cross-links can significantly increase the strength of the shear interactions between nanotubes [86, 87], but these effects are not considered in the present study.

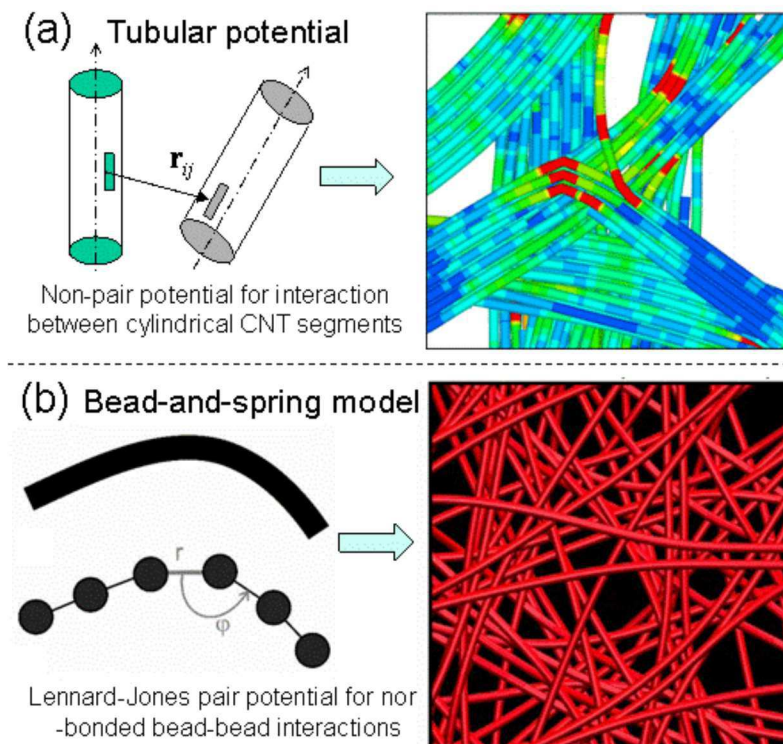


Figure 2.6: Schematic representation of the tubular mesoscopic model (a), and the bead and spring model (b). The CNT configurations in the right panels are fragments of CNT networks obtained in the simulations performed with the two models. In (a) the CNTs are colored by their local radii of curvature where the red color corresponds to buckled segments. The configuration in (b) is from ref. [58] The CNTs do not bundle together due to the artificial friction present in the bead and spring model, but the mesoscopic model with the tubular potential does accurately reproduce this behavior.

2.4 Heat bath

2.4.1 Temperature control through thermostats

The primary advantage of using a mesoscopic model is that it is less computationally intensive because of the reduced number of degrees of freedom. For simulations where local thermodynamic equilibrium can be assumed the effect of the missing degrees of freedom on energy distribution can be neglected. For these cases, a thermostat control such as the one introduced by Berendsen and co-workers [88] is oftentimes used. This scheme couples the system to a heat bath at a fixed temperature. If the system's temperature fluctuates a temperature difference will be established with the heat bath and the temperature of the system is exponentially restored towards the heat bath temperature, such that

$$\frac{dT}{dt} = \frac{T_0 - T}{\tau} \quad (2.17)$$

where the T_0 is the heat bath temperature, T is the temperature of the system, and τ is a time constant. The Berendsen thermostat is efficient and commonly used for larger systems where it is approximately consistent with a canonical ensemble. Another scheme commonly used is that proposed by Nosé [89] and advanced by Hoover [90], which is more realistic in that it achieves a canonical temperature distribution. The formulation of this approach is more complicated than the Berendsen thermostat, introducing an additional degree of freedom in the Hamiltonian for the system, but provides more accurate results for smaller systems. The mesoscopic code implements Berendsen's method as it provides an adequate temperature control for the large scale systems used in the simulations.

2.4.2 *Inclusion of heat bath in mesoscopic code for CNTs*

Although the Berendsten thermostat mitigates temperature variations in a system, it does so on a global level. That is, the kinetic energy of the entire system is scaled by redistributing the temperature to all of its parts. However, in dynamic processes occurring on timescales too short to assume the establishment of thermal equilibrium the local energy dissipation becomes important. If a system absorbs a large amount of energy in a localized region, such as during a high-velocity impact of a projectile with CNTs as shown in Figure 2.7, the kinetic energy around this site will be artificially large due to the missing degrees of freedom in the mesoscopic model. It is therefore necessary to incorporate these absent degrees of freedom implicitly in the form of a heat bath coupled to the dynamic degrees of freedom of individual CNTs. Energy is exchanged between the explicit dynamic degrees of freedom and the heat bath variables, and a general approach was proven for an analogous case of energy transfer between the electrons and the lattice in metals [91]. In CNTs, however, there is no obvious physical distinction between low-frequency acoustic vibrational modes explicitly represented in the mesoscopic model and the higher frequency modes that the heat bath represents. Nonetheless, based on previous MD simulations [92, 93] that show limited coupling of the high (optical) and low frequency (acoustic) vibrational modes in CNTs, the distinctness of these modes appears justified. Furthermore, simulations show that the bending oscillations in cantilevered [94, 95], free [96], and clamped [97] CNTs only diminish gradually,

and that there is a bottleneck in phonon transfer between the acoustic vibrational modes and the optical modes [97].

One important parameter in developing a heat bath approach is the heat capacity of the heat bath. This is calculated by first adding up all of the dynamic degrees of freedom represented in the mesoscopic model and then subtracting them from the experimentally determined specific heat of the CNT. Another important parameter for the heat bath approach is the rate at which energy transfers between the two sets of vibrational modes, can be extracted from atomistic MD simulations.

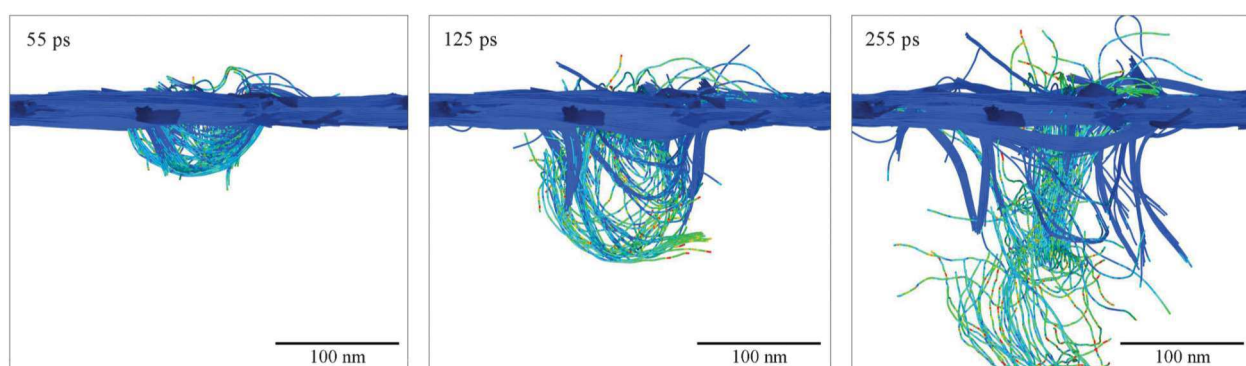


Figure 2.7: Snapshots from mesoscopic simulation of the high-velocity impact of a spherical projectile with a diameter of 100 nm, a density of 2.8 g/cm^3 and an initial velocity of 1000 m/s on a free standing 20-nm-thick CNT film. The snapshots are shown for 55, 125, and 255 ps after the onset of the impact. The film has a density of 0.2 g/cm^3 , and the CNTs in the film are arranged in a continuous network of bundles. The nanotubes are colored by their local kinetic energy, and the projectile is not shown in the snapshots.

2.4.3 Heat capacity of the heat bath

The details of implementing the heat bath approach are presented in ref [77], and only a brief overview will be given here. First, the totality of the vibrational modes in a CNT can be separated into four distinct groups: the bending acoustic (BA), longitudinal acoustic (LA), radial (RAD), and the remaining heat bath (HB) modes. Without the heat bath, the mesoscopic model only explicitly represents the low frequency BA and LA modes, and it currently does not account for the RAD modes because CNT diameter is fixed throughout the mesoscopic simulations. The HB modes represent all of the degrees of freedom that are not represented in the coarse-grained model. Figure 2.8 schematically illustrates how the atomistic model is related to the mesoscopic model, where

the atomistic representation of the CNT is partitioned into nodal segments. The CNT unit length is long enough to account for all LA and BA modes, and is equal to the mesoscopic segment length in this analysis.

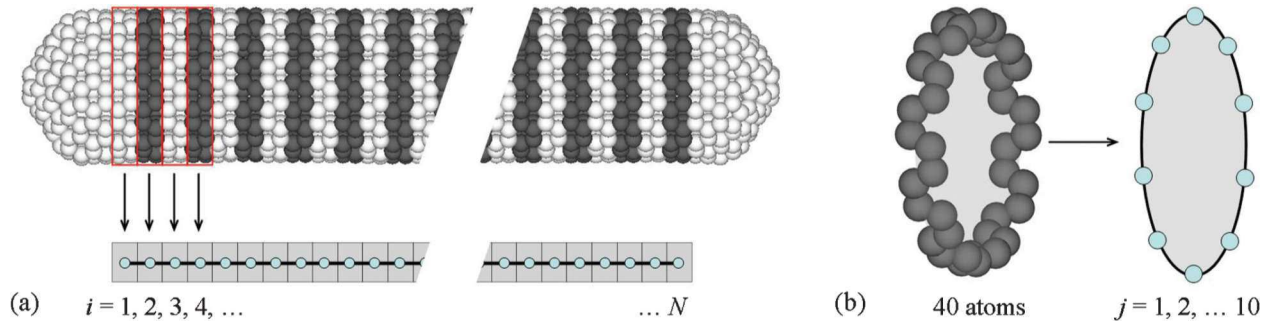


Figure 2.8: Schematic illustration of the mapping of (a) the atomic model of a (10,10) CNT to a chain of coarse-grained particles and (b) a unit cell ring of the (10,10) CNT to a closed chain of 10 point masses. The coarse-grained representations are used in the analysis of the partitioning of the vibrational energy between the longitudinal, bending, and radial modes. Taken from ref [77].

The potential and kinetic energies associated with each group of modes are calculated to define their instantaneous total energy. For the LA modes, the potential energy is defined as

$$U_{LA} = \frac{1}{2} \frac{k_{str}}{a} \sum_{i=1}^{N-1} (|\mathbf{r}^{i+1} - \mathbf{r}^i| - a)^2 \quad (2.18)$$

and for the BA modes, it is

$$U_{BA} = \frac{1}{2} k_{bnd} a \sum_{i=2}^{N-1} \left(\frac{1}{R_i} \right)^2 \quad (2.19)$$

where \mathbf{r}^i is the position of the node i , a is the equilibrium separation between the nodes, k_{str} and k_{bnd} are the stretching and bending force constants, respectively, and R_i is the local radius of curvature at node i . The corresponding kinetic energies are found by taking the nodal velocity components, \mathbf{v}^i , both parallel and perpendicular to the local elastic line, $\mathbf{e}^i = (\mathbf{r}^{i+1} - \mathbf{r}^{i-1}) / |\mathbf{r}^{i+1} - \mathbf{r}^{i-1}|$ for internal nodes and to the line directed along two end segments for nodes $i = 1$ and N . For the LA modes, the kinetic energy is written as

$$T_{LA} = \frac{1}{2} m \sum_{i=1}^N (\mathbf{v}^i \cdot \mathbf{e}^i)^2 \quad (2.20)$$

and for the BA modes, it is written as

$$T_{BA} = \frac{1}{2} m \sum_{i=1}^N [(\mathbf{v}^i)^2 - (\mathbf{v}^i \cdot \mathbf{e}^i)^2] \quad (2.21)$$

where m is the total mass represented by each node. For the LA modes, $E_{LA} = T_{LA} + U_{LA}$ can be used without further modification to the equations. However, the equation for the potential energy of the BA modes must be rewritten in order to account for the periodic fluctuations commensurate with large-amplitude bending oscillations. This is done by a normal mode analysis that sums the small bending oscillations relative to a fixed axis, and the BA potential energy is thus reconstructed as a sum of energies contained in each of the mesoscopic normal modes.

Despite lack of radial modes in the mesoscopic model, they are still distinguished in the atomistic simulations from the rest of the modes. The kinetic energy of the RAD modes is obtained by summing the radial velocities of the particles of a unit cell (see Figure 2.8b) over all of these rings

$$T_{Rad} = \frac{1}{2} \frac{m}{n} \sum_{i=1}^N \sum_{j=1}^n (v_{R,j}^i)^2 \quad (2.22)$$

where $v_{R,j}^i$ is the radial component of the velocity of particle j in unit cell ring i with respect to the center of mass of the ring. The equation can be decomposed to a single summation of the radial modes.

Then, the heat bath energy can be obtained from the equation

$$E_{HB} = E_{CNT} - (E_{LA} + E_{BA} + E_{Rad}) \quad (2.23)$$

2.4.4 Dissipation of stretching and bending vibrations into heat bath

The rate of energy dissipation from the stretching and bending vibrations depends how large the temperature difference is between the heat bath and the remaining degrees of freedom.

Another factor influencing the rate of energy dissipation is whether the nanotube is buckled or not. For the LA modes, the differential equation to describe this rate is given by

$$\frac{d}{dt}(E_{LA} - E_{LA}^{\theta}) = -\gamma^{LA} \left(\frac{E_{LA} - E_{LA}^{\theta}}{E_{LA}^{\theta}} \right)^{\alpha^{LA}} (E_{LA}^{\theta})^{\beta^{LA}} \quad (2.24)$$

where $\frac{E_{LA} - E_{LA}^{\theta}}{E_{LA}^{\theta}}$ is the relative excess energy with respect to the equilibrium LA energy at the heat bath temperature θ , E_{LA}^{θ} and the tunable parameters α^{LA} , β^{LA} , and γ^{LA} are fitted from atomistic simulations. Analogous to the LA modes, the equation describing the dissipation of energy from the BA modes is

$$\begin{aligned} \frac{d}{dt}(E_{BA} - E_{BA}^{\theta}) &= -\gamma^{BA(I)} \left(\frac{E_{BA} - E_{BA}^{\theta}}{E_{BA}^{\theta}} \right)^{\alpha^{BA(I)}} (E_{BA}^{\theta})^{\beta^{BA(I)}} \\ &\quad - \gamma^{BA(II)} \left(\frac{E_{BA} - E_{BA}^{\theta}}{E_{BA}^{\theta}} \right)^{\alpha^{BA(II)}} (E_{BA}^{\theta})^{\beta^{BA(II)}} \\ &\quad \times H[(E_{BA} - E_{BA}^{\theta}) - E_{BA}^*] \end{aligned} \quad (2.25)$$

where $H(E)$ is the Heaviside step function, and E_{BA}^* is the critical excess energy for the onset of buckling. The rest of the terms have corresponding definitions to equation (2.24), but for the BA modes. One difference between equation (2.24) and equation (2.25) is the inclusion of additional dissipation regimes for the BA modes. Regime I represents small bending deformations without buckling, and regime II accounts for buckling kinks in the CNT. In the buckling regime, the energy decay rate sharply increases over that for the harmonic buckling regime, and the parameters in this regime are found to be insensitive to temperature. However, the dissipation associated with the harmonic bending is still active in the buckling regime, but contributes insignificantly to the total dissipation.

2.4.5 Dissipation of acoustic vibrations in the mesoscopic model

The heat bath modes can be either associated with a localized portion of a CNT or with the entire CNT. However, due to the large, non-local wavelengths typically resulting from acoustic excitations, and the high thermal conductivity of CNTs, we opt to associate the heat bath with the

whole tube. The rates of energy dissipation and the heat capacity of the heat bath for the mesoscopic model are taken from the results of the atomistic simulations. To reproduce the gradual dampening of the acoustic vibrations, a restoring force, F_d^i , is introduced for a node i for the sum of the stretching and bending dampening contributions,

$$F_d^i = -\xi_{str} m^i v_{str}^i - \xi_{bnd} m^i v_{bnd}^i \quad (2.26)$$

where m^i is the mass of a part of the nanotube represented by the node i and ξ_{str} and ξ_{bnd} are the stretching and bending dampening coefficients, respectively, that are chosen to match the dissipation rates from the atomistic simulations. The dampening force is added to the force term calculated in the mesoscopic code, mitigating the translation motion of the segments. So that CNT momentum is conserved, the contributions of the dampening forces to the net force and torque are subtracted out, and the damping forces are renormalized to maintain the appropriate dissipation rate.

As described in the previous section, the energies of the stretching and bending modes are comprised of both kinetic and potential energy components, and for a given heat bath temperature, θ , the instantaneous dissipation is defined by equations (2.24) and (2.25). Since there are many more modes associated with the heat bath relative to the LA and BA modes, the heat bath temperature slowly increases with the acoustic energy transfer, and the time dependence derivatives for E_{LA}^θ and E_{BA}^θ can be neglected, so that

$$\frac{dE_{str}}{dt} \approx \frac{d(E_{LA} - E_{LA}^\theta)}{dt} \text{ and } \frac{dE_{bnd}}{dt} \approx \frac{d(E_{BA} - E_{BA}^\theta)}{dt} \quad (2.27)$$

Therefore, at every time step, Δt , the stretching and bending energy transferred to the heat bath in the mesoscopic code is represented as

$$\Delta E_{str} = \frac{d(E_{LA} - E_{LA}^\theta)}{dt} \Delta t \text{ and } \Delta E_{bnd} = \frac{d(E_{BA} - E_{BA}^\theta)}{dt} \Delta t \quad (2.28)$$

The dampening force coefficients are taken [91] as

$$\xi_{str} = \frac{\Delta E_{str}}{\Delta t \sum_{i=1}^N m^i (\mathbf{v}_{str}^i)^2} \text{ and } \xi_{bnd} = \frac{\Delta E_{bnd}}{\Delta t \sum_{i=1}^N m^i (\mathbf{v}_{bnd}^i)^2} \quad (2.29)$$

and the energy removed from the LA and BA modes is transferred to the heat bath as

$$\Delta\theta = \frac{1}{c_{HB}} (\Delta E_{str} + \Delta E_{bnd}) \quad (2.30)$$

where c_{HB} is the heat capacity of the heat bath modes, and $\Delta\theta$ is the increase in the heat bath temperature, such that $\theta(t + \Delta t) = \theta(t) + \Delta\theta$.

2.4.6 Localized energy dissipation

Although the dampening forces describe the energy dissipation from the LA and BA modes to the heat bath modes at small strains, at larger strains the rate of dissipation increases dramatically, and deformation is much more localized. The globally acting dampening force does a poor job at removing energy from buckled nodes, and tubes remain buckled for an artificially large number of oscillation periods. Therefore, an additional dissipation mechanism is introduced to account for the axial and bend buckling regimes in the form of hysteresis loops in the stretching and bending potentials. The idea behind this approach is illustrated in Figure 2.9, where the potential for compressive strain is shown. At a critical strain, $|\epsilon_{str}^{bcl}|$, the CNT axially buckles, and the potential switches from a harmonic form to a linear form. Furthermore, there is a drop in the potential energy, ΔE_{str}^{bnd} , corresponding to the rapid transfer of energy to the heat bath in the buckling regime. When the strain diminishes, the linear potential remains in effect until a strain $|\epsilon_{str}^{bcl-\min}|$, so that the energy deposited in the heat bath is not reintroduced to the acoustic modes. The heat bath temperature is increased as $\Delta\theta = \Delta E_{str}^{bcl} / c_{HB}$, and the value of ΔE_{str}^{bcl} can be tuned by adjusting the value for $\epsilon_{str}^{bcl-\min}$. The latter parameter is chosen so that the energy dissipated matches the results of the atomistic simulations. An analogous approach is followed for the BA modes. The inclusion of the hysteresis method in the mesoscopic model results in a more accurate reproduction of the energy transfer from acoustic modes to the higher frequency optical modes found in atomistic simulations, relative to simulations without the hysteresis approach.

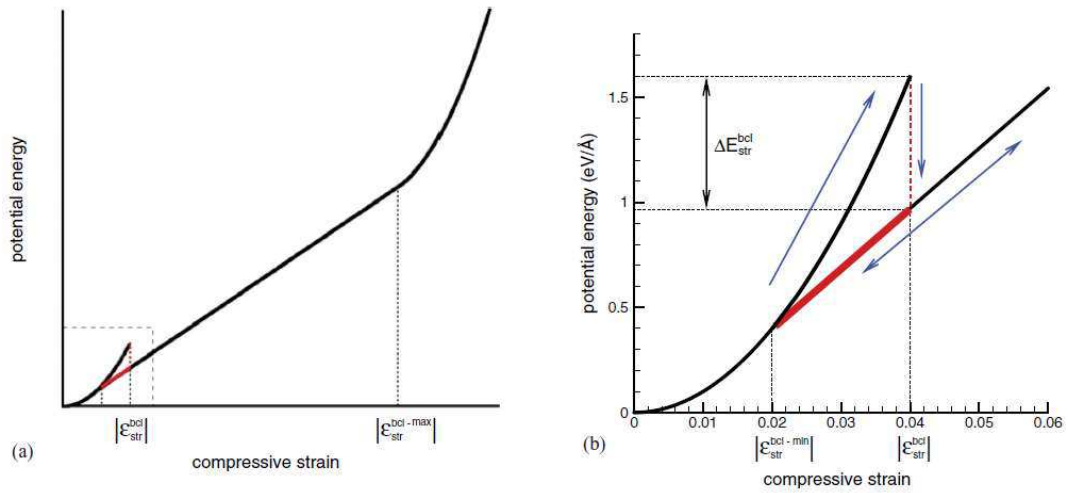


Figure 2.9: An illustration of the hysteresis approach to the localized energy dissipation upon buckling in the mesoscopic model. The compressive part of the axial strain energy is shown schematically in (a), and an enlarged view of the hysteresis region is shown in (b). The blue arrows in (b) represent the path followed when a buckling kink is created. The red segments of the plot are the irreversible parts of the strain energy hysteresis. ΔE_{str}^{bcl} is the amount of energy transferred to the heat bath of the CNT in each buckling cycle. Taken from ref [77].

3 Structural self-organization of carbon nanotubes into vertically aligned arrays

3.1 Introduction

Carbon nanotube (CNT) materials possess an attractive combination of structural, mechanical, and transport properties, and continue to hold high promise for a broad range of practical applications [98, 99]. One type of CNT material with pronounced directional anisotropy, vertically aligned carbon nanotube (VACNT) arrays, are of particular interest for applications with stringent requirements for the mechanical strength, toughness, and thermal energy dissipation.

The VACNT arrays, also known as VACNT “forests,” [12, 100, 101] are typically composed of long (up to centimeters [101]) CNTs extending through the whole length of the arrays. These materials are usually produced by chemical vapor deposition (CVD) [28, 102-108], where a hydrocarbon gas reacts with catalytic metallic nanoparticles and decomposes to provide carbon for continuous growth of CNTs. The mass density, types and diameters of constituent CNTs, nanotube areal density, and the mesoscopic structure of VACNT arrays can be strongly affected by the CVD growth conditions [8–10], type, size, and dispersion of the catalyst nanoparticles [106], as well as the properties of the substrate [107, 108]. The VACNT arrays have been shown to exhibit a unique combination of mechanical resilience (ability to support large reversible deformation and absorb mechanical energy) and high anisotropic thermal conductivity in the direction of CNT alignment [32], which makes them good candidates for applications requiring both heat management and mechanical energy dissipation.

The mechanical and transport properties of CNT forests are highly sensitive to the arrangement of individual CNTs into mesoscopic structural elements of the network materials, such as CNT bundles and branching structures, which produces materials characterized by different bundle size distribution, porosity, and the degree of nanotube entanglement. The structural characteristics of CNT forests are not uniquely defined by the length and flexural rigidity of CNTs and material density, but can be modulated by changing the parameters of the production process, mechanical and chemical post-processing, radiative treatment, etc. The empirical exploration of the broad space of structural parameters of anisotropic CNT network materials is

challenging [28, 109] and the structural optimization can be greatly assisted by computer modeling targeting the structure – properties relationships.

Using the mesoscopic model described in chapter 2, a method for *in silico* preparation of structurally distinct VACNT arrays based on the variation of the initial inclination of nanotubes with respect to the direction of alignment and the annealing temperature is detailed in section 3.2. The results of the structural characterization of VACNT arrays of different density are presented and related to the sample preparation procedure in section 3.3. The effect of CNT length on the structure of VACNT arrays is considered in section 3.4. Several examples of the applications benefiting from the fine control over mesoscopic structure of VACNT samples enabled by the developed sample preparation method are provided in section 3.5, and the results are summarized in section 3.6.

3.2 Making VACNT forests *in silico*

A series of computational VACNT samples composed of single-walled carbon nanotubes (SWCNTs) and featuring distinct structural characteristics are generated and equilibrated using the mesoscopic force field model described in chapter 2. In order to produce realistic *in silico* SWCNT forests, the CNT diameter and nanotube areal density (i.e., the number of nanotubes grown on a unit area of the substrate) are selected to match those characteristic of experimentally grown VACNT arrays. The ranges of the CNT diameters and areal densities reported in literature for SWCNT forests grown by CVD are illustrated by several representative examples [74–78] in Figure 3.1. Due to the narrow distribution of CNT diameters typically found in SWCNT forests [75–79], a constant diameter of 1.357 nm, characteristic of (10,10) CNTs [47], is selected for all nanotubes in the computational samples.

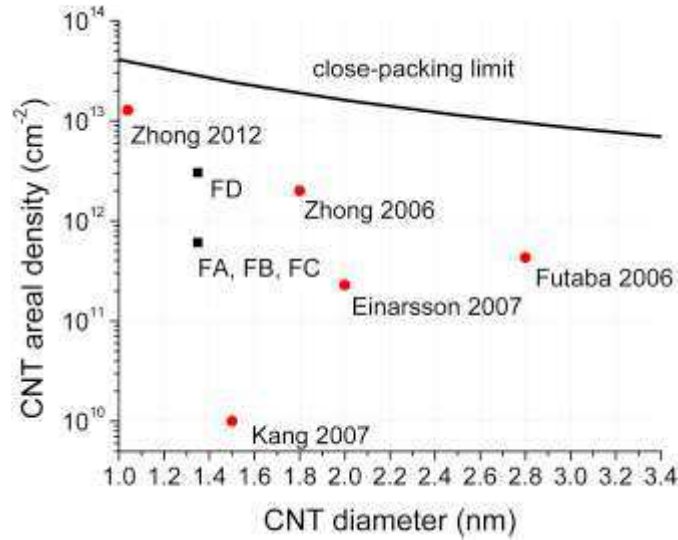


Figure 3.1: Chart showing the areal densities and CNT diameters of five representative SWCNT forests grown by CVD (marked as Zhong 2012 [78], Kang 2007 [76], Zhong 2006 [74], Einarsson 2007 [77], and Futaba 2006 [75]) along with the four SWCNT forests generated in silico in this work (marked as FA, FB, FC, and FD).

The CNT areal density of experimental samples illustrated in Figure 3.1 exhibits a large, more than three orders of magnitude, variability. The areal density is an important parameter as it directly affects the structural characteristics of the network of bundles generated during the growth of a CNT forest. The balance between the inter-tube interaction energy and bending energy of CNTs, which defines the propensity of nanotubes to join the bundles or form interconnects between the bundles, is to a big extent controlled by the areal density of CNTs. To investigate the effect of the areal density on the structural characteristics of the CNT forests, the computational samples are generated in this work for two values of the areal density. Three samples, designated as FA, FB, and FC in Figure 3.1, have an areal density of $6.09 \times 10^{11} \text{ cm}^{-2}$, and one denser sample, FD, has a five times higher areal density of $3.05 \times 10^{12} \text{ cm}^{-2}$.

Another important consideration is the choice of the length of CNTs. If the nanotubes are too short, then the degree of CNT-CNT interactions and connectivity of CNT networks is limited by the relatively large energy penalty associated with bending the nanotubes needed to form bundles. Computational treatment of very long nanotubes, however, is costly, as the number of dynamic units (nodes) for which the equations of motion are solved in mesoscopic simulations is proportional to the CNT length. The length of the nanotubes in the experimentally grown VACNT forests illustrated in Figure 3.1 range from several micrometers to hundreds of micrometers, but

the microstructural characteristics are already well-defined at the micrometer scale. Therefore, in order to cost-effectively reproduce the microstructure observed in experiments, the length of CNTs is chosen to be 2 μm in the computational VACNT samples considered in this section. The dependence of the structural characteristics of VACNT forests on the CNT length is discussed and illustrated by simulations performed for shorter, 200 and 600 nm, forests in section 3.4.

Once the initial parameters are selected, there are two ways to proceed for making a realistic forest microstructure. Either the forest can be “grown” by lengthening the nanotubes over the course of a simulation [61] or the fully sized nanotubes can be made to self-organize [80]. We chose the latter option because it is more straightforward, and has already been proven to be effective in generation of CNT films, or “buckypaper,” with random orientation of nanotubes within the planes of the films [47–49].

As the first step of the sample generation, perfectly straight nanotubes are randomly placed on a substrate at a certain inclination with respect to the substrate surface normal (the choice of the inclination angle is discussed below). The positions of CNT segments (two nodes) adjacent to the substrate are fixed, so that these segments stay at their initial inclination during the self-organization of nanotubes into a network of bundles. In the course of the generation of the initial forest, a new CNT is only added to the sample if the minimum gap between the surfaces of the new and any of the CNTs already present in the sample is larger than the equilibrium distance of 3.14 Å [47]. If the new CNT is too close to an existing CNT, the nanotube is not added and another random location for the next CNT is selected. This acceptance-and-rejection process of the random generation of new nanotubes continues until a desired material density is reached.

The random placement of the nanotubes on the substrate is done within a rectangular area of pre-defined dimensions. For all computational samples but sample FD, periodic boundary conditions are applied in the lateral directions, parallel to the surface of the substrate. These boundary conditions make it possible to represent VACNT forests extending much further than the actual lateral dimensions of the computational system. The choice of the lateral dimensions of the computational system is defined by the condition that the sample is sufficiently wide to ensure that any nanotube would not span more than half of the computational domain at any time during the simulation. This condition is more stringent than the requirement of the absence of CNT self-interactions and is imposed in this work to ensure that the structural characteristics of the generated

samples are not affected by the periodic boundary conditions. Due to the difference in the maximum initial inclination of the nanotubes with respect to the substrate normal (see below), different lateral dimensions are chosen for samples FA, FB, FD ($0.64 \mu\text{m} \times 0.64 \mu\text{m}$), and sample FC ($12.82 \mu\text{m} \times 1.82 \mu\text{m}$). The parameters of the VACNT samples generated with 2- μm -long (10,10) CNTs are summarized in Table 3.1.

Table 3.1: Parameters of the CNT forests generated in the mesoscopic simulations. The CNT spacing is defined as center-to-center distance assuming hexagonal packing of the nanotubes. Data files defining the structures of computational samples listed in this table are accessible from Ref. [110].

Forest	Density (g/cm ³)	Areal density (CNT/cm ²)	Volume occupancy	CNT spacing (nm)	CNT length (μm)	Lateral size ($\mu\text{m} \times \mu\text{m}$)	Number of CNTs	Max. initial inclination θ_{max} (deg.)
FA	0.02	6.09×10^{11}	0.9%	13.77	2	0.64×0.64	2,498	0.6°
FB						0.64×0.64	2,498	12°
FC						2.00×2.00	20,438	27°
FD	0.1	3.05×10^{12}	4.52%	6.16	2	0.64×0.64	12,676	0.6°

In our first attempt to generate CNT forests, all nanotubes are initially oriented perpendicular to the substrate, and the process of self-organization of CNTs into a network of bundles is induced by bringing the system to a high temperature, maintaining the temperature for 1 ns using the Berendsen thermostat algorithm [82], and then relaxing the sample at 300 K. A large fraction of the nanotubes ($\sim 55\%$), however, is found to remain isolated from any of the neighboring CNTs in samples with density of 0.02 g/cm^2 , even when the thermal annealing is performed at a temperature as high as 10,000 K (the model does not include the possibility of thermal decomposition of CNTs, and the temperature is defined based on the average kinetic energy of mesoscopic dynamic units of the model). The relatively high bending energy associated with bringing the vertically-oriented nanotubes into bundles is preventing the formation of continuous networks of bundles, commonly observed in experiments [3–14,74–79,83,84], through the high temperature annealing alone.

In order to facilitate the formation of interconnected network of bundles, the algorithm used for the generation of VACNT arrays is modified by introducing a random inclination of the straight nanotubes relative to the substrate normal. This way, the nanotubes can more easily

interact with each other during the high temperature stage of the sample preparation and join different bundles along the height of the forest. Moreover, we found that the maximum inclination of the CNTs can serve as a parameter that effectively controls the microstructure of the VACNT arrays. Thus, the three-step process developed for the generation of VACNT samples with tunable structural characteristics can be described as follows. First, a sample composed of straight nanotubes with initial inclinations with respect to the substrate normal chosen randomly in a range from 0° to a maximum angle Θ_{max} is generated. Then, the initial sample undergoes thermal annealing in a mesoscopic dynamic simulation performed at a temperature of 5000 K for 1 ns. During this high temperature stage, the initially straight and isolated nanotubes self-organize into a continuous network of bundles, as schematically shown in Figure 3.2, where the shape of a representative nanotube before and after annealing is highlighted. Finally, the VACNT forest is quenched to 300 K and allowed to relax until a metastable configuration, defined as a state where the rate of change in the inter-tube interaction energy slows down to a level below 0.05% per ns, is reached. Note that the computational procedure described above cannot be directly mapped to laboratory conditions, where a variety of growth and post-processing procedures have been developed to control the degree of nanotube alignment in VACNT forests, e.g., Refs. [4,8,85,86]. Nevertheless, as demonstrated below, in sections 3.3 and 3.4, the choice of Θ_{max} can be used as an effective way to tune the structural characteristics of the computational samples and to reproduce the structure of experimental samples in the mesoscopic simulations.

The procedure described above is applied in this work for generation of three VACNT forests with density of 0.02 g/cm^3 and one forest with a higher density of 0.1 g/cm^3 . The parameters of the four samples are provided in Table 1. The structure of the low-density forests is controlled by the maximum initial inclination of the nanotubes, Θ_{max} , chosen to be 0.6° , 12° , and 27° in the three forests denoted as FA, FB, and FC, respectively. The VACNT forest with a density of 0.1 g/cm^3 , five times greater than that of the other three forests, is prepared using the same method and the maximum inclination of 0.6° , i.e., the same as in the sample FA. This higher-density sample is denoted as FD in Table 3.1 and further discussion. The results of the structural characterization of the four VACNT forests are presented in the next section.

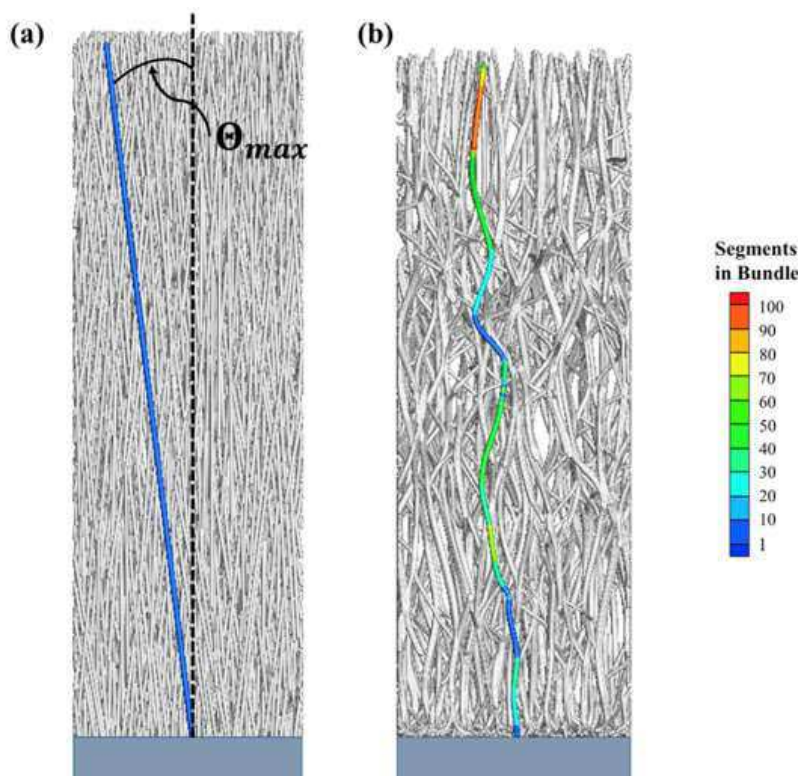


Figure 3.2: Schematic representation of the procedure used for the generation of VACNT samples. Straight CNTs are first randomly placed on a substrate with a random inclination with respect to the substrate normal θ , ranging uniformly from zero to a maximum angle θ_{max} (a). The high temperature annealing followed by a relaxation at 300 K is used to induce self-organization of CNTs into a continuous metastable network of interconnected bundles (b). A single representative nanotube is highlighted, colored by its local bundle thickness, and shown in front of the other nanotubes. All other nanotubes are colored gray.

3.3 Structural characteristics of VACNT forests

The visual views of three lower-density VACNT forests generated in silico as described above are provided in Figure 3.3, where the CNT segments are colored by local thickness of bundles they belong to. The bundle thickness is defined as the number of CNTs in a bundle cross section. Therefore, an isolated CNT segment has a bundle thickness of one and is colored blue in Figure 3.3. Despite having the same average density and being composed of CNTs of the same length and type, the three VACNT forests have distinct structures characterized by different thicknesses of nanotube bundles and densities of interconnects between the bundles. The nanotubes are assembled into fewer number of thicker bundles in sample FA, the bundles are the

thinnest and most numerous in forest FC, while forest FB is intermediate between these two extremes.

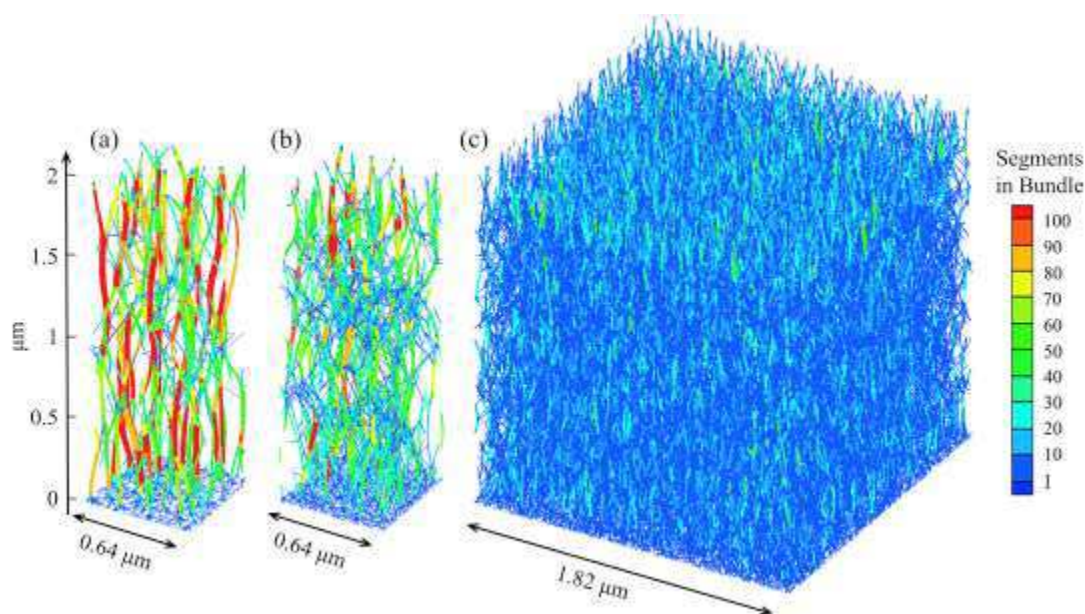


Figure 3.3: Side views of computational samples of forests FA (a), FB (b), and FC (c) generated in mesoscopic simulations. The CNT segments are colored by the local bundle thickness (number of segments in a bundle cross section). Data files defining the structures of the computational samples shown in this figure are accessible from Ref. [110].

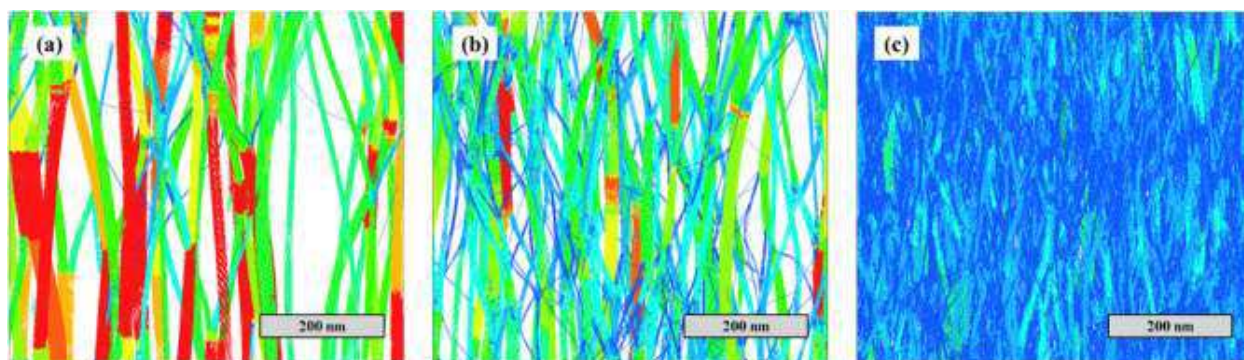


Figure 3.4: Enlarged views of computational VACNT forests FA (a), FB (b), and FC (c) illustrating the degree of interconnection among the bundles. The coloring scheme is the same as in Figure 3.3.

The degree of interconnection between the bundles in the network structures of VACNT forests can be characterized by the extent to which individual nanotubes are parts of multiple

bundles. Visually, the difference between the forests' morphologies can be seen from Figure 3.4, where enlarged views of the network structures are shown for each of the three forests. It is apparent from Figure 3.4 that, on average, CNTs in sample FC tend to be parts of larger number of bundles as compared to samples FB or FA. This observation is not surprising given the initial inclinations of the nanotubes in each sample, but has important implications for mechanical and thermal properties of the forests.

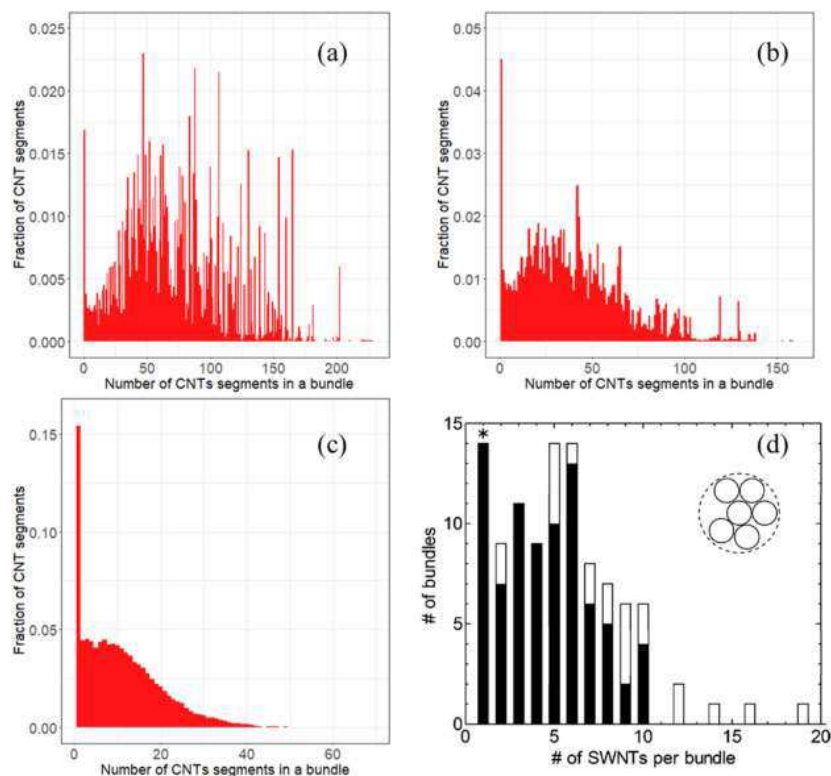


Figure 3.5: The bundle thickness distributions calculated for computational samples FA (a), FB (b), and FC (c), as well as for a laboratory-grown forest analyzed in Ref. [77] (d). In the computational and experimental CNT forests, the bundle thickness is expressed in the number of nanotubes present in bundle cross sections, and each bin covers a thickness increment by 1 CNT segment. In (d), the filled bars are for SWCNT bundles where the number of nanotubes can be reliably counted in TEM images, while the unfilled bars are estimates based on the visual thickness of the bundle. The star marks the number of isolated SWCNTs, and could be higher than the estimate shown in the figure.

The structural differences between computational samples generated with different initial maximum inclinations of CNTs can be quantified by considering bundle thickness distributions shown for the three samples in Figure 3.5a–c. The bundle thickness distributions calculated for

samples FA and FB are qualitatively similar, although the distribution is narrower and shifted to smaller bundle sizes in sample FB. In sample FC, a big fraction of the nanotube segments ($\sim 16\%$) are not in contact with other segments. However, as can be seen from Figure 3.4, this is the result of nanotubes spanning across the sample and participating in multiple bundles connected by isolated portions of CNTs, rather than entire CNTs remaining isolated from the neighboring CNTs. The maximum thickness of bundles found in the simulated network structures FA, FB, FC is equal to 230, 162, and 70 nanotube segments, respectively.

The structures of the computational samples can be related to the results of experimental analysis of the bundle thickness distribution in a VACNT forest of comparable density ($0.035\text{--}0.05\text{ g/cm}^3$), reported in Ref. [77] and reproduced in Figure 3.5d. Experimentally, the bundle thickness distributions were determined through inspection of transmission electron microscope (TEM) images of VACNT forests composed of $2\text{-}\mu\text{m}$ -long SWCNTs. The filled bars in Figure 3.5d correspond to the bundles where the number of CNTs can be reliably counted based on the TEM images and the unfilled bars are the estimates based on the bundles where the number of CNTs was not clear from the images.

The fraction of individual (isolated) CNTs in the computational sample FC (Figure 3.5c) is close to that in the experimental VACNT forest, $\sim 15\%$, while the width of the distribution is almost twice wider in the computational sample than in the experimental one. Although the agreement between the experimental and computational bundle size distributions in Figure 3.5c and d are only semi-quantitative, we note that the thickness of the CNT bundles and other structural characteristics can be effectively controlled by the CNT synthesis parameters in experiments [4,8,85,86] and by the choice of the initial maximum inclination angle Θ_{max} in the computational procedure. Two laboratory-grown SWCNT forests are shown in Figure 3.6. The sample shown in Figure 3.6a [77] is the one used in the analysis of the bundle size distribution illustrated by Figure 3.5d. As discussed above, bundle size distribution and overall structure of this forest are similar to those of the computer-generated sample FC. Another CVD grown forest of similar density (0.03 g/cm^3), shown in Figure 3.6b [75], exhibits thicker bundles and a remarkable visual similarity to the computational sample FA. Both the *in silico* and laboratory-grown forests in Figure 3.4a and Figure 3.6b are characterized by similarly sized and oriented bundles. Interestingly, since the three computational samples, FA, FB, and FC, have the same basic

parameters (material density, length and type of the CNTs), the results of the simulations suggest that the forest morphology is not uniquely dictated by the nominal parameters of the CNT network material, but can be altered to a large degree by the sample preparation method.

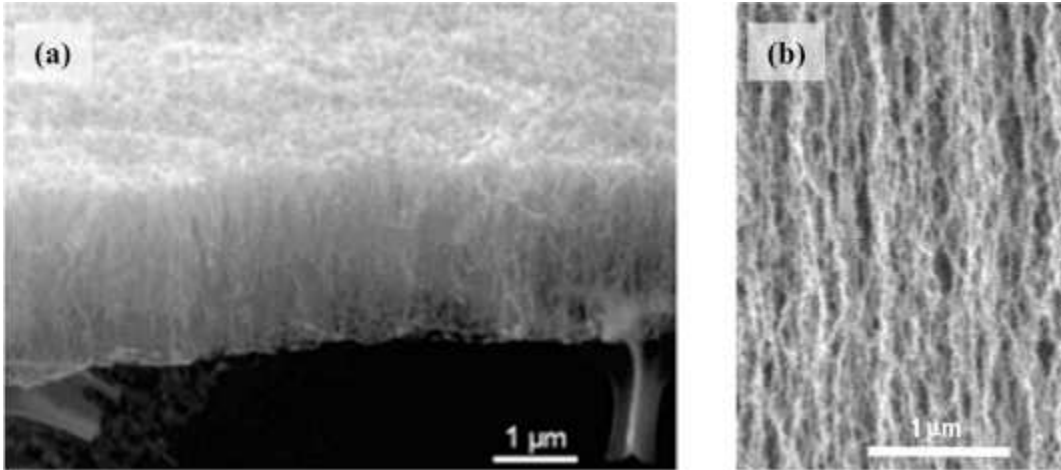


Figure 3.6: Scanning Electron Microscopy (SEM) images of CVD grown SWCNT forests with smaller [77] (a) and larger [75] (b) nanotube bundles.

The ability to accurately control the microstructure of computer-generated VACNT forests can be further evaluated by performing statistical analysis of the connection between the initial maximum CNT inclination angle Θ_{max} and the resulting structural characteristics of the anisotropic networks. The structural characteristics of the computational samples FA, FB, and FC are summarized in Table 3.2 and include the average tilt of CNT segments with respect to the direction of VACNT alignment $\langle \theta \rangle$, average bundle size $\langle N_B \rangle$, maximum bundle size N_B^{max} , standard deviation (SD) of the bundle size, and magnitude of the Herman orientation factor (HOF) defined as $S = \frac{1}{2}[3\langle \cos^2 \theta \rangle - 1]$, where θ is the local angle between a nanotube and the vertical axis, and the angle brackets $\langle \rangle$ denote averaging over all CNT segments in a sample. The HOF quantifies the extent of the orientation of nanotubes with respect to an axis of interest, and ranges from -0.5 to 1 , where values of -0.5 , 0 , and 1 correspond to perpendicular alignment, isotropic orientation, and parallel alignment with respect to the axis, respectively.

Table 3.2: Statistical information on the structural parameters of three computational forests of the same density of 0.02 g/cm^3 . The average tilt of CNT segments $\langle \theta \rangle$, average bundle size $\langle N_B \rangle$, maximum bundle size N_B^{max} , standard deviation (SD) of the bundle size, and magnitude of the

Herman orientation factor (HOF) are listed for computational samples FA, FB, and FC. The coefficients of determination R^2 are listed for linear dependencies of the structural parameters on Θ_{max} .

Sample [Θ_{max}]	$\langle\theta\rangle$	$\langle N_B \rangle$	N_B^{max}	SD	HOF
FA [0.6°]	13.7°	77	230	43	0.88
FB [12°]	17.6°	42	163	28	0.82
FC [27°]	19.4°	12	70	9	0.79
R^2	0.92	0.98	1.00	1.00	0.93

Remarkably, all of the structural parameters of the three samples listed in Table 3.2 exhibit nearly linear dependences on the maximum inclination angle Θ_{max} , as shown by the nearly perfect values of the corresponding coefficients of determination (R^2). The clear statistical link between the structural material parameters and Θ_{max} suggests that the sample preparation procedure described in section 3.2 can be used to precisely engineer the microstructure of a VACNT forest to match that of an experimental material of interest.

Finally, the effect of material density on the structural characteristics of computer-generated VACNT structures can be evaluated by considering the higher density sample FD. Although the density of this sample (0.1 g/cm^3 or $3.05 \times 10^{12} \text{ cm}^{-2}$) is about an order of magnitude below the close-packing limit and does not quite compare with the densest laboratory-grown forests produced by advanced growth techniques [78,83,84] or post processing methods [75], it nonetheless is higher than density of majority of VACNT forests reported in literature, e.g., Figure 3.1. The visual inspection of the microstructure of sample FD shown in Figure 3.7a and b suggests that the size of bundles is comparable to that of sample FA, Figure 3.3a and Figure 3.4a. Indeed, despite the five times higher density of sample FD, the bundle size distribution shown in Figure 3.7c is similar to the distribution shown for sample FA in Figure 3.5a. The forest FD has an average bundle thickness of 71, very close to that of 77 calculated for FA, although the maximum number of segments in a bundle for FD is 301 compared to 230 for FA. The more densely packed structure of sample FD, however, is characterized by higher degree of vertical alignment, with the average angle between the CNT segments and the vertical axis, $\langle\theta\rangle$, equal to 8.4° , and the magnitude of HOF equal to 0.95. The results of the structural characterization of sample FD agree well with the

correlation between density and the degree of CNT alignment observed in laboratory-grown forests [4], and imply that at high densities, the variation of microstructure exhibited by CNT forests is more constrained by crowding of the nanotubes.

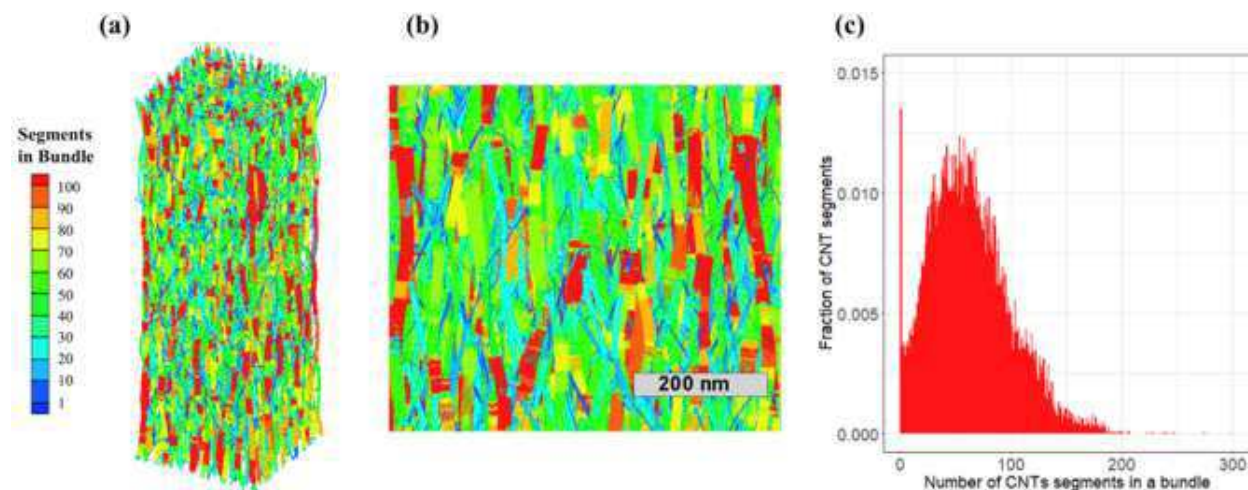


Figure 3.7: The overall view (a), an enlarged fragment (b), and the bundle thickness distribution (c) of the computational sample FD. In (a) and (b), the CNT segments are colored by the local bundle thickness (number of segments in a bundle cross section), and in (c) each bin covers a thickness increment by 1 CNT segment. Data file defining the structure of the computational sample shown in this figure is accessible from Ref. [110].

3.4 The effect of CNT length in short VACNT forests

All the results discussed above are for VACNT forests composed of 2- μm -long CNTs, where the effects of the substrate and free surfaces of the VACNT arrays on the structural organization of the networks of bundles is limited to relatively shallow bottom and top layers of the samples (Figure 3.3), while the internal structure can be assumed to be largely unaffected by the finite length of the CNTs. The length effect, however, can be expected to be more significant for shorter VACNT arrays, warranting an investigation of the length dependence of the VACNT structures presented in this section.

To reveal the length dependence of the structural parameters of the VACNT forests, two additional sets of VACNT forests composed of nanotubes with lengths of 200 nm and 600 nm are prepared using the method described in section 3.2. The initial VACNT samples are cubic, i.e., have dimensions of $200 \times 200 \times 200 \text{ nm}^3$ and $600 \times 600 \times 600 \text{ nm}^3$. In each set, three samples of

the same areal density of $6.09 \times 10^{11} \text{ cm}^{-2}$ are prepared with initial maximum CNT inclinations of 0.6° , 12° , and 27° . Except for the CNT length, all other parameters of the sample preparation procedure are identical to the ones used in the generation of samples FA, FB, and FC discussed in the previous section.

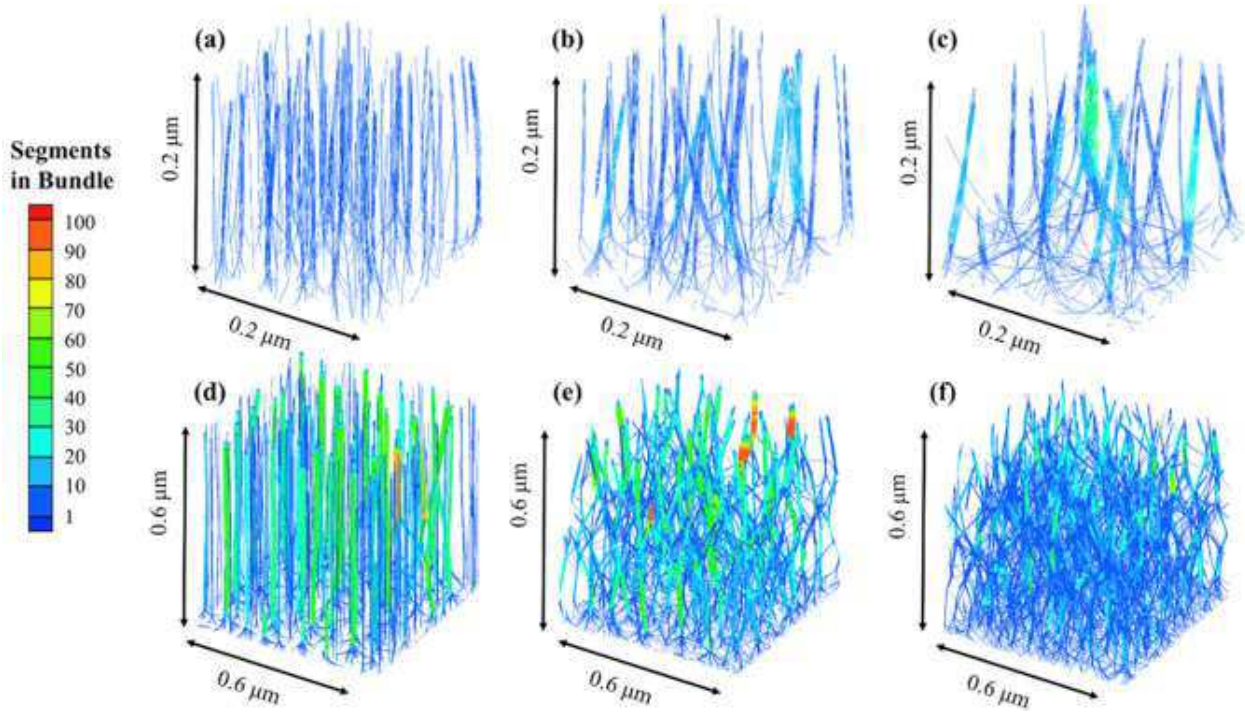


Figure 3.8: Side views of computational VACNT samples composed of nanotubes with lengths of 200 nm (a–c) and 600 nm (d–f) generated in mesoscopic simulations according to the procedure described in section 3.2. The CNT segments are colored by the local bundle thickness (number of segments in a bundle cross section).

The relaxed structures of the samples generated with 200- and 600-nm-long nanotubes are shown in Figure 3.8. Here we notice that, regardless of the initial inclination, the shortest (200 nm) forests do not display the complex morphology of the 2- μm -long samples (Figure 3.3), but rather form smaller and largely isolated bundles even when the initial maximum inclination of CNTs is 27° . The limited connectivity between the bundles in this case cannot be enhanced by further increase of the maximum inclination angle, as the lateral divergence from the point of origin on the substrate that corresponds to $\theta = 27^\circ$ is about 91 nm for a 200-nm-long straight CNT, which is more than 6 times larger than the characteristic distance between the CNTs on the substrate (see Table 3.1). Thus, the virtual absence of participation of CNTs in multiple bundles is not related in

this case to the lack of initial interactions, but is defined by the high bending energy penalty associated with the formation of interconnects between the bundles at such a short length-scale. Indeed, the characteristic length of branching of CNT bundles in Figure 3.3 and Figure 3.4, and well as the typical length of nanotube segments participating in different bundles that can be seen for the nanotube highlighted in Figure 3.2, are both exceeding 200 nm.

When the height of the forest is increased to 600 nm, the degree of interconnection between the CNT bundles increases (Figure 3.8d–f), and the structures become more similar to those observed for 2- μm -long forests (Figure 3.3). The sample with the smallest maximum inclination angle of $\theta_{max} = 0.6^\circ$ still exhibits mostly straight bundles with a rather limited degree of interconnection between the bundles (Figure 3.8d). This observation can be explained by the limited initial interaction between the inclined nanotubes, as the maximum lateral divergence from the point of origin on the substrate that corresponds to $\theta = 0.6^\circ$ is only 6.2 nm for a 600-nm-long straight CNT, which is more than twice smaller than the spacing between the CNTs on the substrate (see Table 3.1). As a result, the nanotubes are mostly forming bundles with their nearest neighbors and are unlikely to participate in multiple bundles, thus limiting the degree of inter-bundle connectivity in the VACNT array shown in Figure 3.8d. In samples generated with larger maximum inclination angles, Figure 3.8e and f, the nanotubes do participate in multiple bundles and self-organize into interconnected networks of bundles similar to those obtained for longer forests and discussed in section 3.3.

Table 3.3: Statistical information on structural parameters of six computational forests of the same density of 0.02 g/cm^3 composed of CNTs with lengths L_{CNT} of 200 nm and 600 nm. The average tilt of CNT segments $\langle\theta\rangle$, average bundle size $\langle N_B \rangle$, maximum bundle size N_B^{max} , standard deviation (SD) of the bundle size, and magnitude of the Herman orientation factor (HOF) are listed for computational samples generated at maximum inclination angles θ_{max} of 0.6° , 12° , and 27° .

Sample: L_{CNT}, θ_{max}	$\langle\theta\rangle$	$\langle N_B \rangle$	N_B^{max}	SD	HOF
200 nm, 0.6°	5.6°	4	10	3	0.96
200 nm, 12°	11.5°	7	24	5	0.89
200 nm, 27°	20.5°	10	36	9	0.73
600 nm, 0.6°	5.7°	28	82	19	0.95
600 nm, 12°	17.2°	22	98	18	0.82
600 nm, 27°	22.9°	10	65	9	0.72

The discussion based on the visual analysis of the computer-generated samples can be supported by quantitative analysis of the structural characteristics provided in Table 3.3 for the 200 and 600 nm VACNT forests. Both the average and maximum bundle sizes, $\langle N_B \rangle$ and N_B^{max} , are smaller in the samples generated with 200- and 600-nm-long CNTs, as compared to the 2- μ m-long VACNT samples discussed in section 3.3 and listed in Table 3.2. The gap in the bundle sizes is particularly large for the shorter 200 nm VACNT forests, but decreases with increasing Θ_{max} for both sets of samples. The structural parameters listed in Table 3.2 and Table 3.3 become similar in all three sets of the samples generated at the largest maximum inclination angle of 27° , although the structure of the shortest VACNT array is still visually distinct, as apparent from comparison of snapshots shown in Figure 3.3c, Figure 3.4c and Figure 3.8c and f. Interestingly, the similar bundle sizes at the largest are approached through different trends observed for the 200-nm-long forests, where $\langle N_B \rangle$ and N_B^{max} increase with increasing Θ_{max} , and the 600-nm-long forests, where the bundle sizes decrease with increasing Θ_{max} (the non-monotonous dependence of N_B^{max} on Θ_{max} for 600 nm VACNT array can be attributed to the high susceptibility of N_B^{max} to statistical fluctuations). The latter trend is similar to the one observed for the 2- μ m-long forests (see Table 2), suggesting that the factors controlling the structural parameters of the 600-nm-long and 2- μ m-long forests are similar.

Overall, we can conclude that while it is possible to produce short VACNT arrays with the average structural parameters similar to those of longer VACNT forests, the network structures characterized by interconnected bundles and typically observed in experiments [3–14,74–79,83,84] can only be built of CNTs that are ~ 300 – 500 nm or longer. The distinct structure of the short VACNT arrays observed in the simulations is not a result of the limitations of the computational sample preparation procedure, but a reflection of the natural energy minimization in forests consisting of short nanotubes.

3.5 Application of mesoscopic modeling to investigation of mechanical and thermal properties

The development of the sample preparation method capable of reproducing, for the first time, the experimentally observed mesoscopic structure of vertically aligned networks of nanotube bundles opens up a broad range of opportunities for investigation of mechanical and thermal

transport properties of this important class of CNT materials. In this section, we only provide a few examples illustrating some of the potential applications of the dynamic mesoscopic model by preliminary results of first mesoscopic simulations performed for VACNT forests generated as discussed in section 3.2.

One broad area where the mesoscopic modeling can be highly instrumental is the analysis of the deformation mechanisms that control the mechanical properties of VACNT forests. The understanding of the mechanical properties is critical for a variety of applications, including energy absorption [29, 111, 112], electromechanical probing [113], fabrication of compliant contact structure for semiconductor packaging [114] and compression-modulated filter membranes [115]. One of the types of mechanical deformation that is commonly realized in the applications is the uniaxial compression of VACNT forests. The mechanical characteristics, including elastic modulus, yield stress, and resilience, characterizing uniaxial compression of VACNT forests reported in the literature are spanning several orders of magnitude [116-119]. Moreover, the recovery of uniaxially compressed VACNT forests also vary from near perfect [29, 120] to mediocre [30, 31]. The large variability of the mechanical properties is related to the high sensitivity of the structural organization of these network materials to the growth methods and conditions [28, 121], as well as to the presence of CNT defects [122, 123] and contamination. Forest density and density gradients within a sample also influence the mechanical response during compression, and several works report linear dependence of the mechanical properties, such as the stiffness and elastic modulus, on density [123-125].

The relationship between the structural characteristics and mechanical properties of VACNT materials can be effectively and systematically explored in mesoscopic simulations performed for computational samples with realistic structures. This exploration is enabled by the computational procedure described in this paper and providing a high level of control over the structural characteristics of vertically aligned networks of nanotube bundles. A series of snapshots from a small-scale simulation of the uniaxial compression of a VACNT forest, shown in Figure 3.9a–c, illustrates some of the capabilities of the mesoscopic modeling. The folding and bowing of the short CNT bundles in this simulation is facilitated by collective bending buckling of nanotubes in localized regions of bundles (red segments in the snapshots), which reduces the resistance of bundles to the bending deformation. The corresponding stress-strain curve predicted in the

simulation (Figure 3.9d) agrees well both qualitatively and quantitatively with stress responses measured in VACNT forest compression experiments [31]. In particular, three characteristic regimes, (i) elastic, (ii) plateau, and (iii) densification, commonly reported for VACNT forests [31, 32, 126], can be clearly identified in the simulated stress-strain curve shown in Figure 3.9d. A thorough analysis of the uniaxial compression of *in-silico* VACNT forests is presented in a chapter 4.

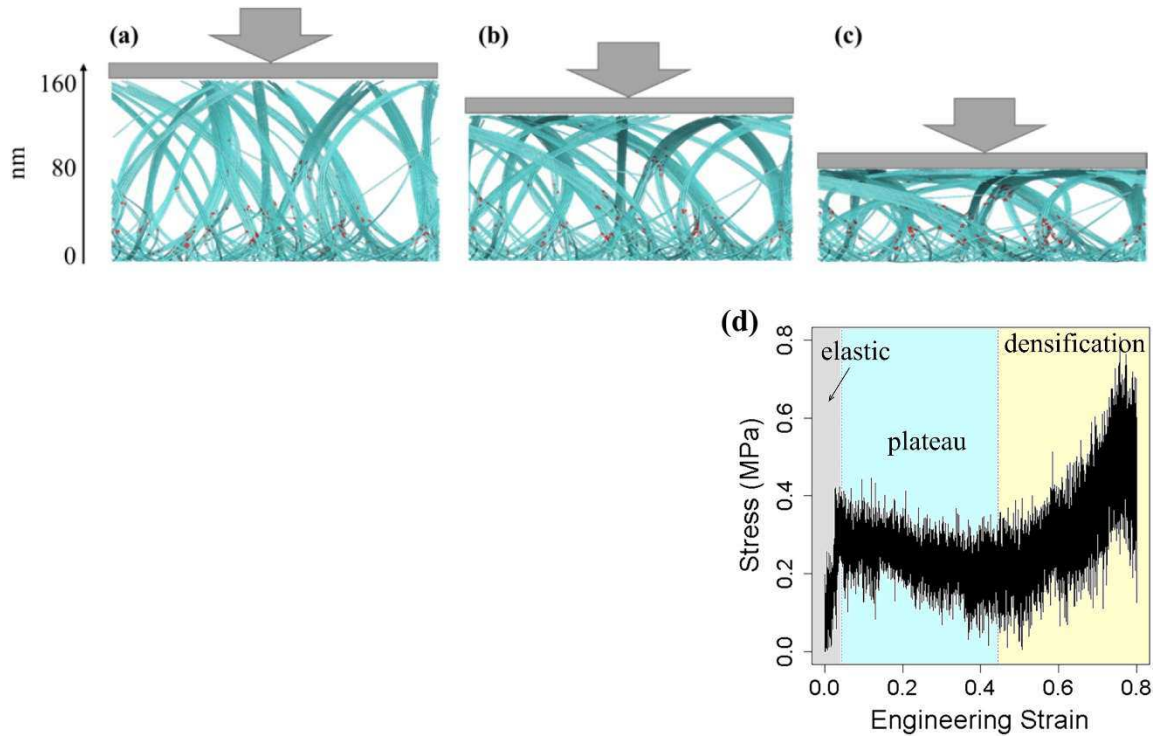


Figure 3.9: A series of snapshots (a–c) and a stress-strain dependence (d) obtained in a mesoscopic simulation of uniaxial compression of the VACNT forest composed of 200-nm-long (10,10) CNTs prepared with $\theta_{max} = 27^\circ$ (see Figure 3.8c). The snapshots are shown for compressive engineering strain of 0.2 (a), 0.4 (b) and 0.6 (c). The indenter velocity is 10 m/s, which corresponds to a deformation rate of $5 \times 10^7 \text{ s}^{-1}$. The CNT segments adjacent to the buckling kinks are colored red.

The mesoscopic simulations can also be used for investigation of thermal transport properties of CNT networks, which hold promise as thermal interface materials. Indeed, the values of the cooling rate reported for different CNT-based on-chip integrated cooling solutions for transporting and dissipation of heat from microelectronic devices are as high as 100 Wcm^{-2} [127] or even 5000 Wcm^{-2} [128], making CNT materials viable candidates for cooling systems of the

next-generation microprocessors [128-133]. Moreover, the high degree of anisotropy of thermal conductivity of VACNT forests [27, 134, 135] opens up attractive opportunities for guiding the heat transport along a desired path in thermal management applications. In order to realize these opportunities, however, a clear understanding of the key microstructural features and elementary processes that control thermal transport properties of CNT network materials has to be achieved.

With the flexible approach to the generation of computational samples discussed in this chapter, it is possible to perform a thorough investigation of the dependence of thermal conductivity on the structural characteristics of the anisotropic network structures. The values of thermal conductivity can be calculated by connecting the opposing sides of a CNT sample to two heat baths with different temperatures, obtaining the steady-state temperature profile along with the heat flux through the sample, and fitting the results to the Fourier law [59, 70, 76, 78]. The values of the intrinsic thermal conductivity of CNTs and inter-tube conductance, needed for parametrization of the mesoscopic description of the heat transfer, can be obtained from results of experimental measurements, e.g., [136-139], or molecular dynamics simulations, e.g., [45-53, 76].

The mesoscopic modeling of the heat transfer is illustrated in Figure 3.10 for VACNT samples FA, FB, and FC discussed in sections 3.2 and 3.3. All CNT segments falling within 300 nm sections of either the top or base of the forest are assigned fixed temperatures, 300 and 600 K on the cold and hot sides, respectively, and the remaining nanotube segments are colored by the heat flux in the steady state regime. A visual inspection of the heat flux distributions suggests that the average heat flux is greatest in FA, and decreases for FB and FC samples. One can also discern that the heat flux is higher in the CNTs that belong to thick bundles crossing the sample from the hot to the cold heat bath regions, and is smaller for thin bundles and individual CNTs serving as interconnects between the thick bundles. This observation is in contrast to the results of the calculations performed for CNT films with random orientations of CNTs within the plane of the film [60, 76, 78], where the heat flux passing through the CNTs that are parts of the inter-bundle connections is found to be, on average, higher than in other parts of the network structures [76].

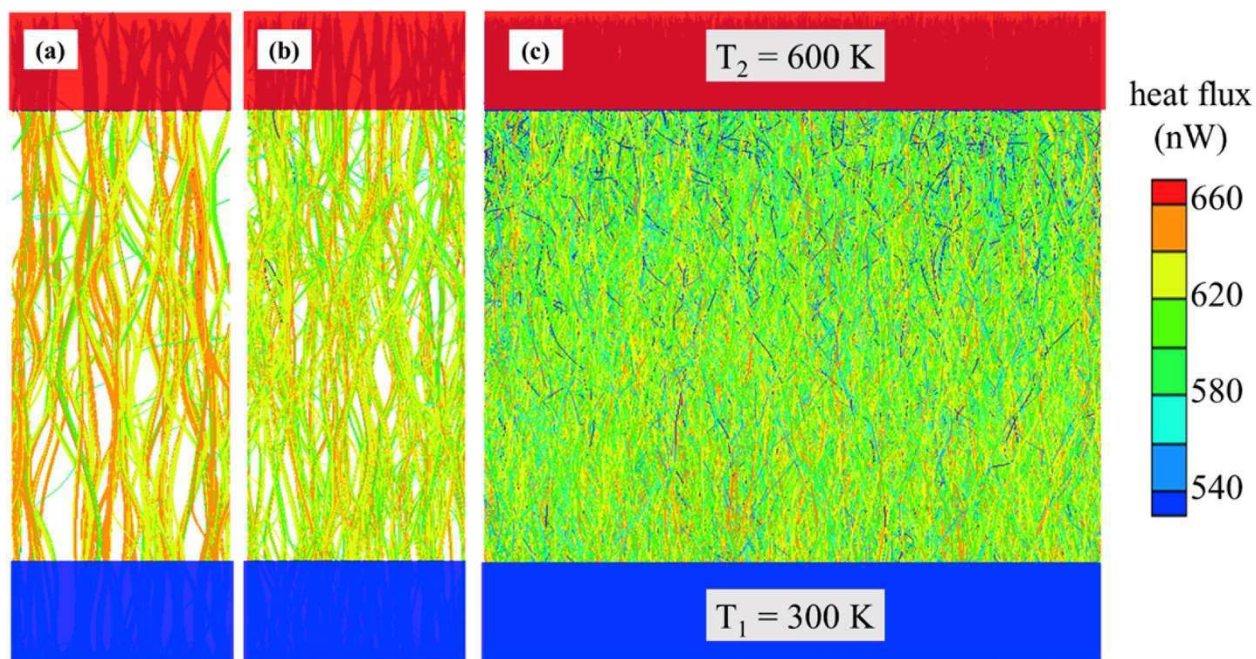


Figure 3.10: The steady-state heat flux along the nanotubes obtained in the calculations of thermal conductivity of the VACNT samples FA (a), FB (b), and FC (c), see Table 1. The calculations are done assuming an intrinsic conductivity of $2000\text{ W m}^{-1}\text{K}^{-1}$ for individual CNTs, and the inter-tube conductance is parametrized based on the results of atomistic simulations as explained in Refs. [53, 60, 70, 76, 78].

The predicted values of thermal conductivity of the VACNT samples are 17.6 , 17.2 , and $16.4\text{ Wm}^{-1}\text{K}^{-1}$ for VACNT samples FA, FB, and FC, respectively. These computational predictions fall well within the admittedly large, range of values measured for VACNT forests and fibers, e.g., $2.1\text{ Wm}^{-1}\text{K}^{-1}$ [109, 140], $42\text{ Wm}^{-1}\text{K}^{-1}$ [135], and more than $200\text{ Wm}^{-1}\text{K}^{-1}$ [134]. The corresponding effective conductivities recalculated on “per nanotube” basis are 1929 , 1874 , and $1771\text{ Wm}^{-1}\text{K}^{-1}$ for the FA, FB, and FC samples, respectively. Given that the actual intrinsic conductivity of individual nanotubes is fixed at $2000\text{ Wm}^{-1}\text{K}^{-1}$ in the calculations, the reduction of the effective conductivity is reflecting the “loss” of the conductivity due to the arrangement of CNTs into the continuous network. This reduction of the thermal conductivity exhibits a clear correlation with the decrease in the bundle size and the degree of CNT alignment, as can be seen from the structural characteristics of the three samples listed in Table 3.2.

Overall, the preliminary simulations performed for the VACNT forests reveal a significant sensitivity of the thermal conductivity to the structural details of the CNT networks and suggest

that the conductivity can be controlled through the structural modification of VACNT materials with nominally identical macroscopic parameters, such as material density, type and length of the CNTs. Similar to CNT films [60], the thermal conductivity can be evaluated for different directions of the imposed heat flux, and the values of the conductivity can be related to the degree of anisotropy of the material structure. Moreover, the calculation of the thermal conductivity for transient structures produced in the simulations of the mechanical loading, such as the ones shown in Figure 3.9, can help to quantify the effect of the deformation on thermal transport and, in particular, reveal the changes in the conductivity upon critical events, such as the onset of collective buckling in CNT forests under compression or material failure under tension.

As a final example, out of many potential applications of the mesoscopic modeling of VACNT forests, we consider the CNT forest response to a high-velocity impact by a submicron projectile. The impact resistance of CNT materials is relevant to the exploration of the performance of these multifunctional low-density materials in aerospace applications [141, 142] or as a protective armor [143], in the form of either pure CNT materials [144-146] or composites [147] reinforced with nanotubes. Using the mesoscopic model, we are in a position to methodically study the effect the CNT forest microstructure has on the absorption of the projectile energy. The development of the local heat bath approach, describing the energy redistribution between the collective degrees of freedom explicitly represented in the mesoscopic model and the internal degrees of freedom that correspond to the high-frequency atomic vibrations [77], enables a realistic representation of the energy dissipation in simulations of high-strain-rate deformation or impact loading, where the system can be expected to strongly deviate from the conditions of thermal equilibrium. As an illustration of this area of applications of mesoscopic modeling, a series of snapshots from a simulation of a platinum nanoparticle with diameter of 100 nm impacting the sample FB with an initial velocity of 100 m/s is shown in Figure 3.11. Interestingly, a global deformation of the forest occurs despite the relatively small size of the nanoparticle. This suggests that the structural arrangement of nanotubes into the continuous network plays a key role in how the energy of the projectile is absorbed and redistributed. Overall, the several examples briefly discussed above demonstrate that mesoscopic simulations performed for realistic computational samples generated with the method developed in this work are capable of capturing the complex interplay of an array of processes defining the mechanical behavior of CNT network materials under conditions of both quasi-static deformation and dynamic impact loading.

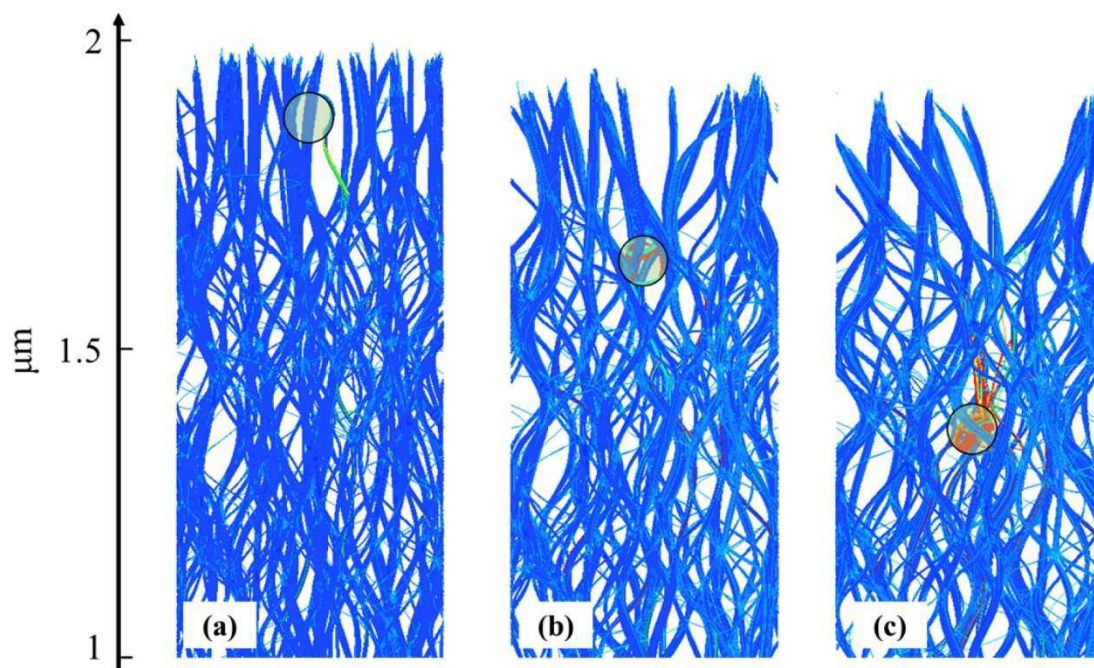


Figure 3.11: Snapshots from a mesoscopic simulation of a high-velocity impact of a spherical Pt projectile with a diameter of 100 nm, a density of 21.45 g/cm^3 and an initial velocity of 100 m/s on the VACNT sample FB (see Table 3.1). The snapshots in (a), (b), and (c) are shown for 2.5 ns, 6.0 ns, and 10.0 ns after the impact, respectively. The nanotubes are colored by their local kinetic energy, and the location of the projectile is shown by a semitransparent circle drawn in front of the VACNT configuration. Note that although it appears that the projectile is exchanging energy with the CNTs only in its localized vicinity, the entire forest is deformed during the collision, as evidenced by the shrinking height of the sample.

Overall, the several examples briefly discussed above demonstrate that mesoscopic simulations performed for realistic computational samples generated with the method developed in this work are capable of capturing the complex interplay of an array of processes defining the mechanical behavior of CNT network materials under conditions of both quasi-static deformation and dynamic impact loading.

3.6 Summary

An effective and flexible method for *in silico* preparation of structurally distinct mesoscopic samples of vertically aligned networks of nanotube bundles is developed and applied to VACNT forests and CNT fibers. The method involves generation of an initial sample composed of straight nanotubes inclined with respect to the axis of the CNT forest/fiber, followed by a high-temperature

annealing performed in a mesoscopic dynamic simulation and leading to structural self-organization of CNTs into an interconnected continuous network of CNT bundles.

The structures of the *in silico* generated VACNT forests and CNT fibers are characterized in terms of the bundle size distribution, average and maximum bundle sizes, the magnitude of the Herman orientation factor, the average tilt of CNT segments with respect to the direction of nanotube alignment in the forest/fiber structures, and the average tortuosity of the nanotubes. The structural parameters of the computational samples are compared with available experimental data and the ability of the developed computational procedure to produce structures closely matching those observed in experiments is demonstrated. Moreover, the structural parameters of the computational samples are found to exhibit a nearly linear dependence on the maximum angle of the initial inclination of nanotubes with respect to the direction of CNT alignment, thus providing an opportunity to precisely engineer the microstructure of computational samples to match those of particular experimental materials of interest.

The development of the sample preparation method capable of reproducing the experimentally observed mesoscopic structure of anisotropic networks of nanotube bundles opens up a broad range of opportunities for the computational exploration of structure – properties relationships in VACNT forests and CNT fibers. These opportunities are illustrated by first results obtained in mesoscopic simulations of the uniaxial compression and nanoparticle impact resistance of VACNT forests, as well as the heat transfer through the aligned interconnected networks of bundles.

4 Uniaxial compression and recovery of VACNT forests

4.1 Introduction

Vertically aligned carbon nanotube (VACNT) arrays, also known as carbon nanotube (CNT) “forests,” [100] hold significant promise as mechanically strong and resilient lightweight materials. When subjected to compressive loading, VACNT arrays exhibit a number of fascinating properties caused by collective interactions among CNTs organized into anisotropic networks of bundles, such as collective or coordinate buckling [29, 126] leading to the formation of microscopic wavy patterns on surfaces of the deformed samples and enabling compression up to 85% strain for thousands of cycles with almost complete recovery after unloading [29]. The impressive ability of VACNT forests to withstand repeated loading while maintaining high uniaxial stress makes them ideally suited for use as light-weight, energy absorbing materials, cushions, and pressure sensors [29, 32, 71, 116, 148, 149]. Compared with conventional low-density foams, CNT materials often exhibit a superior combination of compressive strength, recovery rate, fatigue resistance, and sag factor characterizing cushioning quality [29, 32, 116].

Not all VACNT forests, however, show good resilience, and some undergo significant plastic deformation after a single loading cycle [30, 31]. A clear understanding of microscopic structural parameters of anisotropic CNT networks that define the balance between reversible and irreversible modes of material deformation is needed for targeted fine-tuning of the mechanical properties required for engineering applications. CNT diameter and forest density have been shown to be among the key factors that define how well a forest would recover after uniaxial compression [28]. Denser forests consisting of multi-walled nanotubes (MWCNTs) with large diameters are found to be stiffer and better able to recover after CNTs form new contacts with each other via van der Waals non-bonded interactions during compression, resulting in a better resilience in cyclic loading. The superior resilience of MWCNT forests can, in part, be attributed to the specifics of bending buckling deformation, which is characterized by appearance of localized ripples along the outer wall of a MWCNT rather than buckling kinks observed for single-walled CNTs (SWCNTs) [80, 150, 151]. This results in a strong inter-wall repulsion that acts as a restoring force for straightening of MWCNTs. Conversely, sparser forests, especially those consisting of CNTs with fewer walls, are prone to plastic deformation as the nanotubes irreversibly aggregate during compression. These differences are partially responsible for variability in the

magnitude of mechanical properties (*e.g.*, modulus of elasticity, modulus of resilience, loss coefficient) of VACNT forests reported in the literature [116-119]. Other important factors affecting the mechanical response of VACNT forests are the CNT-CNT contact density and morphology [152, 153], CNT surface roughness [118, 154], presence of defects [123, 155], and strain rate [31, 32, 153, 156]. Table 4.1 provides ranges of elastic properties for structurally distinct VACNT forests taken from Ref [28]. Therein, the modulus of resilience is the energy per unit mass that a material can store elastically. Mathematically, the mass specific modulus of resilience is defined as the quotient of the square of the yield strength (σ_y) over twice the elastic modulus (E) times the material density (ρ), *i.e.*,

$$U = \frac{\sigma_y^2}{2E\rho} \quad (4.1)$$

Table 4.1: Typical range of mechanical properties of multi-walled VACNT forests with mass densities ranging from 0.008 to 0.2 g/cm³ [11].

Yield Strength (MPa)	Elastic modulus (MPa)	Modulus of resilience (kJ/kg)
0.02-10	1-150	0.03-3.6

A systematic evaluation of factors affecting the mechanical properties of VACNT forests through *in situ* tests and *ex situ* analysis, however, is hampered by the difficulty of growing VACNT forests with precisely controlled structural characteristics, as well as by the large number of structural parameters, such as CNTs diameter, length, and number of walls, forest density, degree of alignment, bundle size distribution, porosity, presence of defects and cross-links, *etc.*, which have to be controlled during the growth process. Under conditions when it is difficult, if not impossible, to grow a series of samples with the controlled variation of some of these structural characteristics while keeping other characteristics fixed, predictive and reproducible computer simulation presents an attractive approach to the exploration of the multi-dimensional space of structural parameters of CNT network materials and their effect on the mechanical properties.

Faithfully reproducing the multiscale nature of VACNT forests, from the atomic structure of CNTs to their arrangement into complex networks of interconnected bundles, has been a long-standing challenge for traditional materials modeling techniques. At the atomic scale, the

molecular dynamics (MD) technique [35] has been widely used to simulate the mechanical and thermal transport properties of individual nanotubes, *e.g.*, [38-49] and small groups of CNTs, *e.g.*, [50-53, 157]. Although the investigation of the properties of individual nanotubes and their interactions is a necessary step in the analysis of the behavior and properties of CNT network materials, macroscopic properties of these materials are defined by the collective interactions of thousands of nanotubes organized into a network of bundles. The macroscopic properties, therefore, cannot be derived directly from the properties of individual nanotubes and can only be addressed in simulations performed at a length scale that encompasses a sufficiently large representative part of the network structure, which is far beyond the capabilities of the atomistic MD model.

To close the gap between the well-established atomistic description of individual nanotubes and the macroscopic properties of CNT materials that can be formulated at the continuum level in terms of constitutive relationships, a number of mesoscopic computational models [54-57] capable of simulating the collective behavior and properties of large CNT ensembles, *e.g.*, [55, 58-60], have been developed. The common features of several alternative mesoscopic models proposed for CNT materials [54-57] include the coarse-grained description of nanotubes, where nanotube segments composed of many atoms are represented by a highly reduced number of dynamic degrees of freedom. In addition, they share similar formulations of the internal parts of the mesoscopic force fields that account for the stretching and bending deformation of individual nanotubes, and are parameterized based on the results of atomistic simulations. The different models, however, adopt very distinct computational approaches for the description of the non-bonded van der Waals inter-tube interactions.

The first and most straightforward mesoscopic approach to the description of CNT-CNT interactions is based on the bead-and-spring model [54], commonly used in coarse-grained simulations of polymers [61]. In this approach, the van der Waals inter-tube interactions are modeled through spherically symmetric pair-wise interactions between mesoscopic nodes representing segments of nanotubes. Due to its simplicity, the bead-and-spring model has become a popular choice for mesoscopic modeling of CNT films [58, 62-68] and VACNT arrays [69]. As discussed in Refs. [55, 57, 59, 70], however, the pair-wise interactions between the “beads” in the bead-and-spring model introduce large artificial barriers for relative displacements of neighboring

CNTs, which prevents long-range rearrangements of CNTs required for their self-assembly into continuous networks of bundles and strongly affects the structure and mechanical behavior of the CNT materials.

More recently, a “finite beam element” model [71] describing van der Waals inter-tube interactions by linear elastic bar elements added at localized “contacts” has been proposed and applied for simulation of the mechanical behavior of two-dimensional (2D) CNT forests. Although the model is capable of reproducing some of the general experimentally observed features of the stress-strain response of VACNT forests undergoing uniaxial compression, the 2D nature of the model and the description of CNT-CNT interactions by strongly localized bonds that cannot be broken in the course of the forest “growth” or compressive deformation prevent application of this model for realistic simulations of structural self-organization or mechanical properties of the CNT network materials.

More advanced descriptions of non-bonding inter-tube interactions that do not produce the artificial corrugation of the inter-tube interactions have recently been developed, namely a mesoscopic model [55, 72, 73] based on the distinct element method [74, 75] and a model representing nanotubes as a sequence of cylindrical segments [56] interacting with each other through the tubular potential method [57]. The latter approach has been parametrized to provide a realistic description of nonlinear deformation, buckling [59] and mechanical energy dissipation in individual CNTs [77], as well as collective heat transfer in CNT materials [50, 60, 70, 76]. This model is detailed in chapter 2, and is used in the present chapter for simulation of the uniaxial compression of VACNT forests. An overview of the computational samples used in the simulations is provided in section 4.2 and is followed by presentation of the results of the simulations. A detailed discussion of the effect of the mesoscopic structure of the VACNT forests, compression rate, material density, and the interaction of the CNTs with the indenter on the mechanical properties and deformation behavior of the VACNT forests is provided in section 4.3. The results of the simulations of repetitive loading and unloading of a VACNT forest over five cycles are presented in section 4.4 for two different types of CNT - indenter interactions. Finally, a summary of the results is given in section 4.5.

4.2 Computational samples of VACNT forests

The generation of computational samples for mesoscopic modeling of the mechanical compression and recovery of VACNT forests is done with a recently developed method described in Ref. [158]. The method involves generation of an initial sample composed of straight nanotubes inclined with respect to the axis of the CNT forest, followed by a high-temperature annealing performed in a mesoscopic dynamic simulation which leads to the structural self-organization of CNTs into an interconnected network of CNT bundles. The choice of the maximum angle of the initial inclination of nanotubes with respect to the direction of preferred CNT alignment is found to provide a high degree of control over the structure of computational samples, thus enabling the generation of microstructurally distinct VACNT forests with tunable bundle thickness distribution and degree of nanotube alignment.

The three samples used in the present study are composed of (10,10) single-walled CNTs (SWCNTs) with a diameter of 1.357 nm [57], typical for SWCNT forests grown by chemical vapor deposition (CVD) [13, 159-162]. The CNT areal density (*i.e.*, the number of nanotubes per unit area of the substrate) of experimental samples exhibits a large, orders of magnitude, variability [13, 159-161] and, in order to explore the effect of density on the mechanical properties of VACNT forests, computational samples with different areal densities are considered. The first two samples, designated as FA and FB, have the same density 0.02 g/cm^3 (areal density of $6.09 \times 10^{11} \text{ CNT/cm}^2$) but differ in their microstructure. The CNTs of FA are highly oriented and form smaller bundles as compared to FB, where CNTs are poorly oriented but arranged into thicker bundles. The third sample, designated as FC, has a five times higher density of 0.1 g/cm^3 (areal density of $3.05 \times 10^{12} \text{ CNT/cm}^2$). Its bundles are much thicker than those of FB, and its nanotubes are moderately inclined. For each sample, Table 4.2 provides details on the density, average CNT segment tilt, average bundle size, maximum bundle size, and magnitude of the Herman orientation factor (HOF) defined as $S = \frac{1}{2}[3\langle \cos^2 \theta \rangle - 1]$, where θ is the local angle between a nanotube segment and the vertical axis and $\langle \dots \rangle$ denotes averaging over all CNT segments in a sample. The HOF quantifies the extent of the orientation of nanotubes with respect to an axis of interest, and ranges from -0.5 to 1, where values of -0.5, 0, and 1 correspond to perpendicular alignment, isotropic orientation, and parallel alignment with respect to the axis, respectively. The bundle size is defined locally as

the number of CNTs in a bundle cross-section, and a CNT is considered to be a part of a bundle if it is within the range of inter-tube interaction potential from any other nanotube in a bundle.

For all of the computational samples, the length of CNTs is fixed at 200 nm, periodic boundary conditions are applied in the lateral directions (parallel to the surface of the substrate), and the lateral size of the computational system is chosen to be $200 \times 200 \text{ nm}^2$ to ensure that the mechanical behavior of the computational samples is not affected by the periodic boundary conditions. Although 200 nm is relatively short as compared to multi-micron-long samples typically used in experimental studies [29, 32, 126, 163, 164], we find that the stress-strain response and deformation behavior observed for VACNT forests in laboratory compression tests are reproduced in the simulations performed with the short forests. At the same time, the use of the relatively small computational systems allows us to perform a comprehensive parametric study of the dependence of deformation behavior and mechanical response of the computational VACNT forests on (1) the sample density and microstructure, (2) rate of compressive deformation, and (3) nature of the CNT - indenter interaction. Such systematic study would not be feasible for longer CNTs (and correspondingly larger lateral dimensions of the computational samples) due to the high computational cost of the simulations. Indeed, for a $200 \times 200 \times 200 \text{ nm}^3$ coarse-grained VACNT forest consisting of 248 nanotubes represented by approximately 25,000 dynamic elements (samples FA and FB), 1 ns of simulated time with a time step of 10 fs takes approximately 12 wall-clock hours on 16 standard compute nodes of *Comet* supercomputer at the San Diego Supercomputer Center [165] accessed through the Extreme Science and Engineering Discovery Environment (XSEDE) [166]. Given that a simulation of a uniaxial compression down to the engineering strain of 0.8 with an indenter velocity of 10 m/s takes 16 ns, running a large number of simulations for systems composed of longer tubes would put a significant strain on the available computational resources. Instead, we address the effect of CNT length on the mechanical properties of VACNT forests by performing a smaller number of simulations for forests composed of longer CNTs. The results of these simulations will be reported in the chapter 5.

Table 4.2: Statistical information on structural parameters of three computational forests used in the simulations of compressive deformation reported in this paper. The density ρ , average tilt of CNT segments $\langle\theta\rangle$, average bundle size $\langle N_B \rangle$, maximum bundle size N_B^{max} , and Herman orientation factor HOF are listed for computational samples FA, FB, and FC.

Sample	ρ (g/cm ³)	$\langle\theta\rangle$	$\langle N_B \rangle$	N_B^{max}	HOF
FA	0.02	5.6°	4	10	0.96
FB	0.02	20.5°	10	36	0.73
FC	0.1	16.4°	108	315	0.83

All simulations reported in this paper are performed at a constant temperature of 300 K, enforced by the Berendsen thermostat algorithm [88]. The stresses are calculated from the total force that the forest exerts on the indenter. The engineering strain is defined with respect to the length of the CNTs within the forest (*i.e.*, 200 nm), rather than the maximum initial forest height, which is shorter than 200 nm by less than 1%. For the convenience of representation of stress-strain dependences for VACNT forests undergoing compressive loading, we adopt a sign convention where the stress is positive in compression, and present the magnitude of the engineering strain as a positive quantity.

4.3 Uniaxial compression of VACNT forests

In this section, we discuss four sets of simulations of the uniaxial compression of forests FA, FB, and FC. In the first three subsections, the VACNT forests are not attached to the indenter, rather interacting with it in a purely repulsive manner. The role of the mesoscopic structure of the forest, rate of compression, and density of the material are analyzed in the first three subsections. In the last subsection, the effect of the CNT – indenter interaction is addressed based on the results of additional simulations in which the top parts of the CNTs are attached to the indenter.

4.3.1 Role of microstructure

In our first set of simulations, we consider forest samples FA and FB, which have the same density and differ only by their structural characteristics (*i.e.*, thickness of the bundles and CNT inclination, as seen in Table 4.2). Both forests are compressed at an indenter velocity of 10 m/s, corresponding to a deformation rate of 5×10^7 s⁻¹ for these 200-nm-long VACNT forests. Note that 10 m/s is a relatively fast velocity compared to the ones typically used in experiments, 1-1000 nm/s. While matching the experimental deformation rates in our simulations is not feasible due to

computational limitations, the stress-strain curves obtained in the simulations are in a reasonable semi-quantitative agreement with experimental observations, suggesting that further reduction of the deformation rate is unlikely to result in major changes in the deformation mechanism. Indeed, the analysis of the dependence on the deformation behavior on the rate of compression reported in section 4.2 reveals substantial changes in the shape of stress-strain curves upon the reduction of the indenter velocity from 50 m/s to 20 m/s, and only moderate quantitative changes upon further decrease of the velocity to 10 m/s.

Snapshots from the two simulations are shown in Figure 4.1, where nanotube segments adjacent to the buckling kinks are colored red. In both cases, the top parts of the nanotubes form a dense layer right below the indenter. As the indenter presses down on the forest, the nanotubes reorganize themselves to fit into the smaller volume. Ideally, the dense packing of CNTs would correspond to a horizontal, close-packed alignment of nanotubes along the substrate. However, the attachment of the nanotubes to the substrate limits the CNT rearrangement and activates multiple modes of the forest deformation. One scenario occurs when the CNT fold over in a coordinated fashion from the base of the forest at a height where many CNTs coalesce into thick bundles. The CNTs move together when bundled, and this deformation mechanism is favored when the nanotubes belong to the thicker, less oriented bundles of FB. This deformation mode, referred to here as “folding” (the bundles fold over at their bases) is illustrated in a snapshot shown for FB compressed to 0.6 strain (Figure 4.1b). Another possible response of CNT bundles to the compression is lateral deflection along its height, or bowing outward from the initial axis of the bundle. This deformation mode, referred to herein as “bowing,” is observed for thinner, more oriented bundles, and is exemplified in a snapshot shown for FA at 0.6 strain in Figure 4.1a. Although both folding and bowing deformation modes can be identified in each of the two computational samples in Figure 4.1, the prevalent deformation mode is defined by structural characteristics of the samples. In particular, the smaller, more oriented bundles of FA tend to bow outward near the indenter head, while the larger, less oriented bundles of FB tend to fold near the base of the forest.

Turning our attention to the bending buckling of the nanotubes, visual analysis of Figure 4.1 suggests that at a strain of 0.6 or higher CNT buckling is more prevalent in sample FA as compared to FB, and that the additional buckling appearing at later stages of compression is much more localized. In fact, FA has approximately 50% more buckling kinks than FB at a strain of 0.6, and

more than double the number of buckling points of FB at a strain of 0.8. This difference can be attributed to the prevalent modes of deformation discussed above for the two samples. When bundles bow out in FA, bending stress concentrates in localized regions of the bundles, leading to the collective buckling of many nanotubes across the corresponding bundle cross-sections. A clear example of this localized collective buckling can be seen in the upper part of the bundle outlined in a snapshot shown for 0.6 strain in Figure 4.1a. The folding mode of deformation characteristic of FB differs in that the bending stress resulting from compression is localized at the base of the forest, and the curvature in the upper portions of thick bundles does not reach the level required to induce bending buckling [59].

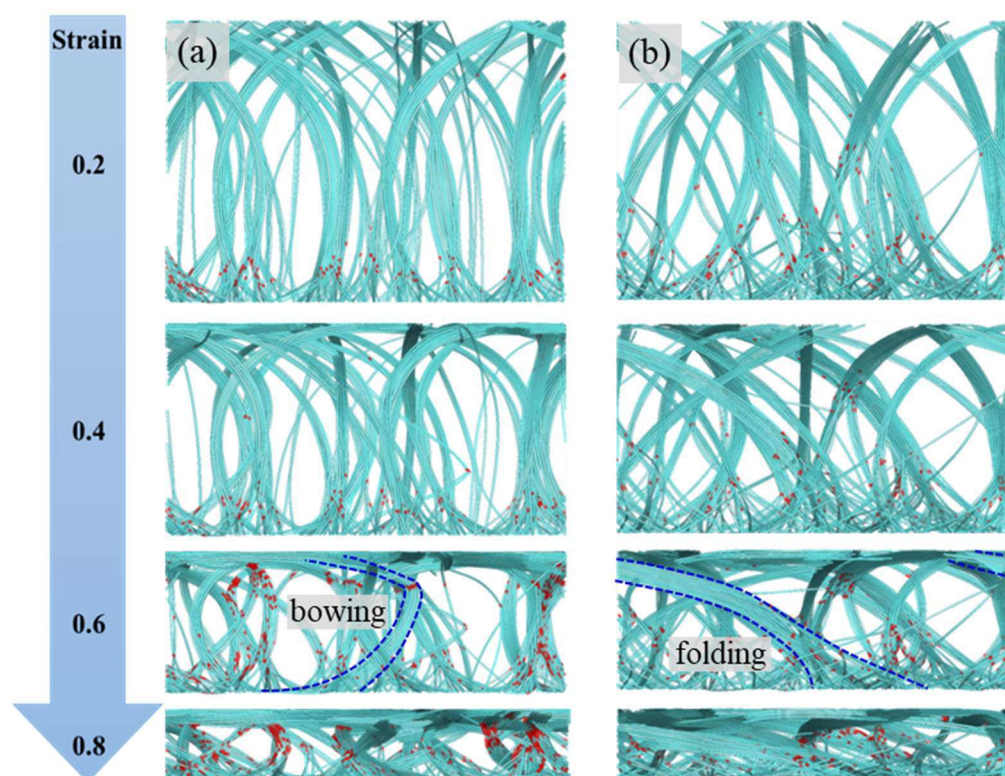


Figure 4.1: Snapshots from simulations of uniaxial compression of computational samples FA (a) and FB (b) up to a maximum strain of 0.8 with an indenter velocity of 10 m/s. From top to bottom, the strain is 0.2, 0.4, 0.6, and 0.8. The CNT segments adjacent to buckling kinks are colored red. Two bundles exemplifying the bowing and folding modes of deformation are outlined by blue dashed lines in the snapshots for 0.6 strain in (a) and (b), respectively.

Note that neither FA nor FB exhibit the ubiquitous periodic buckling observed in experimental studies of the compression of VACNT forests [29, 31, 124, 126] characterized by the buckling

instability extending across the whole sample thickness and producing an accordion-like wavy pattern, distinct from the natural wrinkling observed during the compression of a sheet [167]. According to the classical Euler-Bernoulli beam theory [168], the critical stress at which a column under compression deflects laterally is inversely proportional to the square of its height. Hence, the difference in the nanotube length between the computational samples and many of the CVD-grown forests can be partly responsible for the absence of the repeated coordinated buckling in the computational forests [169]. Another important factor is the pristine nature of the computational samples, which do not have any defects or density variation along the vertical axis. Defects and the density gradients have been found to play a key role in the onset of coordinated buckling. In particular, the coordinated buckling often starts near the base of the forest, where the density can be lowest [31, 32, 124, 163], and CNT diameter may be smaller [28]. Our samples do not have such types of preferential nucleation sites, and hence periodic buckling may be suppressed. Finally, the periodic boundary conditions applied in the lateral directions eliminate free surfaces on the sides of the samples and prevent the surface nucleation of the buckling instability [29, 31, 126].

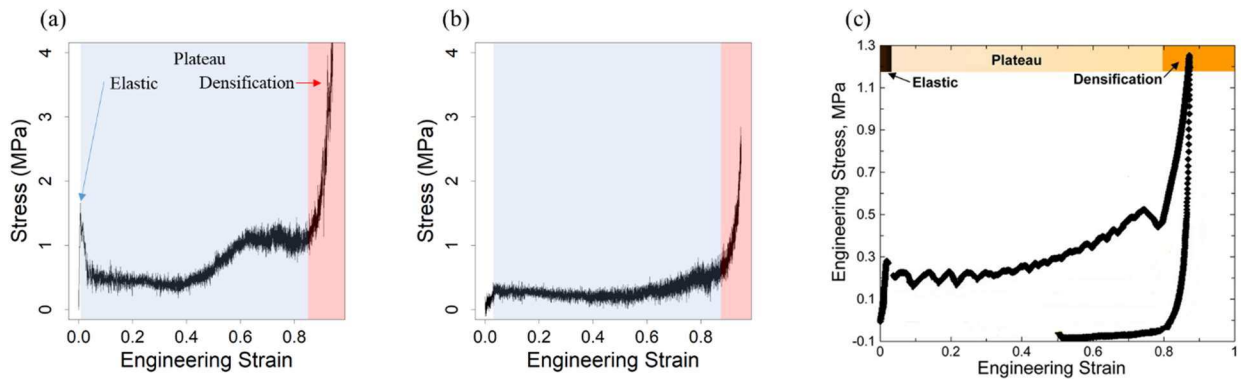


Figure 4.2: Stress-strain dependences obtained in the simulations of uniaxial compression of computational samples FA (a) and FB (b) with an indenter velocity of 10 m/s, and a typical experimental stress-strain curve measured for a VACNT forest compressed at 1000 nm/s (adapted from Ref. [124]) (c). The white, blue, and red shaded regions in (a) and (b) correspond to the elastic, plateau, and densification regimes of the compressive deformation, respectively.

The measurement of the stress-strain relationship is a common way to evaluate the mechanical properties of the VACNT forests. The stress-strain response of VACNT forests is usually similar to that of conventional foam-like materials and is characterized by three distinct regimes, as

illustrated by Figure 4.2c [124]. The initial deformation proceeds in an elastic regime characterized by a sharp increase in stress without noticeable structural changes in the material. After the initial buckling event, which can involve multiple bundles, the stress drops, giving way to the plateau regime. For VACNT forests, the plateau regime is often characterized by a corrugated, upward trending stress-strain response produced by repeated, localized, coordinated buckling occurring along the height of the forest. Buckling occurring in this regime may be either reversible or irreversible, depending on the CNT types and structural characteristics of the forest. Finally, at high strains, the forest cannot readily deform via soft bending and buckling modes, and the densification regime characterized by material stiffening is reached. It is important to note that the terms “elastic,” “plateau,” and “densification” do not necessarily correspond to a particular mode of deformation and are herein used to denote the stress-strain response only. For instance, the deformation occurring in what we term the elastic region is not necessarily entirely reversible due to the metastable nature of the VACNT samples. The elastic modulus and the yield strength used for characterization of the “elastic region” of stress-strain dependence are formally defined here as the slope of the initial stress increase and the maximum stress of the “elastic peak,” respectively.

The stress-strain curves obtained in the simulations performed for samples FA and FB are shown in Figure 4.2a and Figure 4.2b, respectively. Comparing these plots to Figure 4.2c, we see that the three characteristic deformation regimes are clearly present. Following the unshaded elastic regime, two shaded regions identify the plateau (blue), and densification (red) regimes, which were visually discerned. Despite the much shorter length of the nanotubes and differences in the CNT types and deformation conditions, the magnitude of the stress response is in a good agreement with the experimental results, especially for the loading of sample FB. This semi-quantitative agreement suggests that the simulations capture the main deformation mechanisms that define the shape of the stress-strain curves under compressive loading. Interestingly, although the collective buckling of individual CNT bundles does not lead to the lateral propagation of the buckling instability through the computational samples (Figure 4.1), the low stress plateau regime is still reproduced in the simulations, suggesting that the macro-scale periodic buckling of the forest is not the main cause of (or a necessary condition for) the flat low-stress region of the stress-strain dependence.

When drawing an analogy between the stress-strain behavior of VACNT arrays and cellular foams, it is prudent to differentiate two types of mechanical response of foam structures. Most common open and closed-cell foams exhibit bending-dominated behavior characterized by bending of the cell walls during deformation, whereas the cell walls stretch in foams exhibiting stretching-dominated deformation response [170]. From a mechanical standpoint, the bending-dominated foams are compliant but well suited for energy absorption applications due to their extended and flat plateau stress regime, while the stretching-dominated foams have a large elastic peak followed by post-yield softening, and are generally quite stiff [171]. Although the deformation mechanisms of conventional cellular foams and VACNTs are not directly comparable, there are still some interesting parallels between the stress-strain responses of each type of material. The large spike in the elastic stress of sample FA (Figure 4.2a) is similar to that of a stretch-dominated structure, whereas sample FB (Figure 4.2b) behaves more like a bending-dominated foam structure. The analogy between the mechanical response of foams and VACNTs are further discussed in section 4.3.2, where the role of the deformation rate is considered.

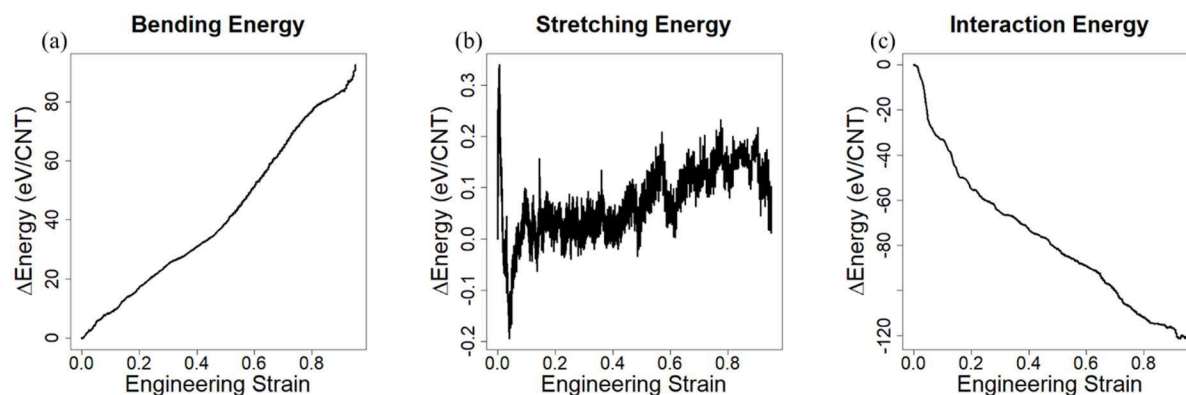


Figure 4.3: Plots of the changes in (a) bending, (b) axial stretching, and (c) inter-tube interaction energies per nanotube in sample FA undergoing compression at an indenter velocity of 10 m/s.

In the initial elastic responses of the two samples, FA has a larger yield strength (1.66 MPa) and elastic modulus (284 MPa) as compared to FB (0.44 MPa and 8.67 MPa yield strength and elastic modulus, respectively). The reason for the more robust elastic response of sample FA is that a greater fraction of vertically-oriented nanotubes undergoes a substantial axial compression before the onset of bending and buckling. This is evidenced by a spike in the CNT stretching

energy shown in Figure 4.3b at the initial stage of compression, occurring at the same strains where the elastic stress reaches its peak values (Figure 4.2a). The plots of the bending, axial, and inter-tube interaction energies shown in Figure 4.3 for sample FA compressed at 10 m/s are qualitatively quite similar to those of sample FB (not shown), except for the absence of the pronounced axial stretching energy peak at low strains.

The initial part of the plateau regime, below 0.4 strain, is similar for forests FA and FB, although the average stress is somewhat lower for sample FB, Figure 4.2a,b. At this stage of the deformation, the CNTs in both samples are able to shift themselves into low resistance configurations with relative ease. At higher strains, above 0.4, the difference between the stress-strain responses of forests FA and FB becomes apparent, as the stress exhibits a substantial increase for FA but remains fairly level for FB. This difference can be related to the distinct dominant deformation modes exhibited by the two samples. The buildup of stress in FA is attributed to the higher resistance bowing deformation, whereas the softer folding deformation mode allows for a fairly level plateau stress. At 0.6 strain, the bundles in FA are heavily bowed along their entire height (Figure 4.1a). Bending becomes pronounced along the height of the entire forest rather than being mainly confined at the base of the nanotubes and near the indenter, as reflected by the proliferation of buckled segments. In the case of FB, the bending of CNTs takes places through folding at the base (Figure 4.1b), and this mechanism does not fundamentally change with increased strain, resulting in a relatively level stress throughout the plateau regime. As strain increases to 0.6 for sample FA, a small dip in stress is observed as bending buckling once again becomes more localized (see Figure 4.1). As a result, the bending energy concentrates in small regions along the lengths of the CNT bundles and less force is exerted on the indenter, causing the overall drop in stress.

Finally, at strains above ~ 0.85 , the densification regime begins, marked by the sharp increase in stress. During this final stage of compression, CNTs within the forest become increasingly bent and packed so that they cannot significantly rearrange themselves to reduce stress. The bending energy begins to quickly increase in the densification regime and the CNT interaction energy starts to level (Figure 4.3), reflecting the increased constraints on the nanotube rearrangements.

We conclude this section by noting that the characteristic three stage stress-strain response observed experimentally for VACNT forests is reproduced for both forests FA and FB, and that

their elastic stress responses fall well within the range reported for *in situ* uniaxial compressions. The two samples of the same density but different bundle thickness and orientation discussed in this section exhibit similar sequence of compressive deformation regimes, while the average plateau and densification stresses are larger in the sample with smaller, more oriented CNT bundles.

4.3.2 Role of compression rate

The effect of the compression rate on the mechanical response of uniaxially compressed VACNT forests has been a subject of recent investigations [31, 32, 153, 156]. Faster compression has been linked to higher resilience, stiffness, and energy dissipation [31, 32, 153, 172, 173]. Moreover, slowly compressed forests are found to undergo permanent buckling, while forests subjected to rapid compression exhibit better recovery [32, 153]. It is speculated that under conditions of fast loading the multi-walled CNTs are unable to reorganize themselves into the locally buckled structures that form, in a largely irreversible manner, when the forests are loaded more slowly. Furthermore, the stress peak in the elastic regime is observed to broaden with strain rate, and the shape of the stress undulations in the plateau regime evolves from smooth sinusoidal oscillations to much sharper sine-squared modulations at greater strain rates [31].

To better understand the effect of the compression rate on the mechanical properties of VACNT forests, we repeat the simulations presented in the previous section at higher indenter velocities of 20 and 50 m/s (deformation rates of 10^8 and 2.5×10^8 s⁻¹, respectively). A snapshot showing sample FB at 0.6 strain is presented for each of the three loading rates in Figure 4.4, with the corresponding stress-strain curves shown in Figure 4.5. Analysis of the snapshots indicates that the increase in the loading rate shifts the dominant deformation mechanism from the “folding” to the “bowing” type (refer to Figure 4.1), and that the bundles coarsen less during the shorter deformation time corresponding to the higher compression rates. The latter observation is quantified by the plots of the average bundle thicknesses shown in Figure 4.6 for each of the three compression rates. The unstrained sample FA has a smaller average bundle thickness than unstrained sample FB and exhibits greater bundle coarsening with strain. However, at all but the slowest loading rate, the average bundle thickness in sample FA does not exceed the average bundle thickness of sample FB. By and large, a decrease in the compression rate leads to a more substantial coarsening of the bundles. This effect is particularly evident for forest FA, whereas the

strain effect is less pronounced for sample FB (Figure 4.6). The observed trends can be explained by the greater amount of time available for nanotube rearrangement into thicker bundles at slower deformation rates, as well as by a more sluggish rearrangement of the thicker bundles initially present in the unstrained sample FB.

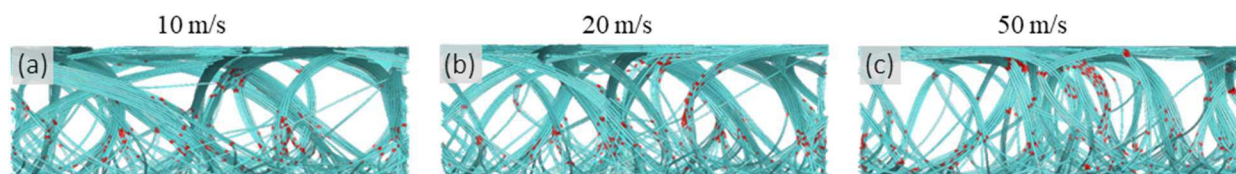


Figure 4.4: Snapshots of sample FB compressed at indenter velocities of (a) 10 m/s, (b) 20 m/s, and (c) 50 m/s to an engineering strain of 0.6.

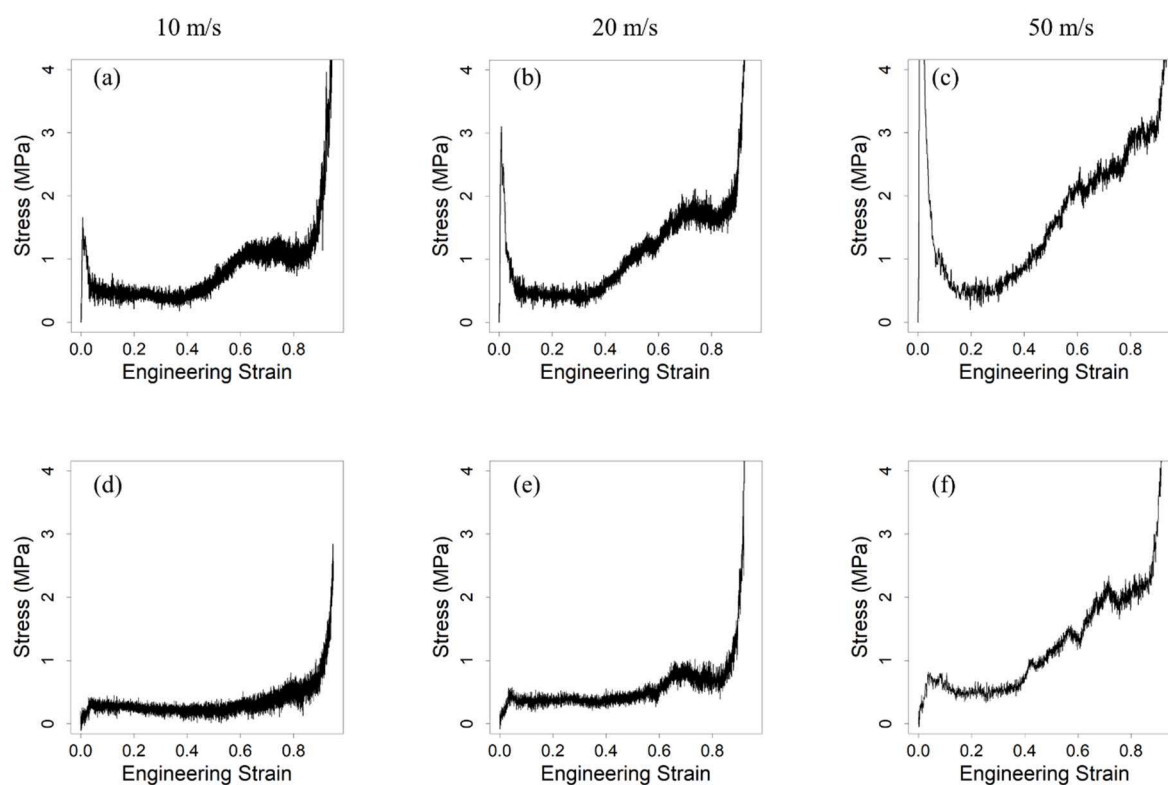


Figure 4.5: Stress-strain response of samples FA (a-c) and FB (d-f) compressed at indenter velocities of 10 m/s, 20 m/s, and 50 m/s. The corresponding strain rates are 5×10^7 , 10^8 , and 2.5×10^8 s^{-1} .

Turning our attention to the stress-strain curves shown in Figure 4.5, we notice that the general shapes of the curves are qualitatively similar for the two slower compressions, but that at 50 m/s the stress and its slope are more strongly affected by the loading rate. This trend of increasing material stiffness results from the nanotubes having insufficient time to reorganize themselves into low energy configurations as the compression rate increases. In FA, the increase in the yield strength (up to 7.21 MPa at 50 m/s) is particularly pronounced due to a more significant axial compression of the CNTs at the initial stage of the deformation (see the corresponding discussion in section 4.3.1). The increase in the strain rate also results in an increase in the modulus of resilience, which characterizes the maximum energy that can be absorbed in the elastic regime, see equation 1. Even at the higher strain rates, however, the values of the modulus of resilience calculated for samples FA and FB each fall within the broad range of experimentally measured values listed in Table 4.1.

Continuing with the analogy to cellular foams discussed in section 4.3.1, the changes in the stress-strain curve with increasing strain rate observed in the simulations can be related to a shift from the bending-dominated to stretching-dominated mechanical response of foams. Not only does the elastic stress increase, but a post-yield softening regime becomes more apparent at higher strain rates, which is also observed in *in-situ* compression experiments for CNT forests [31]. Hence, depending on the rate of compression, VACNT forests could adopt the mechanical behavior of both stretching- and bending-dominated foam structures. The broadening of the stress peak characterizing the post-yield softening arises at higher compression rates due to the reduced time that the CNTs have to reorganize themselves in a way that minimizes stress on the indenter, resulting a more gradual reduction of stress with strain.

The compression rate also affects the stress response in the plateau regime, where the plateau becomes shorter and gives way to the rising stress as the rate of the deformation increases (Figure 4.5). This effect can be explained by the limitations on the deformation paths the nanotubes can take during compression at higher loading rates. Although bending buckling of the nanotubes mitigates the stress in the plateau regime, the slower compression enables the nanotubes to rearrange themselves so that bending energy is further minimized. The change in the plateau regime has important implications for energy absorption, where an ideal energy absorber is characterized by a flat and long plateau stress. The results of the simulations suggest that the loading rate may strongly influence energy absorption properties of VACNT forests.

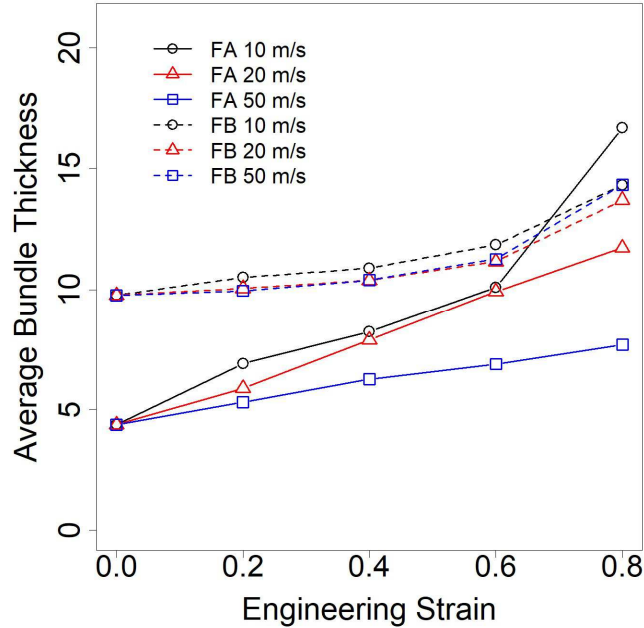


Figure 4.6: The evolution of the average bundle thickness in samples FA and FB compressed with indenter velocities of 10, 20, and 50 m/s up to 0.8 engineering strain.

4.3.3 Role of density

The areal density of a VACNT forest is an important parameter that directly affects the structural characteristics of the network of bundles generated during forest growth [12]. The balance between the inter-tube interaction energy and bending energy of CNTs, which defines the propensity of nanotubes to join the bundles or form interconnects between the bundles, is to a large extent defined by the areal density of the CNT array. To investigate the effect of the areal density on the structural characteristics and mechanical properties of the CNT forests, we prepared sample FC with a density of 0.1 g/cm^3 , or five times that of samples FA and FB used in the simulations discussed in the previous two sections. The structural characteristics of sample FC can be found in Table 4.2. Notably, while the values of structural parameters characterizing the degree of CNT alignment, $\langle \theta \rangle$ and HOF, place sample FC in between samples FA and FB, the average and maximum bundle sizes, $\langle N_B \rangle$ and N_B^{max} , are much larger than those in the lower-density forests.

The dense forest is compressed at indenter velocities of 10, 20, and 50 m/s, with snapshots for the slowest and fastest compressions provided in Figure 4.7. Like the lower-density sample with thicker bundles (sample FB), the bundles of nanotubes in sample FC tend to move in a coordinated

way when compressed, with the bundles folding near the substrate. The folding of the bundles becomes less coordinated with increasing deformation rate, and a progressively larger number of bundles undergo bowing deformation. Similar to the simulations discussed in section 4.3.2, the contribution of the bowing deformation mode leads to higher stresses at all stages of the deformation.

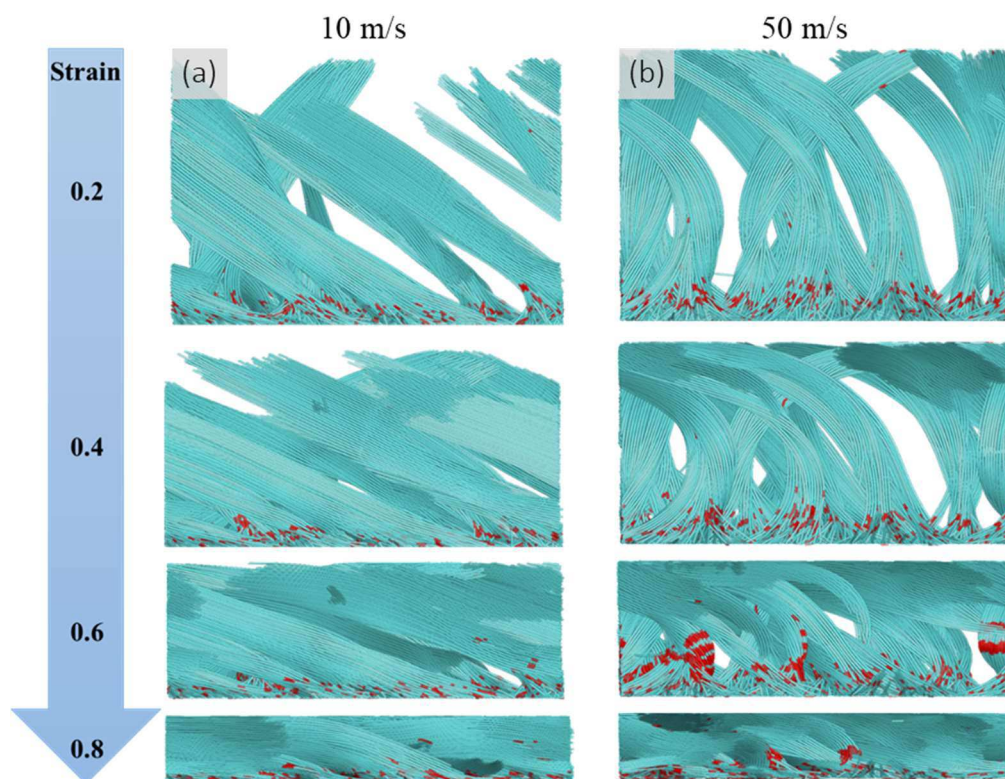


Figure 4.7: Snapshots from simulations of a computational sample FC compressed at indenter velocities of (a) 10 m/s and (b) 50 m/s up to a maximum strain of 0.8. From top to bottom, the strain is 0.2, 0.4, 0.6, and 0.8. The CNT segments adjacent to buckling kinks are colored red.

The stress-strain plots obtained for sample FC and shown in Figure 4.8 are qualitatively similar to those predicted in simulations for sparser forests (Figure 4.2 and Figure 4.5). Remarkably, many of the quantitative characteristics of the mechanical response of sample FC are also comparable to those of the samples with five times fewer CNTs. In particular, the yield strength and elastic modulus calculated for sample FC are similar to those of sample FA when the simulations performed at the same compression rate are compared. The yield strength increases by a factor of less than two from FA to FC, and the elastic modulus differs between the two forests by less than

20% for the same loading rate. These observations can be explained by a greater average inclination of CNTs in sample FC as compared to sample FA (see Table 4.2). The more inclined nanotubes offer less resistance to the indenter during the elastic stage of the compression, since they deform predominately by bending rather than by axially compression, which was identified in section 4.3.1 as the source of the initial spike in the stress-strain curve.

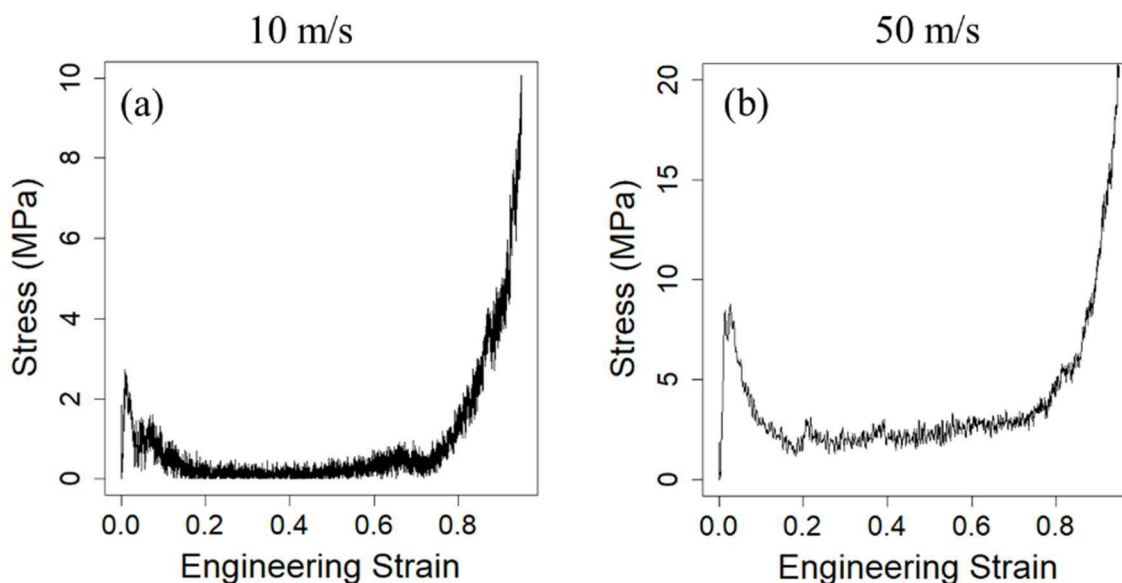


Figure 4.8: Stress-strain response of sample FC compressed at indenter velocities of (a) 10 m/s and (b) 50 m/s. The corresponding deformation rates are 5×10^7 and 2.5×10^8 s⁻¹. Note the twice larger scale of the stress axis used in (b).

The plateau stress evolves similarly between samples FA, FB, and FC at both low and high compression rates. Although the slopes and magnitudes of the plateau stresses of all three samples are comparable at 10 m/s, the slope of the stress increases more rapidly with the deformation rate for sample FC. An explanation comes from the decreased nanotube mobility in the denser forest, where CNTs tend to belong to thick bundles and are largely compelled to deform with the original parent bundles. As a result, the nanotubes cannot reorganize themselves via low energy bending and localized buckling deformations as much as they do so in sparser forests with smaller bundles.

At the final stage of the compression, a sharp increase in stress signifies the transition to the densification regime (see Figure 4.8). Similar to the simulations discussed in preceding sections, the sharp rise in the magnitude of the stress in this regime does not appear to be related to CNT

crowding and repulsion between the nanotubes, since the inter-tube interaction energy decreases until the end of the simulation. Instead, at the high strains, the localized bending of the thick bundles becomes extreme, resulting in a large force against the indenter (see snapshots for 0.8 strain in Figure 4.7). At larger strain rates, the picture differs slightly, as the tubes start to buckle further away from the base (e.g., see snapshot for 0.6 engineering strain in Figure 4.7b) and bending is distributed more uniformly along the nanotubes. In each case, the higher density and thicker bundles of FC result in a large rise in stress at lower strains compared to the sparser forest samples.

4.3.4 *Role of CNT interaction with indenter*

In all simulations discussed above, the interaction of CNTs with the indenter is assumed to be purely repulsive, presenting no barriers for lateral sliding (zero traction) of CNTs with respect to the indenter. In real compression experiments, however, there is generally at least some attractive interaction between the CNTs and the indenter (either non-bonding or chemical). In other words, the adhesion between the nanotubes and the indenter can manifest itself in an attractive force resisting the indenter pull off from the VACNT forest during unloading of a compressed sample [172, 174]. One can also expect that the constraints on the lateral slip of the nanotubes with respect to the surface of the indenter is likely to affect the deformation behavior, particularly for short forests subjected to compression. To gain insights into the effect of the interaction between the CNTs and the indenter on the mechanical characteristics of VACNT forests undergoing compressive deformation, a series of simulations is performed for samples where the top segments of the nanotubes located within 10 nm from the indenter are permanently affixed to the indenter. These segments move together with the indenter during the compression and have no rotational freedom. The CNTs that have their top ends falling below the 10 nm cutoff distance from the indenter in the initial sample do not “stick” to it even if they get closer to the indenter during the deformation and are not affected by this boundary condition. Since the tops of many of the nanotubes are effectively “glued” to the indenter, we, shorthanded, refer to these simulations as “glue” simulations, while the simulations where the tops of the CNTs are not attracted to the indenter are referred to as “free” simulations.

The first set of glue simulations is performed for sample FA and is illustrated by snapshots shown for indenter velocities of 10 and 50 m/s in Figure 4.9. Here, the nanotubes cannot deform via the folding deformation mode and, even at the slowest strain rate, the deformation proceeds

through bowing of the CNT bundles. Similar to the free simulations performed for low-density samples FA and FB (see Figure 4.1 and Figure 4.4), bending deformation of the top parts of the CNTs leads to the formation of a dense layer adjacent to the indenters. However, since the nanotubes cannot slide along the indenters in the glue simulations, bowing of CNT bundles readily results in localized regions of collective bending buckling along the height of the bundles. This effect is particularly noticeable in Figure 4.9a, where most of the CNT bundles feature well-defined regions of localized buckling (red CNT segments) at 0.6 engineering strain. In contrast, snapshots of the analogous free simulation, where CNTs interact repulsively with the indenter, show a lesser degree of buckling kink localization within the bundles (Figure 4.1a). Moreover, some of the bundles in the glue simulations are observed to undergo higher-order bending producing “S” shaped, serpentine bundle shapes, such as the one outlined by dashed curves in a snapshot shown for 0.2 strain in Figure 4.9b. The formation of such bending modes requires significantly higher loads and is not observed in simulations performed with the free tops of CNTs.

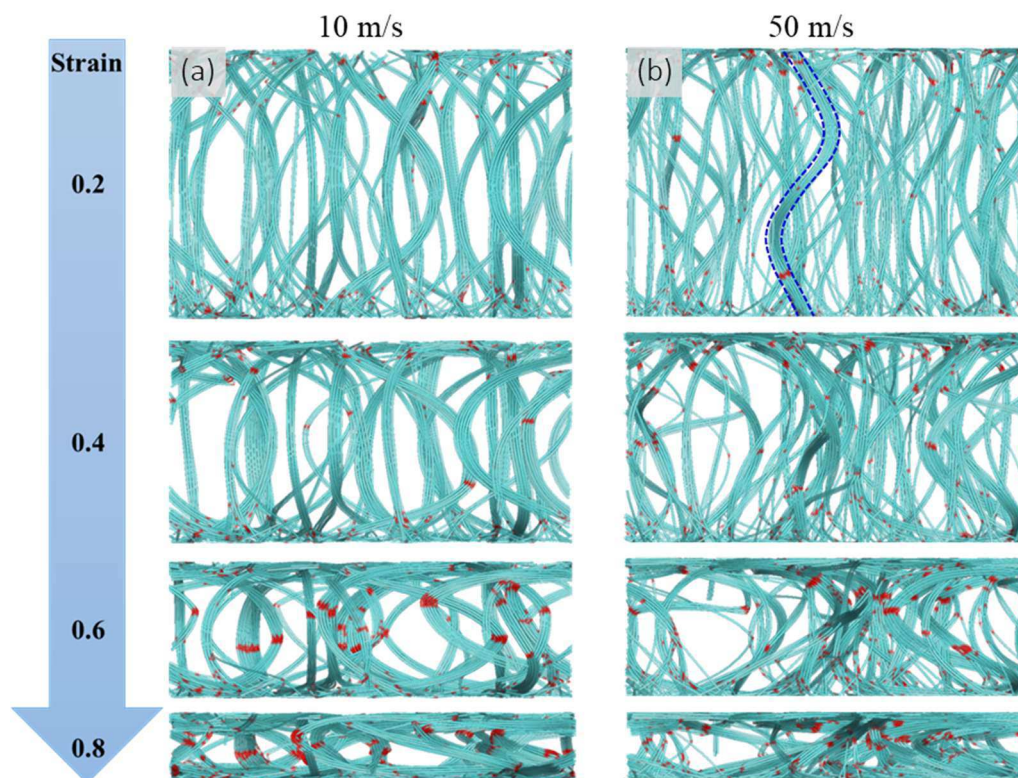


Figure 4.9: Snapshots from “glue” simulations of sample FA compressed at indenter velocities of (a) 10 m/s and (b) 50 m/s up to a maximum strain of 0.8. From top to bottom, the strain is 0.2, 0.4, 0.6, and 0.8. The tops of the nanotubes are attached to the indenter, and the CNT segments

adjacent to buckling kinks are colored red. A bundle exemplifying the higher-order serpentine bending of CNT bundles is outlined by blue dashed lines in the snapshots for 0.2 strain in (b).

To make the connection between the boundary conditions applied to the nanotubes at the location of the indenter, we can turn for a qualitative guidance to the classical Euler-Bernoulli beam theory [168], which predicts the following expression for the critical load, or maximum stress, that a column can withstand without buckling:

$$P_{cr} = \frac{n^2 \pi^2 E I}{(KL)^2} \quad (4.2)$$

where E is the bending modulus, I is the moment of inertia about the axis of buckling, L is the length of the column, n is the column buckling mode, and K is an effective length factor defined by the boundary conditions applied at the ends of the column. The theory behind this equation has been successfully applied to the investigation of buckling [175-177] and wave propagation [178, 179] in CNTs. Due to the complex structure of CNT bundles and their attachment to the substrate and the indenter, however, the classical beam theory can only be used for general qualitative guidance in the analysis of the deformation modes of bundles in VACNT forests. It is also important to distinguish the column buckling of a CNT bundle, which simply refers to the onset of its lateral deflection, from the buckling of a CNT, which is associated with an abrupt change in the shape of the nanotube cross-section and a drop in the resistance of nanotubes to bending at a critical radius of local curvature [59].

Two immediate conclusions one can draw from equation (4.2) are (1) the higher level of stresses needed for activation of higher order column buckling of CNT bundles ($n \geq 2$) leading to the appearance of serpentine-shaped bundles and (2) the increased likelihood that such higher levels of stresses can be generated under conditions when the upper segments of the nanotubes are fixed (the coefficient K decreases from 2 for a column with no constraints on the motion of rotation and lateral translation of the upper end to 0.5 for a column with fixed end segments of the column). Assuming that that equation (4.2) can be applied to the description of bending of CNT bundles under compression, we can expect to see much higher stresses at the initial stage of the deformation in the glue simulations, where both ends of the CNTs are fixed ($K = 0.5$), as compared to the free simulations, where the tops of the CNTs are free to rotate and deflect laterally ($K = 2$).

Examination of the stress-strain curves from the glue simulations (Figure 4.10) reveals that elastic yield strength is much higher for sample FA here as compared to the case where there is no traction between the indenter and the nanotubes (Figure 4.2a). The compression rate dependence of the yield strength in the glue simulations follows the upward trend, similar to that discussed in section 4.3.2 for simulations where the CNTs are unattached to the indenter. The elastic modulus, however, decreases from 2.4 GPa at 10 m/s to approximately 1.9 GPa at both 20 m/s and 50 m/s. The drop in the elastic modulus is in contrast with the results of the simulations with free CNT ends and can be explained by the broadening of the stress peak that corresponds to the transition from the elastic to plateau regimes of the compression with increasing deformation rate. Although the yield strength is higher, the peak of the stress shifts to higher strains with the faster compression of the forest, thus reducing the elastic modulus.

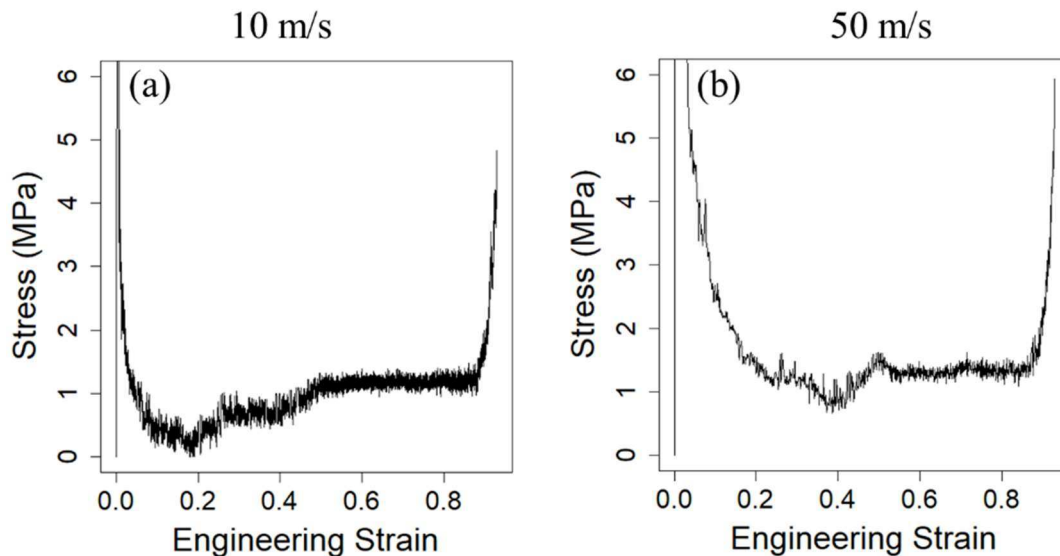


Figure 4.10: Stress-strain response for sample FA compressed at indenter velocities of (a) 10 m/s and (b) 50 m/s, with the tops of the nanotubes attached to the indenter.

The stress peak broadening, or post-yield softening, is also observed in the free simulations, *e.g.*, Figure 4.5, where it is attributed to the inability of nanotubes to reorganize themselves rapidly enough for minimization of stress at each step of the deformation. An additional factor in the case of the glue simulations is the appearance of the higher-order column buckling modes at high loading rates (*e.g.*, snapshot for 0.2 strain in Figure 4.9b), which support larger normal stresses

applied to the indenter ($n = 2$ in equation (4.2)). The S shape adopted by bundles with higher order buckling obstructs the localization of bending energy, and some bundles retain their serpentine configuration throughout the compression. Indeed, comparing snapshots from the two extreme compression rates, the buckled segments are more localized at 10 m/s, compared to 50 m/s (Figure 4.9). In addition, the S shapes of the bundles obstruct bundle-bundle alignment, and therefore can also lead to greater stress on the indenter.

The association of the stress peak broadening with the relaxation of the bending deformation of CNT bundles is supported by the plots of the bending energy as a function of engineering strain for the three compression rates shown in Figure 4.11. The red dashed lines cross at an arbitrary chosen point where 50% of the total increase in the bending energy during the compression has occurred. Note that the corresponding strain is the lowest for the fastest compression rate and the largest for the slowest compression rate. The rapid increase in bending energy at small strains indicates that bending of CNT bundles makes an important contribution to the initial stress peak. Therefore, the broadening of the stress peak at faster compression rates can be related to the sharper increase of the bending stress resulting in the formation of higher order column buckling of CNT bundles, followed by a gradual stress relaxation facilitated by the collective buckling of CNTs localized within bundle cross-sections.

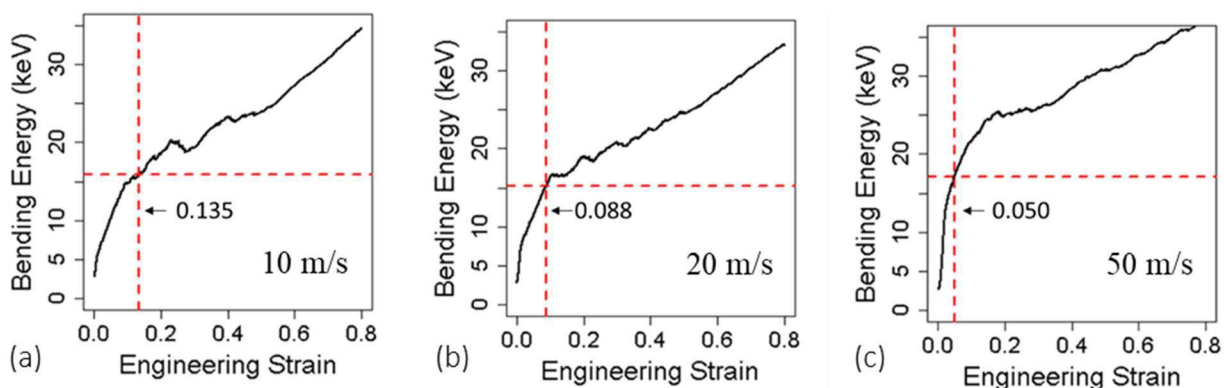


Figure 4.11: Bending energy as a function of engineering strain for sample FA compressed at indenter velocities of (a) 10 m/s, (b) 20 m/s, and (c) 50 m/s, with the tops of the nanotubes attached to the indenter. The red dashed lines cross at a point where 50% of the total increase in the bending energy has occurred, with the corresponding engineering strain labeled in the figure.

Remarkably, the values of the plateau stresses in the glue simulations are comparable to those of the freely compressed sample FA. This observation can be rationalized by the prominent role that collective buckling plays in the glue compressions. Following the multiple localized buckling events occurring in the plateau regime, the overall picture of the deformation does not change much with further increase of the strain. Additional buckled segments form around the sites of the original buckling, and the localization of the bending deformation within the buckled segments ensure a constant level of the material resistance to the indenter within a broad range of strain extending to the densification regime.

The early onset of buckling in the glue simulations is illustrated in Figure 4.12a, where the number of buckling kinks per CNT is shown as a function of strain for sample FA with free and fixed tops of the nanotubes. The nanotubes with fixed ends respond to compression immediately with widespread buckling, which is initially concentrated near the two ends of the CNTs, but later extends to the central parts of CNT bundles undergoing severe bending deformation (Figure 4.9). In the simulations with free ends of the CNTs, the nanotubes slide along the indenter and do not show significant buckling until around 0.4 engineering strain. Near 0.8 engineering strain, the number of buckled kinks becomes comparable for all simulations regardless of the boundary condition at the indenter and the strain rate. Comparing the snapshots at 0.8 strain for FA compressed without attachment to the indenter at 10 m/s (Figure 4.1a) and those from simulations performed at 10 and 50 m/s with the CNTs attached to the indenter (Figure 4.9), we see a visually similar picture. The sections of the compressed forests in the middle of the snapshots are not aligned parallel to the indenter and their relaxation is constrained by limited mobility of the upper and lower parts of the bundles which are incorporated into the two dense layers formed near the rigid substrate and the indenter. Further compression must result in more buckling to alleviate the stress, as the constrained CNTs cannot easily reorient themselves. The compression in the absence of alternative deformation paths leads to the onset of the densification regime signified by the rapid rise of stress, Figure 4.5 and Figure 4.10.

The coarsening of bundles during the compression, discussed in sections 4.3.1 and 4.3.2 and illustrated in Figure 4.6, is less pronounced in the glue simulations, as can be seen from Figure 4.12b. The bundles still coarsen upon compression but, for each loading velocity, the increase in the mean bundle thickness is smaller when the ends of the CNTs are attached to the indenter. The

thinner bundles in the glue simulations can bend and buckle more easily, which contributes to the rapid increase in the number of buckling kinks illustrated by Figure 4.12a.

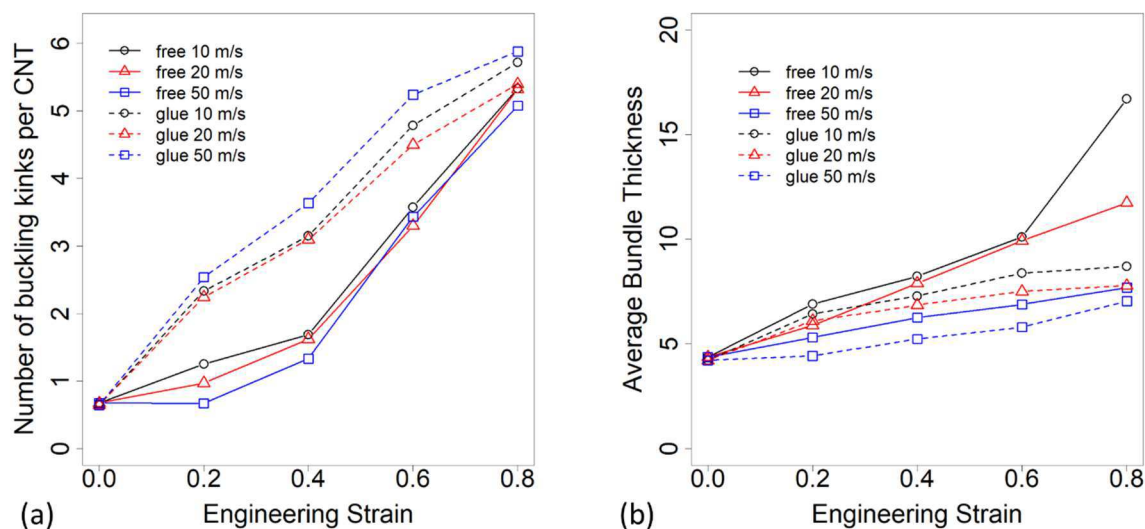


Figure 4.12: The evolution of the number of buckling kinks (a) and the average bundle thickness (b) in free (solid lines) and glue (dashed lines) simulations of sample FA compressed at indenter velocities of 10, 20, and 50 m/s up to 0.8 engineering strain.

To investigate the effect of forest density on the deformation behavior and mechanical properties of VACNT forests with ends of the nanotubes attached to the indenter, we perform a series of glue simulations for sample FC, which has five times higher density and much thicker bundles than sample FA discussed above (see Table 4.2). The snapshots from these simulations are shown in Figure 4.13. Visually, the deformation of sample FC is similar to that of sample FA (Figure 4.9) in that buckling is highly localized along the height of the CNT bundles, and the bundles still aggregate near the indenter. Buckling occurs at lower strains for faster compression rates, and, similarly to the sparser forest, there are multiple buckled regions along the height of some of the nanotube bundles at the compression velocity of 50 m/s.

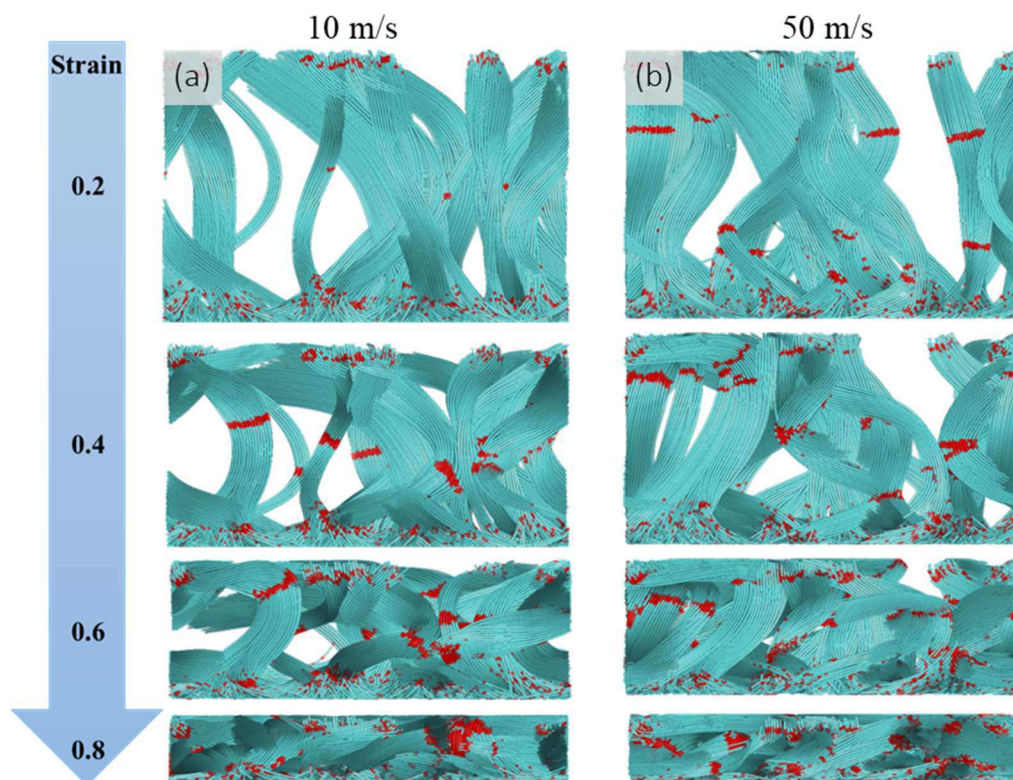


Figure 4.13: Snapshots from “glue” simulations of sample FC compressed at indenter velocities of (a) 10 m/s and (b) 50 m/s up to a maximum strain of 0.8. From top to bottom, the strain is 0.2, 0.4, 0.6, and 0.8. The tops of the nanotubes are attached to the indenter, and the CNT segments adjacent to buckling kinks are colored red.

The stress-strain response shown in Figure 4.14 is, for the most part, qualitatively similar to that of the more rarified forest FA (Figure 4.10), with a large elastic stress peak and a post-yield softening shoulder that is particularly pronounced at faster compression rates, followed by a plateau and densification regions. The average stress in all deformation regimes, however, is substantially higher for the denser forest FC, and scales roughly with the density of the forest. This scaling is in contrast to the weak density dependence of stress magnitude discussed in section 4.3.3 for simulations where the top parts of the nanotubes are free to slide with respect to the indenter.

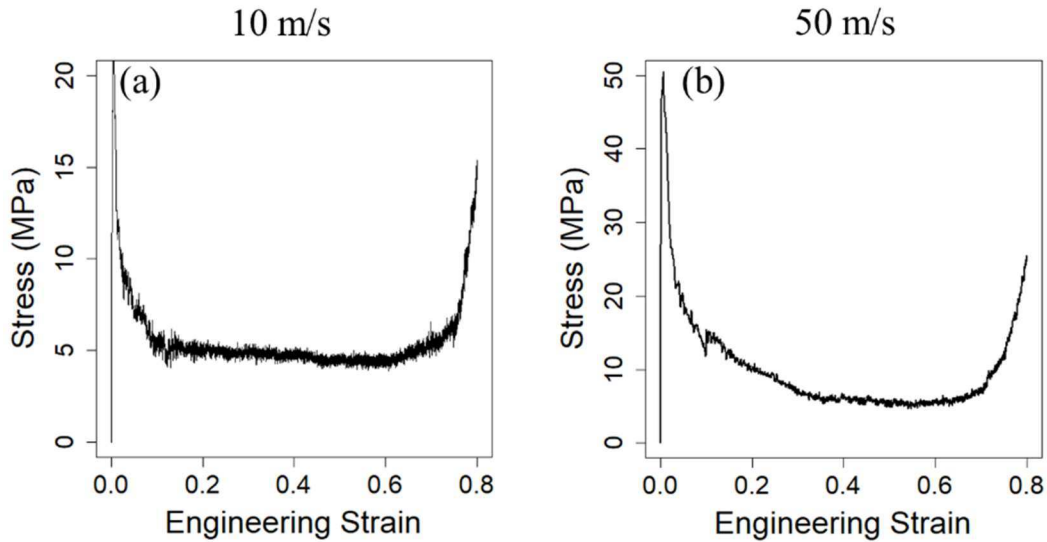


Figure 4.14: Stress-strain response for sample FC compressed at indenter velocities of (a) 10 m/s and (b) 50 m/s, with the tops of the nanotubes attached to the indenter.

4.4 Recovery of VACNT forests

One of the most attractive aspects of the mechanical behavior of VACNT forests is their ability to withstand repeated loading and unloading cycles with minimal permanent deformation [29, 32]. However, in some cases the CNT forest remains substantially deformed after compression [30, 31, 126, 153]. As discussed in the introduction, factors determining the extent to which a forest will recover include the radii of CNTs, types and densities of CNT defects, strain rate, morphology, presence of inclusions, and mass density gradients along the height of the forest. As the first step in the computational analysis of the mechanisms that control the mechanical resilience of CNT forest subjected to cyclic loading, a few series of simulations where sample FA is loaded and unloaded over five cycles are performed. To explore the effect of the interaction with the indenter, both free and glue simulations of cyclic loading are performed and reported below.

4.4.1 Repulsive CNT-indenter interaction

In all simulations of cyclic loading, FA is subjected to five compression-recovery cycles. Each cycle consists of *compression*, where the indenter is depressed at 50 m/s, *unloading*, where the indenter is raised to the original height of 200 nm at the same velocity of 50 m/s, and *relaxation*, where the forest is allowed to recover. The relaxation stage is necessary because the forest recovery overall is significantly slower than the indenter speed of 50 m/s, and the indenter usually detaches

from the forest shortly after the start of unloading. During the relaxation, most of the structural rearrangements in the forest happens within the first few nanoseconds of recovery, and by the time of 10 ns hardly any structural changes can be observed within the sample. Therefore, in the interest of reducing simulation time, we limit the cumulative time of the unloading and subsequent relaxation stage to 10 ns. However, some slow structural rearrangements may still occur after 10 ns at much longer time scales.

Two simulations, with maximal compressive strains of 0.8 and 0.6, are performed for the VACNT forest where the ends of CNTs are unattached to the indenter. Snapshots from the simulations are shown for configurations formed by the end of the 1st, 3rd, and 5th loading-unloading-relaxation cycles in Figure 4.15. Examining the snapshots for the forest compressed repeatedly to 0.8 strain (Figure 4.15a-c), we see that recovery is limited to less than half of the original forest height, and after each cycle the maximum recovery is decreased. A dense layer of horizontally aligned CNT bundles forms at the interface with the indenter and remains stable after the indenter separates from the compressed forest during the unloading stage. The overall structure of the forest undergoes relatively small changes with the successive cycles.

The snapshots from the simulation where sample FA is compressed to a lower maximum strain of 0.6 (Figure 4.15d-f) show a much more significant recovery of the forest after the first cycle. Some of the larger bundles formed during the compression are able to return to an upright position by the end of the first cycle, Figure 4.15d, while others have been entangled and do not fully recover. Furthermore, the bundle size appears on average to be much larger than that in the more strongly compressed forest in Figure 4.15a. Indeed, by the end of the first cycle the average bundle thickness of sample FA compressed to 0.8 strain is less than half of that when the forest is compressed to 0.6 strain (Figure 4.16). Compression results in the coarsening of bundles because the nanotubes are being forced together, but at the high loading rate ($2.5 \times 10^8 \text{ s}^{-1}$ at the indenter velocity of 50 m/s) the CNTs do not necessarily reorganize in the way that minimizes their interaction energy. Furthermore, when the forest is compressed to 0.8 strain, the nanotubes are pushed into forming a metastable network of thinner bundles. When compressed down to intermediate strains of 0.6, however, the CNTs remain sufficiently mobile to allow for substantial coarsening of bundles once the pressure from the indenter is released. Indeed, examination of

Figure 4.16 reveals that the largest increase in bundle size for the forest compressed to 0.6 strain comes during the relaxation stage of the first cycle, *i.e.*, between cycle 0.5 and 1.0.

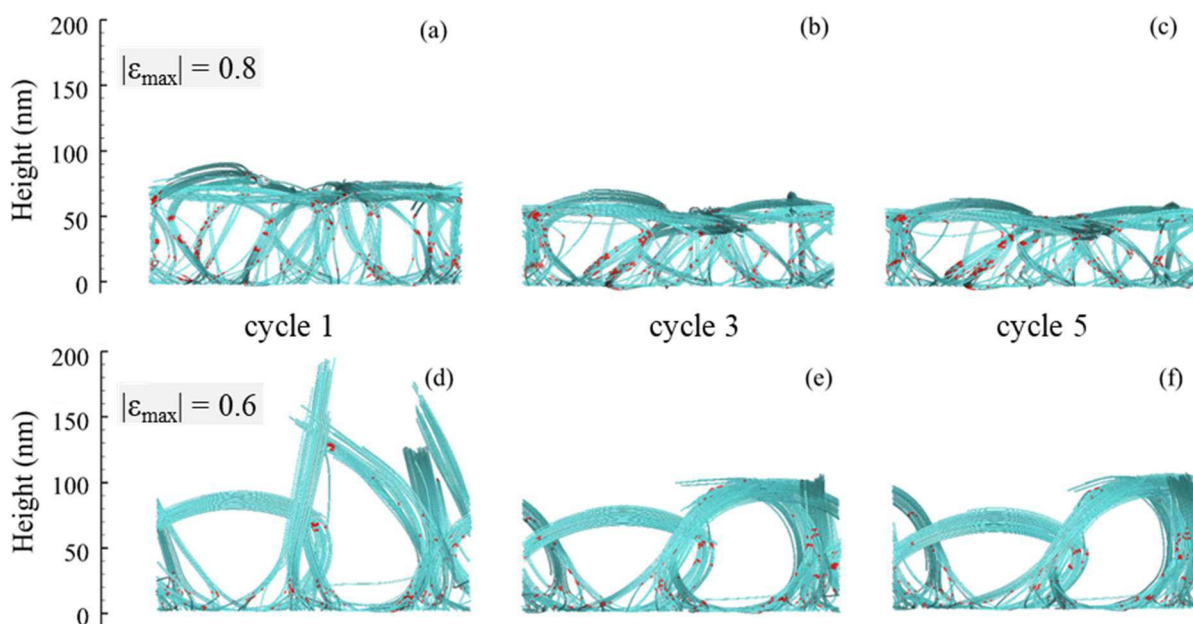


Figure 4.15: Snapshots from two simulations of cyclic loading of sample FA shown at the end of cycles 1, 3, and 5. Each cycle consists of loading and unloading parts performed at indenter velocity of 50 m/s and followed by 7.6 ns of relaxation of the forest in the unloaded state. The loading is done up to a maximum strain of 0.8 (a-c) and 0.6 (d-f). The nanotubes are free to slide with respect to the indenter, and the CNT segments adjacent to buckling kinks are colored red.

The structural changes in the VACNT forests undergoing cyclic loading are reflected by the number of buckling kinks plotted for each simulation in Figure 4.16b. In general, the number of buckling kinks increases when the samples are compressed and decreases when the indenter is removed. The increase is particularly large at the loading stage of the first cycle, and becomes less pronounced in the following cycles. When the compression is up to a strain of 0.8, the substantial increase and partial recession in the number of buckling kinks is observed for the first three cycles, but the variation in the number of buckling kinks becomes muted during the last two cycles. Some of the CNT segments unbuckle as the forest recovers, but the degree of recovery, as seen in Figure 4.15, decreases with each cycle, and the bending deformation becomes increasingly localized within the existing buckled regions of the CNT bundles. Interestingly, when FA is compressed to 0.6 strain only, the increase in the number of buckling kinks during compression is only faintly

observable beyond the first two loading cycles. The high energy cost associated with collective buckling of thick CNT bundles formed in this simulation during the first loading cycle makes the deflection of the bundles by the indenter the favored deformation mode at the intermediate strains.

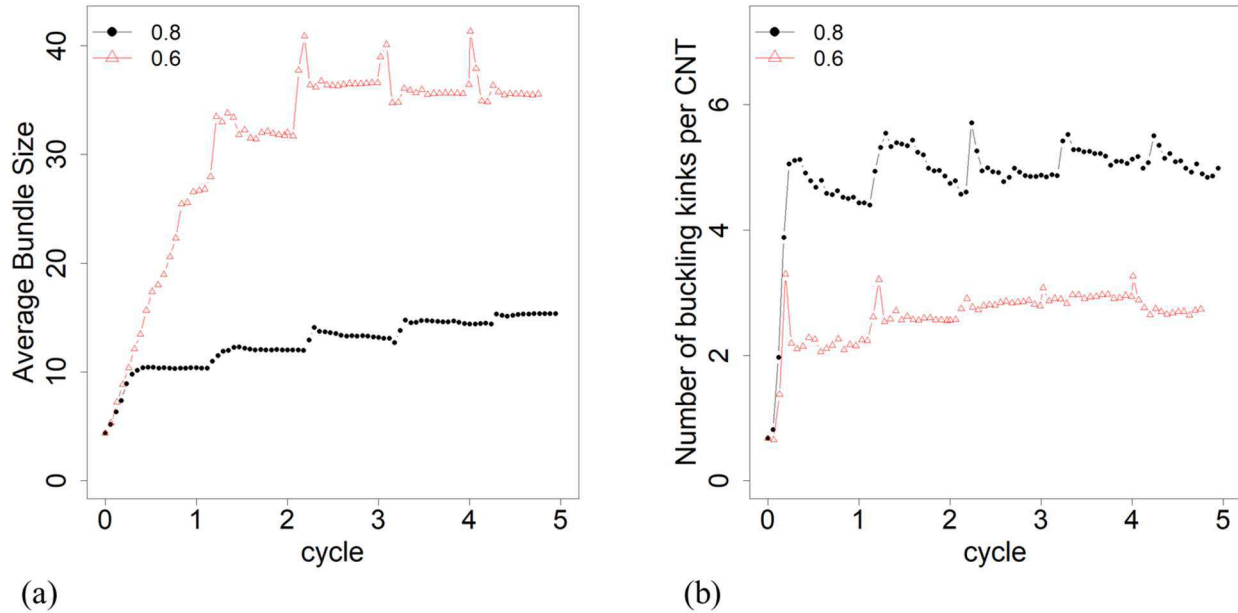


Figure 4.16: The evolution of the average bundle size (a) and number of buckling kinks (b) in two simulations of cyclic loading of sample FA. Each of the five consecutive cycles consists of loading and unloading parts performed at indenter velocity of 50 m/s and followed by 7.6 ns of relaxation in the unloaded state. The loading is done up to a maximum strain of 0.8 (black line and dots) and 0.6 (red lines and triangles). The simulations are performed for nanotubes that are free to slide with respect to the indenter.

The ability of some of the VACNT forests to withstand multiple loading cycles with minimal plastic/irreversible deformation is of particular practical interest and can be quantified by the dimensionless loss coefficient,

$$\eta = \frac{\Delta U_i}{2\pi U_r} \quad (4.3)$$

where $\Delta U_i = \oint \sigma d\epsilon$ is the mechanical energy dissipated in the i^{th} cycle of loading and unloading, ϵ is the strain, and $U_r = \int_{\epsilon_{\min}^i}^{\epsilon_{\max}^i} \sigma d\epsilon$ is the energy stored in the material after one compression.

Here, ϵ_{\min}^i and ϵ_{\max}^i are denoting the minimum and maximum strains during a cycle, where ϵ_{\min}^i is not necessarily equal to zero. The quantity U_r can refer to the area under the stress-strain curve

for the first compression or, alternatively, to the area for the current i^{th} loading cycle [180]. Graphically, the mechanical hysteresis loops for the loading and unloading of sample FA up to 0.6 and 0.8 maximum strains are shown in Figure 4.17b and Figure 4.17c, respectively. The area inside each loop represents the value of ΔU_i obtained for each cycle i by subtracting the area under the unloading curve from the one under the loading curve. Visually, this area shrinks with each successive cycle. Setting U_r equal to the area under the first loading curve, we see that the loss coefficient is decreasing with each successive cycle, Figure 4.17a. This decrease of the loss coefficients reflects an increasing permanent deformation of the forest sample subjected to cyclic loading.

The loss coefficient of the first cycle is almost identical in the two simulations, despite the much more substantial recovery of sample FA compressed to 0.6 strain. The reason is that there is almost no stress from the forest on the indenter at the unloading stage of the cycle, as the indenter is raised with a velocity of 50 m/s, which is too fast for the top part of the forest to follow. As a result, the stress drops down to zero shortly after the start of the unloading (Figure 4.17b), and $\frac{\Delta U_1}{U_r} \approx 1$ in both simulations. The loss coefficients calculated for the subsequent cycles using the values of U_r evaluated for the first cycles are decreasing in both simulations due to the accumulation of irreversible structural changes, which result in the decreasing extent of the recovery. Moreover, in the case of the lower maximum strain of 0.6, the diminishing peak stress leads to a steeper decrease of the loss coefficient during the cyclic loading relative to the simulation with maximum strain of 0.8, where the peak stress remains fairly constant, Figure 4.17b. The persistent peak stress in the latter case can be related to a resilient spring-like structure generated below the topmost, dense layer after the first loading-unloading cycle, Figure 4.15a. The subsequent loading cycles only marginally affect the structure of the lower layer of the forest and the corresponding values of the peak stress.

Overall, the trend in the decay and the magnitudes of the loss coefficient are in a good agreement with experimental data [32, 153], even though the parameters of the simulated forests (*i.e.* CNT diameters, forest height, lack of defects or density gradients) are rather different from most of the laboratory grown samples. Similar to the experiments, we observe the sharp drop in the loss coefficient on the second cycle followed by a gradual decline for subsequent cycles.

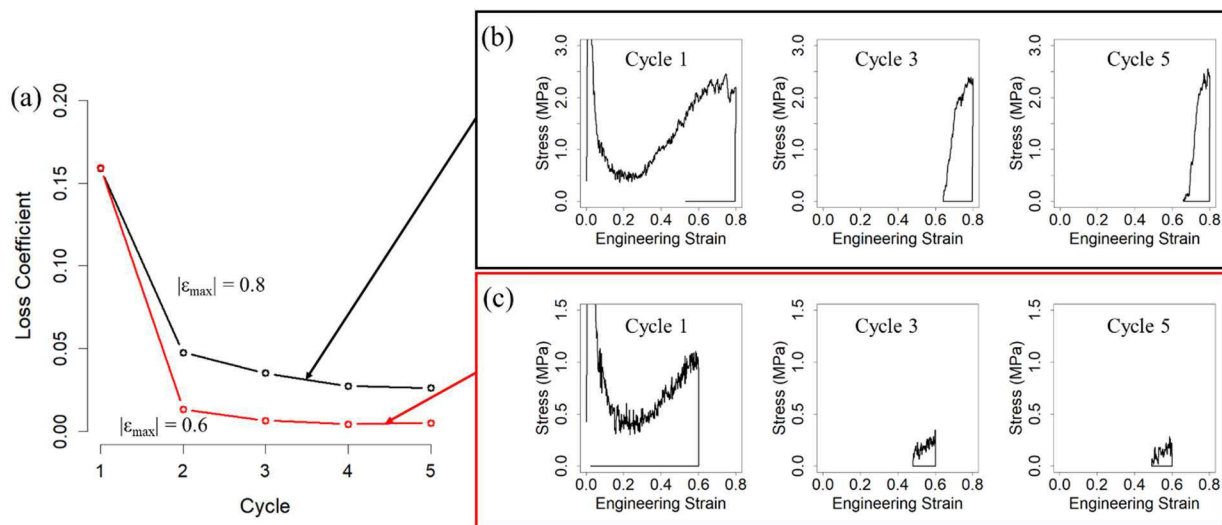


Figure 4.17: Loss coefficient evaluated in simulations of cyclic loading of sample FA done up to a maximum strain of 0.8 and 0.6 (a) and the corresponding stress-strain curves shown for cycles 1, 3, and 5 (b,c). The simulations are performed for nanotubes that are free to slide with respect to the indenter.

4.4.2 CNTs attached to indenter

Additional insights into the resilience of VACNT forests can be gleaned from simulations of cyclic loading in which the tops of the CNTs are attached to the indenter (see section 4.3.4). Similar to the simulations discussed in the previous section, the simulations discussed below are performed for sample FA subjected to five consecutive loading – unloading cycles. However, no relaxation phase is included since the CNTs are fixed to the indenter. The effect of the loading rate is investigated by comparing the results obtained with two velocities of the indenter at the compression and recovery stages of each cycle, 10 and 50 m/s. The forest is compressed to a maximum strain of 0.8 in both simulations. In the initial test simulations, the forest samples were recovered to their initial heights, *i.e.*, back to zero engineering strain. Due to the reorganization of CNTs upon the initial compression, however, large tensile stresses arise when the height of the forest is recovered past 0.2 strain. Therefore, to avoid the large tensile stresses, we limited the recovery of the sample to 0.2 strain with respect to its original height in all simulations discussed in this section. Starting from the second loading-unloading cycle, the duration of one cycle in these simulations is 24 and 4.8 ns for the indenter velocities of 10 and 50 m/s, respectively.

Snapshots from the simulations are shown for configurations generated by the end of 1st, 3rd, and 5th loading cycles in Figure 4.18. We can see that the overall structure changes only marginally after the first loading cycle, and the primary visually apparent difference between the consecutive snapshots is a gradual coarsening of the bundles. The coarsening of the bundles is quantified in Figure 4.19a, where the average thickness of the bundles is characterized by periodic variation of the bundle thickness in each loading and unloading cycle, indicating the temporary formation and splitting of bundles. However, average bundle thickness increases over the course of five cycles.

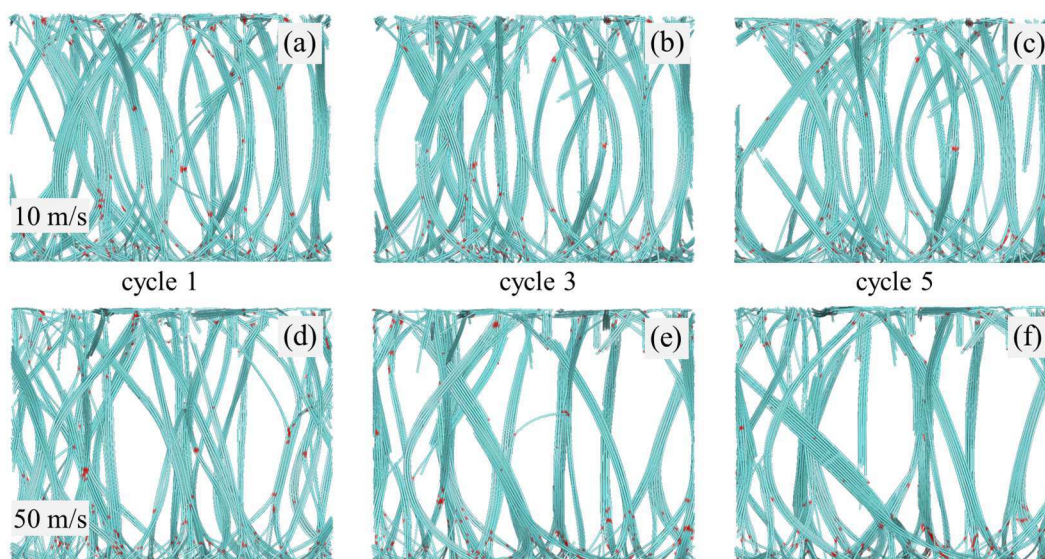


Figure 4.18: Snapshots from two simulations of a cyclic loading of sample FA performed with indenter velocities of 10 m/s (a-c) and 50 m/s (d-f). The unloading is done down to a strain of 0.2 with respect to the original height of the forest. The nanotubes are attached to the indenter, and the snapshots are shown at the ends of cycles 1, 3, and 5. The CNT segments adjacent to buckling kinks are colored red.

An interesting observation is that the average bundle thickness in the sample loaded at a higher deformation rate surpasses that in the slowly loaded sample by the end of the 2nd cycle, Figure 4.19a. Although we rationalized in sections 4.3.2 and 4.3.4 that, due to extra time available for the nanotube reorganization, the CNT bundles coarsen more readily when compressed slowly, the picture becomes more complicated when the forest is attached to the indenter and undergoes multiple loading-unloading cycles. At the slower loading rate, thick and stable bundles form during the first compression, and pronounced coarsening does not occur in subsequent cycles. However, at 50 m/s, the initial compression produces relatively thin bundles, which with additional

cycles continue to coarsen into even thicker bundles than those produced with the 10 m/s loading rate.

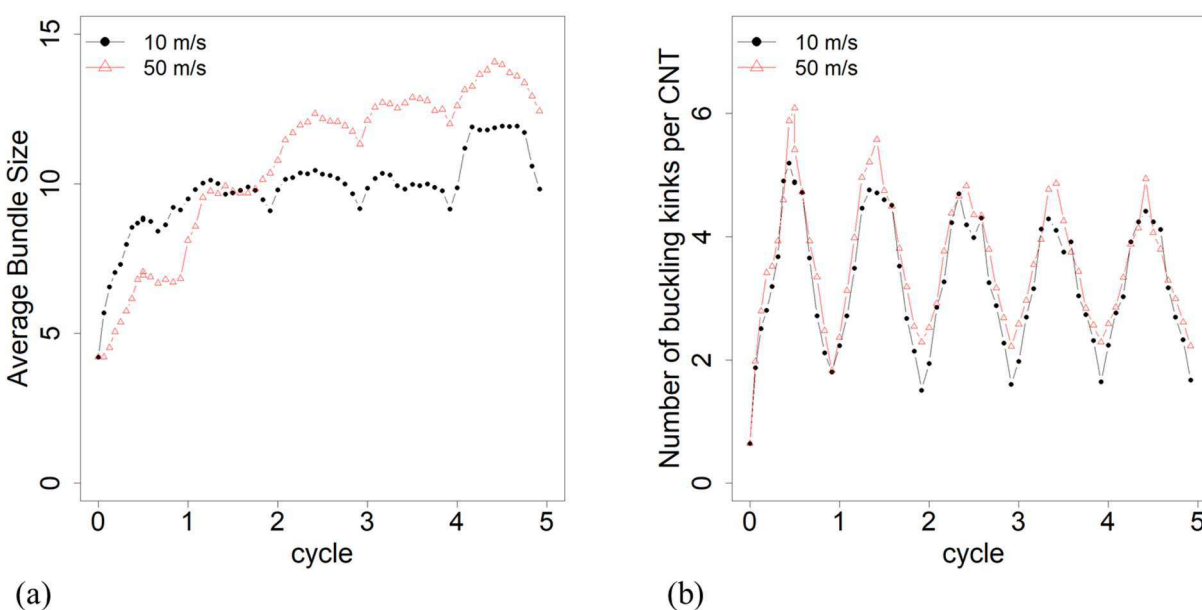


Figure 4.19: The evolution of the average bundle size (a) and number of buckling kinks (b) in two simulations of cyclic loading of sample FA performed with indenter velocities of 10 m/s (black lines and dots) and 50 m/s (red lines and triangles). The nanotubes are attached to the indenter, and the unloading is done down to a strain of 0.2 with respect to the original height of the forest.

The numbers of buckling kinks shown for the two rates of deformation in Figure 4.19b exhibit a nearly linear increase and decrease during the loading and unloading of the sample. The peak number of buckling kinks gradually decreases for the first several loading cycles, and the bending energy (not shown) follows a qualitatively similar trend. These decreases in the peak bending energy and the maximum number of buckling kinks reflect the increased localization of bending deformation with successive cycles. Rearrangement of nanotubes into thicker bundles reduces the number of isolated buckling events in individual CNTs and thin bundles and makes the coordinated localized buckling of bundles the dominant mode of the bending deformation.

The loss coefficients and mechanical hysteresis cycles for the two simulations are shown in Figure 4.20. The stress-strain cycles are different from the ones observed in the simulations where the CNTs interact repulsively with the indenter (Figure 4.17) in that the stress does not drop to zero with the start of the recovery stage of the cyclic loading. Rather, the stress gradually decreases

upon unloading and, due to the entanglement and coarsening of CNT bundles, can become tensile (*i.e.*, negative within the convention adopted in this paper) by the end of the unloading, when the forest pulls back on the rising indenter.

The loss coefficient, calculated for both loading rates using equation (4.3) and plotted in Figure 4.20a, exhibits the same general trend that was observed for the simulations where the CNTs are not attached to the indenter, Figure 4.17a. The slower deformation rate yields a larger loss coefficient since the area under the stress curve during the initial loading, U_r , is similar in magnitude to those in the subsequent loading cycles. For the faster loading rate, the difference between the level of stress realized during the initial loading and stresses observed in the subsequent cycles is greater due to the more extensive structural reorganization of the nanotubes, thus resulting in smaller values of the loss coefficient. The trend of the reduction of loss coefficient in the course of the cyclic loading observed in the simulations is in a good qualitative and quantitative agreement with experimental results obtained for longer MWCNT forests [32, 153].

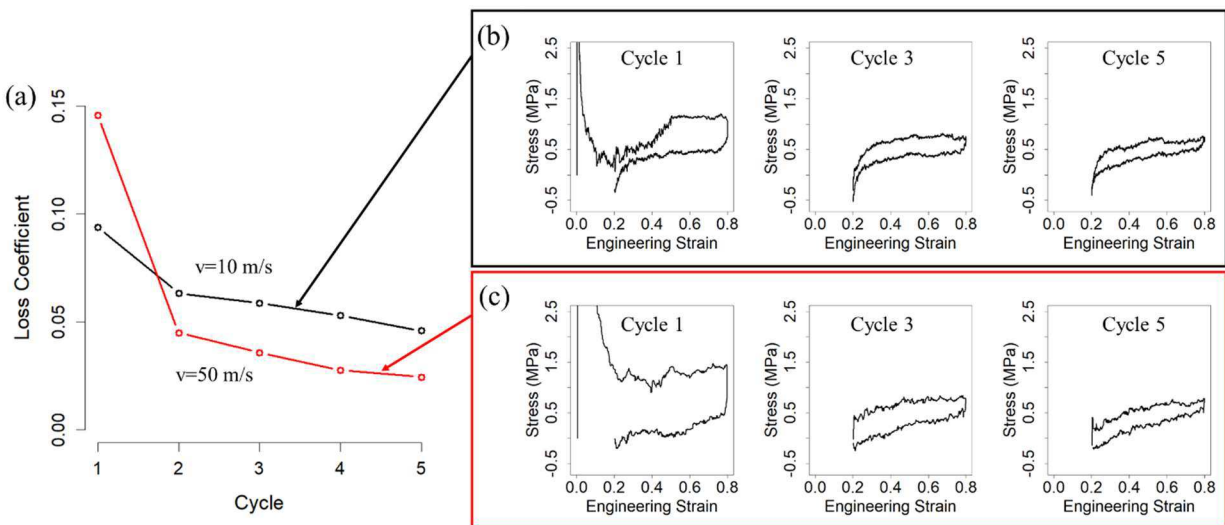


Figure 4.20: Loss coefficient evaluated in simulations of cyclic loading of sample FA performed with indenter velocities of 10 m/s and 50 m/s (a) and corresponding stress-strain curves shown for cycles 1, 3, and 5 (b,c). The nanotubes are attached to the indenter, and the unloading is done down to a strain of 0.2 with respect to the original height of the forest.

4.5 Summary

The mechanical response of short VACNT forests to the uniaxial compression is systematically investigated in mesoscopic dynamic simulations performed for computational samples with

different density and microstructure (bundle size distribution and degree of nanotube alignment). The effects of the loading rate and the interaction of CNTs with the indenter on the mechanical properties and deformation behavior of VACNT forests are studied and related to experimental observations. The mechanisms that control the mechanical resilience of CNT forests are also explored in simulations of cyclic loading of the computational samples.

The simulations provide first insights into structural changes in the networks of interconnected CNT bundles undergoing mechanical deformation and reveal the key elementary processes responsible for the reversible and irreversible modes of the mechanical deformation. Remarkably, the three-stage stress-strain dependence (an elastic peak followed by an extended plateau region and a sharp rise of stress in the densification regime) commonly measured for VACNT forests ranging up to millimeters in height is reproduced in the simulations performed for relatively short forests composed of 200-nm-long nanotubes. Moreover, the mechanical properties derived from the stress-strain curves (*e.g.* elastic modulus, yield strength, modulus of resilience) fall within the ranges reported in experimental studies.

The connections between the structural characteristics of the computational forests and their mechanical response to the uniaxial loading are investigated. The characteristic features of the stress-strain dependence are related to the thickness of CNT bundles and the degree of their alignment along the vertical axes of the forests. In particular, the mechanical behavior of short CNT forests is found to be largely defined by the competition between two distinct mechanisms of CNT bundle deformation: (i) folding of bundles at their bases, prevalent in samples with large bundle inclination with respect to the vertical axis and (ii) bowing of bundles followed by collective buckling of CNTs localized within bundle cross-sections, characteristic of vertically aligned bundles with small initial inclinations. The loading rate and density of the forest are found to have a substantial effect on the parameters of the stress-strain dependence and the deformation mechanisms. Furthermore, the effect of the interaction of CNTs with the indenter is examined, and the deformation of forests with CNT ends attached to the indenter is determined to proceed primarily through localized bending and buckling of bundles, resulting in a relatively level plateau region of stress extending past 0.8 strain.

Additionally, several sets of simulations of VACNT arrays undergoing five loading–unloading cycles are performed to examine the effect of the strain rate and maximum compressive strain on

the mechanical resilience of the nanotube forests. The variation of the magnitude of the loss coefficient over successive loading-unloading cycles predicted in the simulations is in a good agreement with the results of experimental measurements. The maximum compressive strain is found to have a strong impact on the structural rearrangement of the CNTs, thus affecting the forest recovery and the peak stress when the CNTs interact repulsively with the indenter. In the simulations where the CNTs are attached to the indenter, the rate of compression is found to affect the bundling of CNTs, with a faster rate ultimately producing thicker bundles and, therefore, lower loss coefficient as compared to slower compression rates.

Overall, the complexity of the deformation behavior of VACNT arrays, defined by the interplay of different modes of collective bundle deformation, and the high sensitivity of the mechanical response to the forest morphology, density, deformation rate, and interaction with the indenter suggest a broad range of opportunities for tuning the mechanical properties of nanotube forests to the needs of practical applications.

5 Mechanism of deformation and phase transformation during uniaxial compression of VACNT forests

5.1 Introduction

The mechanical response of vertically aligned carbon nanotube (VACNT) forests [100] to compression is comparable to that of cellular foams [171]. In particular, similar to foams, VACNT forests can undergo repeated loading to high strains while maintaining their resilience [29, 116, 181] and exhibit a three regime stress-strain response [31, 32, 182] consisting of an elastic regime where the bending and stretching deformation of CNT bundles does not involve any significant structural changes in the material and stress increases linearly with strain, an extended plateau regime characterized by relatively weak stress dependence on strain and structural rearrangements that do not lead to significant strengthening, and a densification regime where the reorganization within the material becomes spatially constrained, leading to a rapid increase in stress. Despite the similarity of the mechanical behavior, the deformation mechanisms of VACNTs forests and foams are rather different. Foams deform either through bending-dominated mechanisms where cell walls bend and buckle or by stretching-dominated processes where the struts supporting the cell walls are loaded axially [170, 171]. These deformation mechanisms, however, are not applicable to VACNT forests, which are structurally characterized as anisotropic networks of interconnected CNT bundles, quite unlike the cellular motif common to conventional foams.

The complex multi-stage stress-strain dependence of VACNTs undergoing uniaxial compression is commonly attributed to the coordinated, localized buckling of bundles of CNTs occurring periodically along the height of the forest [29, 31, 126]. Specifically, heterogeneity in the density and nanotube alignment in nanotube forests results in preferential nucleation sites for coordinated buckling of CNTs at relatively compliant sections [29, 31, 126, 163], forming a localized high density region at the location of buckling. Analytically, the non-linear, multi-stage stress-strain response of VACNT forests has been described [163, 164, 183, 184] by representing CNT as a series of bi-stable springs [185-187] which are characterized by an energy landscape with two minima separated by a convex ‘spinodal’ region. The energy minima correspond to low and high strain conformations of the spring, and when many springs are connected in series the mechanical response is similar to that of a CNT undergoing compression. The bi-stable spring model saw success in reproducing the characteristic three-regime stress-strain curve of uniaxially

compressed forests [163, 164, 183]. In the latest of these reports [164] the interpretation of the deformation behavior of VACNT forests in terms of a phase transition between a rarefied phase, in which the CNTs are mostly vertically aligned, and a densified, buckled phase stabilized by the inter-tube van der Waals interactions is suggested. This hypothesis was partially motivated by earlier studies of biopolymer (fibrin) network structures exhibiting three-regime stress response to the uniaxial compression similar to that of foams and VACNT forests [188, 189] and deforming by separation into two distinct, coexisting low- and high-density phases. Moreover, the formation of a localized densified region during uniaxial compression has also been observed for VACNT forests [29, 31, 32, 164, 169, 182], *e.g.* see Figure 5.1.

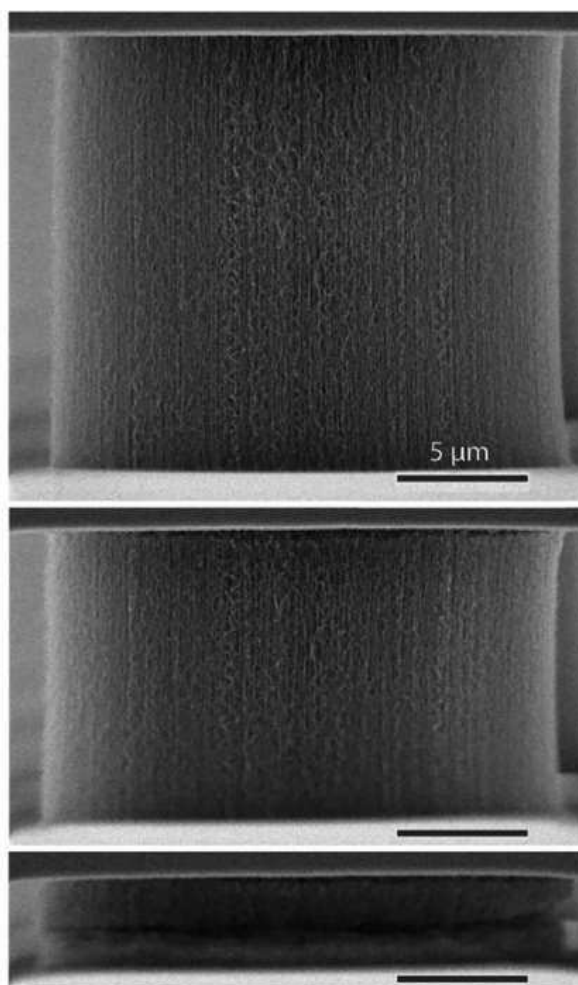


Figure 5.1: SEM showing deformation of a VACNT forest during the elastic, plateau, and densification regimes [164]. Note the formation of a localized densified layer of CNTs near the indenter in the plateau regime which broadens into the densification regime.

Despite the extensive experimental and modeling efforts, and the successes of the bi-stable spring model in reproducing the phase coexistence and stress-strain response of VACNT forests undergoing compression, the structural characteristics of the two phases and the mechanisms of the phase separation remain elusive. Major obstacles to systematic analysis of the mechanisms of mechanical deformation of VACNT forests come from the challenge of growing forest structures with precisely controllable structure, as well as the difficulty of detailed characterization of the structural and energetic parameters of VACNT forests undergoing compression. Computationally reproducing the structure of VACNT forests and inspecting the structural transformations in the course of mechanical deformation is one way to circumvent the problem of detailed structural characterization of experimental samples. The emergence of a new class of coarse-grained mesoscopic models for mesoscopic dynamic simulation of large groups of CNTs [54-57] combined with a recent development of an effective method for the generation of computational samples with tunable microstructures based on guided structural self-organization of nanotubes into anisotropic network structures [158], have enabled realistic modeling of the mechanical deformation of VACNT forests.

First mesoscopic simulations of the uniaxial compression of short VACNT forests [182] have indeed demonstrated the ability of the mesoscopic modeling to reproduce the three-stage stress-strain dependence characteristic of experimental samples and provided initial insights into the dependence of the mechanical behavior of VACNT forests on density, microstructure (bundle size distribution and degree of nanotube alignment), loading rate, and interaction with the indenter. The 0.2- μm -tall forests used in these first simulations, however, are too short for reproducing the periodic coordinated buckling across the sample and testing the hypothesis on the coexistence of low- and high-density phases suggested for interpretation of experimental observations [31, 32, 124, 126, 164, 169].

In this chapter, we extend the mesoscopic simulations to VACNT forests consisting of longer, 0.6- μm - and 2- μm -long, nanotubes, and focus our attention on the mechanism of the phase transformation occurring in the course of the mechanical deformation of the CNT network materials and the nature of the two phases produced by the deformation. The dynamic mesoscopic model, the structural characteristics of *in silico* VACNT forest samples, and the computational setup for simulation of uniaxial compression of the samples are briefly described in section 5.2. The detailed analysis of the phase separation in a 2- μm -tall VACNT forest undergoing uniaxial

compressive deformation is provided in section 5.3. The effect of the microstructure on the mechanical response of VACNT forests is explored in a series of simulations performed for 0.6- μm -tall forests and reported in section 5.4. A brief comparison between simulations where the fracture of CNTs is modeled and neglected is presented in section 5.5. Finally, the main conclusions of this computational study are summarized in section 5.6.

5.2 Computational Method and Setup

5.2.1 *Mesosopic force field for carbon nanotube materials*

The mesoscopic force field model developed for realistic large-scale simulations of CNT materials is based on a coarse-grained representation of individual CNTs as chains of stretchable cylindrical segments [56, 57]. The state of each segment is defined by positions, velocities, and internal temperature of nodes joining the neighboring segments [56]. The dynamics of a system of interacting CNTs is described by solving the equations of motion of classical mechanics for the positions of all nodes [56]. The forces acting on the nodes are calculated based on the mesoscopic force field that accounts for stretching and bending deformation of individual CNTs [56], bending buckling of CNTs [76], as well as for the van der Waals inter-tube interactions [57], with all terms of the potential parameterized based on the results of atomistic simulations. The possibility of both axial and bending fracture of individual CNTs is included in the model, where either event results in clean CNT fragmentation. For (10,10) single-walled carbon nanotubes (SWCNTs), the axial fracture is set to occur at a local strain of 0.279 [43], and the bending fracture occurs at a local bending angle of 120° [39]. In the simulations reported in the present paper, only the bending fracture is observed in some of the nanotubes at the late stage of the VACNT forest compression, but it does not significantly affect the overall mechanical response of the forests (see section 5.5). The mesoscopic force field does not include an explicit description of friction forces related to the relative displacement of tubes with respect to each other, as these forces are too weak to prevent room-temperature rearrangements of defect-free CNTs [83, 84]. The contribution to static friction forces originating from changes in the inter-tube interaction area, however, is fully accounted for in the mesoscopic model, and in the case of pristine CNTs, no significant additional sources of friction exist [85]. The presence of defects, functional groups, and chemical cross-links can significantly increase the strength of the shear interactions between nanotubes [86, 87], but these effects are not considered in the present study.

5.2.2 VACNT forest samples

A series of morphologically diverse computational samples with realistic structural organization is generated *in silico* following the procedure outlined in Ref. [158]. Briefly, the procedure is as follows. First, full length straight CNTs are positioned randomly on a substrate until a prescribed tube density is reached. Each CNT is given an inclination angle with respect to the vertical axis, falling between zero and a specified maximum inclination, Θ_{max} , with uniform probability. Then, the initial sample undergoes thermal annealing in a mesoscopic dynamic simulation performed at a temperature of 5,000 K (the model does not include the possibility of thermal decomposition of CNTs, and the temperature is defined based on the average kinetic energy of mesoscopic dynamic units of the model) for 1 ns. In the course of the thermal annealing, the initially straight and isolated nanotubes self-organize into a continuous network of bundles with the bundle size distribution largely defined by the material density and Θ_{max} [158]. Finally, the computational VACNT forest is quenched to 300 K and allowed to relax until a metastable configuration, defined as a state where the rate of change in inter-tube interaction energy slows down to a level below 0.05 percent per ns, is obtained.

All samples considered in this work consist of (10, 10) SWCNTs with a radius of 0.6785 nm and have a mass density of 0.02 g/cm³ (areal density of 6.09×10^{11} CNT/cm²). The density of the VACNT forest samples falls well within the range of CVD grown samples [13, 159-161, 190], and assigning a uniform radius to every CNT within the forest is a good approximation for the tightly distributed radii of SWCNTs [162]. The tallest *in silico* sample used in the simulation discussed in section 5.3 consists of 2,498 2- μ m-long CNTs on a $0.64 \times 0.64 \mu\text{m}^2$ substrate and is designated as FA (Figure 5.2a). With each internal node (dynamic unit in the mesoscopic model) representing 2-nm-long segment of a nanotube, the computational sample is composed of 2,500,498 nodes. Three smaller samples consist of 0.6- μ m-long CNTs randomly distributed on a $0.60 \times 0.60 \mu\text{m}^2$ substrate and are referred to as FB, FC, and FD (Figure 5.2b-d). These samples are generated with different values of Θ_{max} and are used for investigation of the structural dependence of the mechanical behavior of VACNT forests reported in section 5.4. In all simulations, the periodic boundary conditions are applied in the lateral directions (parallel to the surface of the substrate) directions, thus effectively representing VACNT forests extending much further than the actual lateral dimensions of the computational systems.

The structure of the *in silico* samples is characterized by calculating a set of parameters listed in Table 5.1, including the average tilt of CNT segments with respect to the direction of VACNT alignment (θ), average bundle size $\langle N_B \rangle$, maximum bundle size N_B^{max} , standard deviation (SD) of the bundle size, and magnitude of the Herman orientation factor (HOF) defined as $S = \frac{1}{2}[3\langle \cos \theta \rangle - 1]$, where θ is the local angle between a nanotube and the vertical axis, and the angled brackets $\langle \rangle$ denote averaging over all CNT segments in a sample. The HOF quantifies the extent of the orientation of nanotubes with respect to an axis of interest, in this case the substrate normal, and ranges from -0.5 to 1, where values of -0.5, 0, and 1 correspond to perpendicular alignment, isotropic orientation, and parallel alignment with respect to the axis, respectively.

Among the 0.6- μm -tall forests, sample FB is prepared with the smallest Θ_{max} of 0.6° and has highly vertically oriented, thick CNT bundles with minimal interconnection between the bundles. Sample FD is prepared with the largest Θ_{max} of 27° , is poorly aligned (lowest HOF), and features thinner bundles organized into a more complex, entangled network. Sample FC is prepared with Θ_{max} of 12° and features structural characteristics intermediate between FB and FD samples (Table 5.1). The tallest VACNT forest FA is prepared with the same Θ_{max} as sample FC and has similar degree of alignment, as characterized by $\langle \theta \rangle$ and HOF. The average and maximum bundle sizes, however, are substantially larger in the tall forest, reflecting the increased freedom of nanotubes to join multiple bundles across the height of the forest.

5.2.3 Simulation of the uniaxial compression

Both VACNT forests are compressed at an indenter velocity of 50 m/s, corresponding to a deformation rates of $8.3 \times 10^7 \text{ s}^{-1}$ and $2.5 \times 10^7 \text{ s}^{-1}$ for the 0.6- μm - and 2- μm -long forests, respectively. While the indenter velocity of 50 m/s is a much higher than typical experimental values of 1-1000 nm/s, matching the deformation rates used in experiments is computationally impractical. For instance, for sample FA consisting of over 2.5 million nodes, the compression to 0.9 engineering strain at the indenter velocity of 50 m/s takes 36 ns and requires 1.2M CPU hours on *Comet* supercomputer [165]. The stress-strain curves predicted in earlier simulations of the uniaxial compression of short VACNT forests consisting of 0.2- μm -long CNTs [182], are found to be in a semi-quantitative agreement with those reported in experimental studies, despite the high deformation rates of 5×10^7 to $2.5 \times 10^8 \text{ s}^{-1}$ used in the simulations. Moreover, only moderate quantitative changes in the stress-strain response are observed upon decrease of the deformation

rate from 10^8 to $5 \times 10^7 \text{ s}^{-1}$, suggesting that the physical mechanisms of VACNT deformation are unlikely to change upon further decrease of the deformation rate.

Another consideration at high loading velocities is the formation of a shock wave inside the forest. In a homogenous material, the speed of sound is given by

$$c = \sqrt{E \cdot \rho^{-1}} \quad (5.1)$$

where E is the elastic modulus and ρ is the material density. In section 5.3, the formation of a localized densified phase ($\rho \sim 10^2 \text{ kg/m}^3$), and an elastic modulus of $E \sim 10^6 \text{ Pa}$. Therefore, $c \sim 10^2 \text{ m/s}$, and the question of the role of acoustic shock in the formation of the densified layer may arise at loading rates approaching the calculated speed of sound. However, estimating the speed of sound from equation (5.1) assumes a homogenous material, but the VACNT forest, with its networked structure of overlapping bundles does not qualify as such, making it difficult to estimate the true speed of sound with the forest. To provide a resolution to this question, a simulation of FA was compressed to 0.4 strain was continued where the indenter was held in position without any further compression. Insignificant progression of the densified layer even after 1 ns suggested that the layer was not a result of a shock wave.

The uniaxial compression is simulated with a rigid indenter spanning the entire lateral area of the sample and interacting with the CNTs via a purely repulsive potential. The compression is simulated at a constant temperature of 300 K enforced by the Berendsen thermostat algorithm [88] applied to the coarse-grained units of the model, *i.e.*, the thermal equilibrium between different vibrational models of the system is assumed at all times. The reported stresses are calculated from the total force that the VACNT forest exerts on the indenter. The engineering strain is defined with respect to the length of the CNTs within the forest (*i.e.*, 2 or 0.6 μm), rather than the maximum initial forest height, which is shorter by less than 1%. For the convenience of representation of stress-strain dependences for VACNT forests undergoing compressive loading, we adopt a sign convention where the stress is positive in compression and present the magnitude of the engineering strain as a positive quantity.

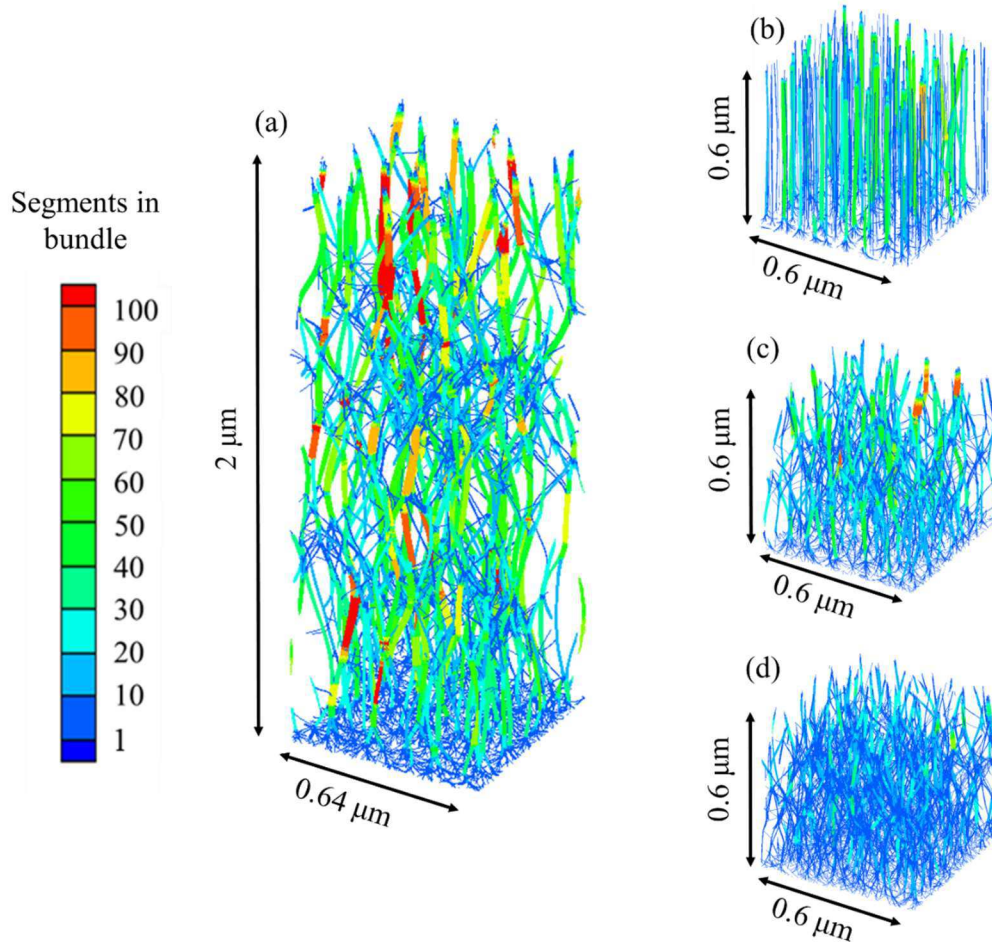


Figure 5.2: Side views of computational VACNT samples composed of nanotubes with CNT lengths of 2 μm , FA (a) and 600 nm, FB, FC, and FD (b-d) generated by mesoscopic simulations. The CNT segments are colored by the local bundle thickness (number of segments in a bundle cross section).

Table 5.1: Statistical information on structural parameters of four computational forests of the same density of 0.02 g/cm^3 and composed of CNTs with lengths L_{CNT} of 2 and 0.6 μm . The average tilt of CNT segments $\langle\theta\rangle$, average bundle size $\langle N_B \rangle$, maximum bundle size N_B^{max} , standard deviation (SD) of the bundle size, and magnitude of the Herman orientation factor (HOF) are listed for computational samples generated at maximum inclination angles Θ_{max} of 0.6° , 12° , and 27° .

Sample	L_{CNT}	Θ_{max}	$\langle\theta\rangle$	$\langle N_B \rangle$	N_B^{max}	SD	HOF
FA	2 μm	12°	17.6°	42	163	28	0.82
FB	600 nm	0.6°	5.7°	28	82	19	0.95
FC	600 nm	12°	17.2°	22	98	18	0.82
FD	600 nm	27°	22.9°	10	65	9	0.72

5.3 Deformation mechanisms and phase separation for 2 μm VACNT forest

5.3.1 Formation of densified phase

In this section, the structural changes resulting from the uniaxial compression of sample FA, composed of 2 μm long CNTs, at a rate of 50 m/s (corresponding to a deformation rate of $2.5 \times 10^7 \text{ s}^{-1}$) are described. While 50 m/s is a much more rapid compression speed compared to the typical 1-1000 nm/s rate used in laboratory tests, matching the rates used in experiment would be computationally impractical. For instance, sample FA consists of over 2.5 million nodes, and even at 50 m/s compression to 0.8 engineering strain takes 32 ns, which required approximately 2,700 wall-clock hours using 384 processors on the state of the art *Comet* supercomputer [165]. We, however, justify the results of the simulations presented in this paper on the basis of our earlier work on the uniaxial compression of various forests consisting of 0.2 μm long CNTs [182] where semi-quantitative agreement is observed between the simulated mechanical stress-strain response of these forests and those reported in experiment. Furthermore, due to the ten times longer length of the CNTs of sample FA compared to the samples compressed in ref [182], the strain rate is an order of magnitude less, and the physical mechanisms of VACNT deformation are unlikely to change at slower compression rates.

All simulations reported in sections 5.3 and 5.4 are performed at a constant temperature of 300 K, enforced by the Berendsen thermostat algorithm [88] and all reported stresses are calculated from the total force that the forest exerts on the indenter. The engineering strain is defined with respect to the length of the CNTs within the forest (*i.e.*, 2 μm or 0.6 μm), rather than the maximum initial forest height, which is shorter by less than 1%. For the convenience of representation of stress-strain dependences for VACNT forests undergoing compressive loading, we adopt a sign convention where the stress is positive in compression, and present the magnitude of the engineering strain as a positive quantity. The rigid indenter used to compress the forests interacts with the CNTs via a purely repulsive potential and spans the entire lateral area of the sample.

In the first simulation, forest sample FA is compressed to 0.8 engineering strain. Snapshots showing the microstructure for the original sample and at four strains during the course of compression are presented in Figure 5.3, where the CNT segments are colored their CNT-CNT interaction energy. In the two tone coloring scale red indicates higher energy (relatively isolated CNTs) and blue indicates lower energy (highly bundled CNTs). Immediately apparent from the

snapshots is the formation of an entangled, densified layer near the compressing indenter. Although the aggregation and entanglement of the tops of CNTs near the indenter was observed previously in simulations of shorter $0.2\ \mu\text{m}$ forests [182] its formation for these samples was unclear. In sample FA, it is apparent that the layer thickens with compressive strain while the remainder of the forest does not undergo the same type of morphological changes. During compression to 0.8 engineering strain, approximately 8% of the 2,500 CNTs in the sample fracture due to bending.

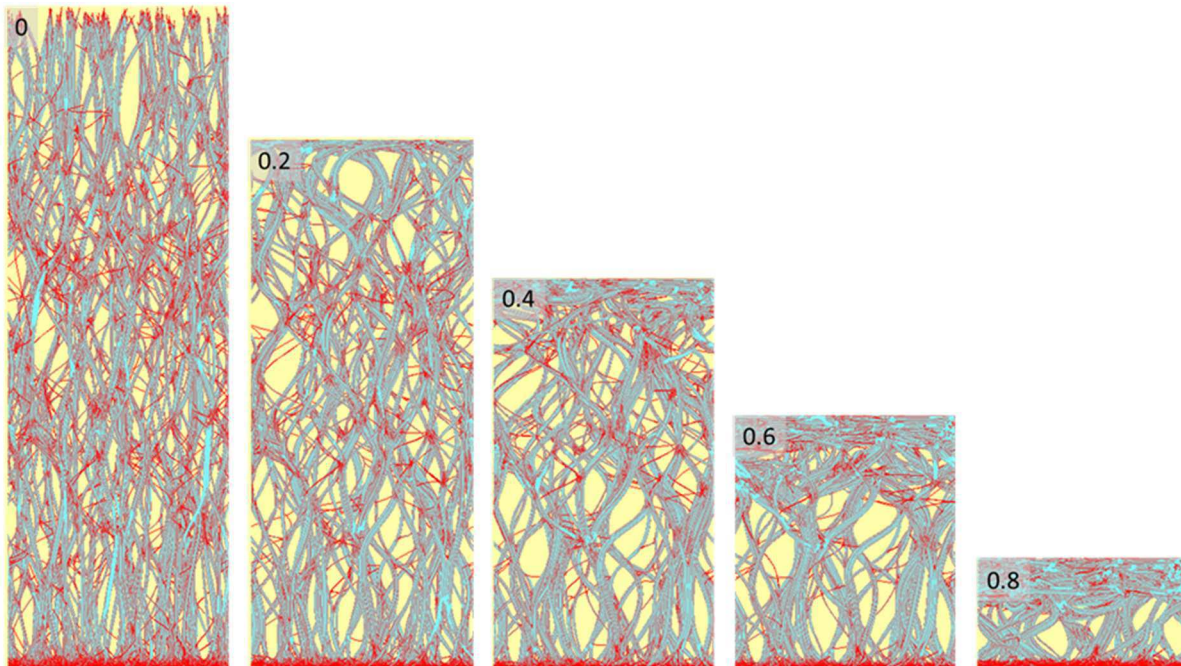


Figure 5.3: Snapshots of the side view from the compression of FA from 0 to 0.8 engineering strain. The two-tone coloring of CNT segments is by CNT-CNT interaction energy where red indicates less favorable interaction (isolated segments) and blue indicates more favorable interaction (highly bundled segments).

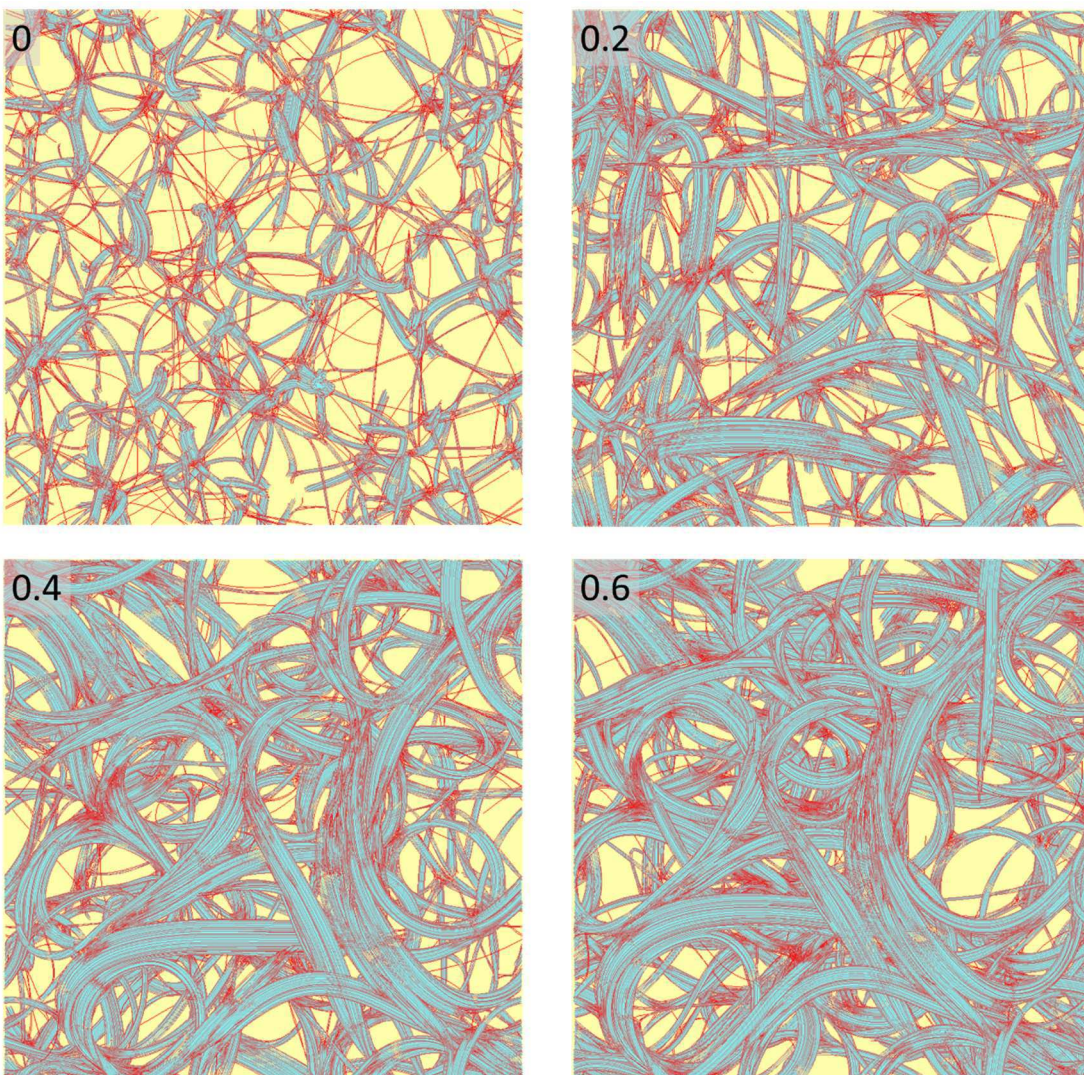


Figure 5.4: Snapshots of the top-down view from the compression of FA from 0 to 0.6 engineering strain in 0.2 increments. The two-tone coloring of CNT segments is by CNT-CNT interaction energy where red indicates less favorable interaction (isolated segments) and blue indicates more favorable interaction (highly bundled segments).

Visually, the dense and perpendicularly oriented layer at the top of the forest looks quite distinct from the lower portion of the forest characterized by vertically oriented bundles. The development of the densified layer has been observed repeatedly, [29, 31, 124, 164, 169] and connections between its formation and the periodic buckling ubiquitous among uniaxially compressed VACNT forests are evident [164]. However, hitherto, the mechanism of layer formation has not been addressed. In Figure 5.4, the top-down views of sample FA throughout

compression are shown. The material falling within the bottom half of the sample height at the corresponding strain is blanked in order to more clearly show the evolution of the top layer. From the snapshots, the progression of the densified layer is seen to happen over four stages. First, at small strains (0.2), the CNT bundles of sample FA locally deflect near the indenter. Next, as the indenter continues to push into the forest, the bent bundles spread out laterally below the indenter and form a densified, poorly aligned network (see snapshot for 0.4 strain). Eventually, the bundles come into contact with one another, and coarsening of bundles can occur. However, with the continuous addition of material to the layer, crowding can prevent more material from easily joining, and the densified phase begins to thicken.

Although the densified and rarified phases are readily discerned from the snapshots of Figure 5.3 and Figure 5.4, tracking the evolution density and orientation throughout the compression of forest FA allows for the quantitative characterization of the two phases. Notice that the top part of the forest is dense and oriented perpendicularly to the substrate, whereas the bottom part is more rarified and aligned with the forest axis. To quantify this observation, two “image” plots prepared using R [191] are shown for mass density and CNT orientation (quantified by HOF) in Figure 5.5. These plots are prepared by first partitioning the original, unstrained forest sample into layers based on height along the forest. Each layer contains a unique set of CNT nodes. During compression, the property of interest is calculated for every node locally in its modified, strained environment. Finally, the average of the property is computed for the set of nodes belonging to each of the original layers. Therefore, in Figure 5.5, every box represents the set of nodes as the laterally adjacent box. The choice of colormap for these plots is “Viridis”, considered to be grayscale and colorblind friendly as well as have excellent perceptually uniformity compared to more traditional rainbow or “jet” colormaps [192].

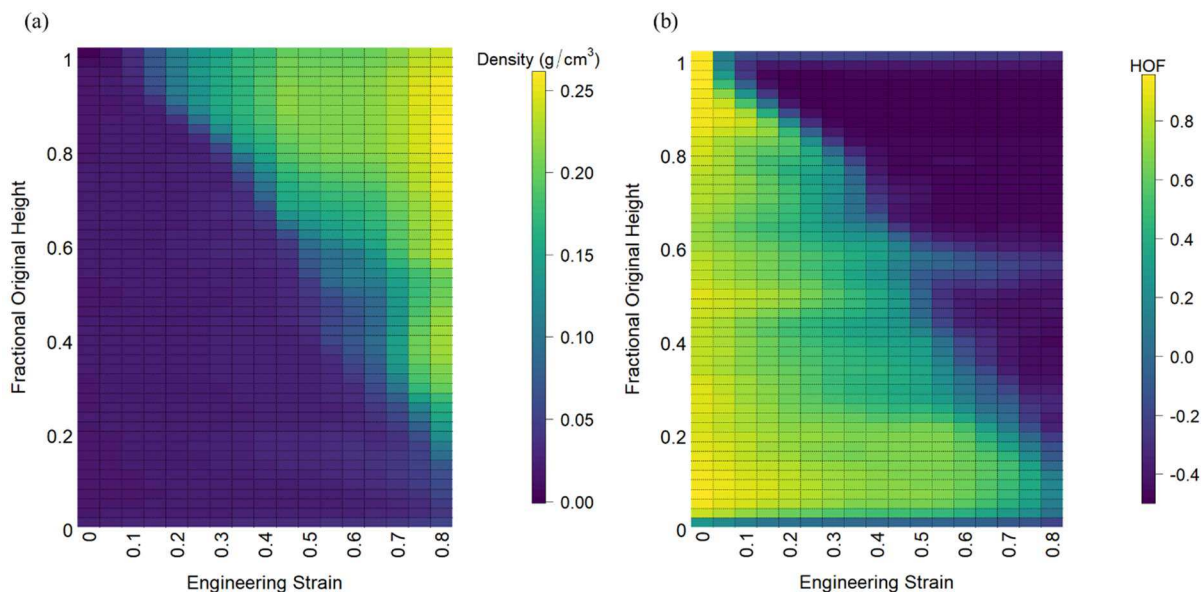


Figure 5.5: Image plots of mass density (a) and HOF (b) calculated from sets of segments partitioned by their original position in the uncompressed forest sample. The plots contain columns corresponding to a set of strains from 0 to 0.8 incremented by 0.05, all with 50 vertical divisions each representing the same CNT node IDs.

Examining Figure 5.5a, where the density along the forest with strain is depicted, there is a distinct boundary between the high density of the layer forming near the indenter and the rest of the forest beginning even at 0.2 strain. With increasing strain, the top layer thickens and densifies in certain places beyond 0.2 g/cm^3 (ten times that of the initial forest density) at strains beyond 0.4. However, despite the theoretical maximum close packed density of (10,10) SWCNTs of about 0.9 g/cm^3 , the density does not increase beyond $\sim 0.25 \text{ g/cm}^3$ even at 0.8 strain, suggesting that constraints imposed on bundle reorganization prevent denser packing for this sample at this compression rate, and instead, the region with this peak density expands with strain. Also apparent is the formation of a density gradient between the two the low and high density regions, which expands at high strains beginning at 0.5. At low strains the transition from low density to high density is sharp, spanning only on the order tens of nanometers. However, once the forest becomes highly compressed, the rigid boundary conditions imposed on the bottoms of the CNTs begins to affect the evolution of the denser layer, since the bundles cannot properly align themselves completely perpendicular to the substrate anymore. Consequently, beginning at 0.5 strain, the density gradient widens as bottom part of the forest also begins to become compacted.

The orientation of the CNTs also changes dramatically from the densified phase to the rarified phase (Figure 5.5b), where even at small strains (>0.1) the HOF of CNTs clearly transitions from approximately -0.5 in the densified layer to 1 in the remainder of the forest. However, the gradient change for HOF is visibly wider than for density at moderate strains (*i.e.* 0.2-0.6). The reason is that as the tops of bundles are forced perpendicular to the substrate, the constrained bottoms of the forest must follow. As a consequence, the transition from vertically to perpendicularly oriented CNT segments is wider than that for density. The shorter the forest the more pronounced the effect is (see section 5.4 and ref [182]). Nonetheless, there is still a clear demarcation between the perpendicularly oriented parts of CNTs in the dense layer and those still in the rarified layer.

5.3.2 Stability of densified phase

The phase separation is a thermodynamically favorable process for sample FA. During compression up to 0.8 engineering strain, the changes in CNT-CNT interaction energy and in bending energy account for $\sim 99\%$ of the change of non-thermal energy. Note that the rise in bending energy is more than offset by the decrease in CNT-CNT interaction energy (see Figure 5.6a and b). Furthermore, from the image plots of CNT-CNT interaction energy and bending energy (Figure 5.6c and d, respectively), the changes in these energies are more localized along certain regions within the forest sample. The interaction energy decreases most prominently within the center of the densified layer (approximately in the range of 0.8-0.9 original fraction height). Above this layer near the top of the forest a region of higher interaction energy comes from the tops of the bundles which interact with the indenter rather than other CNTs. Below, a transition from lower to higher interaction energy is visible corresponding to the interfacial region between dense and rarified states of the forest. The shift between the two phases is also apparent from the image plot of the bending energy (Figure 5.6d), where by 0.4 strain there is a clear central region of relatively high bending energy compared to the two ends of the forest. The proportion of the forest with relatively large bending energy increases with strain, physically corresponding to the bending of the CNT bundles constrained by their rigid bottoms. The decrease of the nanotube interaction energy decreases the energy of the compressed forest, despite the requisite bending, and therefore the structure should in this case be stable after the indenter is removed. Although we do not test this due to the computational expense, plastic deformation was previously observed for 0.2 μm SWCNTs repeatedly loaded and unloaded to both 0.6 and 0.8 strain [182]. Forests

composed of MWCNTs with large diameters, however, are more likely to elastically deform [28] due to the high bending modulus of the CNTs [80, 150, 151].

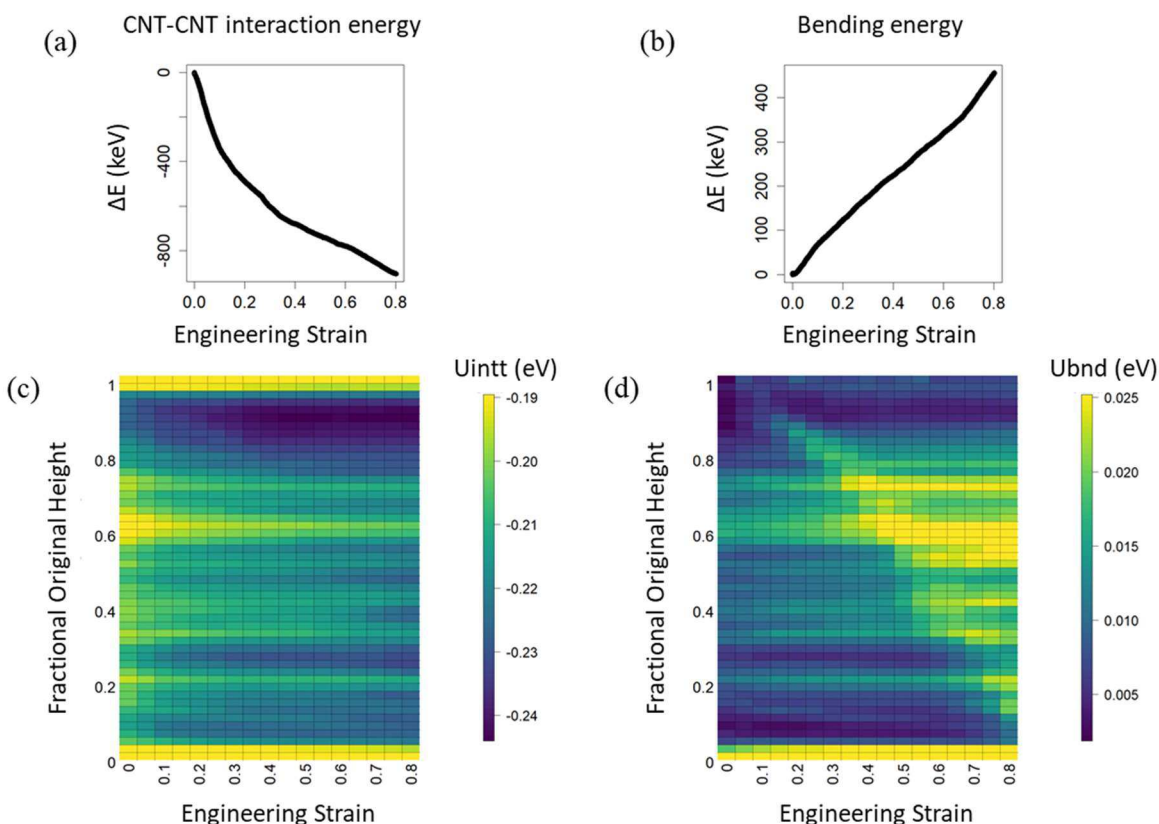


Figure 5.6: Change in CNT-CNT interaction energy (a) and bending energy (b) with engineering strain of sample FA. Image plots of average CNT-CNT interaction energy (c) and average bending energy (d) calculated from sets of segments partitioned by their original position in the uncompressed forest sample. The plots in panels c and d contain columns corresponding to a set of strains from 0 to 0.8 incremented by 0.05, all with 50 vertical divisions each representing the same CNT node IDs.

5.3.3 Origins of coordinated buckling in VACNT forests

An interesting feature in Figure 5.5b is the non-monotonous trend in HOF along the forest at strains above 0.5, where the middle section of the forest has a locally large HOF (less perpendicular orientation) relative to its immediate surrounding, persisting to 0.8 strain. The

localized change in CNT orientation is reminiscent of a section of forest undergoing coordinated buckling, characterized by an accordion-like morphology.

To explain the origin of the local maximum of HOF, we track the evolution of five individual and representative CNTs in sample FA from strain of 0-0.8 (Figure 5.7a). Each colored CNT exists largely separate from the rest at 0 strain, but due to the networked structure CNTs that have their bases hundreds of nm apart can overlap significantly near the top of the forest. At 0.2 strain, the CNTs deflect and bow outward near the indenter as they are compressed, eventually forming the densified layer of highly bent CNT sections at 0.4 strain. However, already at 0.4 strain is visible the deflection of the CNT bundles towards the base of the forest sample. At 0.6 strain, this bowing becomes even more pronounced, and suggests the site of coordinated buckling along the cross-section of the forest sample.

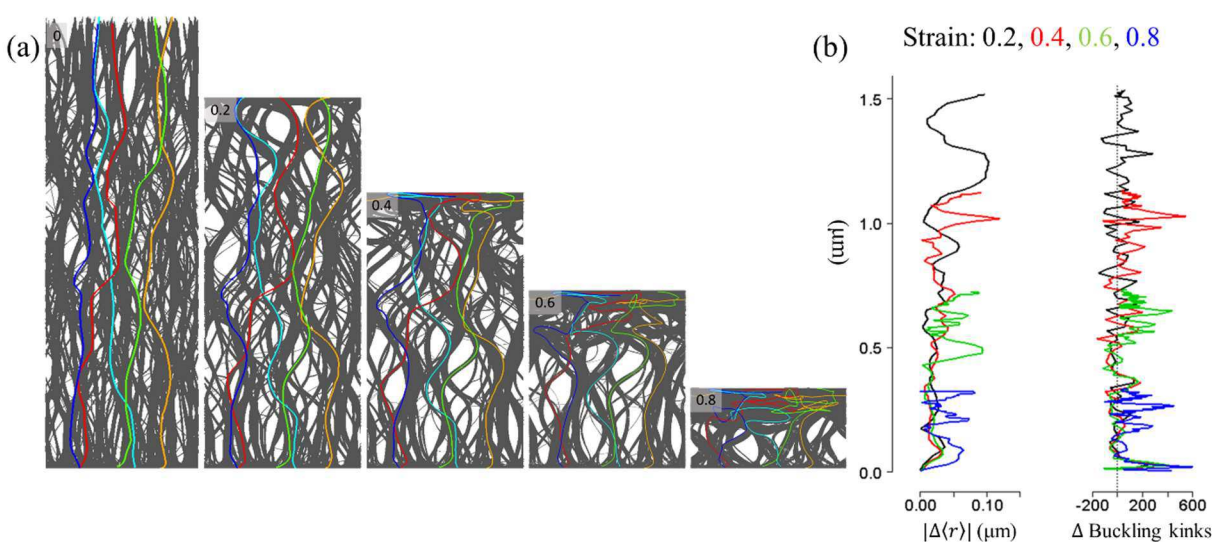


Figure 5.7: Snapshots of the side view from the compression of FA from 0 to 0.8 engineering strain with an overlay showing the geometries of five typical CNTs (a) and the magnitude of the average deviation in the lateral position of the forest relative to its unstrained state ($|\Delta\langle r \rangle|$) and change in the number of buckling kinks relative to the uncompressed sample plotted as a function of height for strains from 0.2 to 0.8 (b).

In addition to the representative CNT geometries given in in Figure 5.7a, plots of the magnitude of the average deviation in the lateral position of the forest relative to its unstrained

state and the change in the number of buckling kinks relative to the uncompressed sample are plotted as a function of height, where each data point corresponding to 1% of the forest mass, for this sample in Figure 5.7b. The magnitude of the average lateral deviation in position is calculated by $|\Delta\langle r \rangle| = \sqrt{\langle x - x_0 \rangle^2 + \langle y - y_0 \rangle^2}$, where x and y are the positions of the nodes at some forest strain and x_0 and y_0 represent their positions at zero forest strain. Note that the statistical information on the shift in lateral positions corroborates the visual representation in Figure 5.7a. The localized peaks in positional change indicate a coordinated shift across the forest, especially at about a height of $0.5 \mu\text{m}$ for the sample compressed to 0.6 strain. Referring back to Figure 5.5b, this shift coincides with the localized fluctuation in forest orientation. This observation relates closely to experimental studies on coordinated buckling of VACNT forests, where CNT segments near the bottom of the forest reorient laterally (Figure 5.8) before buckling [126].

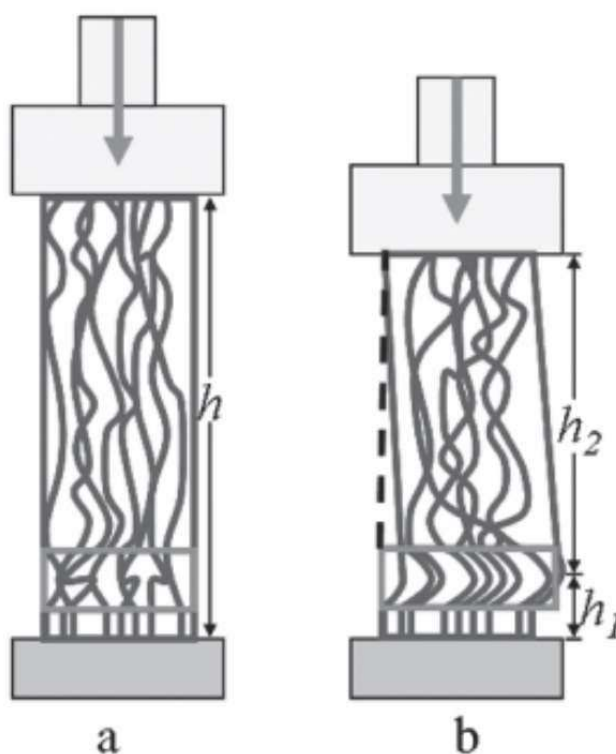


Figure 5.8: Buckling model of a VACNT forest under uniform compression. (a) Initial configuration. (b) Under compression the CNT segments closer to the bottom of the forest reorient laterally. Once the buckling load is reached, the bottom portion of the forest buckles in the direction of the initial lateral reorientation. Figure adapted from ref. [126].

The lateral shift of the CNT segments near the base of the forest is due to the constraint on nanotube motion by both the base of the forest and by the densified layer. As the forest becomes increasingly compressed, the tops of CNTs are held fixed in the dense phase, preventing any significant lateral sliding. With the bottoms of the nanotubes also fixed, CNTs cannot easily orient themselves to continue optimal packing the densified layer. Instead, the CNT segments are forced to bow outward below the densification front. A coordinated shift of bundles can result when one CNT bundle deflects laterally, resulting in the “nucleation” of a preferential direction for surrounding bundles due to the interconnected network structure of the forest.

Although we note a zigzagging of the representative CNTs, coordinated buckling like described in [29, 31, 126] is not strongly evident from the profile of the change in the number of buckling kinks. The majority of buckled CNT segments are present in the densified layer, where the nanotubes are oriented parallel with the indenter. Although a significant spike in the number of buckling kinks is expected near the bottom of the forest sample where the lateral deflection is significant, the noisy distribution of kinked segments makes direct correlation between the two difficult. Nonetheless, as the forest is compressed beyond 0.6 strain, a remarkable shift in the lateral position of the CNTs is a likely precursor for coordinated buckling.

As mentioned previously, the rigid base of the forest becomes increasingly important to the overall deformation with compressive strain. As more material is added to the dense layer, the CNTs must either move side to side so that the tops of the bundles can form a highly bent, alternating, accordion like pattern, or the bundles can bow out laterally. In the case of sample FA, the latter option is observed. Classical Euler-Bernoulli [168] beam theory explains why the first option is not observed for the short 2 μm forest. In particular, the maximum stress that a column can withstand without buckling is given by the expression

$$P_{cr} = \frac{n^2 \pi^2 E I}{L^2} \quad (5.2)$$

where E is the bending modulus, I is the moment of inertia about the axis of buckling, L is the length of the column, and n is the column buckling mode. Here it is important to point out that the term ‘buckling’ in Euler-Bernoulli beam theory refers to a deflection rather than to the deformation

mode undergone by CNTs at a critical radius of curvature. From equation (5.2), the critical stress relates to the number of buckling modes squared, and hence increasing the number of buckled points for a CNT bundle “beam” becomes quite costly, especially for shorter CNTs. However, longer CNT bundles will better tolerate multiple buckling modes, and discrete regions of stacked densified layers are observed for forests that undergo periodic, coordinated buckling [29, 31, 126].

Another reason why periodic buckling is not observed in forest FA can be attributed to the higher flexibility of SWCNTs to bend and contort in ways so that significant buckling can be avoided compared to multi-walled carbon nanotubes (MWCNTs) [80]. Indeed, one report [169] noted that buckling becomes highly periodic beginning only at a MWCNT length of 190 μm , and that the typical period between successive buckling ranges between 3-6 μm , although single coordinated buckling event is still observed for forests as short as 35 μm . Furthermore, in laboratory grown VACNT forests, the presence of density gradients is thought to provide preferential nucleation sites for coordinated buckling [124]. In our *in silico* samples, no such gradients exist along the height of the unstrained forest, and the barriers to the nucleation of coordinated buckling are higher.

Coordinated buckling across the forest is mechanically registered as on the indenter in the form of stress undulations during the plateau regime of stress [31, 32, 124, 126]. The process relieves some of the rising stress of the forest on the indenter, resulting in a rapid drop of stress. Indeed, the stress-strain curve for the compression of sample FA in Figure 5.9 shows a series of undulations with strain. However, the drops in stress are not obviously correlated with discrete events of coordinated buckling across the forest. Rather, the broader drops in the stress are more likely due to a series of CNT bundles buckling in succession.

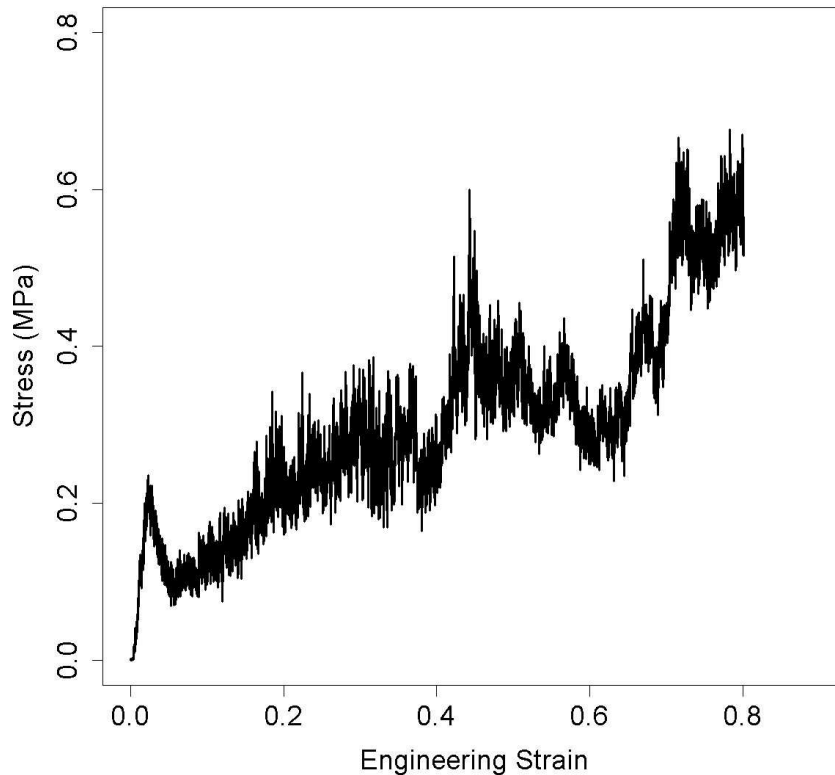


Figure 5.9: Stress-strain response of sample FA compressed at 50 m/s.

5.4 Effect of forest structure and length on deformation mechanisms

The next set of simulations consider forest samples FB, FC, and FD which have the same density (0.02 g/cm^3) and CNT length ($0.6 \text{ }\mu\text{m}$), and differ only by their structural characteristics (*i.e.*, thickness of the bundles and CNT inclination, as can be seen from Figure 5.2 and Table 5.1). The incidence of CNT fracture are 3% for FA, 9% for FB, and 17% for FC at 0.8 strain. Interestingly, the general deformation behavior, the CNT-CNT interaction energies, and the stress on the indenter are almost identical to the same simulation where CNT fracture is not considered (see section 5.5). Previous simulations on the uniaxial compression of $0.2 \text{ }\mu\text{m}$ tall forests revealed a sensitivity of the deformation mechanisms and mechanical response to the sample's structural properties (*i.e.* bundle thickness and orientation), where in particular, less vertically oriented bundles in these smaller forests tended to fold at their base compared to samples with more vertically oriented bundles which bowed outward near their centers [182]. However, the

deformation mechanisms observed may be arise from the shortness of the CNTs, and cannot necessarily be extended to forests with longer CNTs. In this section, the effect of forest structure on the deformation mechanisms during uniaxial compression will be considered for 0.6 μm tall forest. We discuss these results in the context of the 2 μm compression detailed in the preceding section and the results reported for 0.2 μm forests described in detail elsewhere [182]. The forests are compressed at the indenter velocity of 50 m/s (corresponds to the deformation rate of $8.3 \times 10^7 \text{ s}^{-1}$ for the 0.6 μm long VACNT forest).

Snapshots of the compression forests FB, FC, and FD from 0.2 to 0.8 strain are presented in Figure 5.10. Formation of a densified layer near the indenter proceeds similarly as for the tall forest considered in the previous section, and is visible for all samples. However, at higher strains (>0.6) CNT bundles bow outward along much of the height of the forest, a phenomenon also previously observed in shorter, 0.2 μm forests at similar strain [182], rather deforming in a more localized manner as with sample FA. However, visually, the mechanisms of deformation among the three forests are not fundamentally distinct, like in the case of the shortest forests, where the CNTs with greater orientation tended to fold along their bases during compression, while the forests with less oriented CNTs tended to form the denser layer of material near the indenter as the bundle bowed laterally outward [182]. One reason for the insensitivity of deformation mechanism to the microstructure of the samples is the greater bundle entanglement possible with longer nanotubes, as the lateral displacement of the tops of the CNTs is larger at the same inclination angle [158]. Therefore, the CNT bundles cannot easily move independently from one another for the longer CNTs, and clean folding of individual bundles at their bases is impractical.

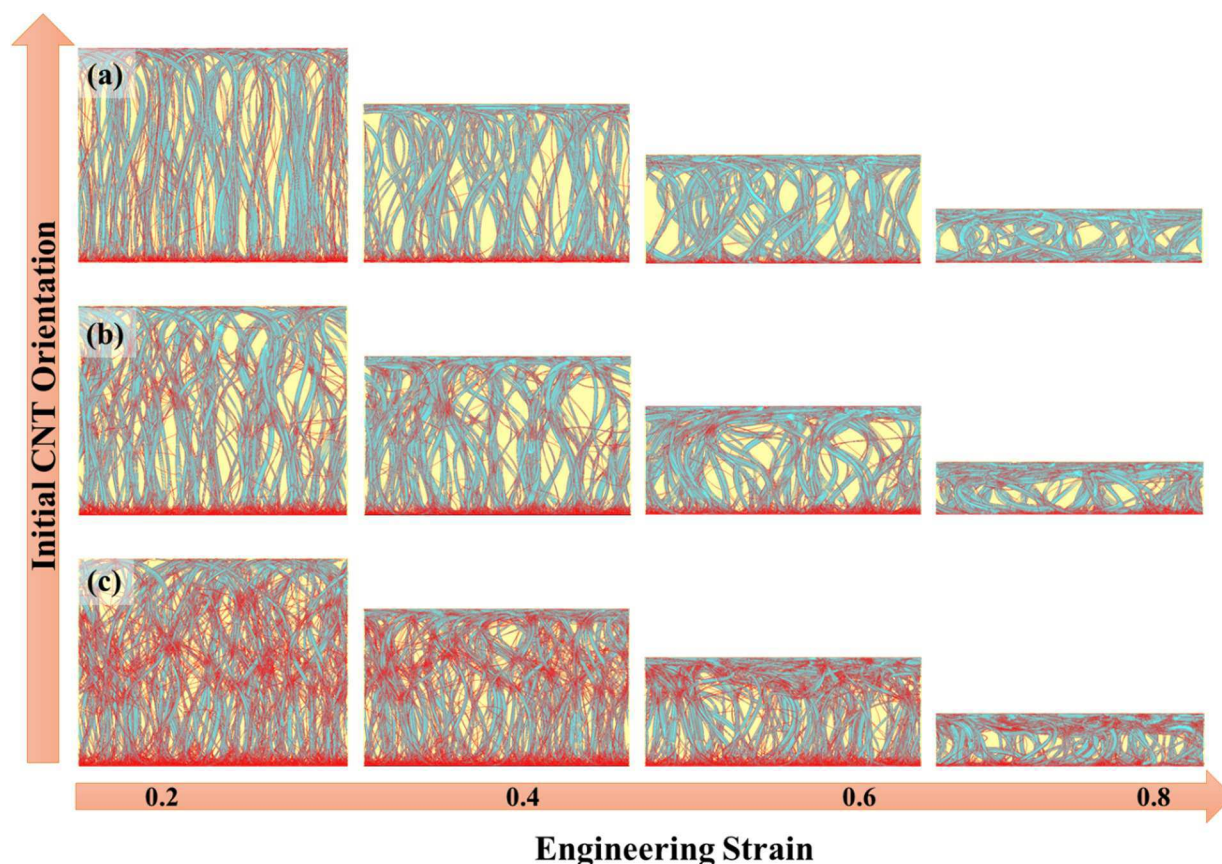


Figure 5.10: Side view snapshots from simulations of uniaxial compression of computational samples FB (a), FC (b), and FD (c) up to 0.8 engineering strain with an indenter velocity of 50 m/s. The CNT segments are colored by their CNT-CNT interaction energy on a two-colored red-blue scale. Red corresponds to high interaction energy (less favorable nanotube interaction) and blue corresponds to low interaction energy (more favorable nanotube interaction).

Information about the density, HOF, magnitude of the average deviation in the lateral position of the forest FB, FC, and FD relative to its unstrained state, and the change in the number of buckling kinks its unstrained state along their normalized height at 0.6 strain is plotted in Figure 5.11. In general, analysis of these plots indicate that transition from the rarified to densified phases is less complex than for sample FA. The density plot shows a sharp transition from the rarified and densified phases for each sample without the intermediate oscillations of sample FA and no significant extrema are seen for any of the forests in HOF throughout their heights. It is also difficult to discern any physically meaningful trends in the average lateral displacement data. However, it is notable that sample FB shows almost no change in the number of buckling kinks

near the indenter in contrast to the other two forests, FC and FD. The reason is attributed to the well aligned and more isolated bundles of sample FB which coordinate CNT motion. But, for the more entangled structures of forests FC and FD, the CNTs spanning bundles are more bent and buckled even before compression, but the inability of these smaller bundles to easily reorganize results in pronounced buckling during compression. The entangled structure of samples FC and FD therefore also explain the broad buckling peak near the indenter. Interestingly, at the base of the sample the number of buckling kinks decreases rather than increases from the unstrained states for all of the samples (FA, FB, FC, and FD), although the difference is most pronounced for FB and least so for FD. During compression, the base of the bundles tend to deflect to one side, and the better alignment of the CNTs can result in a decrease in the number of buckled CNTs (although a significant number CNTs still remain highly bent and buckled). Among the 0.6 μm forest samples, the decrease in the number of buckling kinks as well as the increase in average lateral deflection near the base of the sample is most dramatic for sample FB and least so for FB. The relatively isolated bundles of sample FB can more easily change position during compression compared to the more entangled structures of FC and FD, and therefore are better able shift to more favorable and low resistance configurations.

Stress-strain curves for each forest are plotted in Figure 5.12, showing the characteristic three-stage response of foam materials undergoing uniaxial compression, and are in good quantitative agreement with *in situ* measurements [31, 32]. The first stress peak is most prominent for FA (Figure 5.12a), and comes from the axial compression of its highly oriented CNTs. The forests where the CNTs are less well vertically oriented have a much more muted elastic stress response to the indenter [182]. Next, the plateau stress stage spans strains up to ~ 0.85 . Due to the greater degree of entanglement limiting bundle mobility and their ability to organize themselves in the optimal way to reduce stress, the average stress increases from FB to FC to FD at a strain starting approximately at 0.45. Finally, after 0.85 strain the densification regime is heralded by a sharp increase in stress. At this point, the CNTs have limited ability to reorganize themselves in a low-stress manner, and increasing strain will see the entire forest converted to the densified phase.

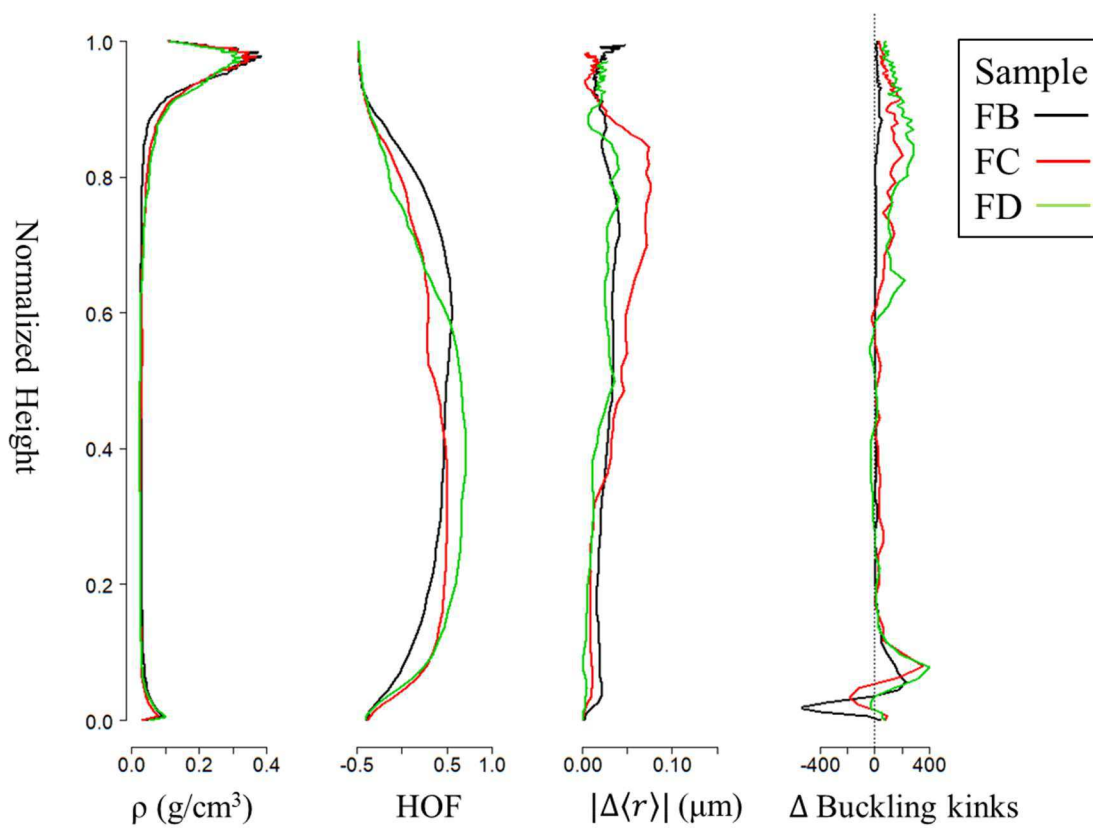


Figure 5.11: Plots of the density, HOF, magnitude of the average deviation in the lateral position of the forest relative to its unstrained state, and the change in the number of buckling kinks its unstrained state along the normalized height of the forest for samples FB, FC, and FD compressed to 0.6 strain.

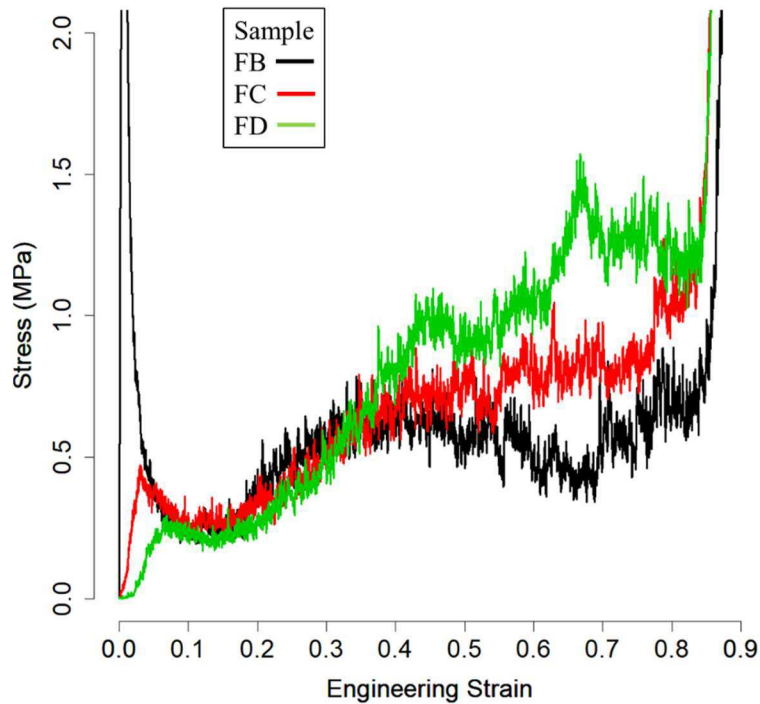


Figure 5.12: Stress-strain response for sample FB, FC, and FD compressed at an indenter velocity of 50 m/s to 0.9 strain.

5.5 Role of fracture during uniaxial compression

The consequence of allowing for fracturing of CNTs due to both bending and stretching is briefly discussed in this section. As previously stated, both axial and bending fracture of CNTs can occur, where either event results in clean CNT fragmentation. For (10,10) single-walled carbon nanotubes (SWCNTs), axial fracture is set to occur at a strain between two nodes of 0.279 [43] and bending fracture at an angle of 120° [39] calculated for three consecutive intratube nodes. For all forests, fracture is due exclusively to the bending of the nanotubes. In the case of sample FA, fracturing is predominantly localized to the densified layer where the transition from parallel to perpendicular orientation of the CNTs with the vertical axis occurs. Despite the propagation of the densified phase with strain, only about 8 % of CNTs are fractured at 0.8 strain for forest FA.

As discussed in section 5.4, the number of fractured CNTs at 0.8 strain increases from FB to FD by more than a factor of 5. The reason is that the CNTs of FD are much more oriented on

average relative to forest FB, resulting in higher connectivity between CNT bundles. The individual CNTs and thin bundles that connect the larger bundles in sample FD are generally characterized by greater inclinations, and hence are more prone to fracture during compression. Although, during compression to 0.8 strain, almost a fifth of CNTs undergo fracture in sample FD the difference in the stress response, bending energy, and CNT-CNT interaction energy compared to the same sample undergoing compression without the possibility of nanotube fracture is negligible except at strains beyond 0.4 (see Figure 5.13a). Even at higher strains, the evolution in stress, bending and CNT-CNT interaction energies is qualitatively similar and the overall picture of deformation (*i.e.* the formation of the localized densified phase) is unaltered when nanotube fracturing is neglected (Figure 5.13b,c,d).

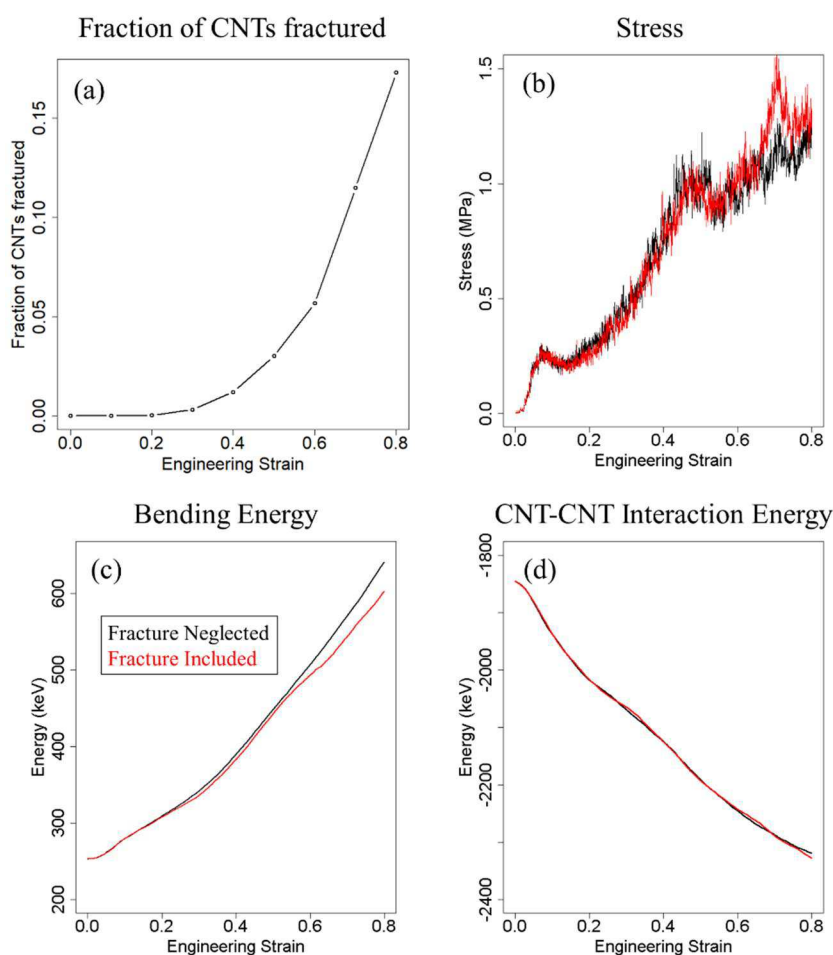


Figure 5.13: Fraction of CNTs fractured with strain (a) and comparison of stresses (a), bending energy (b), and CNT-CNT interaction energy (c) for forest FD where CNT fracture is included and neglected.

5.6 Summary

Mesoscale simulations showing the clear phase separation in a 2 μm VACNT forest undergoing uniaxial compression have been reported in this chapter. A dense phase consisting of CNTs oriented parallel to the indenter and a rarified phase with relatively good vertical alignment are reported and characterized. Additionally, the process leading up to coordinated buckling across the lateral extent of the forest is shown. Finally, the roles of CNT length and forest microstructure are detailed, where the results of simulated uniaxial compression of three structurally distinct 0.6 μm forests are compared to each other as well as to simulations for 0.2 and 2 μm samples. We find that only 2 μm CNTs show evidence of the coordinated buckling process, but that at already 0.6 μm structural differences play less of a role compared to the shorter 0.2 μm samples.

6 Development of a coarse-grained potential for metals

6.1 Introduction

Metallurgy, the study of metals and alloys, is one of the fundamental domains of materials science and engineering, and numerous books are devoted to this subject, *e.g.* [193-195]. Computer modeling is an important way to gain sophisticated understanding of how metallic materials behave, especially under extreme conditions such as short-pulsed laser processing [196] and the growth of films by high energy cluster deposition [197]. The Molecular Dynamics (MD) simulation method (see section 2.1) is the most commonly used method to provide atomistic insight into the behavior of metals and alloys. However, classical MD does not explicitly account for any electronic structure or properties, and metallic bonding cannot be represented by a simple two body “pair” potential such as the ubiquitous Lennard-Jones potential [35, 81], due to the complexities that arise from the environment sensitive electronic structure of metals and the need to account for the directional nature of the bond. In addition, pair potentials overestimate the vacancy formation energy for metals, underestimate the ratio between cohesive energy and melting temperature, and cannot describe properly reproduce their elastic constants.

The embedded atom method (EAM), first proposed by Daw and Baskes [198], addresses some of the inherent limitations with the pair potential, and has become a popular way to approximate metallic bonding in MD simulations. Conceptually, the local environment of the metal atom must be considered so that the dependence of the strength of individual bonds can be accurately determined.

Functionally, the interaction for an atom i is expressed in the EAM by two terms as in equation (6.1)

$$E_i = F_i(\rho_i) + \frac{1}{2} \sum_{j \neq i} \phi_{ij}(r_{ij}) \quad (6.1)$$

The first term is the “embedding” energy, and is the energy associated with placing an atom in the electron environment described by local electron density, ρ_i , calculated by

$$\rho_i = \sum_{j \neq i} f_j(r_{ij}) \quad (6.2)$$

where f_j is a function that describes the contribution to the electronic density at the site of atom i from all atoms j . Hence, the sum over function f_j is the measure of the local density. The next term in equation (6.1) comes from the electrostatic contributions, and is the sum of all pairwise potential, ϕ_{ij} , interactions from the j neighbors of atom i . The total energy of the system is simply the summation of the atomic energies,

$$E_{tot} = \sum_i E_i \quad (6.3)$$

The functional forms of f and ϕ can take on different forms depending on the way they are determined. For instance, the functions can be derived from *ab-initio* calculations or from empirical fitting to data, although the results are usually very similar. In any case, the primary advantage of EAM is its ability to describe the variation of bond strength with coordination. When coordination around an atom increases the strength of its individual bonds is mitigated, and in essence, the EAM is an environment dependent pair potential. However, due to the lack of three-body terms to account for the angular dependence of interaction energy, any covalent effects need to be specially accounted for. An extended version of the EAM by Johnson [199] includes a description of an angular dependence of the electron density function ρ to account for local symmetries in interatomic bonding, and is commonly used for FCC metals. Additional extensions by Johnson and coworkers exist for representing HPC [200] and BCC [201] metals.

Although the EAM has been widely used to represent metals on the atomic level, a coarse-grained description of metals has only recently become available [202]. The subject of chapter 7 is on the ballistic impact of Pt nanoparticles on CNT films, and a Pt nanoparticle even 50 nm in diameter consists of over 4 million atoms. Hence, in simulating the impact of these nanoparticles on CNT films, the metallic particle quickly becomes the dominant factor in the computational cost of the simulation, and therefore a coarse-grained representation of metals is required. The coarse-graining of CNTs has already been discussed in chapter 2, and the rest of this chapter is devoted to the coarse-grained representation of metals. In section 6.2, an existing mesoscale model for metals is described. Limitations of this model are then discussed, and modifications necessary for the simulation of metals under conditions of dynamic loading are reported in section 6.3.

6.2 Quasi-coarse-grained dynamics

An early model for the coarse-grained (CG) representation of metals was developed by Dongare [202]. Termed quasi-coarse-grained dynamics (QCGD), the model extends the EAM to the mesoscale, retaining the advantage of a particle based representation while reducing the cost of simulations. The fundamental assumption of the QCGD method is that every atom within a set in a given volume has the same dynamics. This set of atoms, then, can be represented by a single CG unit or particle. QCGD follows the following formulation: (1) Choose representative atoms (*R*-atoms) from an atomic scale microstructure to reduce the number of atoms being modelled in the system, (2) retain the energetics for the *R*-atoms as would be predicted in MD simulations, and (3) scale the energetics as well as the atomic-scale degrees of freedom of the *R*-atoms to define the energetics of the whole system.

6.2.1 Choosing representative atoms

Appropriate selection of *R*-atoms (*i.e.* the CG units) is crucial for accurate reproduction of the mechanical and thermodynamic properties of the material. Hence, the *R*-atoms are chosen so that they have the same energy and force values as they would have in the MD simulations. For example, the $2 \times 2 \times 2$ atomic unit cell for an FCC lattice is shown in Figure 6.1a. The equilibrium crystalline structure of a material is its thermodynamically stable state, where the positions of atoms in relation to each other is defined. Consequently, a random placement of *R*-atoms would not reproduce the energetics of an atomistic system. Rather, the CG particles need to take on the same general atomistic arrangement, but with their distances between neighbors scaled. With a given crystal structure of a metal, the placement of the *R*-atoms follows naturally. In Figure 6.1b, four *R*-atoms are chosen to form on CG unit cell of the FCC lattice. Note that the structure of the atoms in Figure 6.1a and the *R*-atoms in Figure 6.1b is identical.

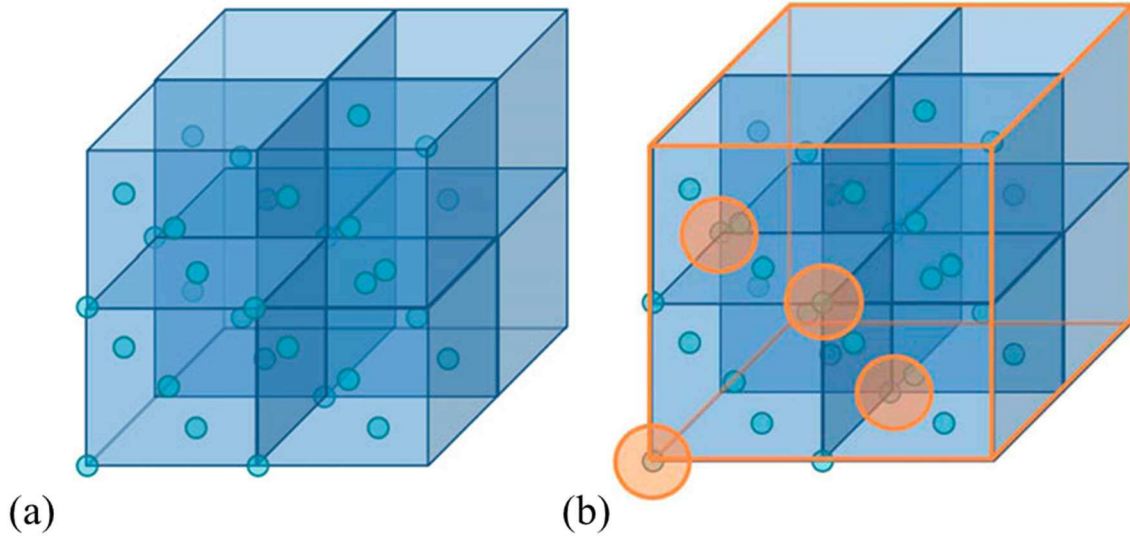


Figure 6.1: (a) A $2 \times 2 \times 2$ unit cell atomistic system (atoms shown by blue circles) and (b) the corresponding representation of the QCGD system (CG particles shown by orange circles at their locations). Taken from ref [202].

6.2.2 Interaction between the R -atoms

Interaction between the R -atoms should preserve the energetics of an analogous atomistic system. The interaction energy between atoms is calculated by the EAM (see equation (6.1)). The QCGD model scales the distance between R -atoms r_{ij}^R by a distance scaling parameter A_{cg} to retain the energy and force values that would be predicted for an atomistic system by modifying equation (6.1) such that

$$E_i^R = F_i \left[\sum_{j \neq i} f_j \left(\frac{r_{ij}^R}{A_{cg}} \right) \right] + \frac{1}{2} \sum_{j \neq i} \phi_{ij} \left(\frac{r_{ij}^R}{A_{cg}} \right) \quad (6.4)$$

For a representation of $n \times n \times n$ unit cells of an atomic system by one CG cell, the parameter A_{cg} is set to be equal to the number of unit cells n represented in each direction, and is equivalent to the cubed root of the number of atoms represented by one R -atom for FCC metals. In the case of Figure 6.1b, $A_{cg} = 2$, and 1 R -atom represents 8 atoms. Hence, the interaction between R -atoms described by equation (6.3) is essential identical to the EAM formulation, save for a distance

scaling parameter. The velocities and kinetic energies of the R -atoms are calculated the same way that as in atomistic MD, and the atomic-level stress tensor for an R -atom is calculated as

$$\sigma_{\alpha\beta}^R(i) = -\frac{1}{\Omega_0} \left[\frac{1}{2} \sum_j F_{ij}^\alpha \left(\frac{r_{ij}^\beta}{A_{cg}} \right) + m_i^R v_i^{R\alpha} v_i^{R\beta} \right] \quad (6.5)$$

where α and β represent the Cartesian components, Ω_0 is the atomic volume of the R -atom, F_{ij} is the force on atom i due to atom j , m_i^R is the mass of the R -atom i , and v_i^R is its velocity.

6.2.3 Energy scaling of R -atoms

In order to reproduce the energetics of the atomistic metal, the energies of the R -atoms need to be scaled to account for all of the atoms represented by these CG units. The energy scaling parameter is $N_{cg} = n \times n \times n$ where $n \times n \times n$ unit cells of the atomic system represented by one CG unit cell. Thus, the potential energy of the CG system for N_R R -atoms is

$$PE^{QCGD} = \sum_{i=1}^{N_R} N_{cg} E_i^R \quad (6.6)$$

and the kinetic energy of the system is

$$KE^{QCGD} = \frac{1}{2} \sum_{i=1}^{N_R} N_{cg} m_i^R (v_i^R)^2 \quad (6.7)$$

The temperature of the CG system is calculated as

$$T = \frac{2}{(N_f^{QCGD}) k_B} KE^{QCGD} = \frac{1}{(N_{cg} N_f^R) k_B} \sum_{i=1}^{N_R} N_{cg} m_i^R (v_i^R)^2 \quad (6.8)$$

Here, N_f^{QCGD} is the number of degrees of freedom for the CG system, which is equal to $N_f^{QCGD} = N_{cg} N_f^R$, where N_f^R is the number of degrees of freedom for an R -atom, and k_B is the Boltzmann constant equal to 8.617×10^{-5} eV/K. The scaling relations for energy and temperature ensure

that the prediction of the mechanical and thermodynamic properties of the CG system are the same as would be predicted for an atomistic system.

6.3 Modification of the QCGD model

The QCGD model in its original form [202] suffers from two major limitations making it unsuitable for simulations of high velocity impact of metal nanoparticles. One issue, common to any coarse-grained description of a material, is that the number of degrees of freedom is reduced, and therefore the heat capacity of the system is underestimated. Under conditions where local thermal equilibrium (*i.e.* equipartition of thermal energy among the collective dynamic degrees of freedom that are explicitly represented in the model and the internal, atomistic degrees that are not present in the coarse-grained description of the material) can be assumed, thermostats (*e.g.* ref [88]) can be used to globally control temperature within the system. However, the assumption of local thermal equilibrium does not always hold, as in the case of localized deformation of metallic nanoparticles during high velocity impact (see section 6.3.4). Under conditions of thermal non-equilibrium, the energy transfer to the missing degrees of freedom becomes important. A general solution to this problem comes from representing the missing atomistic degrees of freedom with internal “heat bath” variables. Indeed, this approach has been used for coarse-grained CNTs [77], outlined in section 2.4, and is described for the QCGD model in sections 6.3.1 and 6.3.2. Then, in section 6.3.3 an additional term for the scaling of forces is added to the QCGD model in order to ensure the reproduction of atomistic thermophysical properties. Finally, the modified QCGD model is tested against atomistic simulations for the deformation of high velocity impact of nanoparticles against a rigid surface in section 6.3.4.

6.3.1 Formulation of heat bath for QCGD model

The CG representation of a set of atoms results in the underestimation of the system’s heat capacity due to the reduction in the number of explicit degrees of freedom. These missing degrees of freedom can be implicitly modeled by a heat bath variables [77, 91]. Then, the energy exchange between the dynamic degrees of freedom explicitly represented in the CG model and the missing degrees of freedom represented by the heat bath can be defined. The technical details of this approach are described in the remainder of this section.

The heat capacity of the degrees of freedom not explicitly present in the QCGD model is equal to the heat capacity of the heat bath C^{HB} , where

$$C^{HB} = C^{exp} - C^{TR} \quad (6.9)$$

Here, C^{exp} is the experimentally determined heat capacity of the metal and C^{TR} represents the heat capacity due to the translation degrees of freedom explicitly present in the QCGD model. Pt is chosen as the metal for the impact simulation of chapter 7, and it has a heat capacity of 25.86 J/(mol K) [203]. Therefore, the heat capacity per Pt R -atom can be equivalently expressed as $2.62 \times 10^{-4} \times N_{cg} \frac{eV}{K}$. Each R -atom has 3 translation degrees of freedom, and hence $C^{TR} = 3k_B = 2.59 \times \frac{10^{-4} eV}{K}$. Therefore, $C^{HB} = (2.62N_{cg} - 2.59) \times 10^{-4} \frac{eV}{K}$.

The rate of energy exchange between the translation and heat bath degrees of freedom is defined by the approach outlined by Ivanov and Zhigilei [91]. First, the temperatures of both the heat bath and the CG particles must be known to calculate how much energy should be transferred from one mode of energy to the other. The temperature due to the translational degrees of freedom of an R -atom, T_i^{TR} , is calculated by averaging the thermal energy, K_j^T for all neighboring particles (for a total of N particles) and dividing by translational degrees of freedom,

$$T_i^{TR} = \frac{2 \sum_{j=1}^N K_j^T}{3Nk_B} \quad (6.10)$$

where $K_j^T = \frac{1}{2} m_i^R (\mathbf{v}_i^T)^2$. Here \mathbf{v}_i^T is the thermal velocity of the particle i , is given by

$$\mathbf{v}_i^T = \mathbf{v}_i - \mathbf{v}^c \quad (6.11)$$

where, \mathbf{v}_i is the total velocity of particle i and \mathbf{v}^c is its center of mass velocity. For an R -atom with a given heat bath temperature T_i^{HB} , the energy exchange between its heat bath and translation energy over time t is described by two coupled differential equations,

$$\begin{aligned} C^{TR} \frac{dT_i^{TR}}{dt} &= A(T_i^{HB} - T_i^{TR}) \\ C^{HB} \frac{dT_i^{HB}}{dt} &= -A(T_i^{HB} - T_i^{TR}) \end{aligned} \quad (6.12)$$

where A is a constant. The first equation in (6.12) describes the energy change of the translation degrees of freedom, and the second equation describes the analogous transfer for the heat bath. The two equations in (6.12) can be combined as

$$\frac{d\Delta T}{dt} = -A \Delta T \left(\frac{C^{TR} + C^{HB}}{C^{TR} C^{HB}} \right) \quad (6.13)$$

where $\Delta T = T_i^{HB} - T_i^{TR}$ is the temperature difference between the heat bath and the translational degrees of freedom. Solving equation (6.13) for ΔT reveals an exponential decay with time.

$$\Delta T = \exp\left(-\frac{t}{\tau}\right) \quad (6.14)$$

Here, the time constant τ is a characteristic time of energy exchange between the heat bath and the translational degrees of freedom. It is system dependent and will be determined in section 6.3.2. In terms of the constant A , τ is expressed as

$$\tau = \frac{1}{A \times \left(\frac{C^{TR} + C^{HB}}{C^{TR} C^{HB}} \right)} \quad (6.15)$$

Then, solving equation (6.15) for the constant A yields

$$A = \frac{C^{HB} C^{TR}}{C^{HB} + C^{TR}} \times \frac{1}{\tau} \quad (6.16)$$

The energy transferred from the heat bath to the thermal motion of the system during a simulation time step is derived from equation (6.12) as

$$\Delta E_i = \Delta E_{HB \rightarrow TR} = A(T_i^{HB} - T_i^{TR})\Delta t \quad (6.17)$$

Under the condition that energy is conserved, an equal amount of energy must be removed from the thermal motion of the R -atom. To do this, a frictional dampening force is applied to the particle,

$F_f = \varepsilon m_i \mathbf{v}_i^T$, with the scaling parameter ε ensuring energy conservation. Therefore, the equation of motion for the R -atoms is defined as

$$m_i \frac{d^2 \mathbf{r}_i}{dt^2} = \mathbf{F}_i + \varepsilon m_i \mathbf{v}_i^T \quad (6.18)$$

where \mathbf{r}_i is the position of particle i , m_i is its mass, and \mathbf{F}_i is the force acting upon it.

Determining the value of ε is done by equating the change in thermal energy of the system to the energy change of the heat bath.

$$\frac{d}{dt} K^T = \frac{d}{dt} \sum_i \frac{m_i (\mathbf{v}_i^T)^2}{2} = \sum_i m_i \mathbf{v}_i^T \frac{d\mathbf{v}_i^T}{dt} = \sum_i m_i \mathbf{v}_i^T \frac{d\mathbf{v}_i}{dt} - \sum_i m_i \mathbf{v}_i^T \frac{d\mathbf{v}^c}{dt} \quad (6.19)$$

The random direction of the thermal velocities means that for a sufficiently large number of neighbor particles the last term in the equation may be neglected. Substituting equation (6.18) into equation (6.19) gives the expression

$$\frac{d}{dt} K^T = \sum_i m_i \mathbf{v}_i^T \frac{d\mathbf{v}_i}{dt} = \sum_i \mathbf{v}_i^T (\mathbf{F}_i + \varepsilon m_i \mathbf{v}_i^T) = \sum_i \mathbf{v}_i^T \mathbf{F}_i + \varepsilon \sum_i m_i (\mathbf{v}_i^T)^2 \quad (6.20)$$

Then, equating equations (6.17) and (6.20) results in

$$\sum_i \mathbf{v}_i^T \mathbf{F}_i + \varepsilon \sum_i m_i (\mathbf{v}_i^T)^2 = A(T_i^{HB} - T_i^{TR}) \quad (6.21)$$

and finally solving for ε

$$\varepsilon = \frac{A(T_i^{HB} - T_i^{TR})}{\sum_i m_i (\mathbf{v}_i^T)^2} - \frac{\sum_i \mathbf{v}_i^T \mathbf{F}_i}{\sum_i m_i (\mathbf{v}_i^T)^2} \quad (6.22)$$

The second term in equation (6.22) comes from the constraint on the thermal energy, and is not involved in the coupling of energy between the heat bath and the dynamic degrees of freedom. It

prevents temperature fluctuations, and is actually used in thermostat methods. However, in this case we do not want to prevent these fluctuations, and hence the term is omitted, so that

$$\varepsilon = \frac{A(T_i^{HB} - T_i^{TR})}{\sum_i m_i (\mathbf{v}_i^T)^2} = \frac{A(T_i^{HB} - T_i^{TR})}{2K^T} = \frac{\Delta E_i / \Delta t}{3k_B T^{TR}} \quad (6.23)$$

With the calculation of the energy transferred to the heat bath and the dampening of the thermal motion of the R -atoms, the heat bath temperature is updated as

$$T_{HB}(i) = T_{HB}(i) - \Delta E_i / C_{HB}^i \quad (6.24)$$

6.3.2 Determination of coupling constant τ

The coupling constant τ (see equation (6.15)) governing the rate of energy transfer between the heat bath and the translational degrees of freedom can be determined either from empirical fitting or by simulation. In general, the value of τ must be separately determined for each level of coarse-graining and for each type of metal. In this section, the procedure to find τ by MD simulations for Pt is described.

A series of MD simulations using the Johnson EAM potential for FCC metals [199] were used to determine τ for four levels of coarse-graining. A cubic system with periodic boundary conditions in all directions was split into sets of atoms corresponding to the number of atoms per one R -atom. Every atom within a particular set was initially given the same velocity vector, with the average thermal temperature of the entire system corresponding to 300 K. The system was then allowed to thermalize under constant energy, as schematically shown in Figure 6.2.

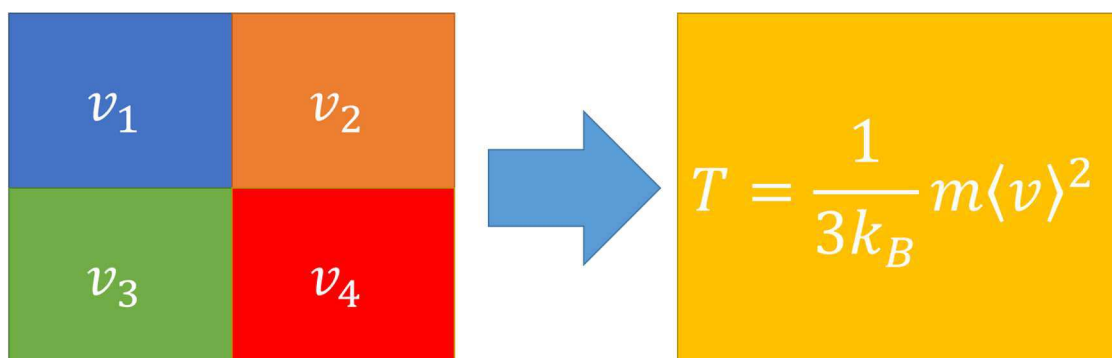


Figure 6.2: Schematic of the approach used to determine the time constant, τ . Localized groups of atoms are initially assigned the same velocity vector and then are allowed to equilibrate. The amount of time this process takes allows for the determination of τ .

This procedure was repeated for four levels of coarse-graining; where 1 R -atom represents 8 atoms, 64 atoms, 216 atoms, and 512 atoms. The temperature evolution for each simulation is shown in Figure 6.3. In each case thermalization of the system occurs within 1 ps. The rapid thermal relaxation of the system is reasonable because it occurs at the speed of sound within a material, which for Pt is 2,800 m/s [203]. Therefore, the value of τ is set so that relaxation occurs at 1 ps for coarse-graining levels between 8-512 atoms per R -atom.

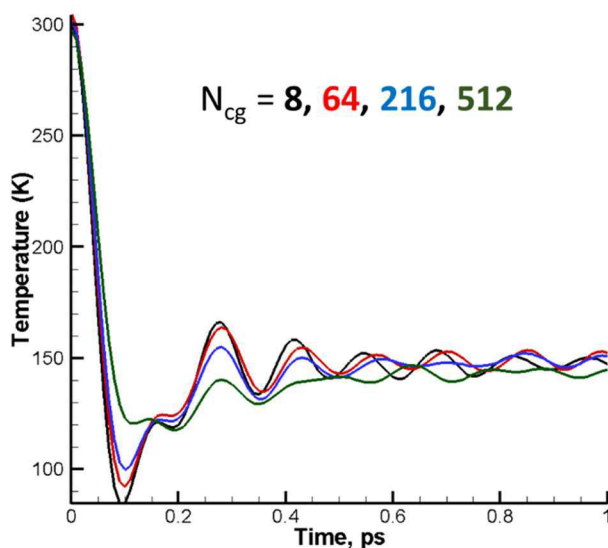


Figure 6.3: Thermalization in atomistic systems where localized groups of atoms consisting of either 8, 64, 216, or 512 members are initially given the same velocity vector.

6.3.3 Force scaling

The QCGD method preserves the forces on the R -atoms that would be calculated with the atomistic EAM potential, and scales the energies of each R -atom according to the number of atoms represented by a CG unit according to equations (6.6) and (6.7). However, the model fails to preserve the atomistic interaction energy per unit volume. An R -atom represents N_{cg} atoms and occupies a volume of N_{cg} atoms, but interacts with neighbor R -atoms through the original atomistic EAM potential with only distances scaled. Therefore, each R -atom is tied to its neighbors by the equivalent force binding individual atoms, and hence the thermophysical properties of a QCGD metal will be underestimated. To remedy this problem, a simple scaling of forces using the interaction energy defined by equation (6.6) must be performed as in

$$F = -\vec{\nabla}PE^{QCGD} \quad (6.25)$$

to ensure that the thermophysical properties of the atomic system are retained in the coarse-grained representation.

6.3.4 Testing of modified QCGD model

Both the original QCGD model and the QCGD model with the additions of the heat bath and force scaling term were tested by comparing the results of the collisions of spherical nanoparticles on a rigid surface. The results of the first set of tests are shown in Figure 6.4, where Pt spheres ($d=6$ nm) represented atomistic ally and for three levels of coarse-graining were collided with a rigid surface with an initial velocity of 100 m/s under the condition of constant energy. Snapshots showing the structure of the sphere before and after collision reveal that at $N_{cg} = 64$ the sphere clearly deforms and that at $N_{cg} = 216$ the sphere disintegrates, in contrast to the atomistic representation where no discernable plastic deformation occurs. Furthermore, although no significant deformation occurs for at $N_{cg} = 8$, the average velocity of the reflecting sphere is 41% lower than for the atomistic case, indicating that center of mass motion is artificially redistributed to the thermal energy of the projectile. Therefore, the QCGD model, even at low levels of coarse graining is inadequate for non-thermal equilibrium conditions.

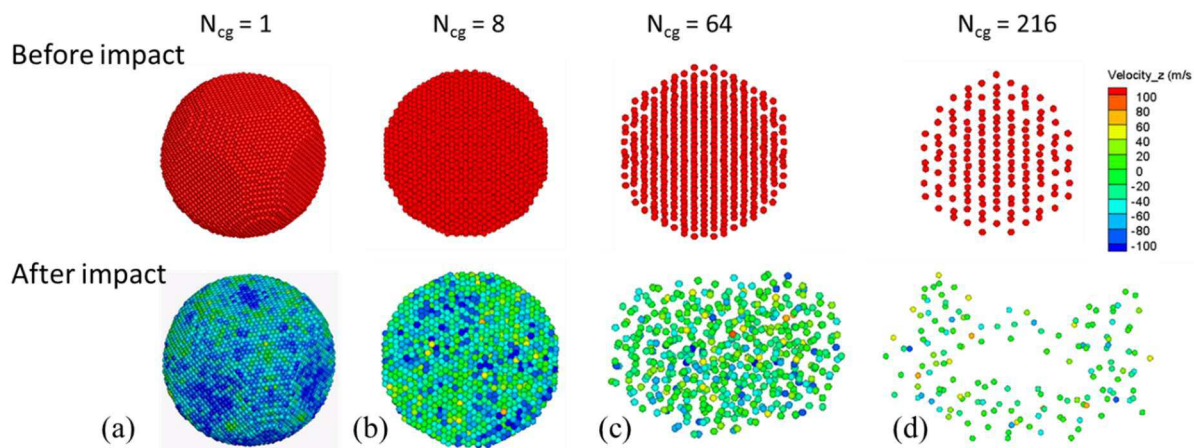


Figure 6.4: Snapshots of Pt sphere ($d=6$ nm) before and after collision at 100 m/s with rigid surface for atomistic representation (a), $N_{cg} = 8$ (b), $N_{cg} = 64$ (c), and $N_{cg} = 216$ (d) with the original QCGD model.

To validate the modifications made to the QCGD model, another series of simulations using the modifications made to the QCGD model (*i.e.* addition of heat bath and scaling of forces) was run. A comparison of the modified QCGD model to the atomistic case is shown in Figure 6.5, where the deformation to a Pt sphere ($d=20$ nm) is shown in snapshots before and after collision with a rigid surface. With the modified potential, the CG projectile responds very similarly to the collision as the atomistic projectile. At an initial velocity of 100 m/s, both the atomistic and coarse-grained projectiles remain intact and retain $\sim 80\%$ of their center of mass velocity. However, at 1,000 m/s, the projectiles break apart. Although only results for $N_{cg} = 128$ are shown in Figure 6.5, the modified QCGD model works similarly well even at $N_{cg} = 512$.

Although the modified QCGD method has been successfully applied for levels of coarse-graining up to $N_{cg} = 512$, caution must be exercised when considering very highly coarsened representations. In the extreme example where one R -atom represents the entire system, no deformation can occur and the metal is infinitely rigid. Highly coarse-grained metals are likewise become artificially stiff as the force needed to move the R -atoms in a system scales with N_{cg} . Therefore, the level of coarse-graining should be limited so that realistic behavior is still observed.

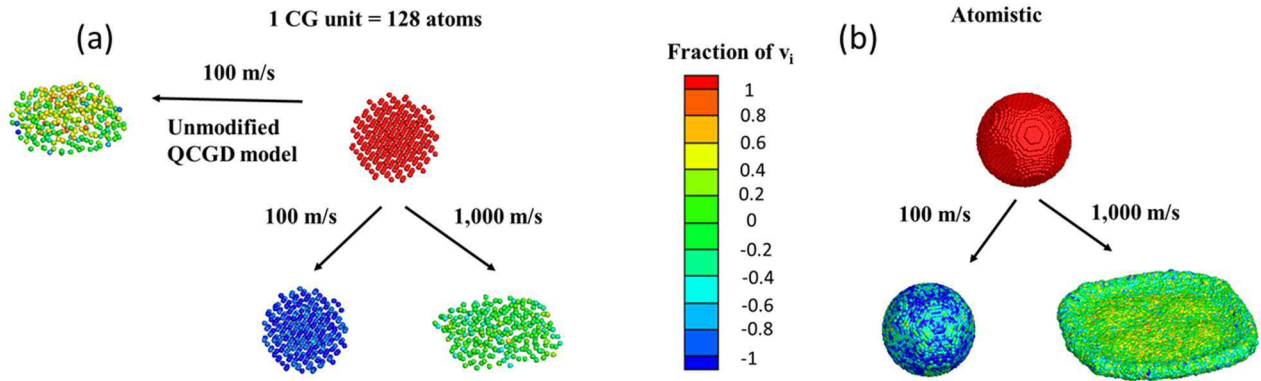


Figure 6.5: Snapshots of Pt sphere ($d=20$ nm) before and after collision with a rigid surface for the case where $N_{cg} = 128$ with the modified QCGD model (a) and the atomistic representation (b). Collisions are shown for initial velocities of 100 and 1,000 m/s. For (a) an additional snapshot shows the deformation to the CG metal after collision at 100 m/s using the original QCGD model.

6.4 Metal-CNT interaction

The modified QCGD potential for coarse-grained metals is suitable for the general modeling of metallic materials, even when local thermal equilibrium cannot be assumed. However, many systems will not be purely metallic, where the interaction between the metal R -atoms and other non-metallic materials needs to be considered. In this section, the potential between the coarse-grained CNT segments of the mesoscopic model (see chapter 2) and the coarse-grained metal R -atoms is described.

Nonbonded interactions are well described by the Lennard Jones pair potential [81]

$$\phi(r) = 4\epsilon \left[\left(\frac{\sigma}{r} \right)^{12} - \left(\frac{\sigma}{r} \right)^6 \right] \quad (6.26)$$

where r is the distance between two interaction particles, ϵ is the interaction energy at equilibrium separation of the two particles (*i.e.* depth of energy well), and σ is the finite distance at which the inter-particle potential is zero. The parameter σ is related to the equilibrium separation distance by $r_{eq} = 2^{\frac{1}{6}}\sigma$. The appropriate values for the two Lennard Jones parameters were determined from the density functional theory (DFT) calculations for a sheet of Pt interacting with graphene where the average binding energy for the Pt-C interaction is determined to be -0.238 eV with an

equilibrium distance of 0.33 nm [204]. The Lennard Jones pair potential exists between every R -atom and CNT node within the cutoff distance of 2.5σ .

Although the values obtained for the Lennard Jones parameters come from atomistic level calculations, they are unmodified for the coarse-grained description of the R -atoms with the CNTs due to the assumption that only the interaction between surface of the metal and the CNT is important. Therefore, even when an R -atom represents many atoms, the interaction with the CNT nodes is assumed to occur with only the surface atoms, and hence the parameters derived for the atomistic system are still assumed valid for the coarse-grained system. However, since the radius of the R -atom increase, it can interact with a greater number of CNT nodes.

7 Ballistic impact resistance of CNT films

7.1 Introduction

Protection from ballistic impact has been a longstanding concern in military and police operations. Vehicles are most commonly armored with metals such as steel, aluminum, and titanium, and personnel typically wear vests made of ceramics or textiles. More recently, the increasing reliance on satellite technology, the continuation of space exploration by National Aeronautics and Space Administration (NASA) and the emergence of personal space travel and payload delivery into orbit by enterprises such as the Space Exploration Technologies Corp. (SpaceX) [205] have promoted the development of lightweight impact resistance materials to protect from the hypervelocity collisions with space debris or micrometeorites in Earth's lower orbit. Conventional armor materials are oftentimes too heavy to be economically used as ballistic shielding on space vehicles. According to NASA, the cost of putting a pound of material into Earth's orbit was ten thousand dollars in 2008 [206]. Although reductions in cost are anticipated over the next ten years, the development of lightweight aerospace materials is still paramount for making transportation to Earth's orbit and beyond economical.

Carbon nanotube (CNT) materials and composites make promising candidates for low density, mechanical strong and resilient ballistic resistant shielding, and have been studied for their applicability for aerospace and defense applications [144, 145, 207-211]. Computer simulation is a particularly valuable tool for studying high speed deformation of both the CNT material and the projectile. Aside from the ability to prepare the system exactly to ensure reproducibility, the deformation mechanisms and channels of energy dissipation are completely accounted for by the output of the simulations, something which is not readily attainable in experimental studies.

Recent work done at Oak Ridge National Laboratory (ORNL) has demonstrated the promise of VACNT arrays as absorbing material [212], highlighting the application of CNT materials as a characterization method. The experiment performed at ORNL is summarized in Figure 7.1a, showing an image intensified charge coupled device (ICCD) images of a Pt ablation plume impacting a fused silica substrate and another substrate covered by VACNTs. The plume is reflected off of the silica substrate but is completely absorbed by the CNTs. Moreover, after characterization, the Pt nanoparticles were found to have punctured through the VACNT forest (Figure 7.1b) and become caught in its networked structure (Figure 7.1c). Knowing the

relationship between nanoparticle size, velocity, and density and the penetration depth into the VACNT forest could serve as the basis of a method for the characterization of metallic plumes generated by laser ablation.

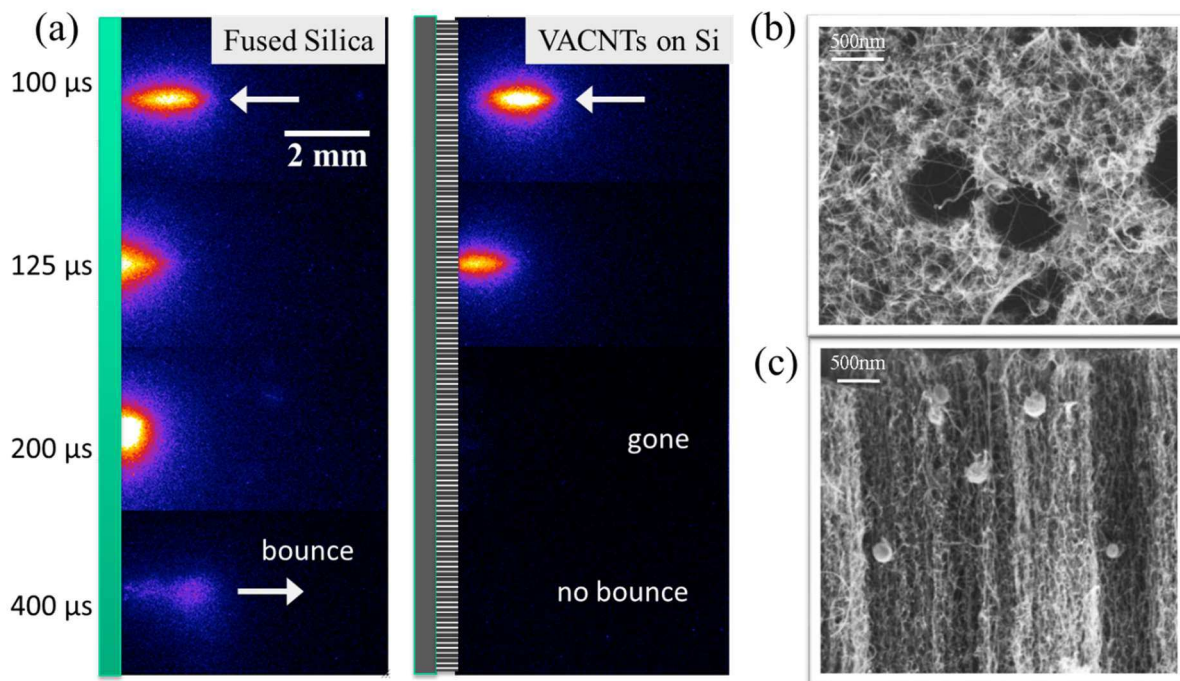


Figure 7.1: Image intensified charge coupled device (ICCD) images of blackbody emission from plumes generated in short pulse laser ablation of a 20 nm thick Pt film and impinging on a fused silica (a) and vertically-aligned CNT forest (b). SEM images of cleaved CNT forest with trapped nanoparticles implanted from the ablation plume are shown in (c). Unpublished results by Christopher Rouleau, Alex Puretzky, and David Geohegan, ORNL (shown with permission from the authors) [212].

In this chapter, simulations of a Pt nanoparticle impacting CNT thin films are used to estimate the penetration depth of a projectile into a film as a function of initial projectile velocity and the thickness of the CNT film. Section 7.2 describes the structural characteristics of the CNT films as well as the coarse-grained. In section 7.3 an analytical expression for the estimated penetration depth as a function of initial projectile velocity is determined, and the results of the simulated impact of a nanoparticle onto CNT films is reported in section 7.4. The results of this work are then summarized in section 7.5.

7.2 CNT films and metal projectile

7.2.1 CNT films

Two *in silico* CNT films were prepared using the tubular mesoscopic model described in chapter 2 (see Figure 7.2) to serve as the targets for impact with a nanoparticle projectile. Both films have a density of 0.2 g/cm^3 and consist of 200 nm long (10,10) single-walled carbon nanotubes (SWCNTs). The preparation of the samples was done by first randomly distributing full length CNTs laterally in a series of layers. CNTs will be added to each layer until the desired density is attained with the condition that no CNTs are at any point closer than 3.14 \AA to one another. The process is repeated for the number of layers corresponding to the desired thickness of the film. Once the film has been generated, a two-stage process of annealing (similar to the one described for VACNT forests in section 3.2) is performed to allow the CNTs to self-organize into a highly networked structure. Periodic boundary conditions are enforced in both lateral directions whereas free boundary conditions exist along the film thickness. During the first stage of the annealing process, the CNTs in the film are heated to 10,000 K, and two pistons, one at either side of the CNT film, with purely repulsive interaction potential ensure that the film maintains a relatively flat surface. After 1 ns of the high temperature stage, the film is quenched to 300 K and allowed to structurally relax for another ns while still using the pistons to maintain its shape. Finally, the pistons are removed and the film is allowed to relax until a metastable configuration, defined as a state where the rate of change in the inter-tube interaction energy slows down to a level below 0.05% per ns, is reached.

7.2.2 Pt nanoparticle

A spherical Pt nanoparticle with a diameter of 50 nm is used as the projectile for all simulations discussed herein and is shown in Figure 7.3. The 50 nm diameter allows the projectile to avoid most of the pores in generated CNT films and is small enough so that any effect from the film not immediately adjacent to the site of impact can be observed. The Pt particle is represented by the modified QCGD approach detailed in chapter 6 using the Johnson EAM potential for FCC metals [199]. It consists of 20,004 coarse-grained (CG) particles, each representing 216 atoms.

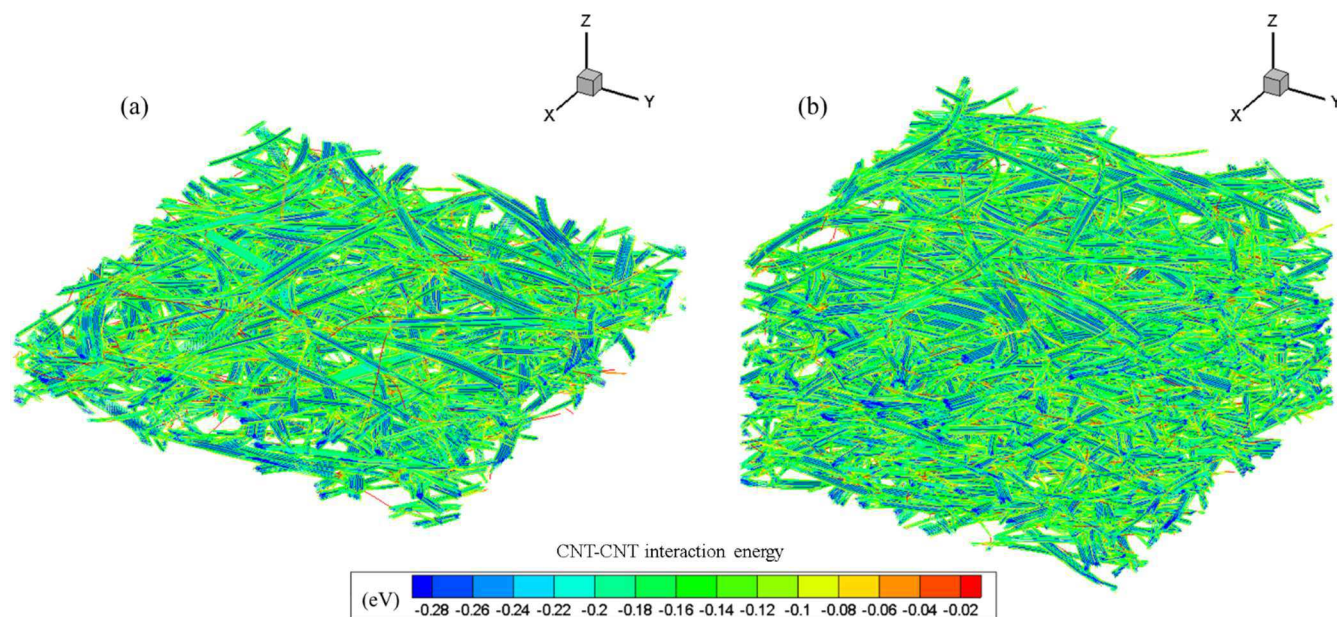


Figure 7.2: Snapshots of CNT films with lateral dimensions of $500 \times 500 \text{ nm}^2$ and thicknesses of (a) 100 nm and (b) 300 nm. Each film has a density of 0.2 g/cm^3 and consists of 200 nm long CNTs. CNT coloring is by interaction energy where blue coloring indicates low (negative) energy and red indicates high energy.

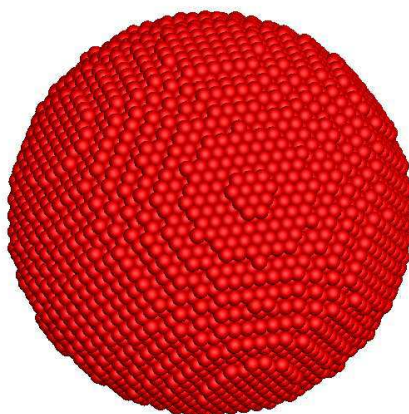


Figure 7.3: Snapshot of spherical Pt nanoparticle represented by the modified QCGD model. The particle consists of 20,004 CG units each representing 216 atoms.

7.3 Analytical determination of projectile penetration

The overarching objective of this work is to provide an analytical model describing the penetration depth of metal nanoparticles impacting CNT films. Mathematically, the change in kinetic energy (E_k) over length of material (z), or decelerating force (F_d), can be expressed as

$$F_d(E_k) = \frac{dE_k}{dz} \quad (7.1)$$

Rewriting equation (7.1) in terms of the material length yields

$$z = \int \frac{1}{F_d(E_k)} dE_k \quad (7.2)$$

Then, the theoretical penetration depth (z_p) of a projectile with an initial translational kinetic energy (E_k^{int}) into the material is

$$z_p = \int_{E_k^{int}}^0 \frac{1}{F_d(E_k)} dE_k \quad (7.3)$$

On the right hand side of equation (7.3), only deceleration force (F_d) is not known *a priori*, and is determined through a series of simulations discussed in section 7.4.

The penetration depth of a projectile into a material does not only depend on its initial velocity. Material properties will also play a large role. In particular, the highly entanglement network structure of CNT films should redistribute the kinetic energy of the projectile across a large area, thereby more effectively slowing down the projectile than in a material where interactions between structural constituents is short-ranged. In addition, the rearrangement of CNTs after impact may further contribute to arresting the projectile. An important question is whether the entangled network of CNTs can more efficiently limit the penetration of a projectile in a thicker film as compared to a series of thinner films (Figure 7.4), and will be discussed in the next section.

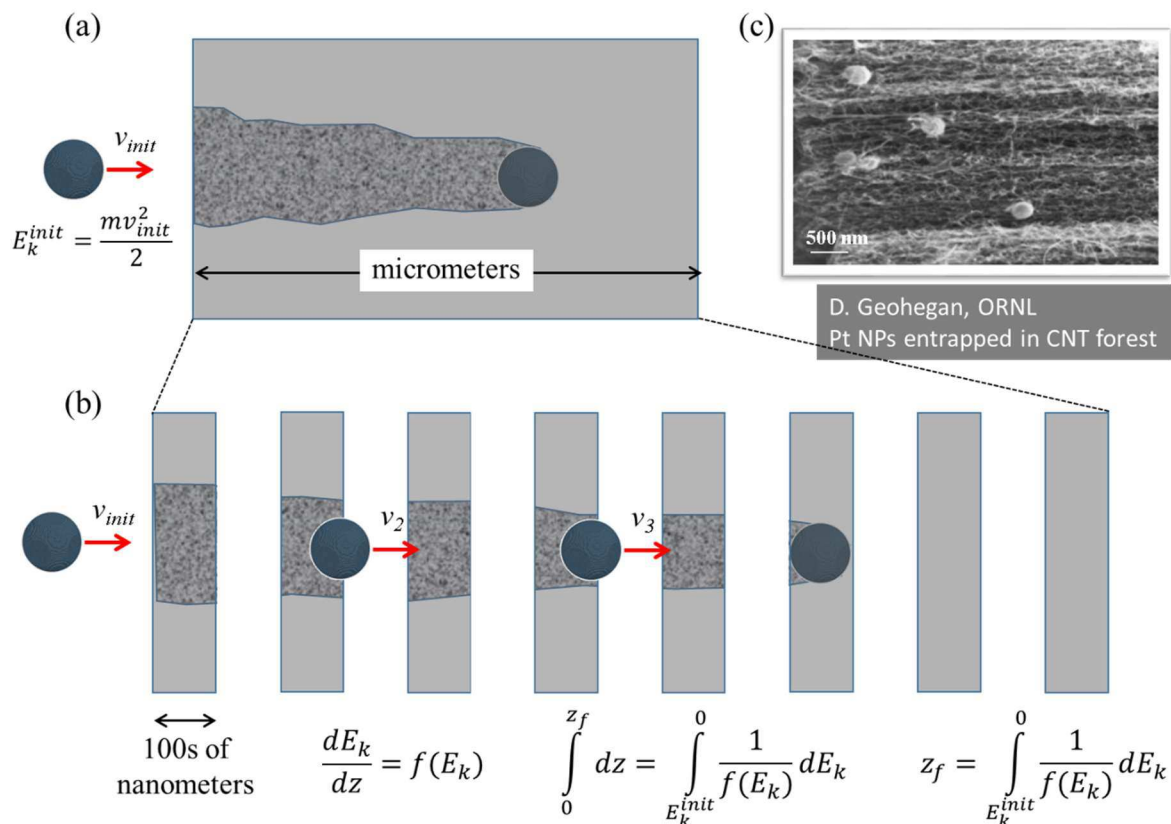


Figure 7.4: What role does the thickness of the CNT film play in arresting the projectile? Schematic visualization of the projectile penetration into a thick CNT film (a) and sequential penetration into multiple thinner films (b). A SEM micrograph of Pt nanoparticles trapped in a VACNT forest (c) [212].

7.4 Impact simulations

The assumption of local thermal equilibrium is difficult to justify under conditions of high velocity impact, and therefore accurately modeling the heat capacity of the material becomes important so that thermal kinetic energy does not become artificially high. Both the CNTs and the Pt nanoparticle are represented by CG models, and hence the number of degrees of freedom is significantly reduced for each of these materials. To account for the contribution to the heat capacity of the missing degrees of freedom not explicitly described in the CG models, a heat bath approach is used (see sections 2.4 and 6.3.1).

In the first set of simulations, the 100 nm thick CNT film (Figure 7.2a) was impacted by a Pt nanoparticle ($d=50$ nm) at five different velocities; 100, 300, 500, 1000, and 2000 m/s to

establish the deceleration force (F_d) as a function of the initial kinetic energy of the projectile (see equation (7.1)). The results are shown in Figure 7.5a, where horizontal axis is in units of velocity rather than kinetic energy for ease of interpretation. Here, the red curve represents the best fit for F_d assuming a quadratic dependence with initial velocity. From the fitted function, the estimated penetration depth of the projectile is calculated with equation (7.3) and plotted in Figure 7.5b. Note that although penetration depth increases with initial velocity, the curve begins to flatten at very high velocities. From a physical standpoint this result makes sense since CNTs will not have the time to deflect from the projectile at the small time scales present for extreme velocity impact. Even though the speed of sound within a CNT ($\sim 18,000$ m/s) dictates the transfer rate of energy along the CNT, transfer between CNTs is less efficient due to their relatively weak coupling via non-bonded interactions. Another consideration is the breaking up of the projectile during its collision with the film. However, although the CG representation of the projectile allows for its disintegration, only minimal, elastic deformation is observed even at 2000 m/s. In addition, the possibility of CNT fracture due to both bending and tensile deformation is included, but less than 1% of the CNTs undergo fracture even at an impact velocity of 2,000 m/s. All of the fracturing in this series of simulations is due only to CNT bending.

With the estimation of penetration depth for the 100 nm CNT film established, the next simulation run was for the projectile impacting the 300 nm thick CNT film (see Figure 7.2b) at a velocity of 1000 m/s. Assuming the same fitted trend of F_d obtained for the 100 nm films, the calculated penetration depth for the deceleration of the projectile was 448 nm, or about 50% more than the 300 nm the projectile actually propagated through. Therefore, the thicker film has significantly greater stopping power than a series of the thinner films.

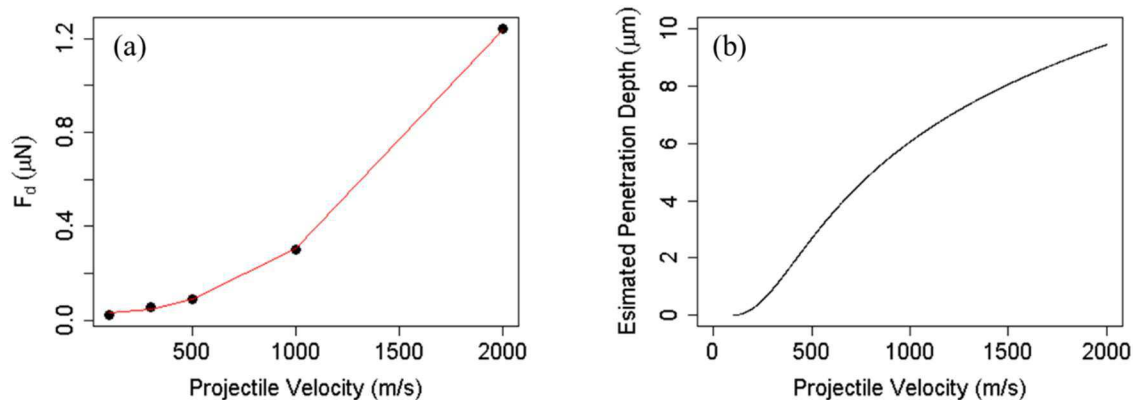


Figure 7.5: Deceleration force for the five impact simulations on 100 nm thick CNT film for initial projectile velocities of 100, 300, 500, 1000, and 2000 m/s (a). The red line represents the fitted curve through the series of points. Estimated projectile penetration depth as a function of initial velocity (b).

During the propagation of the projectile into the film the CNTs must undergo rearrangement as the nanoparticle pushes into the film. The reason that the thicker film can stop the projectile more efficiently than several thinner films is due to the entangled nature of the CNTs which allow for energy to be distributed over a large area. Figure 7.6 shows snapshots of the impact of a projectile with an initial velocity of 1000 m/s onto the 300 nm thick CNT film. The CNTs are colored by their local kinetic energies, and as the projectile makes its way through the film the kinetic energy increases over a larger area of the sample. Indeed, the structure of CNT bundles can be made out in Figure 7.6b,c from the coloring by energy, indicating that the thermalization progresses along channels where CNTs are more strongly in contact with one another. Furthermore, the projectile leaves an energy “wake”, implying that energy evolution is clearly occurring over time outward from the initial impact site. For the thicker film, a greater number of connections between CNTs and the larger number of CNT layers results in more friction as the projectile pushes through the material as compared to the thinner film. In addition, the deflected CNTs in the path of the projectile are increasingly likely to come into contact with more material as the projectile propagates through the film. In a thicker film, the greater accumulation of material in front of the projectile results in better stopping power as compared to the thinner CNT film. At relatively low densities of 0.2 g/cm^3 , the projectile does not push much material out of the film

(see Figure 7.6c). Instead, the CNTs are able to deflect from the path of the projectile, and at times the projectile comes into contacts with voids (as evidenced by Figure 7.7b).

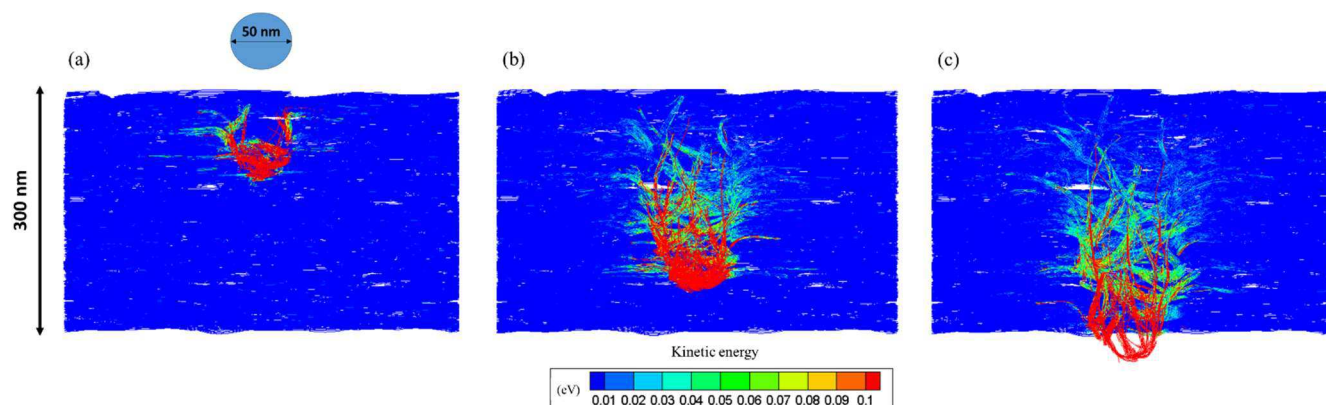


Figure 7.6: Snapshots of the impact of the 300 nm thick CNT film by a Pt projectile with initial velocity of 1000 m/s at times of $t=100$ ps (a), $t=250$ ps (b), and $t=350$ ps (c). The CNTs are colored by their local kinetic energies, and the projectile is blanked.

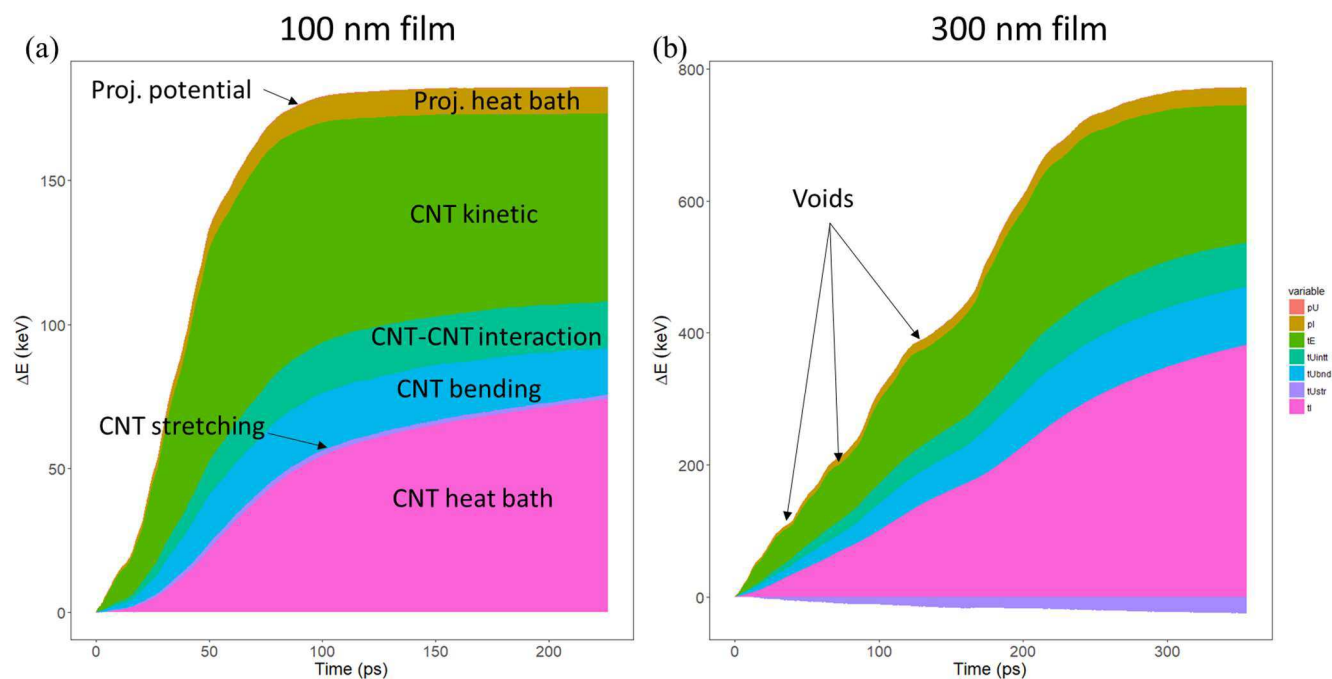


Figure 7.7: Comparison of the energy evolution, excluding the kinetic energy of the projectile, between projectile impact with the 100 nm thick film and the 300 nm thick film. The initial velocity of the projectile is 1000 m/s.

The changes in energy for the ballistic impact on the 100 and 300 nm thick CNT films is plotted in Figure 7.7. The large negative change in the kinetic energy of the projectile is omitted from these plots. For the 100 nm thick CNT film, the increase in CNT kinetic energy and heat bath energy make up the largest changes to the film's energy, where kinetic energy in this case includes both thermal and non-thermal contributions. Changes to the CNT-CNT interaction energy, CNT bending energy, and especially CNT stretching energy are less significant, implying that the reorganization of CNTs is not the primary form of energy dissipation in the system. The same trend holds in Figure 7.7b for the thicker CNT film. One notable feature for the thicker film is a series of undulations in the profile of the change in energies. When the change in energy flattens, the kinetic energy of the projectile does not change significantly, suggesting that a region of relative low density, or void, has been encountered. The density of the films is low enough where the presence of voids is not unusual, and indeed the presence of voids can be seen from Figure 7.2. Finally, note that the changes in energy have not leveled off completely by the end of the simulation, and if continued, energy would be exchanged among different modes. In particular, the heat bath energy would rise until the temperature of the internal degrees of freedom comes into thermal equilibrium with the dynamic degrees of freedom.

7.5 Summary

The first simulations of nanoparticle ballistic impact on CNT films using coarse-grained models for both the projectile and the CNTs were reported in this chapter. Both coarse-grained models made use of the heat bath approach to accurately account for the exchange of energy between the dynamic degrees of freedom explicitly accounted for, and internal degrees of freedom absent in the coarse-grained representations.

A series of impact simulations on a 100 nm CNT film elucidated the velocity dependent deceleration force of the projectile, used to estimate penetration depth. Using the fitted deceleration force obtained from this series of simulations overestimated the penetration depth of a projectile impacting a 300 nm thick film by 50%, indicating that penetration depth is dependent on film thickness.

8 Summary and future work

8.1 Summary of dissertation

Carbon nanotube (CNT) materials constitute a broad class of multifunctional hierarchical materials deriving their properties from the intimate connections between the atomistic structure of individual CNTs, the arrangements of CNTs into mesoscopic structural elements, such as CNT bundles and branching structures, and the structural organization of the mesoscopic elements into a macroscopic network. Due to their unique combination of structural (low density, high surface area, and nanoscale porosity), mechanical (high conformity, ability to support large reversible deformation, and absorb mechanical energy) and transport (thermal and electrical conductivity tunable over a broad range by structural modification) properties, CNT materials are attractive for a variety of applications. The strong structural sensitivity of the mechanical and thermal properties of CNT network materials makes it possible to tune the properties to the needs of practical applications, but also highlights the need for clear fundamental understanding of the structure-property relationships.

In this work, a computational model designed for realistic mesoscale simulation of CNT materials was used to determine the structure-property relationships in VACNT forest. In addition, the ballistic resistance of CNT films is discussed in the second part of this dissertation. The main conclusions from the dissertation are detailed below.

Structural self-organization of carbon nanotubes into vertically aligned arrays

An effective and flexible method for the generation of computational samples for mesoscopic modeling of anisotropic networks of CNT bundles with various degrees of CNT alignment is developed and applied for investigation of structural self-organization of nanotubes into vertically aligned CNT forests and fibers. Structural characteristics of the computational samples, such as bundle size distribution, average and maximum bundle sizes, magnitude of the Herman orientation factor, average tilt of CNT segments with respect to the direction of alignment, and average tortuosity of the nanotubes, are calculated and related to parameters of the sample preparation procedure. Good agreement between the computer-generated and experimentally-grown network structures is demonstrated, and several examples of the applications of the mesoscopic modeling for investigation of mechanical and thermal transport properties of the CNT materials are provided.

The high degree of control over the structure of computational samples, provided by the sample generation procedure, enables fine-tuning of the structural characteristics of *in silico* generated samples to match those to particular experimental materials, as well as an efficient exploration of the multidimensional space of structural parameters aimed at optimization of mechanical and transport properties and establishing structure – property relationships for this important class of network materials.

Uniaxial compression and recovery of VACNT forests

VACNT forests represent a promising class of mechanically strong and resilient lightweight materials, capable of supporting large reversible deformation and absorbing mechanical energy. The mechanical response of VACNT forests to uniaxial compression is defined by various factors, including the material microstructure, its density, height, rate of deformation, and the nature of interaction between carbon nanotubes (CNTs) and the compressing indenter. In this chapter, we used a coarse-grained mesoscopic model to simulate the uniaxial compression of VACNT samples with different densities and microstructures (bundle size distribution and degree of nanotube alignment) to obtain a clear microscopic picture of the structural changes in networks of interconnected CNT bundles undergoing mechanical deformation. The key factors responsible for the coordinated buckling of CNTs, reversible and irreversible modes of deformation in VACNT arrays undergoing uniaxial compression, as well as hysteresis behavior in VACNT arrays subjected to five loading–unloading cycles are investigated in the simulations. The simulation results reveal the important role of the collective buckling of CNTs across bundle cross-sections as well as a complex deformation behavior of VACNT arrays defined by an interplay of different modes of bundle deformation. The loading rate and the CNT attachment to the indenter are found to have a strong effect on the deformation mechanisms and the overall mechanical behavior of VACNT forests. A good agreement with experimental data from *in situ* mechanical tests is observed for the general trends and magnitudes of loss coefficients predicted in the simulations. The forest morphology can strongly alter the mechanical behavior of VACNT arrays with nominally the same general characteristics, such as CNT radius, length, and material density, thus suggesting the opportunity for substantial enhancement of the mechanical properties through the microstructure modification.

Mechanism of deformation and phase transformation during uniaxial compression of VACNT forests

VACNT forests behave mechanically as foams when compressed, exhibiting a characteristic non-linear three stage stress-strain response. However, the fiber structure of VACNT forests is unlike that of cellular foams, and the deformation behavior can be quite different. While numerous works have addressed the mechanical response of forests undergoing uniaxial compression, there still exists uncertainty about the underlying mechanisms of deformation. In this chapter, we presented the results of the uniaxial compression of a VACNT forest with 2 μm long CNTs, and three structurally distinct forests composed of 0.6 μm long CNTs. These simulations showed the formation of a localized densified layer near the compressing indenter in coexistence with the relatively rarified and vertically oriented phase characterizing the unstrained forest. The mechanisms governing the formation and growth of the densified layer are revealed, and an energy analysis of the bending and CNT-CNT interaction energies therein demonstrate the layer's thermodynamic stability. Additionally, the origin of the collective buckling of CNT bundles localized within a forest cross-section is revealed.

Development of a coarse-grained potential for metals

A general purpose coarse-grained model for metals, the Quasi-coarse-grained dynamics (QCGD) model is reviewed and modified for conditions where the assumption of local thermal equilibrium is not valid. In particular, a heat bath approach is used to implicitly represent the degrees of freedom missing from the coarse-grained model so that the correct heat capacity of the mesoscale metal is used in simulations of dynamic loading. In addition, an additional force scaling between coarse-grained units yields added to the QCGD results in the correct thermophysical properties even at high levels of coarse-graining.

Ballistic impact resistance of CNT films

Protecting satellites from space debris or micrometeorites is a growing priority with the renewal of interest in space exploration and the increasing reliance on satellites. CNTs, due to their attractive mechanical properties and their low density, represents an ideal material for the shielding of spacecraft. A series of simulations of mesoscopic simulations of Pt nanoparticle impact on CNT films are presented where the nanoparticle is represented by the modified QCGD model. The

change in velocity of a projectile impacting a 100 nm CNT film at five velocities ranging from 100 – 2000 m/s were fitted to an analytical model to reveal the projectile velocity dependence on its deceleration. An additional simulation using a 300 nm thick CNT film resulted in a greater than expected deceleration based on the results obtained for the 100 nm thick film, suggesting that the film thickness for networked CNT films can significantly contribute to the stopping power of the material.

8.2 Impact of work

The impact of the key results of this work on the advancement of computational methodology and expansion of the areas of application of CNT-based network materials is briefly summarized below.

1. Development of a computational procedure for the generation of realistic *in silico* VACNT materials with controllable CNT bundle size distribution and orientation. By enabling the generation of samples with precise structural characteristics, this method opens a broad range of opportunities for computational studies of the structure-property relationships in CNT network materials.
2. The mechanical behavior of VACNT forests undergoing uniaxial compression was simulated in a variety of systems (forest structure and density, compression rate, and CNT interaction with the indenter). The results of the simulations create a solid general foundation for estimating the mechanical properties of short VACNTs undergoing uniaxial compression for different loading conditions and sample structures.
3. Simulations of the uniaxial compression of VACNT forests on the micron length scale revealed the mechanisms of formation of a localized densified phase near the indenter, and an understanding of how the densified layer forms has been improved. Since a two-phase system has inhomogeneous material properties, future work focused on determining the factors contributing to the thickness and properties of the densified phase will eventually allow for better control of the material properties of forests undergoing uniaxial compression.
4. Building on the QCGD method, a general coarse-grained description of metals suitable for conditions where the assumption of local thermal equilibrium is invalid was developed. The two major modifications to the model include adding a heat bath description of the

degrees of freedom not explicitly present in the coarse-grained metal and recovering the atomistic thermophysical properties with appropriate scaling of interaction forces. The modified QCGD model can serve as a computationally efficient way to study metals and alloys within the general framework of mesoscopic materials modeling.

5. Initial work on the nanoparticle impact on CNT films has revealed the dependence of the penetration depth of the projectile into the film on its initial velocity and the thickness of the film. This work can be extended to develop a general analytical description of the penetration depth of nano-projectiles into CNT films, and has important implications for ballistic shielding of aerospace vehicles and satellites. In addition, VACNT forests have been shown to capture all components of a metal plume generated by laser ablation, and a model to predict the penetration of nanoparticles into the forest could serve as the foundation of a characterization technique to determine the plume composition and nanoparticle size distribution.

8.3 Future work

8.3.1 Ballistic impact resistance of CNT films

Multiple future directions for the work on the ballistic resistance on CNT materials are readily apparent. It has already been determined that the CNT film thickness plays a role in the penetration depth of the projectile, but further simulations will be needed to reveal the nature of this trend with increasing film thickness. In addition, the stopping power of the CNT film has not been measured as a function of CNT length, where an increased length may result in better entanglement between nanotubes and result in a better areal distribution of energy. Film density represents another important variable. The role of CNT length and film density will be the topic of work in the immediate future. Furthermore, the dependence of penetration depth on projectile size relative to the average pore size of the film or the thickness of the nanotube bundles is another avenue worth exploring. Ultimately, the objective of this work is to derive a general analytical expression for estimating the penetration depth of a projectile into a CNT film.

Another important future direction is the continuation of the early work of Geohegan *et al.* at ORNL where it was shown that VACNT forests can completely capture a metallic plume generated by laser ablation. Modeling of the penetration depth of metallic nanoparticles of different sizes and compositions into VACNT forests with distinct structural characteristics can

contribute to the development of a characterization technique for ablation plumes of metals and alloys.

8.3.2 *Thermal properties of CNT materials*

The bulk of this dissertation has focused on the mechanical properties of CNT materials. However, as discussed in sections 1.2 and 3.5, the thermal properties of CNT network materials is also strongly impacted by structural characteristics of the sample. The introduction of a method to generate VACNT forests with controllable structure in chapter 3 makes a study on the structure dependent thermal properties a practical endeavor. Moreover, the evolution of the thermal properties of VACNT forests undergoing uniaxial compression, both in the lateral and longitudinal directions, may prove interesting for anisotropic thermal conduction in foam materials, using the samples generated in chapter 3 and the deformed forests from chapters 4 and 5.

References

- [1] M.-F. Yu, O. Lourie, M.J. Dyer, K. Moloni, T.F. Kelly, R.S. Ruoff, Strength and Breaking Mechanism of Multiwalled Carbon Nanotubes Under Tensile Load, *Science* 287 (2000) 637.
- [2] E. Pop, D. Mann, Q. Wang, K. Goodson, H. Dai, Thermal Conductance of an Individual Single-Wall Carbon Nanotube above Room Temperature, *Nano Lett.* 6 (2006) 96-100.
- [3] S. Huang, X. Cai, J. Liu, Growth of Millimeter-Long and Horizontally Aligned Single-Walled Carbon Nanotubes on Flat Substrates, *J. Am. Chem. Soc.* 125 (2003) 5636-5637.
- [4] S. Basu-Dutt, M.L. Minus, R. Jain, D. Nepal, S. Kumar, Chemistry of Carbon Nanotubes for Everyone, *J. Chem. Educ.* 89 (2012) 221-229.
- [5] M. Ouyang, J.-L. Huang, C.M. Lieber, Fundamental Electronic Properties and Applications of Single-Walled Carbon Nanotubes, *Acc. Chem. Res.* 35 (2002) 1018-1025.
- [6] X. Gui, A. Cao, J. Wei, H. Li, Y. Jia, Z. Li, L. Fan, K. Wang, H. Zhu, D. Wu, Soft, Highly Conductive Nanotube Sponges and Composites with Controlled Compressibility, *ACS Nano* 4 (2010) 2320-2326.
- [7] J. Zou, J. Liu, A.S. Karakoti, A. Kumar, D. Joung, Q. Li, S.I. Khondaker, S. Seal, L. Zhai, Ultralight Multiwalled Carbon Nanotube Aerogel, *ACS Nano* 4 (2010) 7293-7302.
- [8] T.V. Sreekumar, T. Liu, S. Kumar, L.M. Ericson, R.H. Hauge, R.E. Smalley, Single-Wall Carbon Nanotube Films, *Chem. Mater.* 15 (2003) 175-178.
- [9] F. Hennrich, S. Lebedkin, S. Malik, J. Tracy, M. Barczewski, H. Rosner, M. Kappes, Preparation, characterization and applications of free-standing single walled carbon nanotube thin films, *PCCP* 4 (2002) 2273-2277.
- [10] H. Muramatsu, T. Hayashi, Y.A. Kim, D. Shimamoto, Y.J. Kim, K. Tantrakarn, M. Endo, M. Terrones, M.S. Dresselhaus, Pore structure and oxidation stability of double-walled carbon nanotube-derived bucky paper, *Chem. Phys. Lett.* 414 (2005) 444-448.
- [11] W. Ma, L. Song, R. Yang, T. Zhang, Y. Zhao, L. Sun, Y. Ren, D. Liu, L. Liu, J. Shen, Z. Zhang, Y. Xiang, W. Zhou, S. Xie, Directly Synthesized Strong, Highly Conducting, Transparent Single-Walled Carbon Nanotube Films, *Nano Lett.* 7 (2007) 2307-2311.
- [12] M. Xu, D.N. Futaba, M. Yumura, K. Hata, Alignment Control of Carbon Nanotube Forest from Random to Nearly Perfectly Aligned by Utilizing the Crowding Effect, *ACS Nano* 6 (2012) 5837-5844.
- [13] D.N. Futaba, K. Hata, T. Yamada, T. Hiraoka, Y. Hayamizu, Y. Kakudate, O. Tanaike, H. Hatori, M. Yumura, S. Iijima, Shape-engineerable and highly densely packed single-walled carbon nanotubes and their application as super-capacitor electrodes, *Nat. Mater.* 5 (2006) 987-994.
- [14] Z. Wang, Z. Liang, B. Wang, C. Zhang, L. Kramer, Processing and property investigation of single-walled carbon nanotube (SWNT) buckypaper/epoxy resin matrix nanocomposites, *Composites Part A: Applied Science and Manufacturing* 35 (2004) 1225-1232.
- [15] P.G. Whitten, G.M. Spinks, G.G. Wallace, Mechanical properties of carbon nanotube paper in ionic liquid and aqueous electrolytes, *Carbon* 43 (2005) 1891-1896.
- [16] R.L.D. Whitby, T. Fukuda, T. Maekawa, S.L. James, S.V. Mikhalovsky, Geometric control and tuneable pore size distribution of buckypaper and buckydiscs, *Carbon* 46 (2008) 949-956.
- [17] P. Poulin, B. Vigolo, P. Launois, Films and fibers of oriented single wall nanotubes, *Carbon* 40 (2002) 1741-1749.
- [18] X. Zhang, K. Jiang, C. Feng, P. Liu, L. Zhang, J. Kong, T. Zhang, Q. Li, S. Fan, Spinning and Processing Continuous Yarns from 4-Inch Wafer Scale Super-Aligned Carbon Nanotube Arrays, *Adv. Mater.* 18 (2006) 1505-1510.

- [19] N. Behabtu, C.C. Young, D.E. Tsentalovich, O. Kleinerman, X. Wang, A.W.K. Ma, E.A. Bengio, R.F. ter Waarbeek, J.J. de Jong, R.E. Hoogerwerf, S.B. Fairchild, J.B. Ferguson, B. Maruyama, J. Kono, Y. Talmon, Y. Cohen, M.J. Otto, M. Pasquali, Strong, Light, Multifunctional Fibers of Carbon Nanotubes with Ultrahigh Conductivity, *Science* 339 (2013) 182.
- [20] L. Zhang, G. Zhang, C. Liu, S. Fan, High-Density Carbon Nanotube Buckypapers with Superior Transport and Mechanical Properties, *Nano Lett.* 12 (2012) 4848-4852.
- [21] L.A. Girifalco, M. Hodak, R.S. Lee, Carbon nanotubes, buckyballs, ropes, and a universal graphitic potential, *Physical Review B* 62 (2000) 13104-13110.
- [22] A. Thess, R. Lee, P. Nikolaev, H. Dai, P. Petit, J. Robert, C. Xu, Y.H. Lee, S.G. Kim, A.G. Rinzler, D.T. Colbert, G.E. Scuseria, D. Tománek, J.E. Fischer, R.E. Smalley, Crystalline Ropes of Metallic Carbon Nanotubes, *Science* 273 (1996) 483.
- [23] A.G. Rinzler, J. Liu, H. Dai, P. Nikolaev, C.B. Huffman, F.J. Rodríguez-Macías, P.J. Boul, A.H. Lu, D. Heymann, D.T. Colbert, R.S. Lee, J.E. Fischer, A.M. Rao, P.C. Eklund, R.E. Smalley, Large-scale purification of single-wall carbon nanotubes: process, product, and characterization, *Appl. Phys. A* 67 (1998) 29-37.
- [24] U. Dettlaff-Weglikowska, V. Skákalová, R. Graupner, S.H. Jhang, B.H. Kim, H.J. Lee, L. Ley, Y.W. Park, S. Berber, D. Tománek, S. Roth, Effect of SOCl₂ Treatment on Electrical and Mechanical Properties of Single-Wall Carbon Nanotube Networks, *J. Am. Chem. Soc.* 127 (2005) 5125-5131.
- [25] K. Eom, K. Nam, H. Jung, P. Kim, M.S. Strano, J.-H. Han, T. Kwon, Controllable viscoelastic behavior of vertically aligned carbon nanotube arrays, *Carbon* 65 (2013) 305-314.
- [26] R.S. Prasher, X.J. Hu, Y. Chalopin, N. Mingo, K. Lofgreen, S. Volz, F. Cleri, P. Keblinski, Turning Carbon Nanotubes from Exceptional Heat Conductors into Insulators, *Phys. Rev. Lett.* 102 (2009) 105901.
- [27] I. Ivanov, A. Puzos, G. Eres, H. Wang, Z. Pan, H. Cui, R. Jin, J. Howe, D.B. Geohegan, Fast and highly anisotropic thermal transport through vertically aligned carbon nanotube arrays, *Appl. Phys. Lett.* 89 (2006) 223110.
- [28] O. Yaglioglu, A.Y. Cao, A.J. Hart, R. Martens, A.H. Slocum, Wide range control of microstructure and mechanical properties of carbon nanotube forests: A comparison between fixed and floating catalyst CVD techniques, *Adv. Funct. Mater.* 22 (2012) 5028-5037.
- [29] A. Cao, P.L. Dickrell, W.G. Sawyer, M.N. Ghasemi-Nejhad, P.M. Ajayan, Super-compressible foamlike carbon nanotube films, *Science* 310 (2005) 1307-1310.
- [30] Q. Zhang, Y.C. Lu, F. Du, L. Dai, J. Baur, D.C. Foster, Viscoelastic creep of vertically aligned carbon nanotubes, *J. Phys. D: Appl. Phys.* 43 (2010) 315401.
- [31] S.B. Hutchens, L.J. Hall, J.R. Greer, In situ mechanical testing reveals periodic buckle nucleation and propagation in carbon nanotube bundles, *Adv. Funct. Mater.* 20 (2010) 2338-2346.
- [32] S. Pathak, E.J. Lim, P.P. Abadi, S. Graham, B.A. Cola, J.R. Greer, Higher recovery and better energy dissipation at faster strain rates in carbon nanotube bundles: An in-situ study, *ACS Nano* 6 (2012) 2189-2197.
- [33] B.J. Alder, T.E. Wainwright, Phase Transition for a Hard Sphere System, *The Journal of Chemical Physics* 27 (1957) 1208-1209.
- [34] B.J. Alder, T.E. Wainwright, Studies in Molecular Dynamics. I. General Method, *The Journal of Chemical Physics* 31 (1959) 459-466.
- [35] M.P. Allen, D.J. Tildesley, *Computer Simulation of Liquids*, 2 ed., Oxford university press, New York, 2017.

- [36] T.C. Germann, K.A.I. Kadau, TRILLION-ATOM MOLECULAR DYNAMICS BECOMES A REALITY, *International Journal of Modern Physics C* 19 (2008) 1315-1319.
- [37] D.E. Shaw, R.O. Dror, J.K. Salmon, J.P. Grossman, K.M. Mackenzie, J.A. Bank, C. Young, M.M. Deneroff, B. Batson, K.J. Bowers, E. Chow, M.P. Eastwood, D.J. Ierardi, J.L. Klepeis, J.S. Kuskin, R.H. Larson, K. Lindorff-Larsen, P. Maragakis, M.A. Moraes, S. Piana, Y. Shan, B. Towles, Millisecond-scale molecular dynamics simulations on Anton, *Proceedings of the Conference on High Performance Computing Networking, Storage and Analysis, ACM, Portland, Oregon, 2009*, pp. 1-11.
- [38] B.I. Yakobson, C.J. Brabec, J. Bernholc, Nanomechanics of carbon tubes: Instabilities beyond linear response, *Phys. Rev. Lett.* 76 (1996) 2511-2514.
- [39] S. Iijima, C. Brabec, A. Maiti, J. Bernholc, Structural flexibility of carbon nanotubes, *J. Chem. Phys.* 104 (1996) 2089-2092.
- [40] T. Xiao, K. Liao, Nonlinear elastic properties of carbon nanotubes subjected to large axial deformations, *Phys. Rev. B* 66 (2002) 153407.
- [41] T. Belytschko, S.P. Xiao, G.C. Schatz, R.S. Ruoff, Atomistic simulations of nanotube fracture, *Phys. Rev. B* 65 (2002) 235430.
- [42] S.L. Mielke, D. Troya, S. Zhang, J.L. Li, S.P. Xiao, R. Car, R.S. Ruoff, G.C. Schatz, T. Belytschko, The role of vacancy defects and holes in the fracture of carbon nanotubes, *Chem. Phys. Lett.* 390 (2004) 413-420.
- [43] K.M. Liew, X.Q. He, C.H. Wong, On the study of elastic and plastic properties of multi-walled carbon nanotubes under axial tension using molecular dynamics simulation, *Acta Mater.* 52 (2004) 2521-2527.
- [44] C.M. Wang, Y.Y. Zhang, Y. Xiang, J.N. Reddy, Recent studies on buckling of carbon Nanotubes, *Appl. Mech. Rev.* 63 (2010) 030804.
- [45] J. Park, M.F.P. Bifano, V. Prakash, Sensitivity of thermal conductivity of carbon nanotubes to defect concentrations and heat-treatment, *J. Appl. Phys.* 113 (2013) 034312.
- [46] S. Berber, Y.K. Kwon, D. Tomanek, Unusually high thermal conductivity of carbon nanotubes, *Phys. Rev. Lett.* 84 (2000) 4613-4616.
- [47] R.N. Salaway, L.V. Zhigilei, Molecular dynamics simulations of thermal conductivity of carbon nanotubes: Resolving the effects of computational parameters, *Int. J. Heat Mass Transfer* 70 (2014) 954-964.
- [48] Z.P. Xu, M.J. Buehler, Strain controlled thermomutability of single-walled carbon nanotubes, *Nanotechnology* 20 (2009) 185701.
- [49] C.L. Ren, W. Zhang, Z.J. Xu, Z.Y. Zhu, P. Huai, Thermal conductivity of single-walled carbon nanotubes under axial stress, *J. Phys. Chem. C* 114 (2010) 5786-5791.
- [50] W.J. Evans, M. Shen, P. Keblinski, Inter-tube thermal conductance in carbon nanotubes arrays and bundles: Effects of contact area and pressure, *Appl. Phys. Lett.* 100 (2012) 261908.
- [51] A.N. Volkov, R.N. Salaway, L.V. Zhigilei, Atomistic simulations, mesoscopic modeling, and theoretical analysis of thermal conductivity of bundles composed of carbon nanotubes, *J. Appl. Phys.* 114 (2013) 104301.
- [52] L. Hu, A.J.H. McGaughey, Thermal conductance of the junction between single-walled carbon nanotubes, *Appl. Phys. Lett.* 105 (2014) 193104.
- [53] R.N. Salaway, L.V. Zhigilei, Thermal conductance of carbon nanotube contacts: Molecular dynamics simulations and general description of the contact conductance, *Phys. Rev. B* 94 (2016) 014308.

- [54] M.J. Buehler, Mesoscale modeling of mechanics of carbon nanotubes: Self-assembly, self-folding, and fracture, *J. Mater. Res.* 21 (2006) 2855-2869.
- [55] I. Ostanin, R. Ballarini, D. Potyondy, T. Dumitrică, A distinct element method for large scale simulations of carbon nanotube assemblies, *J. Mech. Phys. Solids* 61 (2013) 762-782.
- [56] L.V. Zhigilei, C. Wei, D. Srivastava, Mesoscopic model for dynamic simulations of carbon nanotubes, *Phys. Rev. B* 71 (2005) 165417.
- [57] A.N. Volkov, L.V. Zhigilei, Mesoscopic interaction potential for carbon nanotubes of arbitrary length and orientation, *J. Phys. Chem. C* 114 (2010) 5513-5531.
- [58] S.W. Cranford, M.J. Buehler, In silico assembly and nanomechanical characterization of carbon nanotube buckypaper, *Nanotechnology* 21 (2010) 265706.
- [59] A.N. Volkov, L.V. Zhigilei, Structural stability of carbon nanotube films: The role of bending buckling, *ACS Nano* 4 (2010) 6187-6195.
- [60] A.N. Volkov, L.V. Zhigilei, Scaling laws and mesoscopic modeling of thermal conductivity in carbon nanotube materials, *Phys. Rev. Lett.* 104 (2010) 215902.
- [61] E.A. Colbourn, *Computer Simulation of Polymers*, 1 ed., Longman 1994.
- [62] B. Xie, Y.L. Liu, Y.T. Ding, Q.S. Zheng, Z.P. Xu, Mechanics of carbon nanotube networks: microstructural evolution and optimal design, *Soft Matter* 7 (2011) 10039-10047.
- [63] C. Wang, B. Xie, Y.L. Liu, Z.P. Xu, Mechanotunable microstructures of carbon nanotube networks, *ACS Macro Lett.* 1 (2012) 1176-1179.
- [64] Y. Li, M. Kröger, Viscoelasticity of carbon nanotube buckypaper: Zipping-unzipping mechanism and entanglement effects, *Soft Matter* 8 (2012) 7822-7830.
- [65] Y. Li, M. Kröger, A theoretical evaluation of the effects of carbon nanotube entanglement and bundling on the structural and mechanical properties of buckypaper, *Carbon* 50 (2012) 1793-1806.
- [66] Y. Li, M. Kröger, Computational study on entanglement length and pore size of carbon nanotube buckypaper, *Appl. Phys. Lett.* 100 (2012) 021907.
- [67] M.G. Hahm, H.L. Wang, H.Y. Jung, S. Hong, S.G. Lee, S.R. Kim, M. Upmanyu, Y.J. Jung, Bundling dynamics regulates the active mechanics and transport in carbon nanotube networks and their nanocomposites, *Nanoscale* 4 (2012) 3584-3590.
- [68] J.H. Zhao, J.W. Jiang, L.F. Wang, W.L. Guo, T. Rabczuk, Coarse-grained potentials of single-walled carbon nanotubes, *J. Mech. Phys. Solids* 71 (2014) 197-218.
- [69] Y. Won, Y. Gao, M.A. Panzer, R. Xiang, S. Maruyama, T.W. Kenny, W. Cai, K.E. Goodson, Zipping, entanglement, and the elastic modulus of aligned single-walled carbon nanotube films, *Proc. Natl. Acad. Sci. U.S.A.* 110 (2013) 20426-20430.
- [70] L.V. Zhigilei, R.N. Salaway, B.K. Wittmaack, A.N. Volkov, Computational Studies of Thermal Transport Properties of Carbon Nanotube Materials, in: A. Todri-Sanial, J. Dijon, A. Maffucci (Eds.), *Carbon Nanotubes for Interconnects: Process, Design and Applications*, Springer International Publishing, Cham, 2017, pp. 129-161.
- [71] M.R. Maschmann, Integrated simulation of active carbon nanotube forest growth and mechanical compression, *Carbon* 86 (2015) 26-37.
- [72] Y.Z. Wang, C. Gaidau, I. Ostanin, T. Dumitrică, Ring windings from single-wall carbon nanotubes: A distinct element method study, *Appl. Phys. Lett.* 103 (2013) 183902.
- [73] I. Ostanin, R. Ballarini, T. Dumitrică, Distinct element method modeling of carbon nanotube bundles with intertube sliding and dissipation, *J. Appl. Mech.* 81 (2014) 061004.

- [74] P.A. Cundall, Formulation of a three-dimensional distinct element model--Part 1. A scheme to detect and represent contacts in a system composed of many polyhedral blocks, *Int. J. Rock Mech. Min. Sci.* 25 (1988) 107-116.
- [75] P.A. Cundall, O.D.L. Strack, Discrete numerical model for granular assemblies, *Geotechnique* 29 (1979) 47-65.
- [76] A.N. Volkov, T. Shiga, D. Nicholson, J. Shiomi, L.V. Zhigilei, Effect of bending buckling of carbon nanotubes on thermal conductivity of carbon nanotube materials, *J. Appl. Phys.* 111 (2012) 053501.
- [77] W.M. Jacobs, D.A. Nicholson, H. Zemer, A.N. Volkov, L.V. Zhigilei, Acoustic energy dissipation and thermalization in carbon nanotubes: Atomistic modeling and mesoscopic description, *Phys. Rev. B* 86 (2012) 165414.
- [78] A.N. Volkov, L.V. Zhigilei, Heat conduction in carbon nanotube materials: Strong effect of intrinsic thermal conductivity of carbon nanotubes, *Appl. Phys. Lett.* 101 (2012) 043113.
- [79] L.V. Zhigilei, P.B.S. Kodali, B.J. Garrison, A Microscopic View of Laser Ablation, *The Journal of Physical Chemistry B* 102 (1998) 2845-2853.
- [80] I. Nikiforov, D.B. Zhang, R.D. James, T. Dumitrică, Wavelike rippling in multiwalled carbon nanotubes under pure bending, *Appl. Phys. Lett.* 96 (2010) 123107.
- [81] J.E. Jones, On the determination of molecular fields. —II. From the equation of state of a gas, *Proceedings of the Royal Society of London. Series A* 106 (1924) 463.
- [82] S.J. Stuart, A.B. Tutein, J.A. Harrison, A reactive potential for hydrocarbons with intermolecular interactions, *J. Chem. Phys.* 112 (2000) 6472-6486.
- [83] B. Bhushan, Nanotribology of carbon nanotubes, *J. Phys.: Condens. Matter* 20 (2008) 365214.
- [84] O. Suekane, A. Nagataki, H. Mori, Y. Nakayama, Static friction force of carbon nanotube surfaces, *Appl. Phys. Express* 1 (2008) 064001.
- [85] S. Akita, Y. Nakayama, Interlayer Sliding Force of Individual Multiwall Carbon Nanotubes, *Jpn. J. Appl. Phys.* 42 (2003) 4830-4833.
- [86] T. Filleter, S. Yockel, M. Naraghi, J.T. Paci, O.C. Compton, M.L. Mayes, S.T. Nguyen, G.C. Schatz, H.D. Espinosa, Experimental-Computational Study of Shear Interactions within Double-Walled Carbon Nanotube Bundles, *Nano Lett.* 12 (2012) 732-742.
- [87] J.T. Paci, A.o. Furmanchuk, H.D. Espinosa, G.C. Schatz, Shear and Friction between Carbon Nanotubes in Bundles and Yarns, *Nano Lett.* 14 (2014) 6138-6147.
- [88] H.J.C. Berendsen, J.P.M. Postma, W.F. Vangunsteren, A. Dinola, J.R. Haak, Molecular dynamics with coupling to an external bath, *J. Chem. Phys.* 81 (1984) 3684-3690.
- [89] S. Nosé, A unified formulation of the constant temperature molecular dynamics methods, *The Journal of Chemical Physics* 81 (1984) 511-519.
- [90] W.G. Hoover, Canonical dynamics: Equilibrium phase-space distributions, *Phys. Rev. A* 31 (1985) 1695-1697.
- [91] D.S. Ivanov, L.V. Zhigilei, Combined atomistic-continuum modeling of short-pulse laser melting and disintegration of metal films, *Physical Review B* 68 (2003) 064114.
- [92] S.T. Huxtable, D.G. Cahill, S. Shenogin, L. Xue, R. Ozisik, P. Barone, M. Usrey, M.S. Strano, G. Siddons, M. Shim, P. Keblinski, Interfacial heat flow in carbon nanotube suspensions, *Nat. Mater.* 2 (2003) 731.
- [93] S. Shenogin, L. Xue, R. Ozisik, P. Keblinski, D.G. Cahill, Role of thermal boundary resistance on the heat flow in carbon-nanotube composites, *J. Appl. Phys.* 95 (2004) 8136-8144.
- [94] H. Jiang, M.F. Yu, B. Liu, Y. Huang, Intrinsic Energy Loss Mechanisms in a Cantilevered Carbon Nanotube Beam Oscillator, *Phys. Rev. Lett.* 93 (2004) 185501.

- [95] A. Seiji, S. Shintaro, N. Yoshikazu, Energy Loss of Carbon Nanotube Cantilevers for Mechanical Vibration, *Jpn. J. Appl. Phys.* 46 (2007) 6295.
- [96] D. Danailov, P. Keblinski, S. Nayak, P.M. Ajayan, Bending Properties of Carbon Nanotubes Encapsulating Solid Nanowires, *Journal of Nanoscience and Nanotechnology* 2 (2002) 503-507.
- [97] P.A. Greaney, G. Lani, G. Cicero, J.C. Grossman, Anomalous Dissipation in Single-Walled Carbon Nanotube Resonators, *Nano Lett.* 9 (2009) 3699-3703.
- [98] *Nanotube Superfiber Materials*, William Andrew Publishing, Boston, 2014.
- [99] *Carbon Nanotube for Interconnects: Process, Design and Applications*, Springer 2017.
- [100] E.G. Rakov, Materials made of carbon nanotubes. The carbon nanotube forest, *Russ. Chem. Rev.* 82 (2013) 538-566.
- [101] W. Cho, M. Schulz, V. Shanov, Growth and characterization of vertically aligned centimeter long CNT arrays, *Carbon* 72 (2014) 264-273.
- [102] M. Pinault, V. Pichot, H. Khodja, P. Launois, C. Reynaud, M. Mayne-L'Hermite, Evidence of Sequential Lift in Growth of Aligned Multiwalled Carbon Nanotube Multilayers, *Nano Lett.* 5 (2005) 2394-2398.
- [103] Q. Zhang, W. Zhou, W. Qian, R. Xiang, J. Huang, D. Wang, F. Wei, Synchronous Growth of Vertically Aligned Carbon Nanotubes with Pristine Stress in the Heterogeneous Catalysis Process, *The Journal of Physical Chemistry C* 111 (2007) 14638-14643.
- [104] A.A. Puzov, G. Eres, C.M. Rouleau, I.N. Ivanov, D.B. Geohegan, Real-time imaging of vertically aligned carbon nanotube array growth kinetics, *Nanotechnology* 19 (2008) 055605.
- [105] J.B. In, C.P. Grigoropoulos, A.A. Chernov, A. Noy, Growth Kinetics of Vertically Aligned Carbon Nanotube Arrays in Clean Oxygen-free Conditions, *ACS Nano* 5 (2011) 9602-9610.
- [106] M.H. Rummeli, C. Kramberger, F. Schäffel, E. Borowiak-Palen, T. Gemming, B. Rellinghaus, O. Jost, M. Löffler, P. Ayala, T. Pichler, R.J. Kalenczuk, Catalyst size dependencies for carbon nanotube synthesis, *physica status solidi (b)* 244 (2007) 3911-3915.
- [107] P.B. Amama, C.L. Pint, S.M. Kim, L. McJilton, K.G. Eyink, E.A. Stach, R.H. Hauge, B. Maruyama, Influence of Alumina Type on the Evolution and Activity of Alumina-Supported Fe Catalysts in Single-Walled Carbon Nanotube Carpet Growth, *ACS Nano* 4 (2010) 895-904.
- [108] L. Zhu, D.W. Hess, C.-P. Wong, Monitoring Carbon Nanotube Growth by Formation of Nanotube Stacks and Investigation of the Diffusion-Controlled Kinetics, *The Journal of Physical Chemistry B* 110 (2006) 5445-5449.
- [109] G. Chen, D.N. Futaba, H. Kimura, S. Sakurai, M. Yumura, K. Hata, Absence of an Ideal Single-Walled Carbon Nanotube Forest Structure for Thermal and Electrical Conductivities, *ACS Nano* 7 (2013) 10218-10224.
- [110] F. Data files defining the structures of VACNT computational samples FA, FC, and FD are accessible from. <http://www.faculty.virginia.edu/CompMat/VACNT-samples/>.
- [111] Y. Gogotsi, High-Temperature Rubber Made from Carbon Nanotubes, *Science* 330 (2010) 1332.
- [112] A. Misra, J.R. Greer, C. Daraio, Strain Rate Effects in the Mechanical Response of Polymer-Anchored Carbon Nanotube Foams, *Adv. Mater.* 21 (2009) 334-338.
- [113] O. Yaglioglu, R. Martens, A.J. Hart, A.H. Slocum, Conductive Carbon Nanotube Composite Microprobes, *Adv. Mater.* 20 (2008) 357-362.
- [114] O. Yaglioglu, R. Martens, A. Cao, A.H. Slocum, Compliant Carbon Nanotube-Metal Contact Structures, 2011 IEEE 57th Holm Conference on Electrical Contacts (Holm), 2011, pp. 1-5.
- [115] X. Li, G. Zhu, J.S. Dordick, P.M. Ajayan, Compression-Modulated Tunable-Pore Carbon-Nanotube Membrane Filters, *Small* 3 (2007) 595-599.

- [116] J. Suhr, P. Victor, L. Ci, S. Sreekala, X. Zhang, O. Nalamasu, P.M. Ajayan, Fatigue resistance of aligned carbon nanotube arrays under cyclic compression, *Nat. Nanotechnol.* 2 (2007) 417-421.
- [117] T. Tong, Y. Zhao, L. Delzeit, A. Kashani, M. Meyyappan, A. Majumdar, Height independent compressive modulus of vertically aligned carbon nanotube arrays, *Nano Lett.* 8 (2008) 511-515.
- [118] P.D. Bradford, X. Wang, H.B. Zhao, Y.T. Zhu, Tuning the compressive mechanical properties of carbon nanotube foam, *Carbon* 49 (2011) 2834-2841.
- [119] C.P. Deck, J. Flowers, G.S.B. McKee, K. Vecchio, Mechanical behavior of ultralong multiwalled carbon nanotube mats, *J. Appl. Phys.* 101 (2007) 023512.
- [120] M. Xu, D.N. Futaba, T. Yamada, M. Yumura, K. Hata, Carbon Nanotubes with Temperature-Invariant Viscoelasticity from -196° to 1000°C , *Science* 330 (2010) 1364.
- [121] M. Kumar, Y. Ando, Chemical Vapor Deposition of Carbon Nanotubes: A Review on Growth Mechanism and Mass Production, *Journal of Nanoscience and Nanotechnology* 10 (2010) 3739-3758.
- [122] E.F. Antunes, A.O. Lobo, E.J. Corat, V.J. Trava-Airoldi, A.A. Martin, C. Veríssimo, Comparative study of first- and second-order Raman spectra of MWCNT at visible and infrared laser excitation, *Carbon* 44 (2006) 2202-2211.
- [123] E.F. Antunes, A.O. Lobo, E.J. Corat, V.J. Trava-Airoldi, Influence of diameter in the Raman spectra of aligned multi-walled carbon nanotubes, *Carbon* 45 (2007) 913-921.
- [124] S. Pathak, N. Mohan, E. Decolvenaere, A. Needleman, M. Bedewy, A.J. Hart, J.R. Greer, Local relative density modulates failure and strength in vertically aligned carbon nanotubes, *ACS Nano* 7 (2013) 8593-8604.
- [125] L. Yupeng, K. Junmo, C. Jae-Boong, N. Jae-Do, S. Jonghwan, Determination of material constants of vertically aligned carbon nanotube structures in compressions, *Nanotechnology* 26 (2015) 245701.
- [126] A.A. Zbib, S.D. Mesarovic, E.T. Lilleodden, D. McClain, J. Jiao, D.F. Bahr, The coordinated buckling of carbon nanotube turfs under uniform compression, *Nanotechnology* 19 (2008) 175704.
- [127] K. Kordás, G. Tóth, P. Moilanen, M. Kumpumäki, J. Vähäkangas, A. Uusimäki, R. Vajtai, P.M. Ajayan, Chip cooling with integrated carbon nanotube microfin architectures, *Appl. Phys. Lett.* 90 (2007) 123105.
- [128] F. Yifeng, N. Nabi, W. Teng, W. Shun, H. Zhili, C. Björn, Z. Yan, W. Xiaojing, L. Johan, A complete carbon-nanotube-based on-chip cooling solution with very high heat dissipation capacity, *Nanotechnology* 23 (2012) 045304.
- [129] H. Huang, C.H. Liu, Y. Wu, S. Fan, Aligned Carbon Nanotube Composite Films for Thermal Management, *Adv. Mater.* 17 (2005) 1652-1656.
- [130] X. Liu, Y. Zhang, A.M. Cassell, B.A. Cruden, Implications of catalyst control for carbon nanotube based thermal interface materials, *J. Appl. Phys.* 104 (2008) 084310.
- [131] P.E. Lyons, S. De, F. Blighe, V. Nicolosi, L.F.C. Pereira, M.S. Ferreira, J.N. Coleman, The relationship between network morphology and conductivity in nanotube films, *J. Appl. Phys.* 104 (2008) 044302.
- [132] A. Megumi, H. Kenji, N.F. Don, M. Kohei, B. Tetsuya, Y. Motoo, Thermal Diffusivity of Single-Walled Carbon Nanotube Forest Measured by Laser Flash Method, *Jpn. J. Appl. Phys.* 48 (2009) 05EC07.
- [133] S. Kaur, N. Raravikar, B.A. Helms, R. Prasher, D.F. Ogletree, Enhanced thermal transport at covalently functionalized carbon nanotube array interfaces, *Nature Communications* 5 (2014) 3082.

- [134] J. Hone, M.C. Llaguno, N.M. Nemes, A.T. Johnson, J.E. Fischer, D.A. Walters, M.J. Casavant, J. Schmidt, R.E. Smalley, Electrical and thermal transport properties of magnetically aligned single wall carbon nanotube films, *Appl. Phys. Lett.* 77 (2000) 666-668.
- [135] P. Gonnet, Z. Liang, E.S. Choi, R.S. Kadambala, C. Zhang, J.S. Brooks, B. Wang, L. Kramer, Thermal conductivity of magnetically aligned carbon nanotube buckypapers and nanocomposites, *Current Applied Physics* 6 (2006) 119-122.
- [136] M. Fujii, X. Zhang, H. Xie, H. Ago, K. Takahashi, T. Ikuta, H. Abe, T. Shimizu, Measuring the Thermal Conductivity of a Single Carbon Nanotube, *Phys. Rev. Lett.* 95 (2005) 065502.
- [137] L. Qingwei, L. Changhong, W. Xueshen, F. Shoushan, Measuring the thermal conductivity of individual carbon nanotubes by the Raman shift method, *Nanotechnology* 20 (2009) 145702.
- [138] A.A. Balandin, Thermal properties of graphene and nanostructured carbon materials, *Nat. Mater.* 10 (2011) 569.
- [139] J. Yang, S. Waltermire, Y. Chen, A.A. Zinn, T.T. Xu, D. Li, Contact thermal resistance between individual multiwall carbon nanotubes, *Appl. Phys. Lett.* 96 (2010) 023109.
- [140] T. Ji, Y. Feng, M. Qin, W. Feng, Thermal conducting properties of aligned carbon nanotubes and their polymer composites, *Composites Part A: Applied Science and Manufacturing* 91 (2016) 351-369.
- [141] J. Baur, E. Silverman, Challenges and Opportunities in Multifunctional Nanocomposite Structures for Aerospace Applications, *MRS Bull.* 32 (2007) 328-334.
- [142] T. Ishikawa, Overview of trends in advanced composite research and applications in Japan, *Adv. Compos. Mater* 15 (2006) 3-37.
- [143] R. Yadav, M. Naebe, X. Wang, B. Kandasubramanian, Body armour materials: from steel to contemporary biomimetic systems, *RSC Advances* 6 (2016) 115145-115174.
- [144] K. Mylvaganam, L.C. Zhang, Energy absorption capacity of carbon nanotubes under ballistic impact, *Appl. Phys. Lett.* 89 (2006) 123127.
- [145] K. Mylvaganam, L.C. Zhang, Ballistic resistance capacity of carbon nanotubes, *Nanotechnology* 18 (2007) 475701.
- [146] C. Daraio, V.F. Nesterenko, S. Jin, W. Wang, A.M. Rao, Impact response by a foamlike forest of coiled carbon nanotubes, *J. Appl. Phys.* 100 (2006) 064309.
- [147] L. Sun, R.F. Gibson, F. Gordaninejad, J. Suhr, Energy absorption capability of nanocomposites: A review, *Compos. Sci. Technol.* 69 (2009) 2392-2409.
- [148] F.A. Hill, T.F. Havel, A.J. Hart, C. Livermore, Storing elastic energy in carbon nanotubes, *J. Micromech. Microeng.* 19 (2009) 094015.
- [149] F.A. Hill, T.F. Havel, A.J. Hart, C. Livermore, Characterizing the failure processes that limit the storage of energy in carbon nanotube springs under tension, *J. Micromech. Microeng.* 20 (2010) 104012.
- [150] C.G. Wang, Y.P. Liu, J. Al-Ghalith, T. Dumitrică, M.K. Wadee, H.F. Tan, Buckling behavior of carbon nanotubes under bending: From ripple to kink, *Carbon* 102 (2016) 224-235.
- [151] H. Jackman, P. Krakhmalev, K. Svensson, Mechanical behavior of carbon nanotubes in the rippled and buckled phase, *J. Appl. Phys.* 117 (2015) 084318.
- [152] C.M. McCarter, R.F. Richards, S.D. Mesarovic, C.D. Richards, D.F. Bahr, D. McClain, J. Jiao, Mechanical compliance of photolithographically defined vertically aligned carbon nanotube turf, *J. Mater. Sci.* 41 (2006) 7872-7878.
- [153] S. Pathak, J.R. Raney, C. Daraio, Effect of morphology on the strain recovery of vertically aligned carbon nanotube arrays: An in situ study, *Carbon* 63 (2013) 303-316.

- [154] J.R. Raney, A. Misra, C. Daraio, Tailoring the microstructure and mechanical properties of arrays of aligned multiwall carbon nanotubes by utilizing different hydrogen concentrations during synthesis, *Carbon* 49 (2011) 3631-3638.
- [155] E.F. Antunes, A.O. Lobo, E.J. Corat, V.J. Trava-Airoldi, A.A. Martin, C. Verissimo, Comparative study of first- and second-order Raman spectra of MWCNT at visible and infrared laser excitation, *Carbon* 44 (2006) 2202-2211.
- [156] J.R. Raney, F. Fraternali, C. Daraio, Rate-independent dissipation and loading direction effects in compressed carbon nanotube arrays, *Nanotechnology* 24 (2013) 255707.
- [157] R.D. Downes, A. Hao, J.G. Park, Y.F. Su, R. Liang, B.D. Jensen, E.J. Siochi, K.E. Wise, Geometrically constrained self-assembly and crystal packing of flattened and aligned carbon nanotubes, *Carbon* 93 (2015) 953-966.
- [158] B.K. Wittmaack, A.H. Banna, A.N. Volkov, L.V. Zhigilei, Mesoscopic modeling of structural self-organization of carbon nanotubes into vertically aligned networks of nanotube bundles, *Carbon* 130 (2018) 69-86.
- [159] S.J. Kang, C. Kocabas, T. Ozel, M. Shim, N. Pimparkar, M.A. Alam, S.V. Rotkin, J.A. Rogers, High-performance electronics using dense, perfectly aligned arrays of single-walled carbon nanotubes, *Nat. Nanotechnol.* 2 (2007) 230-236.
- [160] E. Einarsson, H. Shiozawa, C. Kramberger, M.H. Rummeli, A. Gruneis, T. Pichler, S. Maruyama, Revealing the small-bundle internal structure of vertically aligned single-walled carbon nanotube films, *J. Phys. Chem. C* 111 (2007) 17861-17864.
- [161] G.F. Zhong, J.H. Warner, M. Fouquet, A.W. Robertson, B.A. Chen, J. Robertson, Growth of ultrahigh density single-walled carbon nanotube forests by improved catalyst design, *ACS Nano* 6 (2012) 2893-2903.
- [162] G.H. Chen, Y. Seki, H. Kimura, S. Sakurai, M. Yumura, K. Hata, D.N. Futaba, Diameter control of single-walled carbon nanotube forests from 1.3-3.0 nm by arc plasma deposition, *Sci. Rep.* 4 (2014) 3804.
- [163] S.B. Hutchens, A. Needleman, J.R. Greer, Analysis of uniaxial compression of vertically aligned carbon nanotubes, *J. Mech. Phys. Solids* 59 (2011) 2227-2237.
- [164] X.J. Liang, J.H. Shin, D. Magagnosc, Y.J. Jiang, S.J. Park, A.J. Hart, K. Turner, D.S. Gianola, P.K. Purohit, Compression and recovery of carbon nanotube forests described as a phase transition, *Int. J. Solids Struct.* 122 (2017) 196-209.
- [165] Information about the Comet supercomputer can be found by visiting <https://portal.xsede.org/sdsc-comet>.
- [166] J. Towns, T. Cockerill, M. Dahan, I. Foster, K. Gaither, A. Grimshaw, V. Hazlewood, S. Lathrop, D. Lifka, G.D. Peterson, R. Roskies, J.R. Scott, N. Wilkins-Diehr, XSEDE: Accelerating scientific discovery, *Comput. Sci. Eng.* 16 (2014) 62-74.
- [167] M. Alzaid, J. Roth, Y. Wang, E. Almutairi, S.L. Brown, T. Dumitrică, E.K. Hobbie, Enhancing the Elasticity of Ultrathin Single-Wall Carbon Nanotube Films with Colloidal Nanocrystals, *Langmuir* 33 (2017) 7889-7895.
- [168] R. Richards Jr, Principles of solid mechanics, CRC Press, New York, 2000.
- [169] M.R. Maschmann, Q.H. Zhang, F. Du, L.M. Dai, J. Baur, Length dependent foam-like mechanical response of axially indented vertically oriented carbon nanotube arrays, *Carbon* 49 (2011) 386-397.
- [170] V.S. Deshpande, M.F. Ashby, N.A. Fleck, Foam topology bending versus stretching dominated architectures, *Acta Mater.* 49 (2001) 1035-1040.
- [171] M.F. Ashby, The properties of foams and lattices, *Philos. T. R. Soc. A* 364 (2006) 15-30.

- [172] A. Qiu, S.P. Fowler, J. Jiao, D. Kiener, D.F. Bahr, Time-dependent contact behavior between diamond and a CNT turf, *Nanotechnology* 22 (2011) 295702.
- [173] R. Thevamaran, F. Fraternali, C. Daraio, Multiscale mass-spring model for high-rate compression of vertically aligned carbon nanotube foams, *J. Appl. Mech.* 81 (2014) 121006.
- [174] S.D. Mesarovic, C.M. McCarter, D.F. Bahr, H. Radhakrishnan, R.F. Richards, C.D. Richards, D. McClain, J. Jiao, Mechanical behavior of a carbon nanotube turf, *Scripta Mater.* 56 (2007) 157-160.
- [175] M.J. Buehler, Y. Kong, H.J. Gao, Deformation mechanisms of very long single-wall carbon nanotubes subject to compressive loading, *J. Eng. Mater. Technol.* 126 (2004) 245-249.
- [176] A. Sears, R.C. Batra, Macroscopic properties of carbon nanotubes from molecular-mechanics simulations, *Phys. Rev. B* 69 (2004) 235406.
- [177] N. Hu, K. Nunoya, D. Pan, T. Okabe, H. Fukunaga, Prediction of buckling characteristics of carbon nanotubes, *Int. J. Solids Struct.* 44 (2007) 6535-6550.
- [178] S. Adali, Variational principles for transversely vibrating multiwalled carbon nanotubes based on nonlocal Euler-Bernoulli beam model, *Nano Lett.* 9 (2009) 1737-1741.
- [179] S. Narendar, S.S. Gupta, S. Gopalakrishnan, Wave propagation in single-walled carbon nanotube under longitudinal magnetic field using nonlocal Euler-Bernoulli beam theory, *Appl. Math. Modell.* 36 (2012) 4529-4538.
- [180] M.F. Ashby, *Materials Selection in Mechanical Design*, 5 ed., Elsevier, Boston, 2016.
- [181] E.H.T. Teo, W.K.P. Yung, D.H.C. Chua, B.K. Tay, A carbon nanomattress: A new nanosystem with intrinsic, tunable, damping properties, *Adv. Mater.* 19 (2007) 2941-2945.
- [182] B.K. Wittmaack, A.N. Volkov, L.V. Zhigilei, Mesoscopic modeling of the uniaxial compression and recovery of vertically aligned carbon nanotube forests, *Compos. Sci. Technol.* (2018).
- [183] F. Fraternali, T. Blesgen, A. Amendola, C. Daraio, Multiscale mass-spring models of carbon nanotube foams, *J. Mech. Phys. Solids* 59 (2011) 89-102.
- [184] T. Blesgen, F. Fraternali, J.R. Raney, A. Amendola, C. Daraio, Continuum limits of bistable spring models of carbon nanotube arrays accounting for material damage, *Mechanics Research Communications* 45 (2012) 58-63.
- [185] G. Puglisi, L. Truskinovsky, Mechanics of a discrete chain with bi-stable elements, *J. Mech. Phys. Solids* 48 (2000) 1-27.
- [186] G. Puglisi, L. Truskinovsky, Rate independent hysteresis in a bi-stable chain, *J. Mech. Phys. Solids* 50 (2002) 165-187.
- [187] G. Puglisi, L. Truskinovsky, Thermodynamics of rate-independent plasticity, *J. Mech. Phys. Solids* 53 (2005) 655-679.
- [188] O.V. Kim, R.I. Litvinov, J.W. Weisel, M.S. Alber, Structural basis for the nonlinear mechanics of fibrin networks under compression, *Biomaterials* 35 (2014) 6739-6749.
- [189] O.V. Kim, X. Liang, R.I. Litvinov, J.W. Weisel, M.S. Alber, P.K. Purohit, Foam-like compression behavior of fibrin networks, *Biomechanics and Modeling in Mechanobiology* 15 (2016) 213-228.
- [190] G.F. Zhong, T. Iwasaki, H. Kawarada, Semi-quantitative study on the fabrication of densely packed and vertically aligned single-walled carbon nanotubes, *Carbon* 44 (2006) 2009-2014.
- [191] R Core Team, *R: A Language and Environment for Statistical Computing*, R Foundation for Statistical Computing, Vienna, Austria, 2016.
- [192] N. Smith, S.v.d. Walt, A better default colormap for Matplotlib, 2015. <https://www.youtube.com/watch?v=xAoljeRJ3IU>.

- [193] R.W. Cahn, P. Haasen, *Physical Metallurgy* (Fourth, Revised and Enhanced Edition), North-Holland, Oxford, 1996.
- [194] D.A. Porter, K.E. Easterling, M. Sherif, *Phase Transformations in Metals and Alloys*, 3rd ed., CRC Press 2009.
- [195] R. Abbaschian, R. Reed-Hill, *Physical Metallurgy Principles*, 4th ed., Cengage Learning 2008.
- [196] M.V. Shugaev, C. Wu, O. Armbruster, A. Naghilou, N. Brouwer, D.S. Ivanov, T.J.Y. Derrien, N.M. Bulgakova, W. Kautek, B. Rethfeld, L.V. Zhigilei, *Fundamentals of ultrafast laser-material interaction*, *MRS Bull.* 41 (2016) 960-968.
- [197] A.M. Dongare, D.D. Hass, L.V. Zhigilei, *Computational Investigation of the Effect of Cluster Impact Energy on the Microstructure of Films Grown by Cluster Deposition, Clusters and Nano-Assemblies*, World Scientific 2005, pp. 329-339.
- [198] M.S. Daw, M.I. Baskes, Embedded-atom method: Derivation and application to impurities, surfaces, and other defects in metals, *Physical Review B* 29 (1984) 6443-6453.
- [199] R.A. Johnson, Analytic nearest-neighbor model for fcc metals, *Physical Review B* 37 (1988) 3924-3931.
- [200] D.J. Oh, R.A. Johnson, Simple embedded atom method model for fcc and hcp metals, *J. Mater. Res.* 3 (1988) 471-478.
- [201] R.A. Johnson, D.J. Oh, Analytic embedded atom method model for bcc metals, *J. Mater. Res.* 4 (1989) 1195-1201.
- [202] A.M. Dongare, Quasi-coarse-grained dynamics: modelling of metallic materials at mesoscales, *Philos. Mag.* 94 (2014) 3877-3897.
- [203] J.R. Rumble (Ed.), *Handbook of Chemistry and Physics*, 98th ed., CRC Press 2017.
- [204] K. Toyoda, K. Nozawa, N. Matsukawa, S. Yoshii, Density Functional Theoretical Study of Graphene on Transition-Metal Surfaces: The Role of Metal d-Band in the Potential-Energy Surface, *The Journal of Physical Chemistry C* 117 (2013) 8156-8160.
- [205] Space Exploration Technologies Corp. <http://www.spacex.com/>. (Accessed April 2018).
- [206] NASA, Advanced Space Transportation Program: Paving the Highway to Space, 2008. <https://www.nasa.gov/centers/marshall/news/background/facts/astp.html>. (Accessed April 2018).
- [207] P.M. Ajayan, O.Z. Zhou, Applications of Carbon Nanotubes, in: M.S. Dresselhaus, G. Dresselhaus, P. Avouris (Eds.), *Carbon Nanotubes: Synthesis, Structure, Properties, and Applications*, Springer Berlin Heidelberg, Berlin, Heidelberg, 2001, pp. 391-425.
- [208] M.A. Makeev, D. Srivastava, Molecular dynamics simulations of hypersonic velocity impact protection properties of CNT/a-SiC composites, *Compos. Sci. Technol.* 68 (2008) 2451-2455.
- [209] K. Liu, Y. Sun, X. Lin, R. Zhou, J. Wang, S. Fan, K. Jiang, Scratch-Resistant, Highly Conductive, and High-Strength Carbon Nanotube-Based Composite Yarns, *ACS Nano* 4 (2010) 5827-5834.
- [210] N. Yamamoto, A. John Hart, E.J. Garcia, S.S. Wicks, H.M. Duong, A.H. Slocum, B.L. Wardle, High-yield growth and morphology control of aligned carbon nanotubes on ceramic fibers for multifunctional enhancement of structural composites, *Carbon* 47 (2009) 551-560.
- [211] S. Khatiwada, C.A. Armada, E.V. Barrera, Hypervelocity Impact Experiments on Epoxy/Ultra-high Molecular Weight Polyethylene Fiber Composites Reinforced with Single-walled Carbon Nanotubes, *Procedia Engineering* 58 (2013) 4-10.
- [212] C. Rouleau, A. Poretzky, D. Geohegan, Unpublished results, Oak Ridge National Laboratory.